

Dirk Spreemann
Yiannos Manoli

Electromagnetic Vibration Energy Harvesting Devices

Architectures, Design,
Modeling and Optimization



Springer

Electromagnetic Vibration Energy Harvesting Devices

The Springer Series in Advanced Microelectronics provides systematic information on all the topics relevant for the design, processing, and manufacturing of micro-electronic devices. The books, each prepared by leading researchers or engineers in their fields, cover the basic and advanced aspects of topics such as wafer processing, materials, device design, device technologies, circuit design, VLSI implementation, and subsystem technology. The series forms a bridge between physics and engineering and the volumes will appeal to practicing engineers as well as research scientists.

Series Editors:

Dr. Kiyoo Itoh

Hitachi Ltd., Central Research Laboratory, 1-280 Higashi-Koigakubo
Kokubunji-shi, Tokyo 185-8601, Japan

Professor Thomas H. Lee

Department of Electrical Engineering, Stanford University, 420 Via Palou Mall,
CIS-205 Stanford, CA 94305-4070, USA

Professor Takayasu Sakurai

Center for Collaborative Research, University of Tokyo, 7-22-1 Roppongi
Minato-ku, Tokyo 106-8558, Japan

Professor Willy Sansen

ESAT-MICAS, Katholieke Universiteit Leuven, Kasteelpark Arenberg 10
3001 Leuven, Belgium

Professor Doris Schmitt-Landsiedel

Lehrstuhl für Technische Elektronik, Technische Universität München
Theresienstrasse 90, Gebäude N3, 80290 München, Germany

For further volumes:

<http://www.springer.com/series/4076>

Dirk Spreemann • Yiannos Manoli

Electromagnetic Vibration Energy Harvesting Devices

Architectures, Design, Modeling
and Optimization

 Springer

Dr.-Ing. Dirk Spreemann
HSG-IMIT
Institut für Mikro and Informationstechnik
Wilhelm-Schickard-Straße 10
78052 Villingen-Schwenningen
Baden-Württemberg
Germany

Prof. Dr.-Ing. Yiannos Manoli
University of Freiburg
IMTEK
Georges-Koehler-Allee 102
79110 Freiburg
Germany

ISSN 1437-0387

ISBN 978-94-007-2943-8

e-ISBN 978-94-007-2944-5

DOI 10.1007/978-94-007-2944-5

Springer Dordrecht Heidelberg London New York

Library of Congress Control Number: 2012932408

© Springer Science+Business Media B.V. 2012

No part of this work may be reproduced, stored in a retrieval system, or transmitted in any form or by any means, electronic, mechanical, photocopying, microfilming, recording or otherwise, without written permission from the Publisher, with the exception of any material supplied specifically for the purpose of being entered and executed on a computer system, for exclusive use by the purchaser of the work.

Printed on acid-free paper

Springer is part of Springer Science+Business Media (www.springer.com)

*Die Wissenschaft ist ewig in ihrem Quell,
unermesslich in ihrem Umfang, endlos in
ihrer Aufgabe, unerreichbar in ihrem Ziel.*

– Karl Ernst von Baer

Preface

This book investigates the vibration to electrical energy conversion using electromagnetic resonant vibration transducers. A vibration transducer system is intended to power wireless sensor-nodes by harvesting the vibrational energy from the operation environment. In the ideal case batteries or cables can be replaced and the sensor system becomes energy autonomous and maintenance-free.

In recent years a multiplicity of electromagnetic vibration transducers has been developed by different research facilities. In the developments different electromagnetic coupling architectures have been applied which have not been compared yet with respect to their output performance capability. In the first step of this book an optimization approach is established and applied to determine the optimal dimensions (of magnet, coil and if existent back iron components) of eight different commonly applied coupling architectures. The results show that the correct dimensioning is of great importance to maximize the efficiency of the energy conversion. Beyond this there are different optimal dimensions for output power and output voltage generation, respectively. A comparison yields the architectures with best output performance capability. These architectures should be preferred in application whenever possible. The output power between the worst and best architecture can be increased by a factor of 4 and the output voltage by a factor of about 2. All the simulation models have been verified experimentally. In a next step a coil topology optimization has been formulated to find the topology of the coil which yields highest output power for transducers based on oscillating cylindrical magnets. Especially if there is unused space left after the housing of the transducer the results of the topology optimization can be used to maximize the output power.

A prototype development is used to demonstrate how the optimization calculations can be integrated in the design-flow. The operational environment of the development is in a car engine compartment. Acceleration measurements have been performed and most energetic frequencies have been determined. By using transient simulations it is found that nonlinear hardening spring have the potential to maximize the output power. Finally the prototypes have been characterized using frequency response measurements and measurements with stochastic acceleration profiles.

Contents

1	Introduction	1
1.1	Background and Motivation of Vibration Energy Harvesting	1
1.2	Literature Review and “State of the Art” in Electromagnetic Vibration Transducers	2
1.3	Conclusions from the Literature Review	10
1.4	Book Objectives	11
2	Basic Analytical Tools for the Design of Resonant Vibration Transducers	13
2.1	Introduction	13
2.2	Mechanical Subsystem	14
2.2.1	Linear Spring System	14
2.2.2	Nonlinear Spring System	16
2.3	Electromagnetic Subsystem	19
2.3.1	Basics on Electromagnetic Induction	19
2.3.2	Electrical Network Representation	21
2.4	Overall System	24
2.4.1	General Behavior	24
2.4.2	First Order Power Estimation	25
2.5	Characterization and Handling of Machinery Induced Vibration	28
2.6	Conclusions from Analytical Analyses	32
3	Power and Voltage Optimization Approach	37
3.1	Introduction	37
3.2	Investigated Electromagnetic Coupling Architectures	38
3.2.1	“Magnet In-Line Coil” Architectures	38
3.2.2	“Magnet Across Coil” Architectures	40
3.3	Boundary Conditions	41
3.4	Magnetic Field Distribution of Cylindrical and Rectangular Permanent Magnets	43

3.5	Optimization Procedure.....	49
3.5.1	General Calculation Method	49
3.5.2	Evolution Strategy	49
3.6	Architecture Specific Calculation of the Transduction Factor	53
3.6.1	Simulation of “Magnet In–Line Coil” Architectures Without Back Iron.....	54
3.6.2	Simulation of “Magnet In–Line Coil” Architectures with Back Iron.....	56
3.6.3	Simulation of “Magnet Across Coil” Architectures Without Back Iron.....	56
3.6.4	Simulation of “Magnet Across Coil” Architecture with Back Iron	60
4	Optimization Results and Comparison	65
4.1	Introduction	65
4.2	“Magnet In–Line Coil” Architectures.....	66
4.2.1	Architecture A I.....	66
4.2.2	Architecture A II.....	72
4.2.3	Architecture A III	74
4.2.4	Architecture A IV	76
4.2.5	Architecture A V.....	79
4.3	“Magnet Across Coil” Architectures.....	82
4.3.1	Architecture A VI.....	82
4.3.2	Architecture A VII.....	85
4.3.3	Architecture A VIII.....	88
4.4	Conclusion and Comparison of the Coupling Architectures	90
4.4.1	Output Power Generation Capability	92
4.4.2	Output Voltage Generation Capability	93
5	Experimental Verification of the Simulation Models	95
5.1	Introduction	95
5.2	“Magnet In–Line Coil” Architecture.....	99
5.2.1	Architecture A I.....	99
5.2.2	Architecture A II.....	100
5.2.3	Architecture A III	100
5.2.4	Architecture A IV	101
5.2.5	Architecture A V.....	102
5.3	“Magnet Across Coil” Architecture	103
5.3.1	Architecture A VI.....	104
5.3.2	Architecture A VII.....	106
5.3.3	Architecture A VIII.....	107
5.4	Conclusions	107
6	Coil Topology Optimization for Transducers Based on Cylindrical Magnets	109
6.1	Introduction	109

- 6.2 Formulation Strategy 110
- 6.3 Results of the Topology Optimization 115
 - 6.3.1 Progress of Important System Parameters 115
 - 6.3.2 Final Interpretation and Performance of the
Optimal Topology 118
- 7 Application Oriented Design of a Prototype Vibration Transducer 123**
 - 7.1 Introduction 123
 - 7.2 Basis for the Development..... 124
 - 7.2.1 Underlying Vibration Characteristic 124
 - 7.2.2 Design Specifications..... 128
 - 7.3 Optimization of the Prototype Electromagnetic
Coupling Architecture 128
 - 7.3.1 Optimization Based on the Design Specifications 128
 - 7.3.2 Influence of Boundary Condition Parameters 130
 - 7.3.3 Experimental Characterization of the Coupling
Architecture 133
 - 7.4 Resonator Design 134
 - 7.4.1 Finding the Optimal Spring Characteristic 134
 - 7.4.2 FEA Based Design of the Spring Element..... 139
 - 7.4.3 Experimental Characterization of the Spring Element 142
 - 7.5 Prototype Assembling and Performance 143
 - 7.6 Conclusions 150
- 8 Conclusions 153**
 - 8.1 Overview of Main Findings 153
 - 8.2 Suggestions for Further Work 154
- Appendices 157**
- About the Authors 173**
- References..... 175**
- List of Figures 179**
- List of Tables..... 193**
- Index 195**

Nomenclature

Table of Acronyms

AI–AVIII	Architecture I–VIII
DFT	Discrete Fourier Transformation
DSM	Direct stiffness method
EDAM	Electrical domain analog matching
emf	Electromotive force
ES	Evolution strategy
FEA	Finite element analyses
LTI	Linear time–invariant
PCB	Printed circuit board
Rpm	Root per minute
SDOF	Single degree of freedom
TDC	Top dead centre
WSN	Wireless sensor network

Roman Symbols

A, A_n	Area (m ²)
$A_o, A_{Rt,n}$	Overall area function and area of the nth coil turn (m ²)
a	Length (m)
$a(t)$	Acceleration function (m/s ²)
a_i	Individual in ES optimization (Solution candidate)
A_1	Wire area without isolation (m ²)
$A_{T_{c,i}}$	Area of an imaginary coil turn in the centre of the ith cell

(continued)

(continued)

A_w	Cross-section of the winding area (m ²)
B, B_x, B_z	Magnetic flux density (component) (T)
b	Width (m)
B_r	Residual magnetic flux density (T)
$B_{T_{c,i}}$	Magnetic flux density in an imaginary coil turn in the centre of the i th cell
c	Parameter for control of the standard deviation
d	Damping factor (N/m/s)
d_{co}	Wire diameter (without isolation) (m)
$d_e, d_{e,cell}$	Electromagnetic damping factor (N/m/s)
d_m	Parasitic damping factor (N/m/s)
E	Young's modulus (Pa)
E, E_1, E_2	Elliptic integrals of the first kind
f	Frequency (Hz)
F, F_x	Force (component) (N)
$f(x)$	Nonlinear restoring force (N)
f_0	Amplitude of excitation force (N)
f_x	Probability density function
g	Acceleration of gravity (m/s ²)
G	Gap (m)
h	Height (m)
H	Magnetic field intensity (A/m)
H_C	Coercitivity (A/m)
h_{mag}, h_{coil}	Height of magnet and coil (m)
h_n	Height of circular segment (m)
h_S	Height of the spacer (m)
$h_{upp}, h_{lopp}, h_{sheet}$	Height of upper-, lower pole plate and sheet (m)
I	Moment of inertia (kg·m ²)
$i(t), I_1, I_2$	Current (A)
J	Surface current density (A/m ²)
k	Spring rate (N/m)
K	Elliptic integrals of the second kind
k_{co}	Copper fill factor (1)
$k_t, k_{t,cell}$	Transduction factor (of cell in coil design domain) (V/m/s)
l	Length of wire (m)
l'	Length of wire (m)
L_{coil}	Coil inductance (H)
l_{pr}	Piston rod length (m)
l_{red}	Reduced length of the physical pendulum (m)

(continued)

(continued)

m	Mass (kg)
M	Magnetization (A/m)
m_{osc}, m_p, m_{pr}	Mass of oscillating components, piston and piston rod (kg)
M_r	Residual magnetization (A/m)
N	Dimension of search space (1)
N, N_1, N_2	Number of windings (1)
N_c	Number of windings in the cell
N_{lat}	Windings in lateral direction (1)
N_{long}	Windings in longitudinal direction (1)
P_{max}, P	(Maximum) Power (W)
P_a	Population (1)
P_{cell}	Power of a cell in coil design domain (W)
$P_{cs,max}, P_{cs}$	(Maximum) displacement constraint power (W)
Q	Point charge (C)
Q	Quality factor
R	Frequency ratio (1)
R'	Resistance per meter (Ω/m)
R, R_1, R_2	Radius (m)
R_{ca}	Radius of crank arm (m)
$R_{Coil}, R_{cell}, R_{cell, opt}$	Resistance of coil, cell and optimal cell resistance (Ω)
$R_{i,min}$	Minimal inner radius (m)
$R_{load,opt}$	Optimal load resistance (Ω)
R_t	Radius of coil turn (m)
S_U	Tensile strength (Pa)
R_m	Middle radius (m)
$R_{mag}, R_{coil}, R_{upp}, R_{pc}$	Radius of magnet, coil, upper pole plate and pole core (m)
R_i, R_o	Inner/Outer Radius (m)
$R_{p0.2}$	Yield strength (Pa)
$R_{t,n}$	Radius of coil turn (m)
S	Line current density (A/m)
T	Time (s)
$T_{c,i}$	Imaginary coil turn in the centre of the cell
t_0	Depth of immersion at the resting position (m)
V_{constr}	Construction volume (m^3)
$V_{Rcell,opt}$	Voltage at optimal cell resistance (V)
x, x_0, x_1, x_2	Position coordinates (m)
X	Amplitude of mass motion (absolute coordinates) (m)
X_{Coil}	Coil reactance (Ω)
$x_i, x_{P,i}, x_{O,i}$	Vector with genes of parents respectively offspring's

(continued)

(continued)

x_1	Maximum inner displacement limit (m)
x_m	Amplitude of ansatz function (m)
y, y_0	Position coordinate (m)
Y, Y_{acc}	Amplitude of the excitation (m, m/s ²)
Z	Amplitude in relative coordinates (m)
Z	Position coordinate (m)
Z_{Coil}	Impedance of electrical circuit (Ω)
Z_{max}	Maximum inner displacement limit (m)

Greek Symbols

α', α''	Length (m)
$\Gamma_{P,max}, \Gamma_P$	(Maximum) Output power proportionality factor
E	Electromotive force (V)
$\zeta_{e,min}$	Minimal normalized electromagnetic damping factor
ζ, ζ_e, ζ_m	Normalized damping factor (combined, electromagnetic, parasitic)
η	Number of coil turns per unit length (m ⁻¹)
λ	Number of offspring's
λ_{cp}	Ratio of crank arm length to piston rod length
μ_{nl}	Nonlinearity parameter (N/m ²)
μ	Permeability (H/m)
μ_0	Relative permeability (H/m)
μ_{ini}	Number of individuals in the start population
Π_1, Π_2	Elliptic integrals of the third kind
ρ_{bi}	Density of back iron material(kg/m ³)
ρ_{mag}	Density of the magnet (kg/m ³)
ρ_s	Success rate
$\sigma, \sigma_{min}, \sigma_{max}$	Standard deviation (minimal, maximal)
φ	Angle (rad)
$\varphi_1, \varphi_2, \varphi_3$	Independent variable
φ_m	Magnetic flux (Wb)
Φ	Fitness of the individuals (power respectively voltage)
ψ	Phase angle of absolute motion (rad)

(continued)

(continued)

ω	Angular frequency (rad/s)
ω_{nl}	Nonlinear resonance angular frequency of the undamped system (rad/s)
ω_d	Resonance angular frequency of the damped system (rad/s)
ω_n	Resonance angular frequency of the undamped system (rad/s)
Ω	Global coil design domain

Chapter 1

Introduction

1.1 Background and Motivation of Vibration Energy Harvesting

In our daily life smart sensors have become an essential part increasing comfort, security and efficiency in many industrial and civilian application areas such as automotive, aircraft and plant industry, industrial and home automation or machine and health monitoring. Going one step further it does not come as a big surprise that there is a steady increase of wireless sensor networks (WSN) following the paradigm of ubiquitous computing. Many of nowadays applications would not be possible without the advance in miniaturizing the size and reducing the power consumption of electronics and the progress in wireless technologies. As a further advance smart sensors and WSN will tend to be even more embedded and mobile in the future. With a higher level of integration numerous new applications become possible.

However, the power supply of the sensor nodes evokes some serious challenges for the widespread implementation of WSN's. Because the sensors need to be wireless, the power is usually provided by primary or secondary batteries. It must be said that as long as the battery survives the life-time of the sensor node, batteries are often an appropriate solution. This is because the energy density of primary and secondary batteries has significantly increased over the last two decades [4]. Nevertheless batteries have some unavoidable drawbacks. The most important one for application in WSN's is that the energy is inherently limited. Thus the battery must be replaced or recharged sooner or later. Especially in difficult to access applications or applications with many sensor nodes this is often not feasible because maintenance becomes too costly. Another characteristic of batteries is the typical operating temperature range of -55°C to $+85^{\circ}\text{C}$ which might be insufficient in some applications. Energy Harvesting opens up new ways to solve these problems. Just as for the alternative energy sources in the power economy the basic idea behind energy harvesting is to convert non-electric ambient

energy from the sensor environment into electrical energy. The primary goal is to obtain an energy autonomous, maintenance-free sensor system with (at least theoretically) unlimited life time. In contrast to the alternative energy sources in the power economy environmental protection aspects plays a subordinate role in energy harvesting devices.

Commonly used environmental energy sources are heat, light, fluid flow or kinetic energy [53]. This book focuses on the conversion of kinetic energy in form of vibrations which is a very promising approach for industrial applications. For example every machine with rotary parts is forced to vibrate due to imperfection in balancing. So far, existing vibration transducers are commonly based on three different conversion mechanism namely piezoelectric [37], electromagnetic [27] and for micro fabricated devices electrostatic [43]. In rather seldom cases the effect of magnetostriction [49] and magnetic shape memory alloys [39] has been investigated as well. A general approach for the comparison of the different conversion mechanisms has been presented in [70]. Especially for the aimed cubic centimeter range transducers in this book the electromagnetic transduction mechanism based on Faraday's law of induction is expected to be among the most efficient. Another advantage of the electromagnetic conversion is the huge design flexibility. In contrast to this advantage, piezoelectric vibration converters are in most cases based on simple beam and disc elements.

This book considers the design and optimization of electromagnetic vibration energy harvesting devices.

1.2 Literature Review and “State of the Art” in Electromagnetic Vibration Transducers

Since the earliest electromagnetic vibration transducers have been proposed at the end of the 1990s [15, 65] a multiplicity of electromagnetic based vibration transducers have been developed by numerous research facilities. The transducers basically differ in size, electromagnetic coupling architecture, excitation conditions and output performance. Actually electromagnetic resonant vibration transducers are already commercially available [5, 6, 8]. So far commercial vibration transducers are typically add-on solutions, greater than 50 cm³ and they fulfil standard industrial specifications such as ingress protection (IP code, IEC 60529), operating conditions (like the temperature range, shock limit and so on) or the requirements for electrical equipment in hazardous areas (ATEX/IECEx). Nevertheless, requests from industry show that beyond the existing add-on solutions there is a great demand for application specific solutions. This is because in each application the required output power, the available vibration level and the overall mass and volume will be significantly different. Moreover, it is often necessary that the sensor system needs to be integrated in an existing subassembly. Especially for applications where the volume of the transducer is a critical parameter these facts show that the

available output power of a vibration transducer can only be optimally used with application-specific customized developments. In this case it can be guaranteed that the transducer is not under or overdimensioned with respect to the size and the output performance.

The primary purpose of this introduction is to give a basic overview of the recent research achievements in electromagnetic vibration conversion. One suitable way to classify electromagnetic vibration transducers is to use the electromagnetic coupling architecture. An obvious and popular coupling architecture is a cylindrical magnet, which oscillates inside a coil. A silicon micromachined implementation of such an architecture with discrete magnet was reported in 2007 by C. Serre et al. at the University of Barcelona [14] (Fig. 1.1a). The prototype delivered a maximum power output of 55 μW at a voltage level of about 80 mV for excitation with 5.1 μm amplitude at about 300 Hz (18 m/s^2). Another silicon bulk micromachined transducer with discrete magnet designed to convert acoustic wave energy was published in 2008 by T. Lai et al. at the Feng Chia University [76]. With a total dimension of 3.3·1 mm³ a maximum open circuit voltage of 0.24 V was obtained for excitation at resonance frequency (470 Hz). A macro scale implementation of this architecture has been used by S. Cheng et al. at the University of Florida in 2007 to verify equivalent circuit models of electromagnetic vibration transducers [68]. With the assembled device an output power of 12.5 mW could be generated at the resonance frequency of about 68 Hz and 30 Ω load resistance. X. Cao et al. at the University of Nanyang assembled another macro scale device [81]. The converter delivered an output power of 35 mW and an output voltage of about 15 V for excitation at the resonance frequency of 43 Hz with 3 mm amplitude. This corresponds to a very high acceleration level of 219 m/s^2 . The output power was processed in an energy harvesting circuit with feedforward and feedback DC-DC PWM Boost converter fabricated in 0.35 μm CMOS technology. A group from the University of Hong Kong presented a PCB integrated solution as well as an AA battery size transducer [59] (Fig. 1.1b). A special feature of this transducer is that beyond the first eigenfrequency (linear oscillation) also higher eigenfrequencies of the system (tilting oscillation) are considered for conversion. The aim was to increase the bandwidth. However due to the large gap between the coil and the magnet the effectiveness of the conversion definitely decreases for the first eigenfrequency. A modification of the previous coupling architecture has been used by G. Naumann at the Dresden University of Technology in 2003 [34]. In this development a linear supported magnet oscillates between two repulsive arranged magnets. The magnetic forces yield a nonlinear spring system. For excitation with stochastic vibrations in an automobile environment a maximum output voltage of 70 mV at a power of 7 μW has been obtained. For harmonic excitation 610 mV and 200 μW are possible with an excitation amplitude of 5 mm at 16 Hz. This corresponds to a rather high acceleration level of about 50 m/s^2 . The same modification has been published by C.S. Saha et al. at the Tyndall National Institute in 2008 [17] (Fig. 1.1c). Beyond harmonic excitation measurements the transducer was placed inside a rucksack. Average load power of 0.95 mW could be obtained during walking and 2.46 mW under slow running conditions. The same architecture

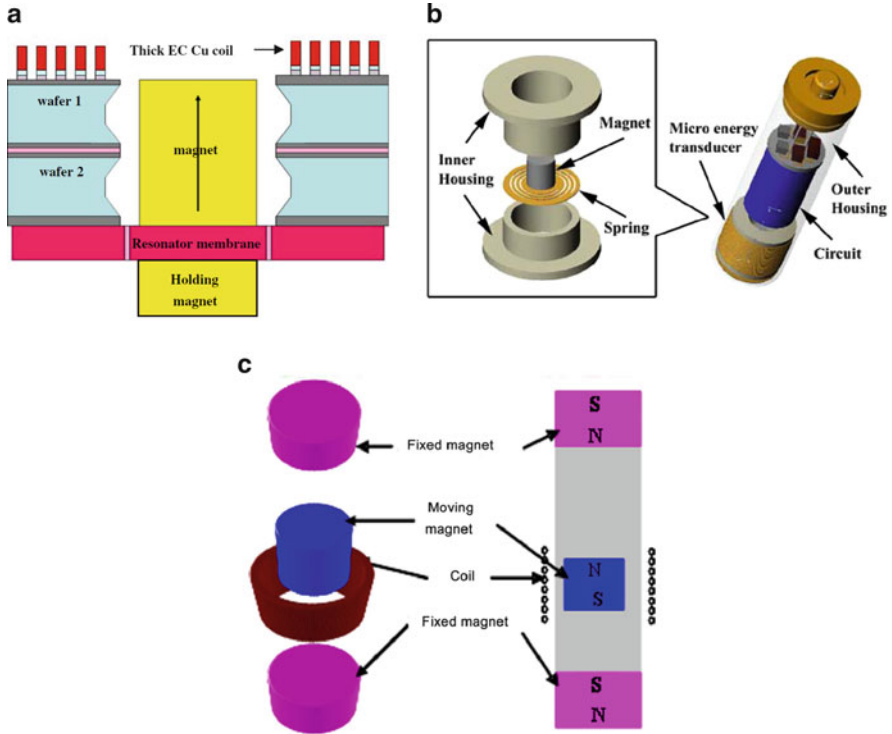


Fig. 1.1 Commonly applied coupling architecture where a magnet oscillates inside a coil. (a) Microfabricated implementation [14], (b) AA size transducer with multi modal resonating structure [59] and (c) with opposite polarized magnets used in a rucksack [17]

has also been considered by D.J. Domme from Virginia Polytechnic Institute in 2008 [26]. With an operating range of 12–24 Hz and an acceleration amplitude of 36.7 m/s^2 an average output power of 5.5 mW has been obtained. Further examples of this architecture can be found in [33, 57, 69].

Another commonly applied coupling architecture (often used in microfabricated devices) is that of a magnet which oscillates towards a coil without immersion. Based on this architecture P. Wang from the Shanghai Jiao Tong University presented a prototype device in 2009 [61] (Fig. 1.2a). With a not optimized prototype a peak to peak voltage of 18 mV and $0.61 \mu\text{W}$ could be generated for an excitation of 14.9 m/s^2 at 55 Hz. The same coupling architecture has also been used in [11] by B. Yang from the National University of Singapore in 2009 (Fig. 1.2b). The transducer is based on a multi-frequency acrylic beam structure. At the first two eigenfrequencies (369, 938 Hz) the maximum output voltage and power are $1.38 \text{ mV}/0.6 \mu\text{W}$ and $3.2 \text{ mV}/3.2 \mu\text{W}$ for an excitation amplitude of $14 \mu\text{m}$. Another development based on this architecture has been used by D. Hoffmann at HSG-IMIT in 2009 [18]. The development is based on micro-machined flexible polyimide films and planar micro-coils (Fig. 1.2c). The assembled device is capable of generating a

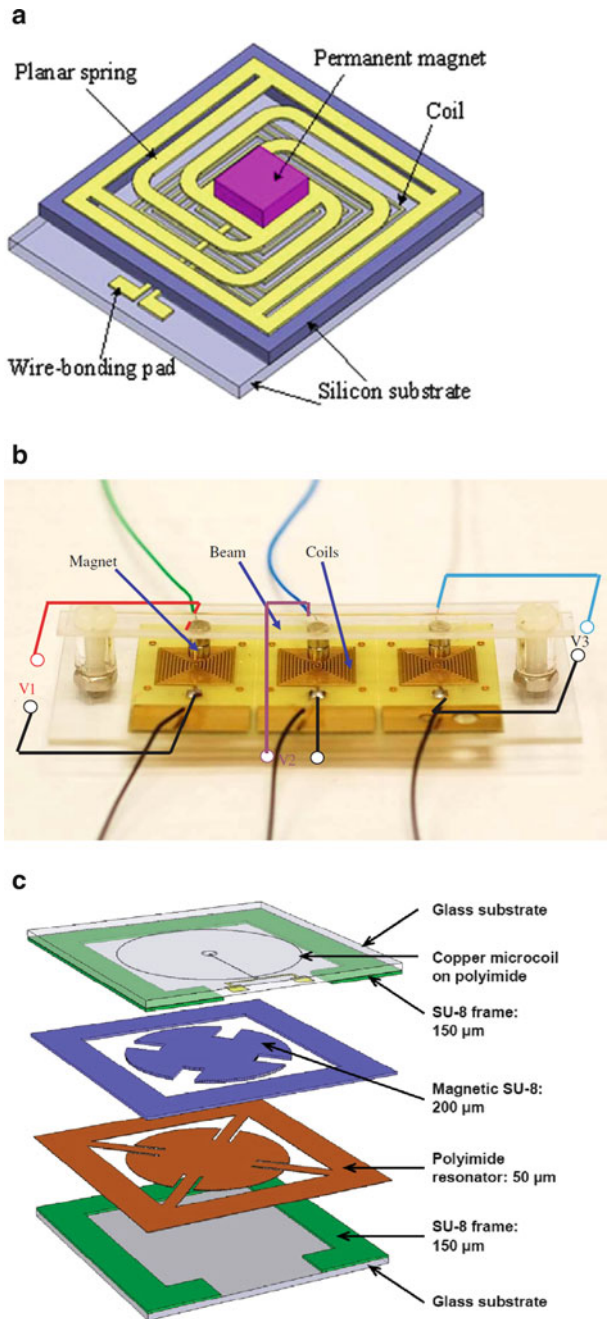


Fig. 1.2 Often favoured coupling architecture in microfabricated transducers where a magnet oscillates towards a coil without immersion. (a) Harvester with electroplated copper planar spring and discrete NdFeB magnet [61], (b) multi-frequency energy harvester based on acrylic beam [11] and (c) transducer based on micro-machined flexible polyimide films and planar coils [18]

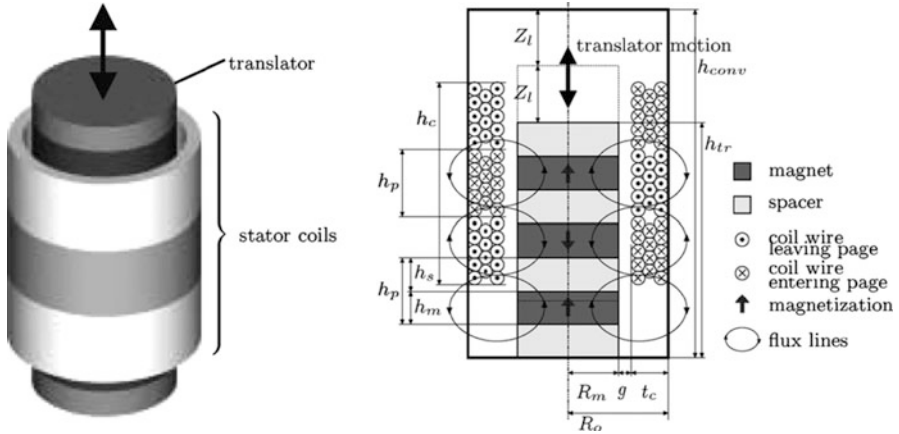


Fig. 1.3 Coupling architecture based on opposite polarized magnets [78]

peak power up to $5 \mu\text{W}$ (70 mV at $1,000 \Omega$) from a harmonic excitation with 90 m/s^2 at the resonance frequency of 390 Hz . Further developments using this architecture have been presented in [15] and [7].

In 2007 T. von Büren and G. Tröster from ETH Zürich developed a multi magnet micro-power transducer. The coupling architecture is based on opposite polarized magnets which provide the oscillating mass [78] (Fig. 1.3). Unlike most of the previous described work extensive finite element analyses (FEA) based optimization calculations have been applied for dimensioning the magnet and the coil. Designed for body worn applications $2\text{--}25 \mu\text{W}$ have been obtained during normal walking depending on the mounting position. Previously, this architecture had also been applied by K. Takahara at the Muroran Institute of Technology in 2004 [46]. This development focuses on the conversion of vehicle vibration. With a prototype 36 mW has been obtained at a voltage level of 1.6 V . For use as a regenerative shock absorber in vehicle suspensions the architecture has also been considered in a development presented by L. Zuo in 2010 [50]. The transducer was capable of generating $16\text{--}64 \text{ mW}$ at a suspension velocity of $0.25\text{--}0.5 \text{ m/s}$. A similar architecture with opposite polarized ring magnets instead of cylindrical magnets and oscillating coil instead of oscillating magnets has been used by M. Ruellan in 2005 [55].

So far the presented architectures had the oscillation direction always in-line with the coil symmetry axis. The resulting geometry is typically cylindrical. However there are also architectures where the oscillation direction is perpendicular to the coil symmetry axis which typically yields a cubic geometry. A silicon micromachined moving coil version of such an architecture has been presented by E. Koukharenko from the university of Southampton in 2006 [31] (Fig. 1.4a). The prototype was capable of generating up to 104 nW for an excitation with 3.9 m/s^2 at $1,615 \text{ Hz}$. In [74] the same group presented a transducer based on discrete

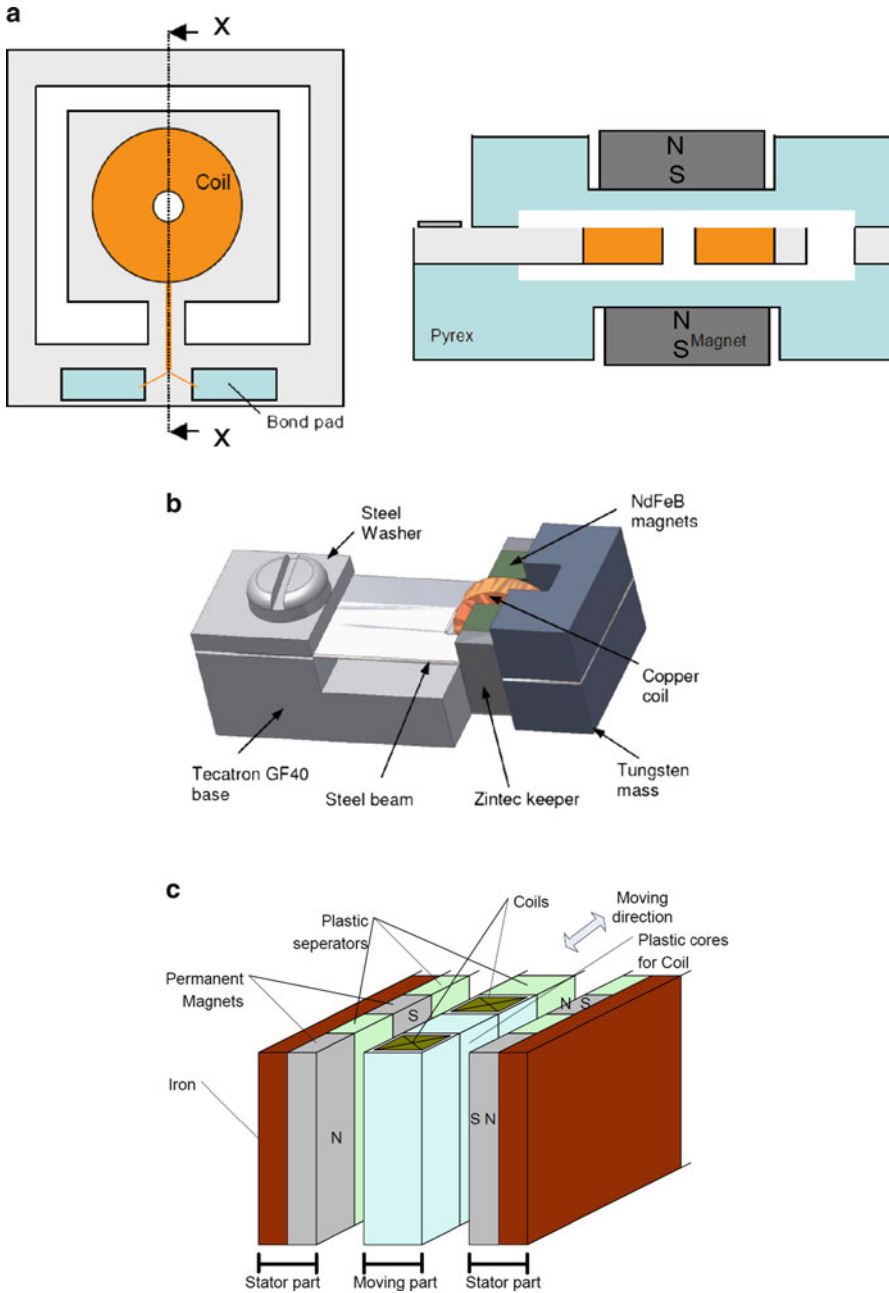


Fig. 1.4 (a) Silicon micromachined moving coil version of a magnet across coil arrangement [31]. (b) Moving magnet version based on discrete components [74] and (c) complete fine-mechanical implementation used to convert human motions [60]

components (Fig. 1.4b). The prototype was capable of generating $46 \mu\text{W}$ with an excitation amplitude of 0.59 m/s^2 at a (resonance) frequency of 52 Hz. A pure fine-mechanical transducer using a quite similar coupling architecture has been presented by P. Niu in 2008 [60] (Fig. 1.4c). This transducer was designed to convert human motions like arm swinging, horizontal foot movement or up-down centre of gravity movement during walking. The authors report an average power output of up to 100 mW at a voltage level of greater than 5 V for different body-worn operation conditions. A rotary suspended prototype with magnetic springs has been developed by Z. Hadas in 2010 [83]. When excited with the (nonlinear) resonance frequency of 18 Hz and an acceleration amplitude of 4.9 m/s^2 26 mW could be converted at a voltage level of about 9 V. Actually this kind of electromagnetic coupling architecture has also been considered for a tunable device by D. Zhu in 2010 [25]. Even though the tuning mechanism is not self-powered so far, the resonance frequency could already be tuned from 67.6 to 98 Hz. In this range the prototype produced a power of $61.6\text{--}156.6 \mu\text{W}$ when excited at a constant acceleration level of 0.59 m/s^2 . With the intent increasing the bandwidth this kind of coupling architecture has also been used in combination with a piecewise-linear oscillator by M. Soliman in 2008 [56]. Experimental measurements show that the bandwidth could be increased by 240%. However because this increase is based on a nonlinearity the benefit significantly depends on the excitation and the history of the system. In other words, to affirm the benefit in a specific application, the underlying excitation must be taken into account.

So far the reviewed prototype developments are based on commonly used coupling architectures. However a basic characteristic of the electromagnetic conversion mechanism is that the implementation of the electromagnetic coupling can be realized in various kinds. Hence, there are a number of further architectures that have been applied. Some of them are rather specific [52] but on the other hand it surprises that the well known coupling architecture of moving coil loudspeakers has not been considered for vibration transducers as often as might have been expected. Prototype developments of such a “loudspeaker” based coupling architecture, for example, has been presented by H. Töpfer in 2006 [36] and J.K. Ward in 2008 [42] (Fig. 1.5).

Altogether the existing prototype transducers range from 0.1 to 100 cm^3 in size and from hundreds of nW to 100 mW in power. It must be said that an absolute comparison is rather difficult. This is because up to now there is no testing standard for vibration energy harvesting devices. Consequently the devices have been tested under different conditions (harmonic vs. impulse vs. stochastic excitation, simple resistive load vs. matched load vs. complex load circuit, ...). Moreover important parameters for an absolute comparison are often omitted or ambiguous (which components are included in the denoted volume, rms vs. amplitude vs. peak-to-peak values, ...). Nevertheless an extensive review of electromagnetic vibration transducers has been presented together with the basic scaling laws by D.P. Arnold in [27]. Therein the normalized power density (power related to the volume and the excitation amplitude) of existing prototypes is used as a basis for the comparison. With the normalization the performance of the transducer can be referred to the

Fig. 1.5 Electromagnetic coupling architecture typically used in moving coil loudspeakers has been considered for vibration transducers in [42]

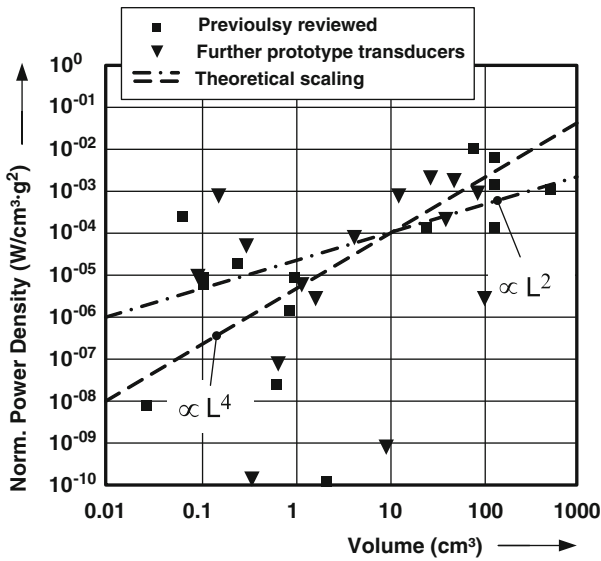
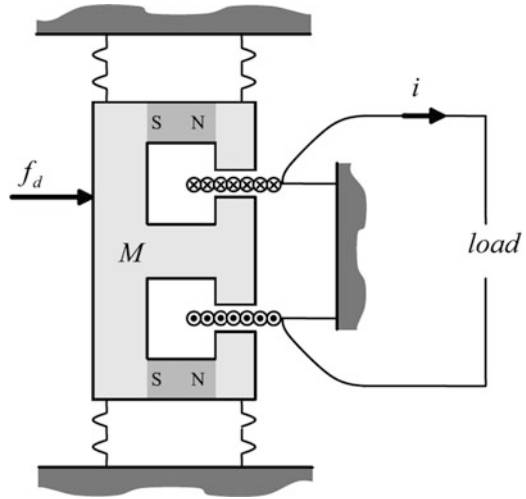


Fig. 1.6 Normalized Power density of previous reviewed vibration transducer prototypes [27] supplemented by transducers reviewed in this book. The *dashed curves* indicate the theoretical scaling

input energy which opens up the possibility for absolute comparison (Fig. 1.6). Even though there are orders of magnitudes between the absolute values of the normalized power density the theoretical scaling law is evident. The diagram has been supplemented with some of the prototype developments reviewed in this book (Table 1.1). At very small dimensions electromagnetic vibration transducers scale

Table 1.1 Comparison of vibration transducer prototypes from the literature review

References	Volume (cm ³)	Resonance frequency (Hz)	Amplitude (g)	Power (W)	Power density (W/cm ³)	Normalized power density (W/cm ³ g ²)
<i>U. Barcelona</i> [14]	1,8 ^a	385	2.98	$5.5 \cdot 10^{-5}$	$3.1 \cdot 10^{-5}$	$3.4 \cdot 10^{-6}$
<i>U. Florida</i> [67]	42 ^a	66.7	1	$1.3 \cdot 10^{-2}$	$3.0 \cdot 10^{-4}$	$5.5 \cdot 10^{-4}$
<i>U. Hong Kong</i> [81]	85	42	21	$3.5 \cdot 10^{-2}$	$4.1 \cdot 10^{-1}$	$9.3 \cdot 10^{-4}$
<i>TU. Dresden</i> [34]	1.17	16	5.14	$2.0 \cdot 10^{-4}$	$1.7 \cdot 10^{-4}$	$6.5 \cdot 10^{-6}$
<i>U. Cork</i> [17]	12.5	8	0.039	$1.5 \cdot 10^{-5}$	$1.2 \cdot 10^{-6}$	$7.7 \cdot 10^{-4}$
<i>U. Freiburg</i> [29]	4.4 ^a	98	1	$3.6 \cdot 10^{-4}$	$8.1 \cdot 10^{-5}$	$8.1 \cdot 10^{-5}$
<i>U. Virginia</i> [26]	112	16	3.74	$5.5 \cdot 10^{-3}$	$4.9 \cdot 10^{-5}$	$3.5 \cdot 10^{-6}$
<i>U. Shanghai</i> [62]	0.31	280	1	$1.7 \cdot 10^{-5}$	$5.6 \cdot 10^{-5}$	$5.6 \cdot 10^{-5}$
<i>U. Singapore</i> [11]	10	369	7.67	$6.0 \cdot 10^{-7}$	$6.0 \cdot 10^{-8}$	$1.0 \cdot 10^{-9}$
<i>HSG-IMIT</i> [18]	0.68	390	9	$5.0 \cdot 10^{-6}$	$7.4 \cdot 10^{-6}$	$9.1 \cdot 10^{-8}$
<i>Lumedyne</i> [7]	27	57	0.24	$4.1 \cdot 10^{-3}$	$1.5 \cdot 10^{-4}$	$2.6 \cdot 10^{-3}$
<i>U. Southampton</i> [31]	0.1	1,615	0.4	$1.0 \cdot 10^{-7}$	$1.0 \cdot 10^{-6}$	$6.5 \cdot 10^{-6}$
<i>U. Southampton</i> [74]	0.1	52	0.59	$4.6 \cdot 10^{-5}$	$4.6 \cdot 10^{-4}$	$1.3 \cdot 10^{-3}$
<i>U. Brno</i> [83]	50 ^a	18	0.5	$2.6 \cdot 10^{-2}$	$5.2 \cdot 10^{-4}$	$2.1 \cdot 10^{-3}$
<i>U. Ankara</i> [41]	0.38	5,135	74.23	$2.2 \cdot 10^{-7}$	$5.8 \cdot 10^{-7}$	$1.1 \cdot 10^{-10}$

^aVolume estimated

with L^4 and large dimensions with L^2 (L = linear dimension). The reason for this is that at small dimensions the unwanted parasitic (viscous) damping dominates the electromagnetic damping and vice versa.

A possible reason why the published prototype transducers have a significantly different output performance is due to the fact that many different electromagnetic coupling architectures have been applied. The different architectures may inherently have a different output performance capability. Moreover the dimensioning of the electromagnetic coupling architecture components is often based on simplified assumptions, experience, if not intuition. Hence, it may be assumed that many devices operate still well below their maximum possible output performance.

1.3 Conclusions from the Literature Review

Section 1.2 gives an overview on existing work that has been done in the field of electromagnetic vibration transducers. For this reason over 200 papers have been reviewed. The following conclusions can be drawn from this review:

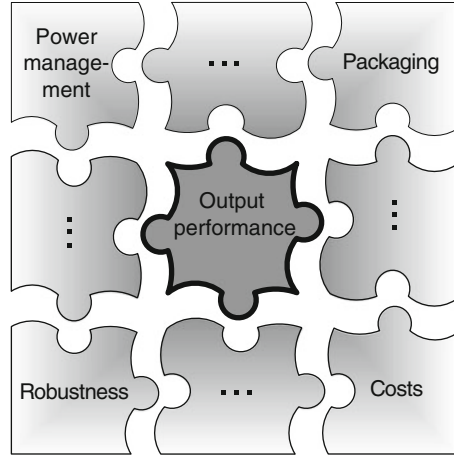
- The existing transducers range from 0.1 to 100 cm³ in size and from hundreds of nW to 100 mW in output power.
- Nearly all vibration transducers (commercial as well as research work) are based on the resonance phenomenon.
- The resonant vibration conversion is inherently limited to narrow band operation.

- The basic analytical theory is commonly known and it is applied to understand the influence of the most important system parameters on the output performance and to reproduce experimental data.
- The analytical theory has barely been involved in the design process where magnetic field calculations and nonlinear effects such as flux leakage, inner displacement limit, or stochastic excitation conditions must also be taken into account.
- Especially for micro scale devices the output voltage is often not sufficient for rectification based on standard techniques [13].
- There is a great interest to increase the operation frequency range using tunable devices [12]. The challenge is to power the actuators, control and application circuit at the same time. So far this could not be demonstrated.
- Many different electromagnetic coupling architectures have been applied. In the majority of cases the reason why a particular architecture has been chosen is not explained.
- The applied coupling architectures have yet not been compared and the question which of them performs best remains unanswered.
- The dimensioning of the most important components of the coupling architecture (magnet, coil and if existent back iron components) is often based on rough simplified assumptions, experience if not intuition.
- The comparison of the results presented in literature is rather difficult because a characterization standard does not exist. Consequently the devices are tested under different conditions (impulse excitation vs. harmonic frequency sweep vs. stochastic excitation, simple ohmic load resistor vs. matched load condition vs. complex load circuit, . . .). Moreover important parameters are sometimes omitted (power respectively voltage response without the corresponding load resistance, plots in logarithmic scale where it is difficult to extract maximum values, volume is not denoted or it is not stated which components are encompassed, . . .).
- In the research work the adjustment of the resonance frequency to an application specific vibration profile is often secondary. Usually the approach is to first build up the transducer and afterwards adjust the vibration to the resonance frequency of the transducer for experimental characterization. In application oriented developments one needs to go the other way round, which definitely brings further challenges in the design process.
- The applied interface circuits for electromagnetic vibration transducers are rather inefficient (typically a simple full wave rectifier with capacitor as storage element).

1.4 Book Objectives

Beside the limitation to narrow band operation (Appendix D) another basic challenge for electromagnetic vibration conversion is the fact that most of the existing vibration transducers operate well below their physically possible

Fig. 1.7 As a vital key role in the design of vibration transducers this book focuses the optimization of the output performance



maximum power. This is because the applied coupling architectures have not yet been classified with respect to their maximum performance capability. Moreover the dimensioning of the most important coupling components (magnet, coil and if present back iron components) is neglected in the majority of cases. Consequently the objectives of this book are:

1. Develop a general optimization approach for the dimensioning of the electromagnetic coupling architecture components.
2. Apply the optimization approach to commonly used coupling architectures and determine the dimensions which maximize their output performance based on overall boundary conditions.
3. Compare and classify the maximum output performance of the electromagnetic coupling architectures.
4. Confirm the integration of the optimization approach in the design flow of an application oriented prototype development of a resonant electromagnetic vibration transducer.

Note that in general different objectives may be taken into account in the optimization process of vibration transducers (Fig. 1.7). However, this book focuses on the optimization of the output performance in terms of the output power and the output voltage. Other aspects like the complexity of the construction or the costs are not considered. They may be taken into account after the technical optimization.

Chapter 2

Basic Analytical Tools for the Design of Resonant Vibration Transducers

2.1 Introduction

The presented review of existing work on electromagnetic inertial vibration transducers in Chap. 1 shows that there has been much interest in the design of vibration energy harvesting devices. Consequently excellent work has been done by numerous research facilities and a multiplicity of micro- and centimeter scale prototype vibration transducers has been developed. The basic analytical theory behind most of the presented devices is commonly known in the energy harvesting society. It is based on a well understood linear second-order spring-mass-damper system with base excitation. Specific analysis of vibration transducers was first proposed by Williams and Yates [15]. Since then the theory has been modified and described in various ways even though the basic findings are more or less the same. In this respect, an analytical expression for the maximum output power that can be extracted from a certain vibration was derived (also for constraints such as the limitation of the inner displacement of the seismic mass [64]) and the optimization of parameters such as the optimal load resistance or the electromagnetic damping factor was discussed. However, as will be shown, in most of these cases it is rather difficult even impossible to use the results of the analytical modelling directly for the design process of application oriented developments. This is because the theory does not consider geometrical parameters and is based on simplifying assumptions which often do not correlate well with the “real world” (e.g. random vibration instead of harmonic excitation, complex load circuit instead of simple resistance or appreciable magnetic flux leakage instead of homogeneous magnetic field distribution). However the analytical modelling is useful for understanding the influence of the most important system parameters. Furthermore it offers a deeper insight into the overall system behavior.

This chapter investigates and summarizes in the following five sections the most important analytical theory behind vibration transducers. The mechanical subsystem of resonant vibration transducers is investigated in Sect. 2.2. Characteristics of harmonic vibration will be discussed for both linear and nonlinear spring system.

Section 2.3 covers the electromagnetic subsystem where the basics of electromagnetism are introduced and the behavior of the electrical network is discussed. The results lead to Sect. 2.4 where the mechanical– and electromagnetic subsystem are combined to an overall system. Here a special focus is laid on the calculation of the output power with respect to the most important system parameters. How to deal with random excitation is described in Sect. 2.5. The chapter concludes with Sect. 2.6 where the most important design rules for the development of resonant electromagnetic vibration transducers based on the analytical approach are summarized.

2.2 Mechanical Subsystem

2.2.1 Linear Spring System

The aim of a vibration transducer is the conversion of vibration energy into electrical energy. However energy from vibration can only be extracted by damping the vibration which is a common task in engineering to protect objects from failure. Thus from the theoretical point of view the theory of developing vibration transducers is similar to the development of passive vibration isolators [30]. However for vibration transducers it is assumed that the energy conversion as well as the mass of the transducer has no effect on the vibration source. This assumption is fulfilled as long as the mass of the transducer is much smaller than the mass of the vibration source. A commonly used linear single degree of freedom mechanical model of a vibration transducer is shown in Fig. 2.1. It consists of a mass m attached to a spring with spring rate k and a damping element with damping factor d . The governing equation of its motion $x(t)$ is:

$$m\ddot{x} = -k(x - y) - d(\dot{x} - \dot{y}). \quad (2.1)$$

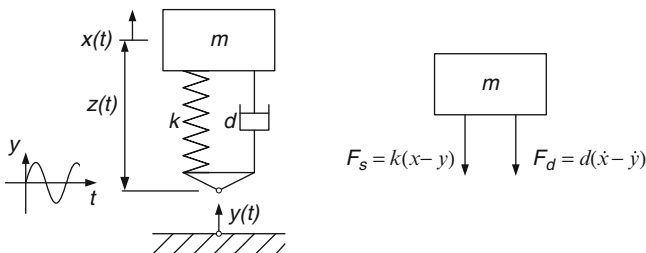


Fig. 2.1 (a) Linear single degree-of-freedom (SDOF) spring–mass–damper model of a resonant vibration transducer with harmonic base excitation. (b) Dynamic free body diagram of the oscillating mass with the forces associated with the spring F_s and the damping element F_d

For relative coordinates:

$$z = x - y, \quad (2.2)$$

the equation becomes:

$$m\ddot{z} + d\dot{z} + kz = -m\ddot{y} = m\omega^2 Y \sin(\omega t). \quad (2.3)$$

The excitation $y(t)$ is assumed to be a harmonic function with the amplitude Y . The theory of this second order differential equation is well known and discussed in a number of textbooks [28, 80]. For this reason only the results which are important for the understanding of the system are discussed here. The solution to Eq. 2.3 can easily be found in the frequency domain with the Laplace transformation:

$$(ms^2 + ds + k) Z(s) = -ms^2 Y(s). \quad (2.4)$$

Rearranging yields the transfer function $G_{mech}(s)$:

$$G_{mech}(s) = \frac{Z(s)}{Y(s)} = \frac{-ms^2}{ms^2 + ds + k}. \quad (2.5)$$

With the natural frequency of the undamped oscillation $\omega_n = \sqrt{k/m}$, the normalized damping factor $\zeta = d/2m\omega_n$ and substituting $s = j\omega$ the transfer function becomes:

$$G_{mech}(\omega) = \frac{\omega^2}{(\omega_n^2 - \omega^2) + 2\zeta\omega_n\omega j}. \quad (2.6)$$

In a final step this transfer function can be written as a function of two variables by introducing the frequency ratio $r = \omega/\omega_n$:

$$G_{mech}(r, \zeta) = \frac{r^2}{(1 - r^2) + 2\zeta r j}. \quad (2.7)$$

This solution can be applied if the excitation is a harmonic function. However since the Laplace equation is linear the sum of several individual solutions is also a solution. In other words, if the excitation is not a harmonic function the solution can be applied as long as the excitation function can be represent as a Fourier series of harmonic functions. This is a great advantage of the frequency domain analysis.

For the steady state solution of Eq. 2.3 in time domain the particular integral has to be solved. The solution can be assumed to be of the form:

$$z(t) = Z \sin(\omega t - \varphi), \quad (2.8)$$

where Z is the amplitude of the relative oscillation and φ the phase between the excitation and the oscillation of the mass. By substituting Eq. 2.8 into Eq. 2.3 the amplitude and phase of steady state motion can be found to be:

$$Z = \frac{m\omega^2 Y}{\sqrt{(k - m\omega^2)^2 + (d\omega)^2}} = \frac{r^2 Y}{\sqrt{(1 - r^2)^2 + (2\zeta r)^2}},$$

$$\tan \varphi = \frac{d\omega}{k - m\omega^2} = \frac{2\zeta r}{1 - r^2}. \quad (2.9)$$

For the absolute motion x the steady-state amplitude and phase are (solution of Eq. 2.1):

$$X = Y \cdot \sqrt{\frac{k^2 + (\omega d)^2}{(k - m\omega^2)^2 + (d\omega)^2}} = Y \cdot \frac{\sqrt{1 + (2\zeta r)^2}}{\sqrt{(1 - r^2)^2 + (2\zeta r)^2}},$$

$$\tan \psi = \frac{md\omega^3}{k(k - m\omega^2) + (\omega d)^2} = \frac{2\zeta r}{1 - r^2}. \quad (2.10)$$

The curves are plotted in Fig. 2.2. In spite of the relative motion, the natural frequency of the absolute motion decreases with increasing damping. The natural frequency of a damped oscillation can be calculated as follows:

$$\omega_d = \sqrt{\omega_0^2 - \zeta^2}. \quad (2.11)$$

2.2.2 Nonlinear Spring System

In the previous section the analytical treatment of a linear spring–mass–damper system was discussed. But for the design of vibration transducers it is also important to understand the behavior of nonlinear spring systems. This is because nonlinearity appears for any real spring if the deflection is only high enough. Moreover in some cases it is possible to increase the output power using nonlinear spring systems. This has been shown by the author in [23]. A more detailed treatment of nonlinear spring systems for energy harvesting devices has been presented in [66, 16]. As a general basis for the understanding of the numerical simulations (carried out in Sect. 7.4.1) this section gives a short introduction on the behavior of nonlinear vibration based on the results in [35]. Note that a deeper understanding of nonlinear systems can only be obtained by simultaneous use of analytical and numerical techniques.

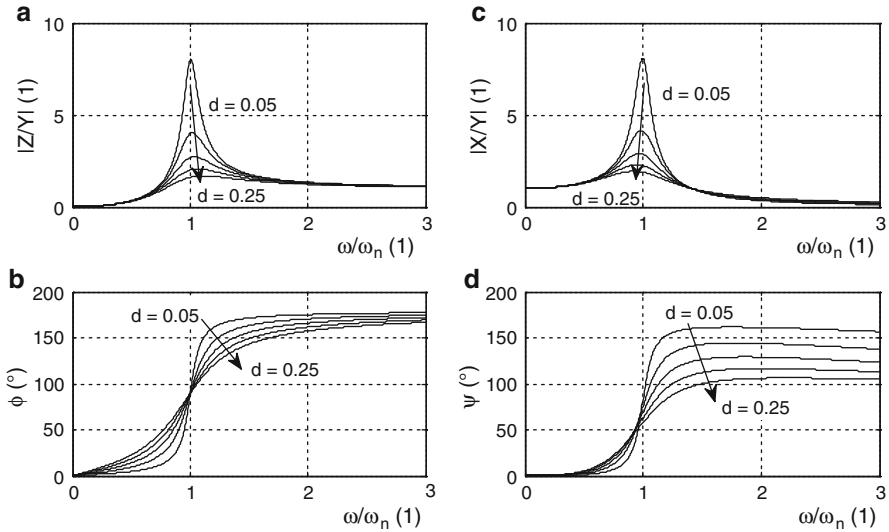
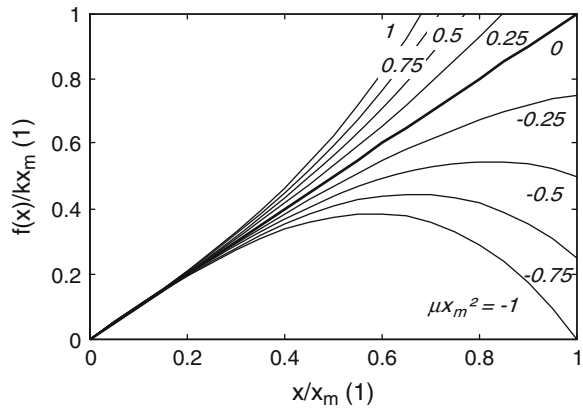


Fig. 2.2 (a) and (b) shows plot of Eq. 2.9, (c) and (d) shows plot of Eq. 2.10. Note that in contrast to the relative motion (a) the natural frequency for absolute motion decreases with increasing damping (c)

Fig. 2.3 Nondimensional plot of the nonlinear restoring force. Softening behavior results for $\mu x_m^2 < 0$ and hardening behavior for $\mu x_m^2 > 0$. A pure linear spring is obtained for $\mu x_m^2 = 0$

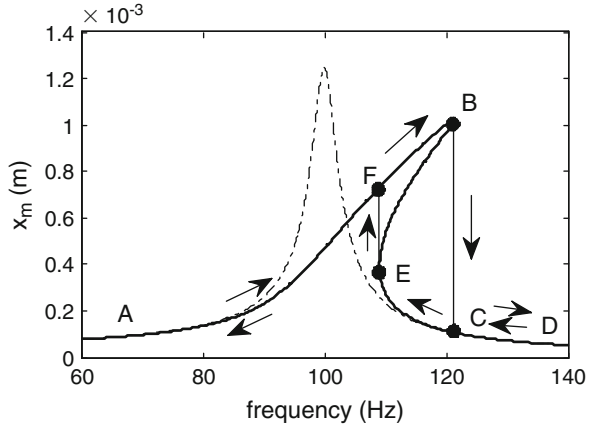


The nonlinear system we need to investigate is similar to the SDOF system shown in Fig. 2.1. The difference is that the restoring force induced by the spring is no more proportional to the spring rate k but is a nonlinear function of the displacement x :

$$f(x) = kx (1 + \mu_{nl}x^2), \tag{2.12}$$

where μ_{nl} is the nonlinearity parameter which is positive for hardening and negative for softening springs. A non-dimensional plot of (2.12) is shown in Fig. 2.3.

Fig. 2.4 Frequency response for nonlinear hardening system. The *dash dotted curve* indicates the response of a linear system



Using a forcing function with an amplitude f_0 as excitation together with (2.12) the corresponding equation of motion can be written as:

$$\ddot{x} + 2\beta\dot{x} + \omega_n^2 x + \omega_n^2 \mu_{nl} x^3 = \frac{f_0}{m} \sin(\omega t + \varphi), \quad (2.13)$$

where $\beta = d/2m$ and ω_n indicates the natural frequency of the undamped motion. This nonlinear differential equation can be solved using the Ritz–averaging method [77]. With $f'(x) = k\mu_{nl}x^3$ and the sinusoidal ansatz function with frequency ω and amplitude z_m it follows:

$$\int_0^T \left(\ddot{x} + 2\beta\dot{x} + \omega_n^2 x + f'(x) - \frac{f_0}{m} \sin(\omega t + \varphi) \right) \cdot \underbrace{x_m \sin(\omega t)}_{\text{ansatz function}} dt = 0. \quad (2.14)$$

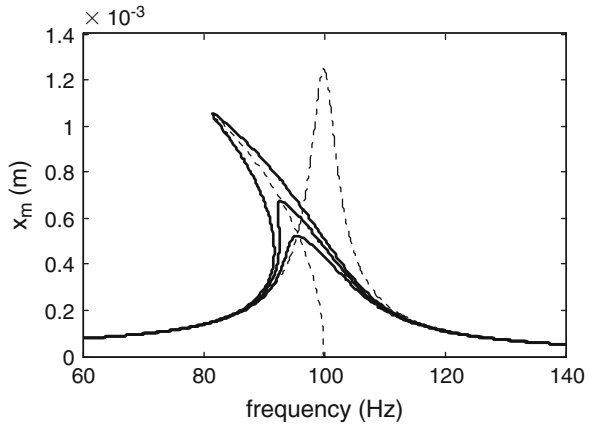
The theory to solve this equation according to the Ritz–averaging method is beyond the scope of this book. The most important result at this point is the displacement amplitude which can be written as:

$$\left[(k - m\omega^2) x_m + \frac{3}{4} k \mu_{nl} x_m^3 \right]^2 + x_m^2 d^2 \omega^2 = f_0^2. \quad (2.15)$$

Typical plots of the frequency response for nonlinear hardening ($\mu_{nl} > 0$) and nonlinear softening ($\mu_{nl} < 0$) systems are given in Figs. 2.4 and 2.5, respectively. Setting the amplitude of the forcing function equal to zero yields the so called backbone or skeleton curve and indicate the frequency of the free oscillation $d = 0$ (included as the dotted curve in Fig. 2.5):

$$\omega_{nl} = \omega_n \sqrt{1 + \frac{3}{4} \mu_{nl} x_m^2}. \quad (2.16)$$

Fig. 2.5 Frequency response of nonlinear system at different damping factors. The *dotted line* is the so called backbone or skeleton curve



The backbone or skeleton curve indicates the change of the nonlinear resonance frequency ω_{nl} as a function of the amplitude. Note that there are regions where the theoretical solution has three possible states for a given single excitation frequency. However in reality this is not possible. For increasing frequency the amplitude function passes through A, B, C and D and for decreasing frequency through D, E, F and A. This effect is also known as the jump phenomenon. In contrast to linear systems the state of nonlinear systems depends on the history. Even though the amplitude responses of nonlinear systems suggest a higher bandwidth compared to the linear system it is very delicate to claim that nonlinear systems have a priori an advantage in this case. The reason for this is that it may be difficult to guarantee that in an application the system operates between F and B and not between E and C.

2.3 Electromagnetic Subsystem

2.3.1 Basics on Electromagnetic Induction

The output power of electromagnetic vibration transducers is related to the particular design of the electromagnetic coupling. Hence factors like size, material properties and geometric configuration of magnet, coil and magnetic circuit play a vital key role in the design process. So far conclusions from literature are often based on very simplifying assumptions. This is because the analytical calculation of the magnetic field is rather complicated for ironless systems and even impossible for systems with back iron. Nevertheless the basic theory of magnetic induction is necessary in order to understand how the electrical energy can be extracted. In electromagnetic vibration transducers the transduction mechanism is based on Faraday's law of induction. This law states that any change of magnetic flux through a conductive

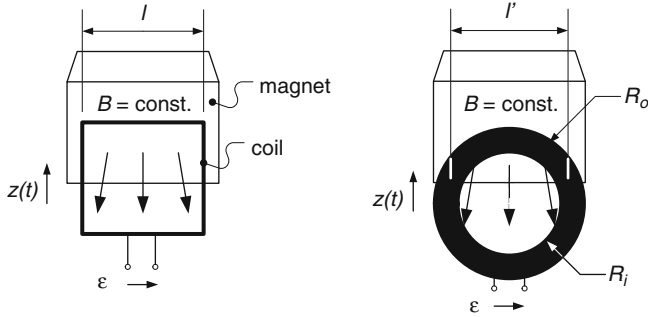


Fig. 2.6 Popular models for linearized electromagnetic transducer analysis. Induction coil arranged in constant magnetic field with (a) rectangular cross section and concentrated windings and (b) circular cross section with spacious windings. Beyond the magnet boundary the magnetic field is assumed to be zero

loop of wire will cause a voltage to be induced in that loop. The magnetic flux is defined as:

$$\varphi_m = \iint_A B dA, \quad (2.17)$$

where A indicates the area enclosed by the wire loop and B is the magnetic flux density. The induced voltage is the so-called electromotive force (*emf*) which is given by:

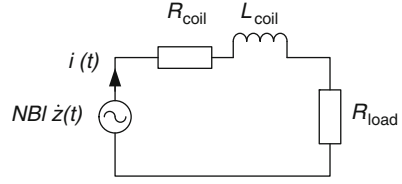
$$\varepsilon = -\frac{d\varphi_m}{dt}. \quad (2.18)$$

If one substitutes the magnetic flux from Eq. 2.17, then the induced voltage becomes:

$$\varepsilon = -\left(\frac{dA}{dt}B + \frac{dB}{dt}A\right). \quad (2.19)$$

From this equation it is evident that for electromagnetic induction it does not matter whether the magnetic field is changing within a constant area or the area is changing within a constant magnetic field. This characteristic offers a wide range of possible implementations of the electromagnetic coupling. Two basic arrangements are shown in Fig. 2.6 [64]. Both of them can be referred to the first term in the sum of (2.19). The coil in Fig. 2.6a has a rectangular cross section with concentrated windings whereas the coil in Fig. 2.6b has a circular cross section and the windings are spacious (more realistic case). These arrangements are often used for analytical evaluation due to the simplicity in calculation in contrast to arrangements where the

Fig. 2.7 Circuit diagram representation of the electromagnetic subsystem for analytical analyses



emf is produced through a diverging magnetic field according to the second term in the sum of (2.19). Such arrangements will be studied in detail in Chap. 3.

For coils with N windings and rectangular cross section the change of overlapping area follows $N \cdot dA / dt = Nl \cdot dz / dt = Nl\dot{z}$. Thus, the emf voltage becomes:

$$\varepsilon = -NBl\dot{z}. \quad (2.20)$$

With the Lorentz force $F = q(\dot{z} \times B)$ (Force on point charge q in electromagnetic field) it is apparent that only wire segments orthogonal to the velocity are responsible for the emf voltage. For coils with circular cross section the length l in (2.20) must be substituted by l' which can maximal be $(R_o + R_i)$. Note that this is only valid for small amplitudes in $z(t)$ or small changes of l' . The large displacement case will be considered in Sect. 3.6.3. Now Eq. 2.18 can be extended using the chain rule:

$$\varepsilon = -\frac{d\varphi_m}{dz} \cdot \frac{dz}{dt} = k_t \cdot \dot{z}, \quad (2.21)$$

where k_t is the transduction factor. The transduction factor equals the magnetic flux gradient and is assumed to be constant in the analytical treatment.

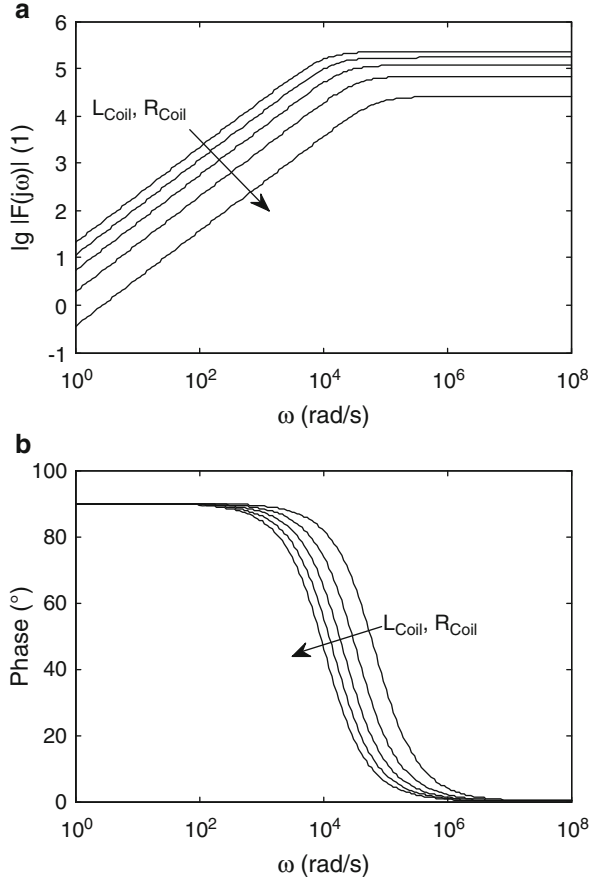
2.3.2 Electrical Network Representation

In the implementation of vibration energy harvesting devices the electrical load will be a complex analog and digital electronic load circuit. In the analytical analysis the ohmic loss of the load circuit is typically represented by a resistor R_{load} in series to the coil resistance R_{coil} and coil inductance L_{coil} as shown in Fig. 2.7. The governing equation is given by:

$$L_{Coil} \frac{di(t)}{dt} + (R_{coil} + R_{load}) i(t) = -NBl \frac{dz(t)}{dt}. \quad (2.22)$$

In the frequency domain with the voltage V at the load resistance this differential equation becomes:

Fig. 2.8 (a) Frequency- and (b) Phase response of the electrical network



$$G_{emag}(s) = \frac{V(s)}{Z(s)} = \frac{-NBI R_{load} s}{L_{Coil} s + R_{Coil} + R_{load}}. \quad (2.23)$$

Magnitude and phase response of the LTI (Linear time-invariant) model is shown in Fig. 2.8 for different values of L_{coil} and R_{coil} . The inductance and resistance of air cored coils can easily be calculated if the copper fill factor of the winding process is known. The copper fill factor is defined as the ratio of the overall wire area (without isolation) A_l to the cross-section of the winding area A_w [47]:

$$k_{co} = \frac{A_l}{A_w} = \frac{\pi \cdot d_{co}^2 \cdot N}{4 \cdot A_w}, \quad (2.24)$$

where d_{co} indicates the wire diameter (without isolation). For the cylindrical coils used in this book (as shown in Fig. 2.9a) we obtain 0.6 as a typical value for k_{co} . An underlying experimental verification is given in Appendix A. Note that there is no possibility for the theoretical calculation of the copper fill factor for wire diameters

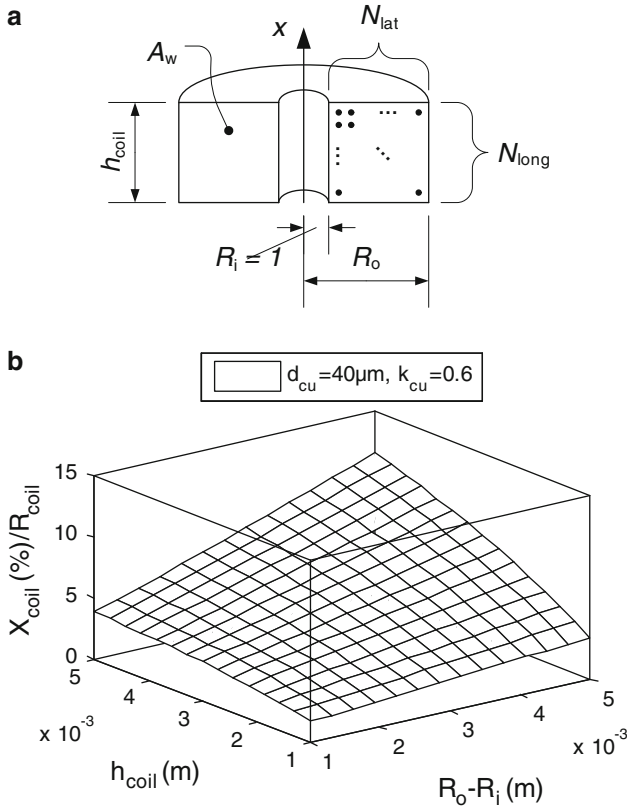


Fig. 2.9 (a) Example of cylindrical air cored coil with inner radius of 1 mm (b) Ratio of resistance R_{coil} to reactance X_{coil} in per cent for different winding areas A_w of the example coil at 100 Hz. For typical winding areas the resistance dominates the impedance

smaller than $200 \mu\text{m}$ [47]. This is because the wire layers are unsystematic and random winding occurs. For a given copper fill factor the number of windings in longitudinal N_{long} and lateral N_{lat} direction can be calculated using:

$$\begin{aligned}
 [N_{long}] &= \frac{2 \cdot h_{coil}}{d_{co} \sqrt{\pi / k_{co}}}, \\
 [N_{lat}] &= \frac{2 \cdot (R_o - R_i)}{d_{co} \sqrt{\pi / k_{co}}}.
 \end{aligned}
 \tag{2.25}$$

With the resistance per meter R' (Enamelled Copper Wires are based on IEC 60317) the resistance can be calculated as follows:

$$R_{coil} = N \cdot 2\pi \cdot \frac{(R_o - R_i)}{2} \cdot R'.
 \tag{2.26}$$

Therein the number of windings N is the product of N_{long} and N_{lat} . The inductance of the considered coils can be determined according to the Wheeler approximations [38]:

$$L_{\text{Coil}} = \frac{3.15 \cdot 10^{-5} \cdot R_m^2 \cdot N^2}{6R_m + 9h_{\text{coil}} + 10(R_o - R_i)}, \quad (2.27)$$

where R_m denotes the middle radius given by $(R_o + R_i)/2$. For low vibration frequencies further simplification can be done because according to the complex impedance of the coil:

$$Z_{\text{coil}} = R_{\text{coil}} + j\omega L_{\text{Coil}}, \quad (2.28)$$

the reactance will be much smaller than the resistance. Figure 2.9b gives the ratio of the resistance (real part) to the reactance (imaginary part) of the impedance for a frequency of 100 Hz and different winding areas. The result shows that especially for large winding areas the reactance is well below 10% of the resistance. Hence it is for simplification matters appropriate to neglect the reactance. In this case impedance matching condition and maximum power transfer to the load can be obtained using the EDAM (Electrical domain analog matching) [58]. The relationship for the optimal load resistance can be expressed as:

$$R_{\text{load,opt}} = R_{\text{coil}} + \frac{k_t^2}{d_m}, \quad (2.29)$$

where d_m denotes the unwanted parasitic viscous damping effects. Beyond the commonly known resistance matching in electrical domain this approach includes also the electrical analog of the parasitic damping.

2.4 Overall System

2.4.1 General Behavior

The previous sections discussed the mechanical and electromagnetic subsystem of vibration transducers. These subsystems can now be combined to an overall system model. The mechanical domain (input force and relative velocity of the mass) and the electromagnetic domain (*emf* and induced current) are related via the transduction factor k_t . For closed circuit condition the *emf* voltage will cause a current to flow. This current creates a magnetic field which opposes the cause according to Lenz's law. The feedback electromechanical force is given by:

$$F = k_t i, \quad (2.30)$$

or together with Eq. 2.21 and Ohm's law:

$$F = \frac{k_t^2}{R_{coil} + R_{load}} \dot{z}. \quad (2.31)$$

Hence the dissipative feedback electromechanical force due to the transducer can be represented by a velocity proportional viscous damping element with the damping coefficient:

$$d_e = \frac{k_t^2}{R_{coil} + R_{load}} = \frac{(NBl)^2}{R_{coil} + R_{load}}. \quad (2.32)$$

Now the transfer functions of the subsystems (2.5) and (2.23) can be combined to an overall input force to output voltage transfer function for the electrodynamic transducer:

$$G_{overall}(s) = \frac{V(s)}{F(s)} = \frac{NBlR_{load}s}{(ms^2 + d_ms + k)(Ls + R_{load} + R_{coil}) + \frac{(NBl)^2}{R_{load}}s}, \quad (2.33)$$

where the displacement of the vibration $Y(s)$ has been replaced by the forcing function $F(s) = -mY(s)s^2$. If the inductance is neglected Eq. 2.33 reduces to:

$$G_{overall}(s) = \frac{NBlR_{load}s}{\left(ms^2 + \left(d_m + \frac{(NBl)^2}{R_{load}}\right)s + k\right)(R_{load} + R_{coil})}. \quad (2.34)$$

The magnitude and phase response of the subsystems and the overall system for system with a resonance frequency of 100 Hz are shown in Fig. 2.10. The dashed curves indicate the influence of the inductance. In the resonance frequency range there is nearly no influence of the inductance observable. A block diagram of the underlying simulation model implemented in Matlab/Simulink[®] is shown in Fig. 2.11.

2.4.2 First Order Power Estimation

Analysis of (2.31) shows that the electromagnetic transduction mechanism can be represented by a dissipative velocity proportional damping element. The maximum power that can be extracted from the vibration is thereby related to the power dissipated in that damper. Starting from the general equation for the power:

$$P(t) = \frac{d}{dt} \int_0^z F(t) dz, \quad (2.35)$$

Fig. 2.10 (a) Magnitude and (b) phase response for the subsystems and the overall transducer system. The *dashed curves* indicate the influence of the inductance

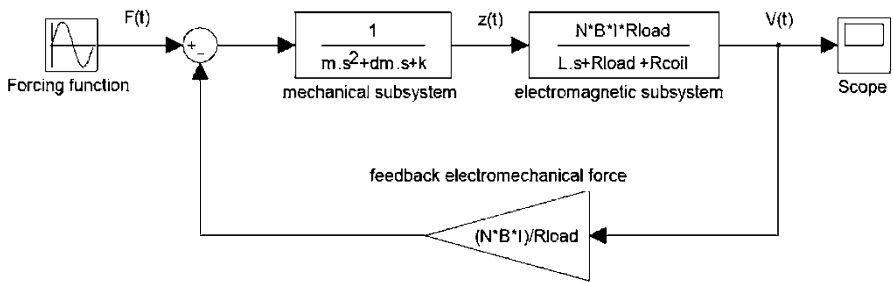
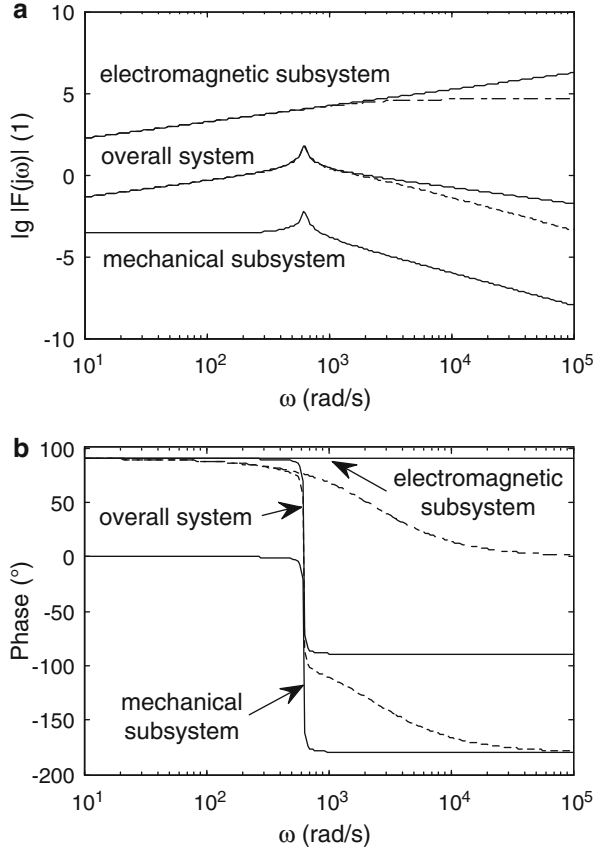


Fig. 2.11 Block diagram of the overall transducer model for simulation in Matlab/Simulink®

the instantaneous dissipated power (together with $F(t) = d_e \dot{z}$) becomes:

$$P(t) = \frac{1}{2} d_e \dot{z}^2. \tag{2.36}$$

The velocity is obtained by the first derivative of the steady state amplitude of (2.9):

$$\dot{Z} = \frac{\omega \cdot r^2 Y}{\sqrt{(1-r^2)^2 + (2(\zeta_e + \zeta_m)r)^2}}, \quad (2.37)$$

where the normalized damping factor has been split into the electromechanical and parasitic part ($\zeta = \zeta_e + \zeta_m$). Substituting this equation into (2.36) the generated electrical power becomes:

$$P = \frac{m\zeta_e \left(\frac{\omega}{\omega_n}\right)^3 \omega^3 Y^2}{\left(1 - \left(\frac{\omega}{\omega_n}\right)^2\right)^2 + \left(2(\zeta_e + \zeta_m) \frac{\omega}{\omega_n}\right)^2} \quad (2.38)$$

This basic equation has first been published by Williams and Yates in [15]. For operation at resonance ($\omega = \omega_n$) (2.38) can be reduced to:

$$P = \frac{m\zeta_e \omega_n^3 Y^2}{4(\zeta_e + \zeta_m)^2} = \frac{m^2 d_e \omega_n^4 Y^2}{2(d_e + d_m)^2}. \quad (2.39)$$

Since the base excitation is a pure harmonic input of the form,

$$\begin{aligned} y(t) &= Y \sin(\omega t), \\ \dot{y}(t) &= Y\omega \cos(\omega t), \\ \ddot{y}(t) &= -Y\omega^2 \sin(\omega t), \end{aligned}$$

the output power may also be expressed as a function of the input acceleration amplitude $|\ddot{Y}| = Y\omega^2$:

$$P = \frac{m\zeta_e \ddot{Y}^2}{4\omega_n(\zeta_e + \zeta_m)^2} = \frac{m^2 d_e \ddot{Y}^2}{2(d_e + d_m)^2}. \quad (2.40)$$

Hence, beyond the parameters of the vibration which cannot be influenced, the output power depends on the oscillating mass and the damping coefficients. The optimal ratio for the damping factors (obtained by setting $dP/d\zeta_e = 0$) is given by $\zeta_e = \zeta_m$ which is also apparent from the plot of Eq. 2.39 in Fig. 2.12 [73]. However, for a high oscillation mass, operation at high vibration amplitudes or for a small parasitic damping factor the optimal value of the electromagnetic damping could violate the maximum allowable inner displacement limit. This results in constrained condition and the electromagnetic damping can be increased which in turn reduces the maximum power. Detailed analysis on this is given in [63, 64]. The minimum

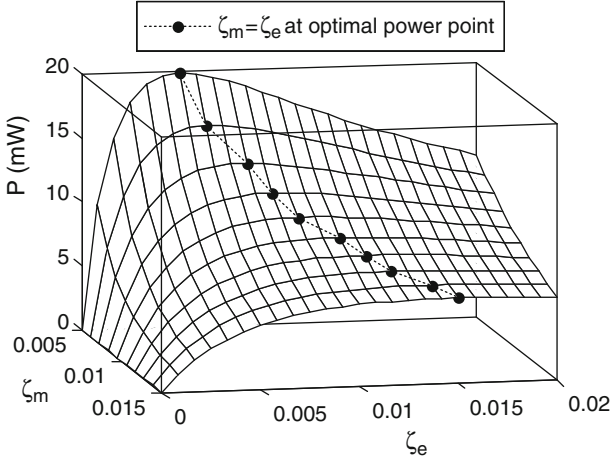


Fig. 2.12 Output power as a function of the electromechanical and parasitic damping

allowable damping factor is given by the rearrangement of the steady state amplitude in (2.9):

$$\zeta_{e,\min} = \frac{1}{2r} \sqrt{r^4 \left(\frac{Y}{Z_{\max}} \right)^2 - (1 - r^2)^2 - \zeta_m}, \quad (2.41)$$

where Z_{\max} denotes the maximum relative displacement. Note that in the same way as in (2.37) the normalized damping factor has been split into an electromagnetic and a parasitic part. This expression can now be substituted into (2.39) to obtain the displacement constrained output power:

$$P_{c,s} = \frac{m\zeta_{e,\min}\omega_n^3 Y^2}{4(\zeta_{e,\min} + \zeta_m)^2}. \quad (2.42)$$

Consequently the maximum power for constrained condition is again obtained at resonance where $\omega = \omega_n$ or $r = 1$ in (2.42):

$$P_{c,s,\max} = \frac{1}{2} m \omega_n^3 Z_{\max} \cdot (Y - 2Z_{\max}\zeta_m) \quad (2.43)$$

2.5 Characterization and Handling of Machinery Induced Vibration

Commonly the vibration source is assumed to perform a pure harmonic motion. Because this kind of excitation is deterministic the response of the system is also deterministic. In this case there is no difficulty in expressing the response in closed

form for any deterministic excitation function as long as the system is linear. However in real applications the vibration source may be a random function. In this case it is not possible to express the response in closed form in time domain. Nevertheless, for the development of vibration transducers it is important to know which resonance frequency maximizes the output power and to be able to make first order power estimation. This can easily be done in frequency–domain rather than time–domain analyses.

The basis for the development of vibration transducers is in general an ensemble of measured acceleration time histories of the vibration source. If the random process is stationary and the temporal mean value and the temporal autocorrelation function are the same for any sample function the process is said to be ergodic [48]. In this case, any single sample function is “representative” and can be used for the development. Ergodic process is also assumed in what follows. The frequency domain representation of the acceleration function $a(t)$ can be obtained using the discrete Fourier transform. Three different example vibration spectra are shown in Fig. 2.13. The measurement data shown in Fig. 2.13a was taken from an air–filter housing of a car engine while driving on a country route. In the frequency content the order related phenomena of the car engine is apparent [20]. The acceleration profile in Fig. 2.13b was measured close to the chisel of a tunnel boring machine and (c), as an example for a noisy harmonic vibration source, was measured on a mould for the fabrication of concrete products. The data was acquired with a sample rate of 1,000 Hz. According to the Nyquist–Shannon theorem frequencies up to 500 Hz can be detected. However the axes are limited to the range of interest and the highest acceleration amplitudes. For a variety of technical vibration sources these highest acceleration amplitudes lie predominantly below 200 Hz. According to Eq. 2.40 the maximum output power is quadratically dependent on the input acceleration amplitude. Hence the most energetic vibration frequencies and thus the preferred resonance frequency of the vibration transducer can directly be identified from the acceleration spectra. If there are two or more frequency ranges with equal acceleration level as shown in Fig. 2.13a it is advisable to choose the frequency range with higher bandwidth in order to reduce the necessity that the resonance frequency matches one particular vibration frequency. Since the suitable resonance frequencies can now be selected the question is how much power can be extracted? A first order power estimation can be obtained by substituting the acceleration amplitude spectra into Eq. 2.40. Actually this is a simplification which assumes that the vibration transducer acts like a narrow band–pass filter. Hence only components of the vibration that are close to the resonance frequency significantly contribute to the output power. For the vibration of the air–filter housing and the tunnel borer machine this first order power estimation is shown in Fig. 2.14. The absolute values are of course dependent on the applied parameter values. The most important parameters used for the calculation of the output power spectra are $d_m = 0.1$ N/m/s, $m = 10$ g and an inner displacement limit of $Z_{\max} = 2$ mm. For the mould vibration the high vibration acceleration amplitude violates the inner displacement limit of the oscillating mass. Thus it is necessary to use (2.43) for the power estimation. To apply this equation to the acceleration spectra the displacement amplitude of the excitation

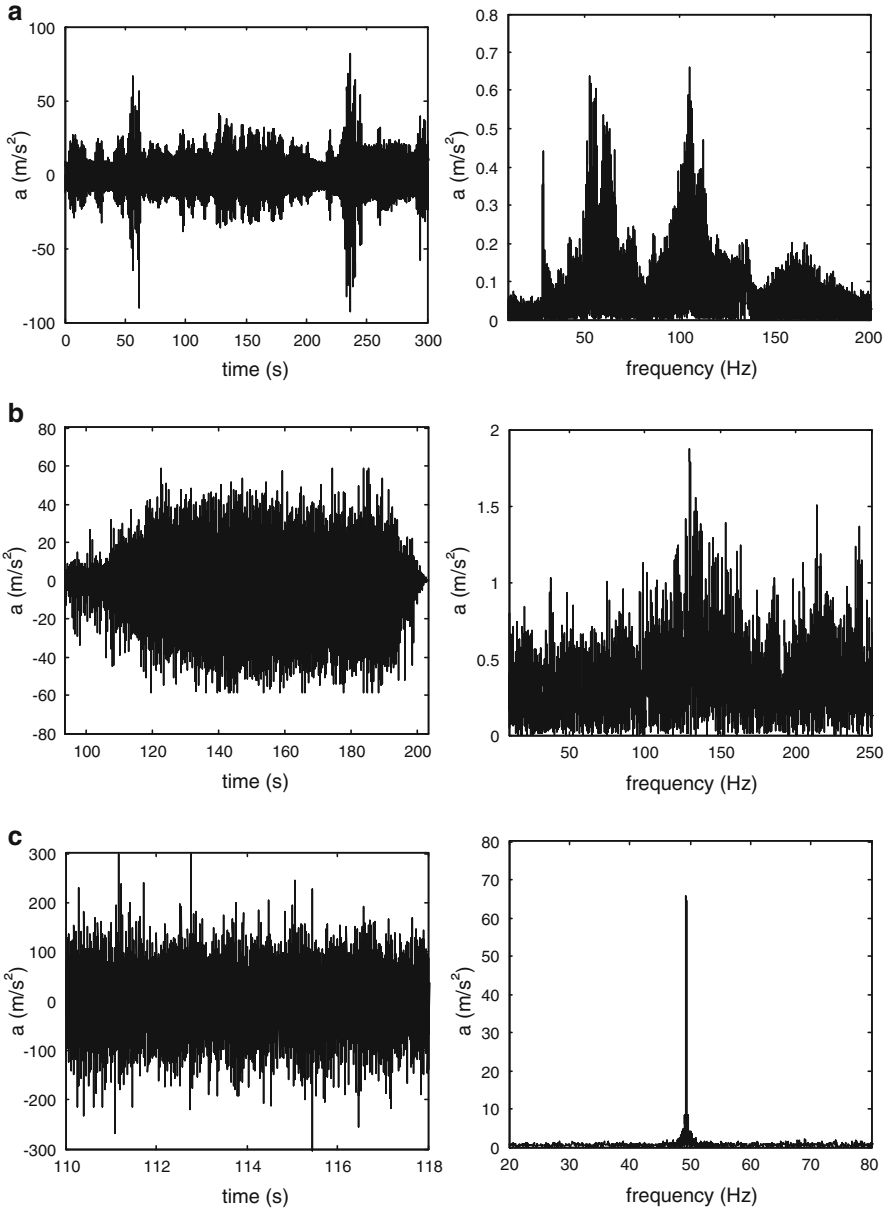


Fig. 2.13 Acceleration (*left*) and frequency content (*right*) of different example vibration sources. (a) air-filter housing of a car engine during country driving route, (b) tunnel boring machine close to the chisel and (c) mould for fabrication of concrete products

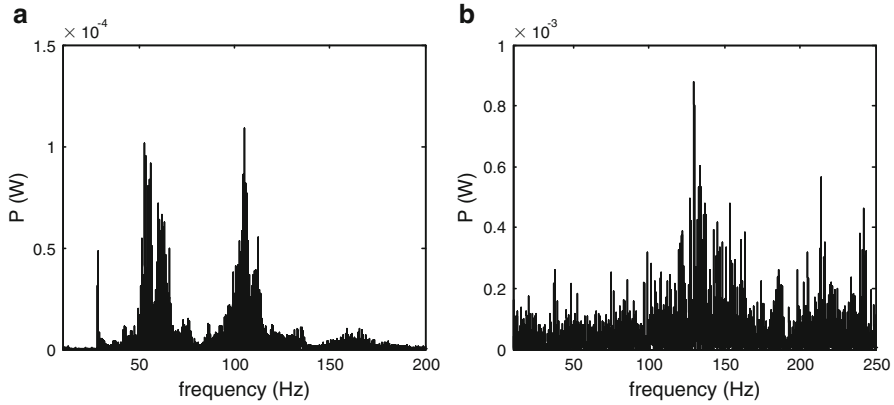
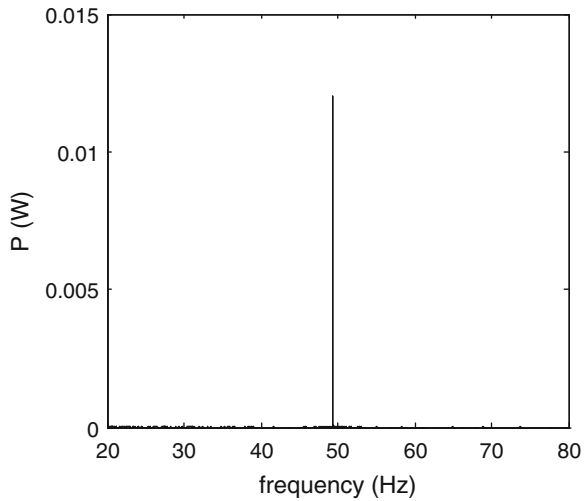


Fig. 2.14 First order power estimation for unconstrained condition for the vibration of the air-filter housing (a) and the vibration of the tunnel borer machine (b)

Fig. 2.15 Due to the high acceleration amplitude of the mould vibration it is appropriate to apply constrained condition for the first order power estimation



Y needs to be replaced by the acceleration amplitude $\ddot{Y} = Y\omega^2$. The result of the output power for the constrained condition is shown in Fig. 2.15. In spite of the constraint condition the output power is rather high. This is because the minimum allowable damping factor based on the applied parameters is also very high (almost 7 N/(m/s)) which results in overdamping. Note that it will not be possible to design such an electromagnetic damping element in application. Nevertheless, the point of interest is to find the maximum output power.

2.6 Conclusions from Analytical Analyses

In this chapter the basic analysis of electromagnetic vibration transducers was summarized based on results from literature. The results are used to understand the behavior of the mechanical and electromagnetic subsystem and to identify the most important parameters for power extraction of the overall system. First order power estimation has been carried out for both harmonic and machinery induced random excitation. For the latter case it has been shown how the most energetic vibration frequency can be identified. As often stated in literature it has been shown that the maximum possible output power can be achieved if the parasitic damping equals the electromagnetic damping coefficient. However, it must be said that even though this conclusion is valid from the theoretical point of view, it has only marginal relevance for the design process of vibration transducers. This is due to the fact that in application oriented developments the construction volume is limited in the majority of cases but the underlying analytical theory does not consider any volume dependent effects so far. By assuming a limited construction volume this can be explained as follows. According to the basic Eq. 2.39 the output power is directly dependent on the oscillating mass. Beside the density of the material the oscillating mass can primarily be increased by its volume which means less space for the implementation of the electromagnetic coupling. For given parameters of the magnet the electromagnetic coupling can in turn primarily be increased by the number of windings which also needs space no more available for increasing the mass. Hence the mass and the electromagnetic damping are no more independent design parameters, which evokes a trade off and the major task is finding the optimum dimensions which yield the maximum output power. As already stated this is a main objective of this book and will be discussed in detail for different electromagnetic coupling architectures later on. However the central issue can be explained and analysed using a model as shown in Fig. 2.16 where a magnet moves relative to a thin coil with rectangular cross section. The construction

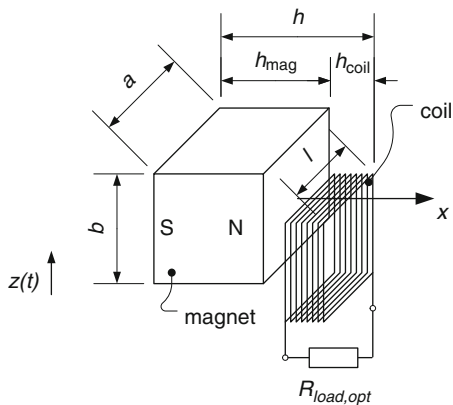
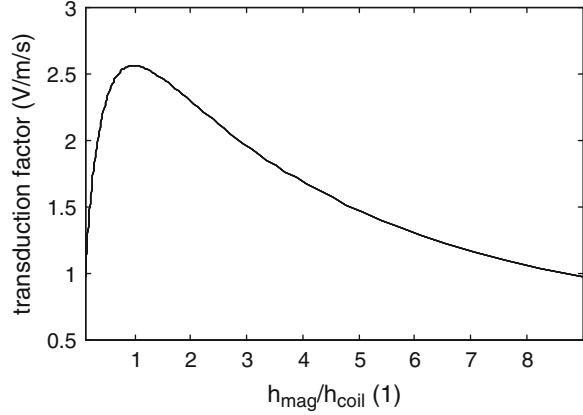


Fig. 2.16 Model of resonant electromagnetic vibration transducer used to investigate volume dependent effects

Fig. 2.17 Magnetic flux gradient at different ratios of h_{mag} and h_{coil}



volume defined by a , b and h is assumed to be fixed. That means an increase of the oscillating mass by increasing h_{mag} involves a decrease of h_{coil} and therewith less windings. Now the question to be answered is which ratio of h_{mag}/h_{coil} yields the maximum output power?

The number of windings N of the thin coil is simply given by the multiplication of h_{coil} with the number of turns per unit length η . With the lateral length a of the rectangular coil together with the resistance per unit length R' the total resistance is then given by $R_{coil} = 4lR'N$. Beyond this the decrease of magnetic field can be taken into account as a first approximation using the magnetic flux density component in x -direction on the centre axis of the magnet which is given by [3]:

$$B_x(x) = \frac{B_r}{\pi} \left(a \tan \left(\frac{b \cdot a}{2x\sqrt{4x^2 + b^2 + a^2}} \right) - a \tan \left(\frac{b \cdot a}{2(h_{mag} + x)\sqrt{4(h_{mag} + x)^2 + b^2 + a^2}} \right) \right), \quad (2.44)$$

where B_r indicates the residual flux density of the magnet. The transduction factor can then be written as:

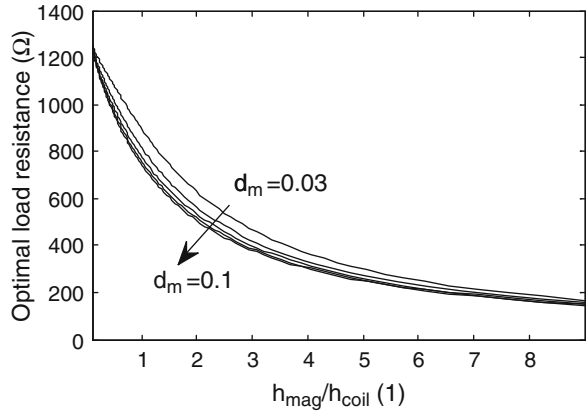
$$k_t = NI \cdot \frac{1}{h_{coil}} \int_0^{h_{coil}} B_x(x) dx. \quad (2.45)$$

A plot of this function is shown in Fig. 2.17. Note that the transduction factor has a maximum at approximately $h_{mag}/h_{coil} = 1$ for this calculation example (parameters listed in Table 2.1). Now the optimal load resistance can be calculated according to (2.29). Results for different parasitic damping factors are shown in Fig. 2.18.

Table 2.1 Parameters used in the construction volume constraint calculation example

Symbol	Description	Value	Unit
<i>Magnet</i>			
B_r	Residual flux density	1	T
ρ_{mag}	Density of magnet	7.8	g/cm ³
<i>Coil</i>			
d_{co}	Wire diameter	40	μm
R'	Resistance per unit length	13.6	Ω/m
<i>Other</i>			
Y_{acc}	Excitation amplitude	10	m/s ²
f	Excitation frequency	100	Hz

Fig. 2.18 The optimal load resistance is dependent on the parasitic damping factor



According to Faraday's law of induction (2.21) in consideration of the displacement amplitude (2.9) together with the electromagnetic damping (2.32) the output voltage can be obtained by applying Ohm's law to the voltage divider. For operation at resonance the equation yields:

$$V_{R_{load,opt}} = k_t \frac{m\omega^2 Y}{\left(\frac{k_t^2}{R_{coil} + R_{load,opt}}\right) + d_m} \cdot \frac{R_{load,opt}}{R_{coil} + R_{load,opt}}. \quad (2.46)$$

Figure 2.19 is a plot of the output voltage for various parasitic damping factors. Again, there exists a ratio of h_{mag}/h_{coil} where the output voltage becomes maximal. With respect to the transduction factor this maximum is shifted to higher values of h_{mag}/h_{coil} and to higher oscillating velocities, respectively. In a final step the resulting output power can be calculated using Joule's law:

$$P_{R_{load,opt}} = \frac{V_{R_{load,opt}}^2}{R_{load,opt}}. \quad (2.47)$$

Fig. 2.19 There are optimal ratio of h_{mag} and h_{coil} where the output voltage gets maximal

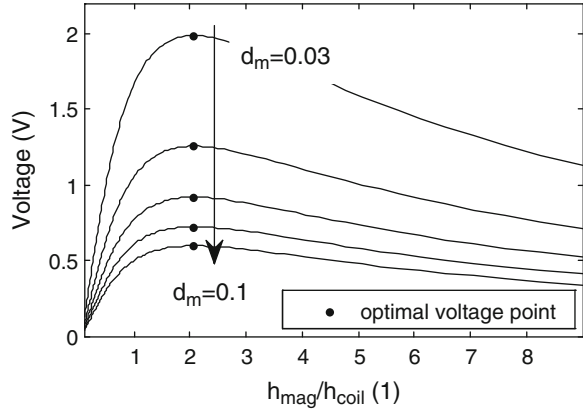
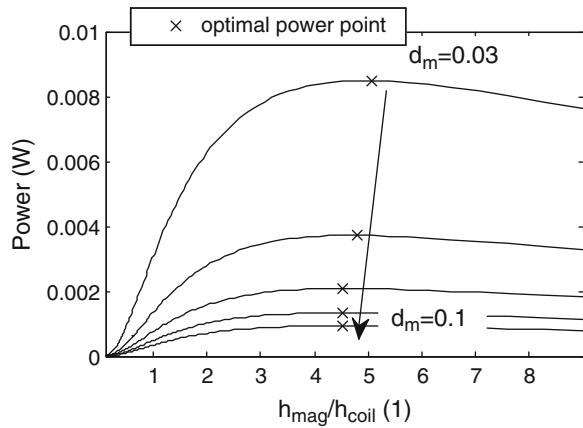
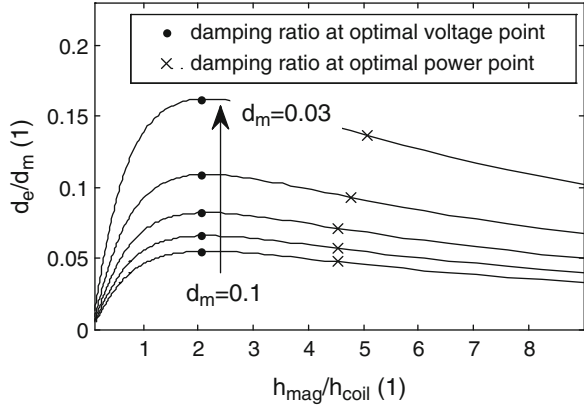


Fig. 2.20 The optimal ratio of h_{mag} and h_{coil} for output power generation are different as for output voltage generation



Consequently the results in Fig. 2.20 show that there is another optimal ratio of h_{mag}/h_{coil} where the output power gets maximal. With respect to the output voltage this optimal ratio is once again shifted to higher values of h_{mag}/h_{coil} and to smaller resistances, respectively. The damping ratios at optimal voltage and optimal power points are given in Fig. 2.21. In comparison to the optimal damping ratio of $d_e/d_m = 1$ stated from the basic analytical theory the damping ratios of this construction volume constrained calculation example are well below 1. However, the damping ratios at the optimal power points are even lower than the maximal obtainable damping ratios. Though, the maximum damping ratios correspond to the optimal voltage operation point. As already stated the reason for this inconsistency is that whenever the construction volume is constrained the oscillating mass and the electromagnetic coupling are not independent. In this case the task is to find optimal values for the geometrical parameters which maximize the output voltage or the output power. In analytical form, the optimization of the geometrical parameters can only be performed for rather simplified assumptions and only for a few coupling

Fig. 2.21 The optimum output voltage is generated at the maximum possible damping factor ratio. In spite to this the damping ratio for optimum output power is less than the maximum value



architectures. This is why the efficient design of electromagnetic devices requires numerical methods especially if ferromagnetic flux-conducting components are used.

The results presented in this chapter lead to the following conclusions for the applicability of the analytical theory in the design process of electromagnetic vibration transducers:

- The result of the basic analytical theory is important for understanding the behavior of the subsystems, identifying most important parameters of the overall system and investigating the interdependencies.
- The output power equations are useful for making first order power estimations under consideration of practical constrains like the inner displacement limit.
- In literature it is often stated that the output power becomes maximum if the electromagnetic damping factor equals the parasitic damping factor. Even though this is correct from the theoretical point of view, it is not applicable as a design guide for constrained construction volume condition.
- Whenever the construction volume is limited the main task is to find the optimal geometrical parameters of magnet and coil rather than optimizing damping ratios.
- It is important to know that there exists a separate optimum for voltage and power optimized design.
- Realizing an optimized design requires the calculation of magnetic field distribution. Analytical solutions based on Maxwell's equations are very difficult and sometimes impossible. Therefore it is necessary to use numerical methods in the design process.
- Once the vibration transducer is complete and frequency response measurements have been performed the analytical theory is, in most of all cases, adequate for accurate simulation of the measurement results as shown in many publications.

Chapter 3

Power and Voltage Optimization Approach

3.1 Introduction

The previous chapter presented the theoretical basis for the analysis of electromagnetic vibration transducers. Therein closed form solutions for first order power estimations have been obtained based on results from literature. These expressions consider harmonic excitation at one single frequency. Because many realistic vibration sources have a rich spectral content, it has been shown how the results can be used to identify most energetic frequencies and how first order power estimation can be performed also in case of random vibration sources. A popular parameter optimization approach in the analytical analysis considers the ratio of the electromagnetic to parasitic damping factor. A slightly advanced model with a constrained construction volume condition has shown that this commonly discussed optimization approach is important for estimating the maximum possible output power but has only marginal relevance for the design of electromagnetic vibration transducers. As demonstrated in Chap. 2 it is more reasonable to find the geometrical parameters of magnet and coil which yield the maximum output power instead of optimizing the damping ratio. The analytical model for comprehending this takes the magnetic field on the centre axis of the magnet into account which is still a simplifying assumption since leakage field effects are neglected. Beside this, the results are restricted to specific architectures and cannot generally be applied to all the architectures presented in the literature overview in Chap. 1. For this reason a very fundamental question to be answered is how the optimized geometrical parameters can be obtained for the different coupling architectures and do architectures exist that have inherently a higher output power and output voltage generation capability?

Based on the analytical analysis this chapter formulates an output power and output voltage optimization procedure for eight different commonly used coupling architectures. The chapter is divided into four subsections. Section 3.2 introduces the coupling architectures considered in this book. They are basically classified into

“Magnet in–line coil” and “Magnet across coil” architectures. Further classification considers whether the architectures have back iron components or not. The following subsection defines the overall boundary conditions for the optimization approach. The most important boundary conditions include the construction volume, the material parameters of magnet and coil, the maximum inner displacement and the parameters of the considered harmonic excitation (namely the amplitude and the frequency). To allow absolute and relative comparison of the performance limit, the same boundary conditions will be applied to each architecture. In subsection four a detailed explanation of the general calculation method for each class of architectures is given. An essential part of the optimization procedure is the accurate calculation of the transduction factor. For this purpose the spatial magnetic field calculation of cylindrical and rectangular permanent magnets are presented. These analytical results are used for all architectures without back iron. However, there is no possibility for the accurate calculation of architectures with back iron based on analytical expressions. In this case the transduction factors are calculated using static magnetic field FEA (finite element analyses).

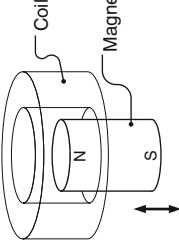
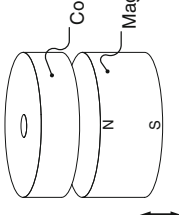
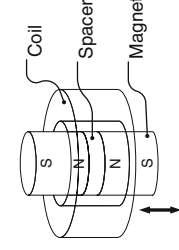
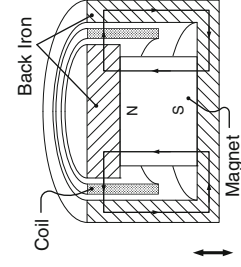
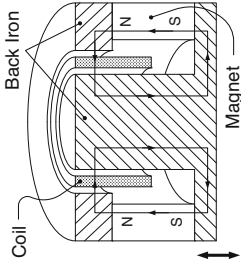
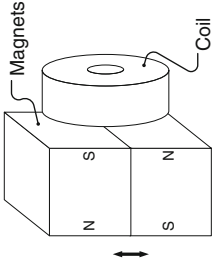
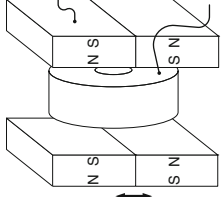
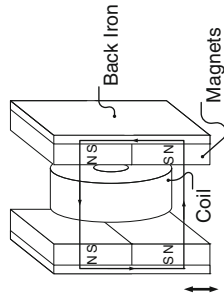
3.2 Investigated Electromagnetic Coupling Architectures

The literature review shows that a lot of different electromagnetic coupling architectures were used to develop electromagnetic vibration transducers. They can be classified according to the arrangement of magnet and coil. A summary of the considered coupling architectures analyzed in this book is given in Table 3.1. In the following subsections these architectures will be explained and optimized in detail. Because the spring and housing of the transducer can be implemented in various ways, only the magnet, coil and (if existent) back iron components will be taken into account in the construction volume. The magnet and the back iron components provide the inertial mass and oscillate relative to the coil which is assumed to be attached to the transducer housing. In all the architectures the coil is cylindrically shaped. Another predefined requirement is that all the components must fit into the construction volume at the resting position of the magnet. It is important to keep in mind that the primary goal of the optimization is to maximize the output power and output voltage. These maximum values are used for the absolute and relative comparison of the architectures. However, as indicated in the introduction Chap. 1, there may be other criteria for the choice of the architecture beyond the electrical output performance (e.g. the geometry, the assembling complexity, magnetic shielding with back iron, costs, . . .).

3.2.1 “Magnet In–Line Coil” Architectures

Whenever the centre axis of magnet and coil is congruent with the oscillation direction the architecture is included in the “Magnet in–line coil” class. There

Table 3.1 Considered electromagnetic coupling architectures

“Magnet in-line coil” architectures	
Without back iron	With back iron
<p>A I</p>  <p>A II</p>  <p>A III</p> 	<p>A IV</p>  <p>A V</p> 
“Magnet across coil” architectures	
Without back iron	With back iron
<p>A VI</p>  <p>A VII</p>  <p>A VIII</p> 	

The architectures are classified into “Magnet in-line coil” (A I – A V) and “Magnet across coil” architectures (A VI – A VIII). Further separation takes the existence of back iron components into account

are three different such architectures without back iron and two with back iron (see Table 3.1). In architecture A I a cylindrical magnet oscillates inside a coil. A special characteristic of this architecture is that the optimal resting position of the magnet is not directly apparent. When the magnet moves through the coil there is a point where the transduction factor becomes maximal. This point is the optimal resting position for the magnet. In architecture A II a cylindrical magnet oscillates towards a cylindrical coil without immersion. Here the resting position is directly given by the maximum inner displacement of the magnet. Another “Magnet in-line coil” architecture without back iron is A III, where two opposite polarized magnets oscillate inside a coil. The gap between the magnets is defined by a spacer and cannot be reduced arbitrarily due to the repulsive force of the magnets. Because the arrangement is symmetrical the resting position is in the middle of the coil. Architecture A IV is the first architecture with back iron. Here a cylindrical magnet with an upper pole plate is positioned inside a ferromagnetic pot. The coil is placed inside the resulting ring shaped air-gap. This magnetic circuit is typically used for electroacoustic loudspeakers as well as Architecture A V [51]. Architecture A V is quite similar to A IV. The only difference is the ring-magnet instead of the cylindrical magnet and the central pole core is therefore made of ferromagnetic material.

3.2.2 “Magnet Across Coil” Architectures

Whenever the centre axis of magnet and coil is orthogonal to the oscillation direction the architecture is included in the “Magnet across coil” class. There are two different “Magnet across coil” architectures without back iron and one with back iron (see Table 3.1). In architecture A VI two rectangular magnets oscillate across a cylindrical coil. To increase the magnetic flux gradient in the coil the magnets are polarized in opposite direction. Architecture A VII is a variation of A VI where the rectangular magnets are arranged on both sides of the coil. An advantage of this architecture is, that the magnetic field in the coil will be somewhat homogenized. On the other hand there are two gaps between the magnets and the coil instead of one gap as in A VI. Whether the advantage compensates this disadvantage cannot be readily answered. In architecture A VIII, based on A VII, back iron is used to channel the magnetic field. It is expected that the back iron increases the magnetic field in the coil. However, because the construction volume is constrained there will be less space for the magnets. Therefore, every advantage implicates also a disadvantage. Hence detailed optimization calculations are necessary to identify which architecture performs best.

3.3 Boundary Conditions

To guarantee a fair comparison of the architectures a set of general boundary conditions are defined for the optimization. These boundary conditions are based on centimeter scale vibration transducers and are listed in Table 3.2. First the construction volume is fixed to 1 cm³. The construction volume is defined as the cylinder or cuboid that encompasses the coil, magnet(s) and (if existent) back iron components at the resting position. The volume of spring and housing is ignored because they can be implemented in several ways. Another fixed geometrical parameter is the gap between static and oscillating components. This minimum gap is necessary to adjust form and position tolerances. The excitation is considered as a pure harmonic vibration with 10 m/s² at 100 Hz. The most important material parameters of the permanent magnet are the residual magnetic flux density and the density of the material. Typical values of neodymium iron boron magnet (NdFeB) are used here. This type of rare earth magnet is often favored in electromagnetic vibration transducers due to the high residual magnetic flux density. A comparison of different permanent magnet materials together with their development potential is shown in Fig. 3.1 [9]. Note that there are also material grades, which allow high temperature applications (up to 220°C) as shown in Fig. 3.2. The back iron components are based on a standard low carbon steel 1010. The corresponding nonlinear initial magnetization curve is shown in Fig. 3.3 [44]. This material is cheap and has a rather high permeability which is desired for efficient magnetic

Table 3.2 Fixed parameters of the overall boundary conditions used for the optimization

Symbol	Description	Value	Unit
<i>Geometry</i>			
V_{constr}	Construction volume	1	cm ³
G	Gap (coil/magnet, back iron/coil)	0.5	mm
Z_{max}	Maximum inner displacement	1	mm
$R_{i,\text{min}}$	Minimal inner radius (for A II and A VI–A VIII)	0.5	mm
<i>Magnet</i>			
B_r	Residual flux density	1.1	T
ρ_{mag}	Density of magnet	7.6	g/cm ³
<i>Coil</i>			
k_{co}	Copper fill factor	0.6	1
d_{co}	Wire diameter	40	μm
R'	Resistance per unit length	13.6	Ω/m
<i>Back iron</i>			
ρ_{bi}	Density of back iron material	7.85	g/cm ³
<i>Other</i>			
Y_{acc}	Excitation amplitude	10	m/s ²
f	Excitation frequency	100	Hz
d_m	Parasitic damping	0.1	N/m/s

Fig. 3.1 Development potential of $(BH)_{\max}$ for permanent magnets [9]

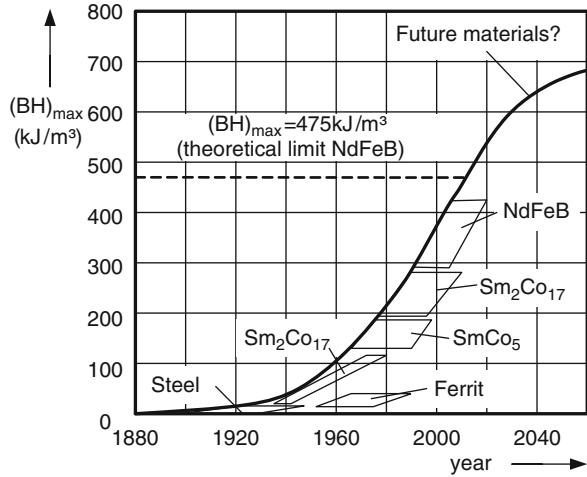
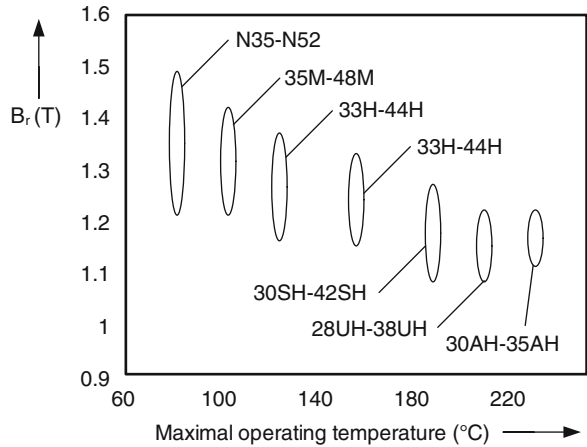


Fig. 3.2 Maximal operating temperature for Neodymium magnets dependent on the material grade



flux conducting. However there are materials with even higher permeability such as permalloy. The permeability is defined as:

$$\mu = \frac{dB}{dH}. \tag{3.1}$$

To avoid numerical problems in the FEA solver due to ambiguity the resulting function of the permeability needs to be monotonically decreasing (see Fig. 3.4). Due to this requirement, the real $\mu(B)$ -function will not be reproduced correctly for small values of the magnetic induction. However for the applied simulations this is irrelevant because the operation point of the material is in the saturation region. The coils are considered to be of enameled copper wire with $40 \mu\text{m}$ in diameter. This is the smallest diameter which can be reasonably processed by hand-soldering.

Fig. 3.3 Initial BH–curve of steel 1010 which is used as material for the back iron components

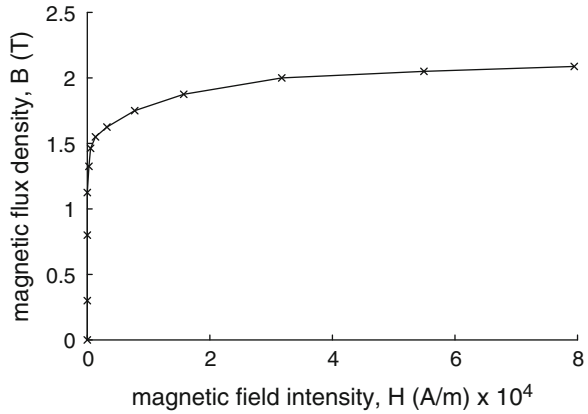
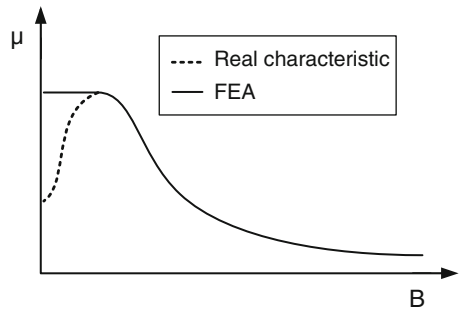


Fig. 3.4 For FEA the $\mu(B)$ function needs to be monotonically decreasing. The *dashed curve* indicates the real characteristic



Experimental results from reference coils have been used to determine the copper fill factor (Appendix A). In the optimization approach the copper fill factor is necessary to calculate the number of coil turns. Note that it is assumed that all the boundary condition parameters can be adapted in equal measure for every architecture. For this reason they are fixed and not part of the optimization.

3.4 Magnetic Field Distribution of Cylindrical and Rectangular Permanent Magnets

In the calculation procedure it is necessary to calculate the magnetic field of cylindrical and rectangular permanent magnets. There are two models that can be used for the calculation of the permanent magnet field distribution. These are namely the scalar potential model and the vector potential model. The scalar potential model assumes fictitious magnetic charges. The vector potential model, based on the molecular current viewpoint is used in this book. The magnetic flux density distribution of cylindrical permanent magnets is therein equivalent to that of a thin

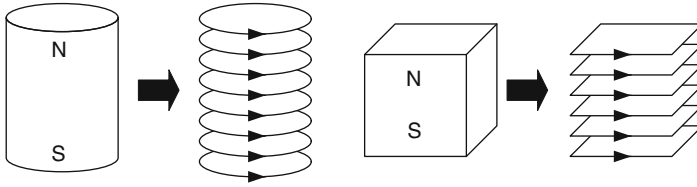


Fig. 3.5 In the applied vector potential model the magnet is equivalent to a current sheet

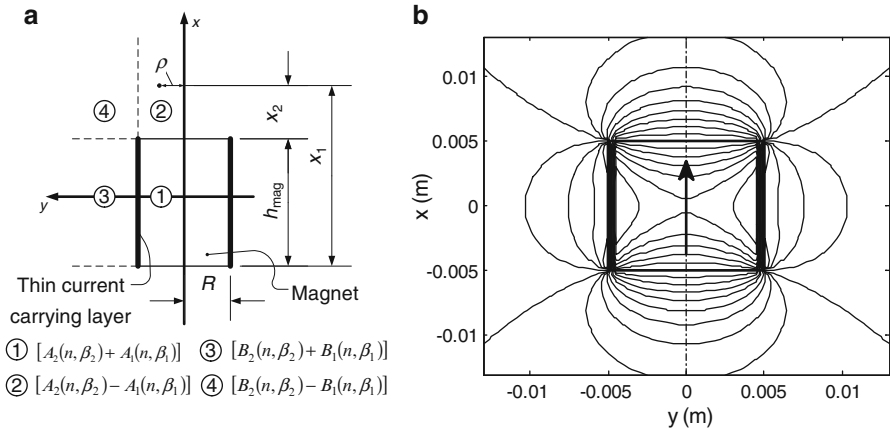


Fig. 3.6 (a) Half-section of a cylindrical permanent magnet (respectively thin layered coil) with four solution domains depending on whether the point of interest is in region 1, 2, 3 or 4. (b) Isolines of the magnetic flux density B_x in the centre plane of a cylindrical permanent magnet calculated with the semi-analytical approach

cylindrical current sheet or a single-layered cylindrical coil with same dimensions (Fig. 3.5). The calculation of magnetic field distribution based on analytical expressions will be used for all architectures without back iron. A common characteristic of all architectures without back iron is that the surface normal to the turns is in the same direction as the vector of the magnetization. Hence for a relative movement between magnet and coil only the component of the magnetic induction parallel to the surface normal to the windings will cause a magnetic flux change in the coil turns. For the calculations presented here it is the only component of interest. The underlying theory of static magnetic field calculation for cylindrical permanent magnets is given in [45] and for rectangular permanent magnets in [82]. The solution for cylindrical permanent magnets is subdivided in four domains (Fig. 3.6a) and can be expressed in cylindrical coordinates as follows:

for $\rho \leq R$:

$$B_x(x, \rho) = \mu_0 \cdot \frac{NI}{2\pi h_{mag}} \cdot [A_2(n, \beta_2) \pm A_1(n, \beta_1)]$$

for $\rho > R$:

$$B_x(x, \rho) = \mu_0 \cdot \frac{NI}{2\pi h_{mag}} \cdot [B_2(n, \beta_2) \pm B_1(n, \beta_1)] \quad (3.2)$$

The factor NI (number of windings multiplied by the current) can be derived from the identity of the current density S on the surface of the magnet and the curl of the magnetization vector. Assuming an area A orthogonal to the coil windings and enclosing half of the side of the coil, NI is given by:

$$NI = \iint_A \vec{S} \cdot \vec{n} d\vec{A} = \oint_C \vec{M} \cdot d\vec{s} = M_r \cdot h_{mag} = \left(\frac{B_r}{\mu_0} \right) \cdot h_{mag}, \quad (3.3)$$

where M_r indicates the residual magnetization and B_r the residual flux density. The plus sign in (3.2) is valid if P lies between $x_1 = 0$ and $x_1 = h_{mag}$. Otherwise the minus sign is valid. The terms in brackets are:

$$\begin{aligned} A_2(n, \beta_2) &= (E_2 + \Pi_2 \sqrt{1-n}) \sqrt{1-\beta_2} \\ A_1(n, \beta_1) &= (E_1 + \Pi_1 \sqrt{1-n}) \sqrt{1-\beta_1} \\ B_2(n, \beta_2) &= (E_2 - \Pi_2 \sqrt{1-n}) \sqrt{1-\beta_2} \\ B_1(n, \beta_1) &= (E_1 - \Pi_1 \sqrt{1-n}) \sqrt{1-\beta_1}, \end{aligned} \quad (3.4)$$

where E_2 and E_1 are complete elliptic integrals of the first kind while Π_2 and Π_1 are the complete elliptic integrals of the third kind in Legendre form. Since these integrals cannot be expressed in terms of elementary functions they are solved numerically using the Adaptive Simpsons' method. The elliptic modulus is:

$$\begin{aligned} k_2^2 &= \beta_2 \cdot n = \frac{4R\rho}{(R+\rho)^2 + x_2^2} \\ k_1^2 &= \beta_1 \cdot n = \frac{4R\rho}{(R+\rho)^2 + x_1^2}, \end{aligned} \quad (3.5)$$

with n as a common parameter:

$$n = \frac{4R\rho}{(R + \rho)^2}. \quad (3.6)$$

The axial symmetric magnetic flux density component in x -direction of a cylindrical permanent magnet is shown in Fig. 3.6b.

For the magnetic field of rectangular magnets analytical expressions can also be derived from the molecular current viewpoint. Based on the Biot–Savart’s law:

$$dB = \frac{\mu_0}{4\pi} \frac{Idl \times r}{r^2}, \quad (3.7)$$

where μ_0 is the magnetic permeability in the air and r is a vector which points from the infinite small current carrying element to an arbitrary point in space $P(x,y,z)$ the solution can be written as [82]:

$$\begin{aligned} B_z(x, y, z) = \int_0^{h_{mag}} dB_z = & -\frac{\mu_0 J}{4\pi} [\phi(y, a - x, z) + \phi(b - y, a - x, z) \\ & + \phi(x, b - y, z) + \phi(a - x, b - y, z) + \phi(b - y, x, z) + \phi(y, x, z) \\ & + \phi(a - x, y, z) + \phi(x, y, z)]_0^{h_{mag}}. \end{aligned} \quad (3.8)$$

where a , b and h_{mag} indicates the length, the width and the height of the magnet (as shown in Fig. 3.7a). Moreover the current density is $J = I/h_{mag}$ and the function ϕ are given by:

$$\phi(\gamma_1, \gamma_2, \gamma_3) = \begin{cases} \arctan \left[\frac{\gamma_1}{\gamma_2} \frac{\gamma_3 - z_0}{\sqrt{\gamma_1^2 + \gamma_2^2 + (\gamma_3 - z_0)^2}} \right] & \text{if } y \neq 0 \\ 0 & \text{if } y = 0 \end{cases} \quad (3.9)$$

The z -component of the magnetic flux density of a rectangular permanent magnet in xz -centre plane is shown in Fig. 3.7b. The results of magnetic field calculations obtained with these equations are in good agreement with FEA results [22]. A comparison between the magnetic field of cylindrical and rectangular permanent magnets obtained with the vector potential model and FEA is given in Appendix B.

So far the magnetic field of single cylindrical and rectangular permanent magnets has been considered. However there are architectures with two or more magnets. As all elements of the architectures without back iron are linear and the relative permeability of NdFeB magnets is close to one the field of the magnets can be calculated separately and afterwards superposed. Example calculation for two

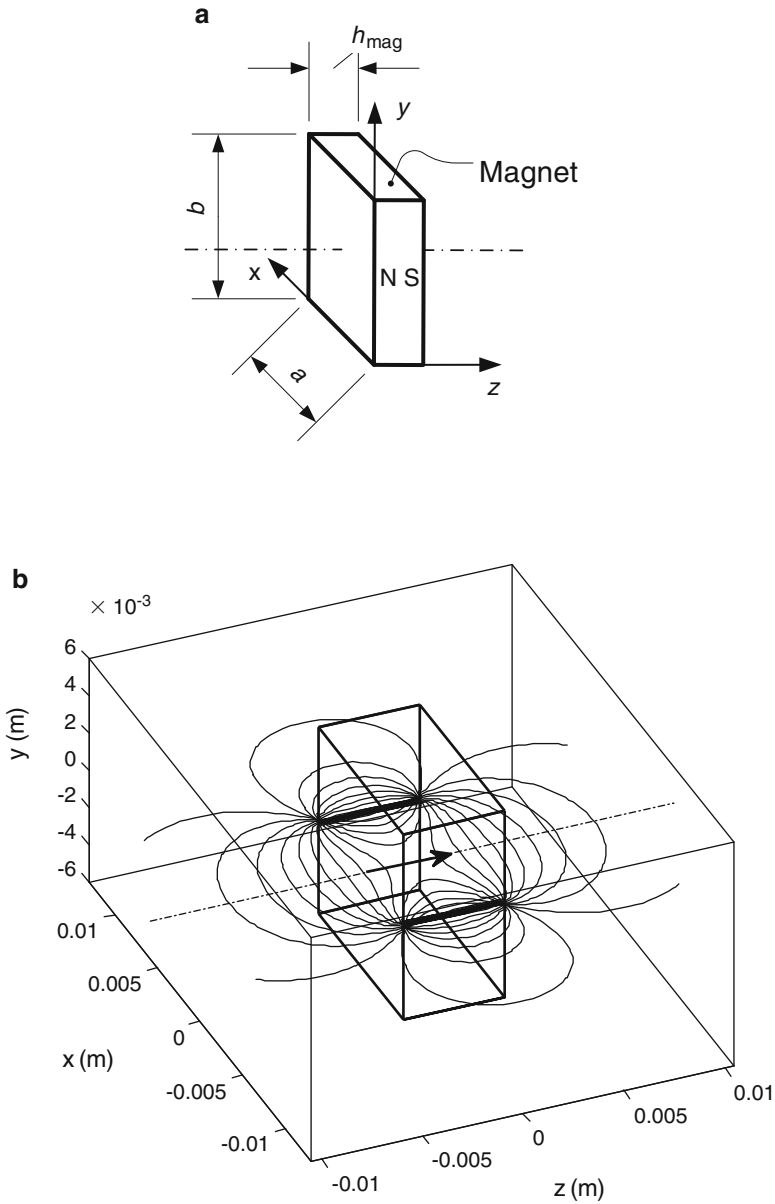


Fig. 3.7 (a) Geometrical parameters and coordinate system for rectangular permanent magnets. (b) Isolines of the magnetic flux density B_z in the xz -centre plane of a rectangular permanent magnet. The arrow points from north- to south-pole

Fig. 3.8 Isolines of the axially symmetric magnetic flux density component in x -direction on the centre plane of two opposite polarized cylindrical magnets (as in A III). The *arrows* point from north- to south-pole

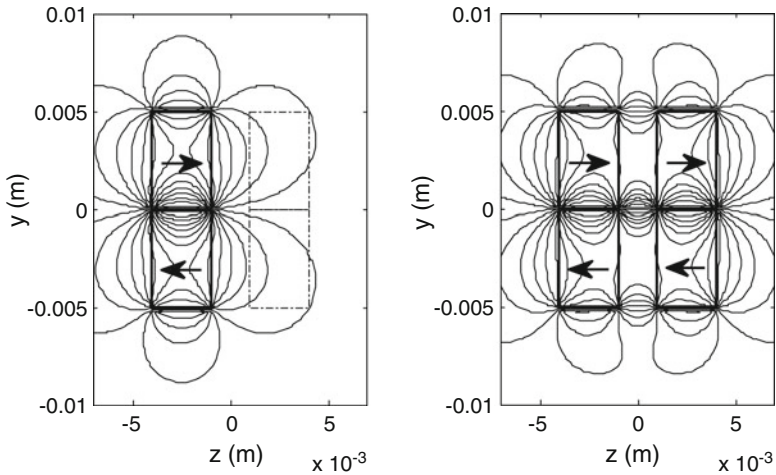
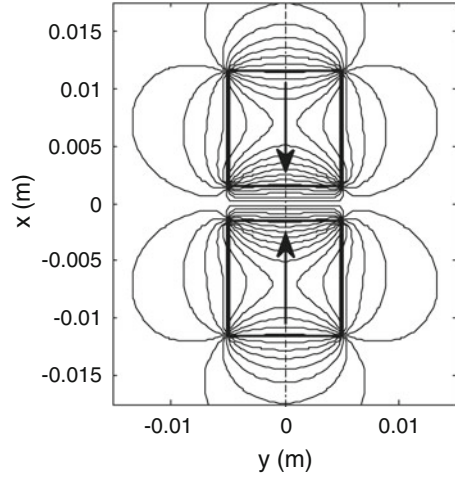


Fig. 3.9 (a) Isolines of the magnetic flux density B_z in the yz -plane of symmetry of two rectangular permanent magnets (as in A VI). The *dashed curves* indicate the position of the magnets as in A VII. The magnetic flux density of this architecture is plotted in (b). The *arrows* point from north- to south-pole

opposite polarized magnets (as in A III) is shown in Fig. 3.8. The superposition of the magnetic field of two and four rectangular permanent magnets (as in A VI and A VII) is shown in Fig. 3.9. As expected the magnetic field between the four rectangular permanent magnets is much more homogeneous than for two magnets.

3.5 Optimization Procedure

3.5.1 General Calculation Method

For optimization purposes it is necessary to calculate the output power and the output voltage independently of the architecture and the underlying geometrical parameters of the magnet, the coil and (if existent) the back iron components. Based on the analytical tools, which have been introduced in Chap. 2, the steps of the analysis for performing this task are shown in the flowchart of Fig. 3.10. Based on the overall boundary conditions the geometric parameters of the solution candidate are defined in the first step. For every set of parameters the coil calculation can be done using (2.25) and (2.26). Dependent on the resulting number of windings and the internal resistance the magnetic field and magnetic flux in the coil at the resting position of the magnet is determined. Note that this part of the calculation method depends on the architecture class. For architectures without back iron the magnetic field calculation is based on Maxwell's equations (refer to Sect. 3.4). For architectures with back iron static magnetic FEA is used to compute the magnetic field. Moreover the calculation of the transduction factor depends on whether the architecture can be referred to the first term or the second term in Eq. 2.19. In the next step the result of the coil resistance together with the transduction factor is used to determine the optimal load resistance, which yields the maximum output power according to EDAM (2.29). For simplification the transduction factor is therefore assumed to be constant, which results in a linearization of the models as will be shown later on in Sect. 3.6.3. Now the electromagnetic damping coefficient (2.32) and the relative amplitude of motion (2.37) as well as the *emf* (2.21) can be calculated. In a final step the resulting output power and output voltage is calculated according to (2.46) and (2.47). Note that the output voltage depends on the load resistance and can theoretically be increased up to the *emf* (for infinite high load resistance). However, in this case the generated output power goes towards zero which does not make sense. Here the output voltage is related to the load resistance which yields maximum output power.

3.5.2 Evolution Strategy

The last section introduced a general calculation procedure where the output power and output voltage can be calculated dependent of the architecture and the geometrical parameters. The number of the geometric parameters n is thereby a subset of the Euclidean space R^n where n is the dimension of the search space. This dimension depends on the architecture class. For the "Magnet in-line coil" architectures without back iron the geometric parameters can be reduced to a 2-dimensional search space. In this case it is appropriate to calculate each combination of the geometric parameters. The result can be illustrated as a 2-dimensional topological

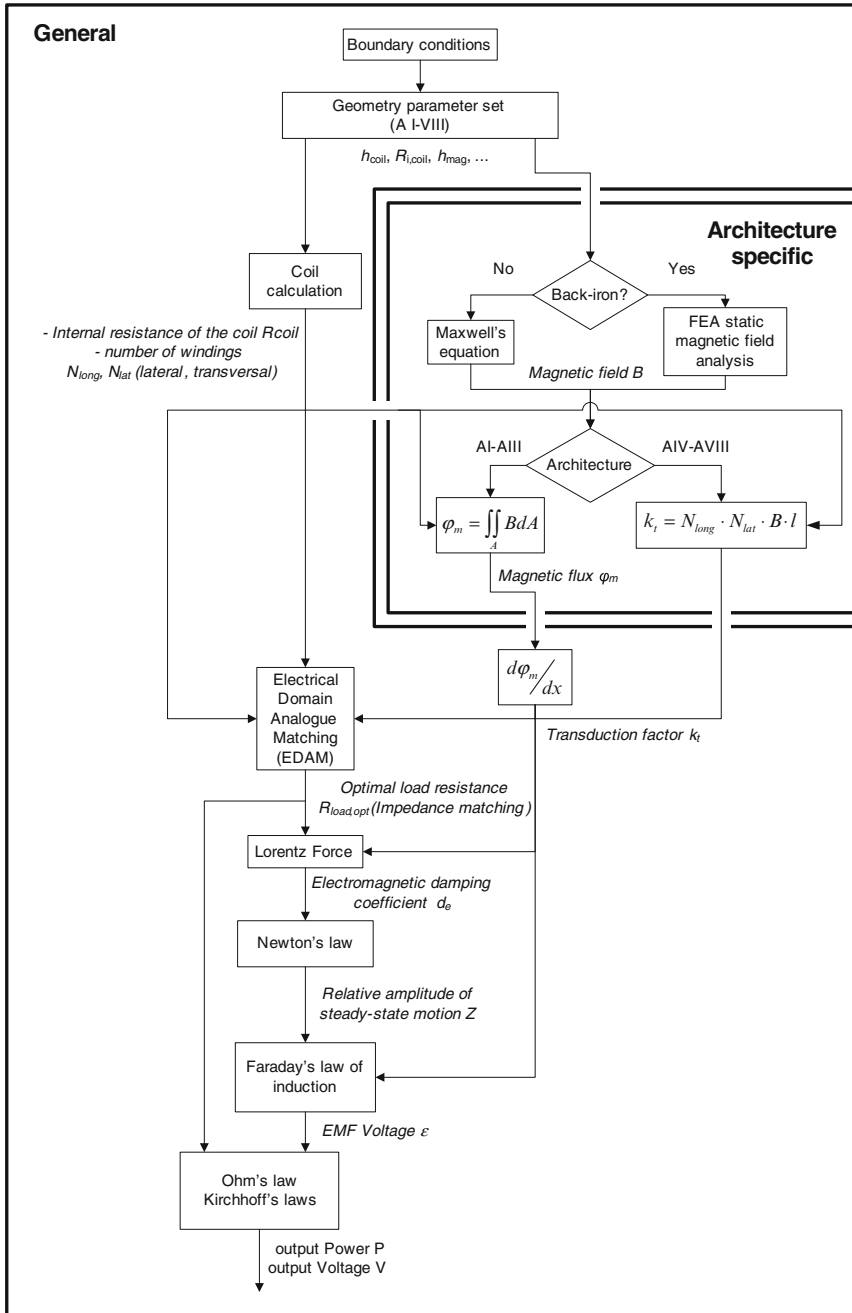
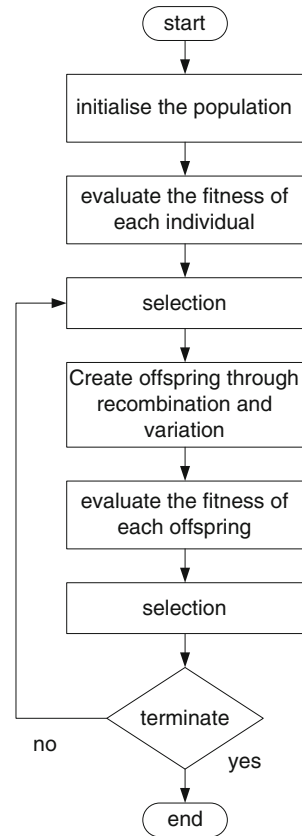


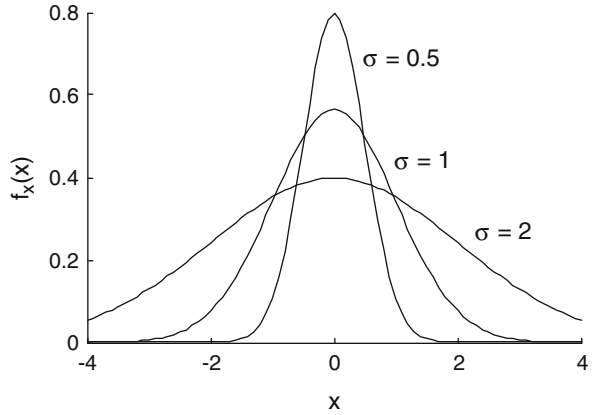
Fig. 3.10 Flow chart of the calculation procedure used in the optimization approach. For each set of geometry parameters (n-dimensional vector dependent on architecture) the output power and output voltage is calculated

Fig. 3.11 Flowchart of evolution strategy (ES)



manifold and the optimal parameter set is simply defined by the global maximum of the surface. However as will be shown in detail (refer to Sects. 4.2.4 and 4.2.5) the “Magnet in–line coil” architectures with back iron lead to a 6–dimensional search space. In this case it requires too much time to compute each combination of parameters and of course there is no geometrical interpretation of the result (6–dimensional topological manifold). In this book the evolution strategy (ES) is used to find optimal parameter sets in the 6–dimensional search space of the “Magnet in–line coil” architectures with back iron [21]. The idea of ES optimization technique is based on the darwinistic evolution, namely the “survival of the fittest”. There are several forms of ES which differ primarily in the selection mechanism [75]. In the following the $(\mu + \lambda)$ variant applied in this book will be discussed. The basic procedure of ES optimization is shown in the flowchart of Fig. 3.11. At the first initialisation phase μ_{ini} individuals $\vec{a}_i = (\vec{x}_i)$ ($i = 1, 2, \dots, \mu_{ini}$) are randomly distributed in the search space. Every individual is thereby a possible solution candidate and consists of n gene where each gene is a geometrical parameter $\vec{x}_i = [x_1, x_2, \dots, x_n]$. Therewith every individual is a point in the search space. All the individuals together form the start population $P_a(t = 0)$. The general

Fig. 3.12 Probability density function of a normal distribution used for the mutation of the genes



calculation method presented in the previous section is used to find the fitness $\Phi(\vec{a}_i)$ of each individual (output power and output voltage, respectively). Now the μ best individuals are selected to create λ offsprings. To create an offspring two different parent individuals are randomly taken out of the μ best individuals. The probability to be taken out is thereby the same for each individual. Afterwards intermediate recombination is used to define the gene of the offspring:

$$\vec{x}_{O,i} = \frac{\vec{x}_{P1,i} + \vec{x}_{P2,i}}{2}. \quad (3.10)$$

The index O indicates the gene of the offspring whereas the index P indicates the gene of the parents. To complete the offspring creation each gene is mutated using:

$$\vec{x}'_{O,i} = \vec{x}_{O,i} + N(0, \sigma), \quad (3.11)$$

where $N(0, \sigma)$ indicates a normally distributed number with a mean value of zero and a standard deviation of σ . These random numbers are generated based on the Ziggurat algorithm. The probability density function is given by (Fig. 3.12):

$$f_x(x) = \frac{1}{\sigma\sqrt{2\pi}} \exp\left(-\frac{x^2}{2\sigma^2}\right). \quad (3.12)$$

Now the fitness $\Phi(\vec{a}'_i)$ of the offspring $\vec{a}'_i = (\vec{x}'_i)$ is determined using the general calculation method. In the next step the μ best individuals are selected out of the union of parents and offspring's yielding the $(\mu + \lambda)$ -selection method. Note that this selection method results in a continuous increase of the fitness of the selected individuals. The steps are repeated until a termination criterion for example a certain

Table 3.3 Applied parameters of the evolution strategy for the optimization of “Magnet in–line coil” architectures with back iron in 6–dimensional search room

Symbol	Description	Value	Unit
μ_{ini}	Number of individuals of the initialization population	100	1
μ	Number of best individuals selected for recombination	15	1
λ	Number of offspring's	100	1
ρ_s	Ratio of successful mutations to all mutations (success rate)	1/5	1
σ_{max}	Maximum standard deviation for the mutation of the genes	0.08	1
σ_{min}	Minimum standard deviation for the mutation of the genes	0.005	1
c	Parameter for dynamic adaption of the standard deviation	0.9	1

number of generations is fulfilled. To achieve best convergence rates the strength of mutation namely the variance is dynamically adapted using the heuristic 1/5–success rule [40]:

The ratio of successful mutations to all mutations (success rate ρ_s) should be 1/5. If it is greater than 1/5, increase the standard deviation, if it is smaller, decrease the standard deviation.

An interpretation of this rule is that an increase of the standard deviation for the next population yields a faster convergence to the optimum (in case of high success rate). If the success rate is small a smaller standard deviation allows a finer investigation of the search space. Formally this can be expressed as:

$$\sigma_{(P+1)} = \begin{cases} c\sigma_{(P)} & \text{if } \rho_s < 1/5 \\ \sigma_{(P)} & \text{if } \rho_s = 1/5 \\ \sigma_{(P)}/c & \text{if } \rho_s > 1/5. \end{cases} \quad (3.13)$$

A recommendation for the parameter c is $0.85 \leq c \leq 1$ [40]. All the parameters used for the evolution strategy applied in this book are listed in Table 3.3. It is important to keep in mind that the evolution strategy is a heuristic optimization technique. Thus it is possible that not the absolute global optimum can be found. However, with experience in the algorithm and the problem which needs to be solved it can be ensured that the solution found by the algorithm is actually a very good one.

3.6 Architecture Specific Calculation of the Transduction Factor

In the introduction of the general calculation procedure in Sect. 3.5.1 it was shown that the calculation of the transduction factor depends on the architecture class (Fig. 3.13). This section gives a detailed introduction on the architecture specific calculation of the transduction factor.

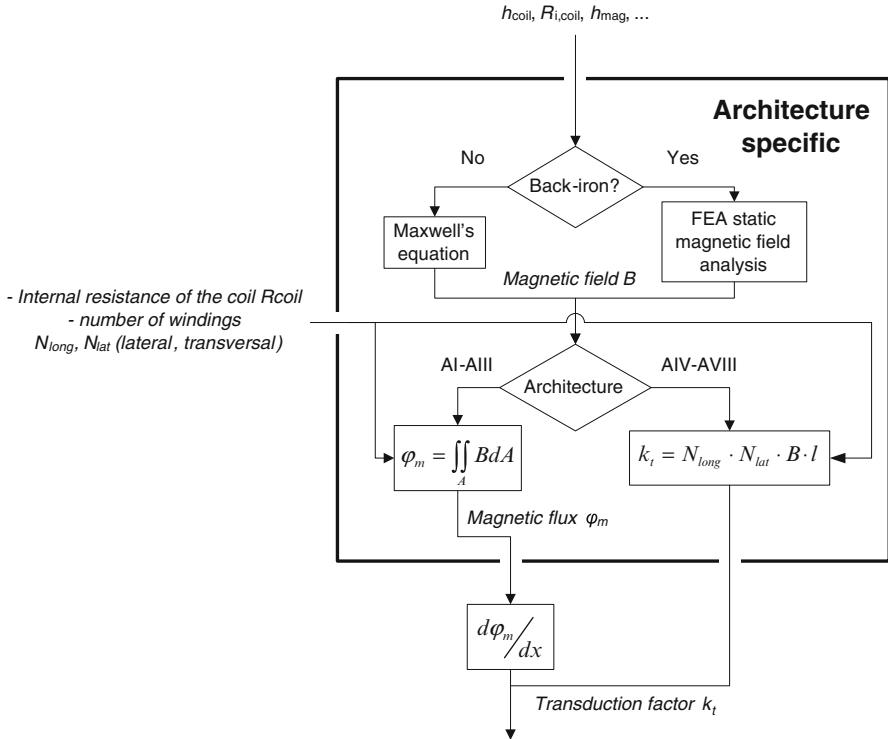


Fig. 3.13 Architecture specific calculation of the transduction factor as a part of the general calculation procedure

3.6.1 Simulation of “Magnet In-Line Coil” Architectures Without Back Iron

In the “Magnet in-line coil” architectures without back iron (A I–A III) the coil moves parallel to the diverging field of the magnet. Therewith the *emf* takes place via the change of magnetic field through a constant area of the coil turns. In general, there are not many possibilities to simplify the calculation of this kind of electromagnetic coupling. In this book the calculation of the magnetic distribution is based on the semi-analytical approach discussed in Sect. 3.4 (3.2). According to the basic Eq. 2.17 the magnetic flux is obtained by integrating the axial component of the magnetic field over the area of the coil turns. Note that coil turns above the magnetic pole contribute with a positive magnetic flux whereas coil turns between the magnetic poles have also regions where the magnetic flux is negative (Fig. 3.14). Subsequently the magnetic flux of the coil is obtained by summarizing the magnetic flux of each coil turn. However for each point of the magnetic field four elliptic integrals have to be solved numerically. For precise results at least 20 points of the

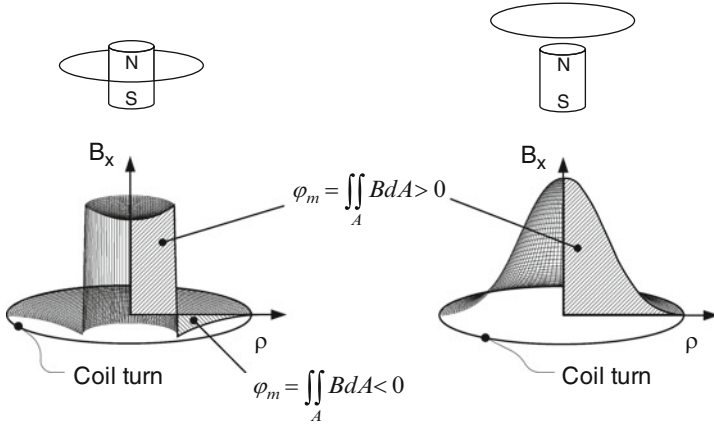
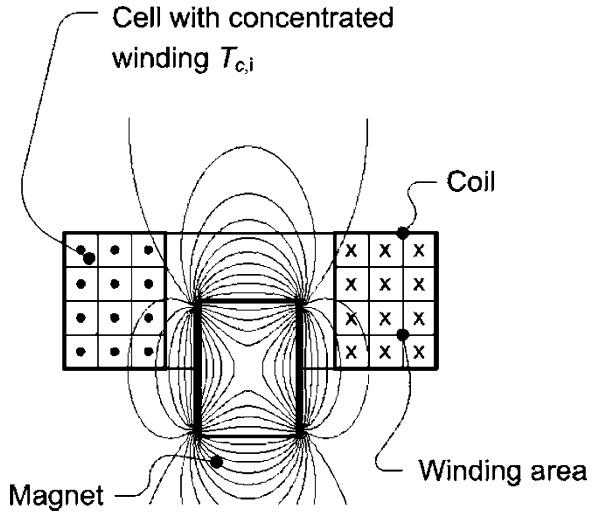


Fig. 3.14 (a) Coil turns between the magnet poles have regions with positive and negative magnetic flux. The discontinuity occurs at $\rho = R_{mag}$. (b) In coil turns above the magnet pole the magnetic flux is positive over the whole coil turn area

Fig. 3.15 To reduce the computation time the winding area of the “Magnet in-line coil” architectures without back iron is divided into cells and the number of windings in a cell are assumed to be concentrated in the centre



magnetic field need to be calculated inside a single turn (dependent on the radius of the turn). Because the coil has possibly more than 3,000 turns the magnetic flux computation would result in the numerical computation of more than 240,000 elliptic integrals which is computationally intensive. To reduce the computation complexity the winding area of the coil is discretized into n cells as shown in Fig. 3.15 (on the example of A I). In the next step the magnetic flux of an imaginary coil turn $T_{c,i}$ in the centre of the n cells is computed. This magnetic flux is assumed

to be representative for all the turns N_c in the cell. The overall magnetic flux in the coil is a summation of the cells magnetic flux contributions:

$$\varphi_m = \sum_{i=1}^n N_c \iint_{A_{T_{c,i}}} B_{T_{c,i}} dA_{T_{c,i}}. \quad (3.14)$$

By doing so, the computation time can be reduced significantly and the result is still accurate. In the last step the magnetic flux gradient is given by the derivative of the magnetic flux function.

3.6.2 *Simulation of “Magnet In–Line Coil” Architectures with Back Iron*

According to the theory of moving coil loudspeakers in electroacoustics [54] the “Magnet in–line coil” architectures with back iron (A IV and A V) can be calculated using the equations of a moving conductor in constant magnetic field (2.20). Because the magnetic field in the air gap is only approximately constant the mean value of the radial magnetic field component in the coil is used as a representative value. This value is obtained using static magnetic FEA. In detail the block integral of the radial component of the B -field in the coil is calculated and afterwards divided by the volume of the coil. The length of the conductor is consequently the length of the wire of the coil. The path of magnetic flux lines for both A IV and A V are shown in Fig. 3.16. Because 2–D static magnetic field analyses have been applied these flux lines are equipotential lines of the vector potential. In principle the magnetic field of A IV spreads primarily on the circumference whereas the magnetic field of A V spreads on the upper side through the air gap. The flux lines for different geometrical parameters of A IV are shown in Fig. 3.17 and for A V in Fig. 3.18.

3.6.3 *Simulation of “Magnet Across Coil” Architectures Without Back Iron*

The “Magnet across coil architectures” (A VI and A VII) operate quite similar to the popular models used for linearized analytical analyses (refer to Sect. 2.3.1). The overlapping area of the coil turns with respect to the magnets is changing during constant magnetic field. However in the analytical analyses the magnetic field has typically either been predefined or calculated only on the centre axis. Beyond this the change of the overlapping area has been assumed to be constant (rectangular coil turns). In this book the magnetic field in the coil volume is calculated based on

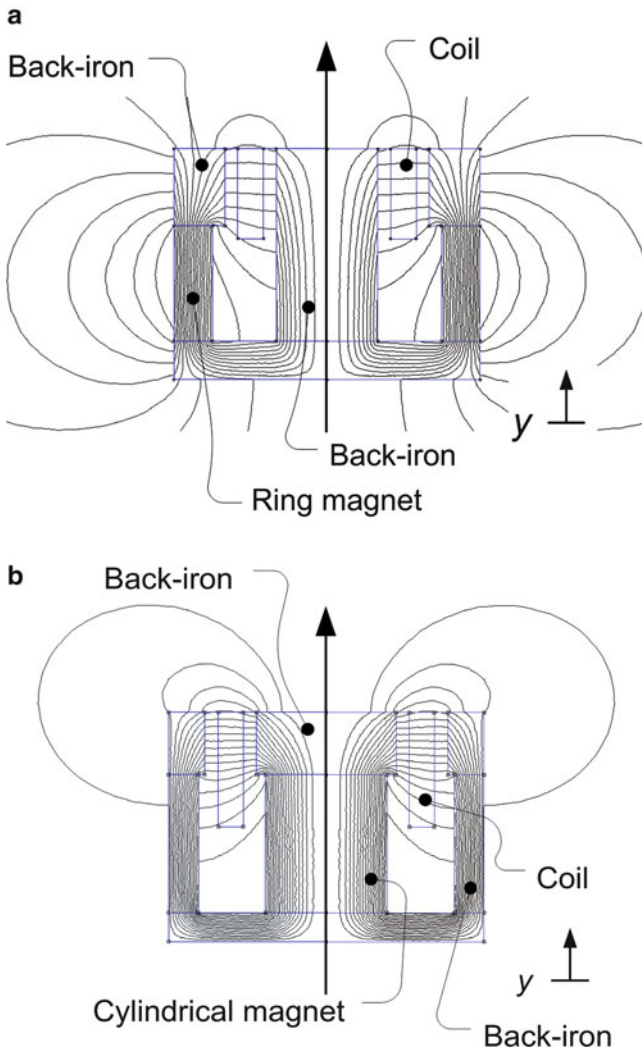


Fig. 3.16 Path of magnetic flux lines for “Magnet in-line coil” architectures with back iron. (a) Architecture A V is build-on a ring magnet whereas architecture A VI is based on a cylindrical permanent magnet (b)

Maxwell’s equations (discussed in Sect. 3.4) to obtain more realistic transduction factors. Based on the assumption of homogeneous field distribution the mean value of the magnetic flux density is used as a representative value. With the gradient of the overlapping area the magnetic flux gradient (which equals the transduction factor) can be calculated. Figure 3.19a shows the geometrical situation when the

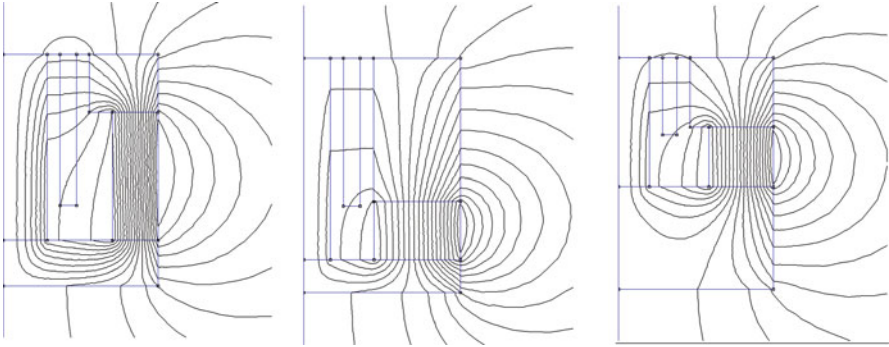


Fig. 3.17 Flux-lines for different example calculation results of A V. The magnetic field spreads mainly on the circumference

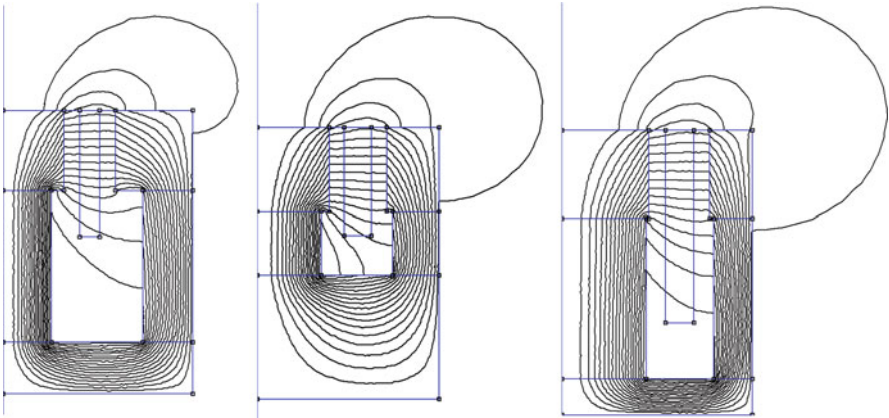


Fig. 3.18 Flux-lines for different example calculation results of A VI. The magnetic field spreads mainly on the upper side

n th circular coil winding moves towards a rectangular magnet. The shaded area indicates the overlapping area. The area of this circular segment is given by:

$$A_{R_{t,n}} = \frac{R_{t,n}}{2} (\varphi - \sin \varphi), \quad (3.15)$$

where $R_{t,n}$ indicates the radius of the n^{th} turn. The angle φ is calculated as follows:

$$\varphi = 2 \arccos \left(1 - \frac{h_n(y)}{R_{t,n}} \right). \quad (3.16)$$

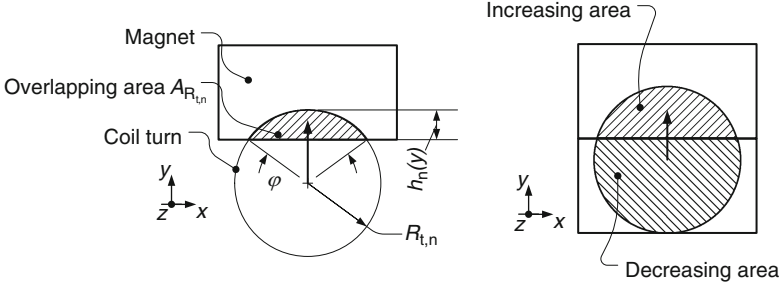


Fig. 3.19 (a) Geometrical situation for a single circular coil turn which moves towards a magnet. This basic geometry is used to obtain the overlapping area function for the situation in the “Magnet across coil” architectures (b)

When the turns move towards the magnet the overlapping area increases together with $h_n(y)$ until φ is 180° and $h_n(y) = R_{t,n}$, respectively. For an arbitrary coil with $N_{lat} = 10$ turns on the lateral side, $N_{long} = 1$ turn on the longitudinal side, outer radius $R_o = 5$ mm and inner radius $R_i = 2.5$ mm the overlapping area functions of the turns for $\{y \leq 0 < R_o\}$ are plotted in Fig. 3.20a. Note that the area of the n th turn starts to increase at $y = (R_o - R_i / N_{lat}) (n - 1)$. With these area functions the overall differential overlapping area function for the geometrical situation in the “Magnet across coil” architectures (Fig. 3.20b) can be calculated. Starting with the summation of the increasing area functions for $\{y \leq 0 < R_o\}$:

$$A_{inc,1} = N_{long} \cdot \sum_{n=1}^{N_{lat}} A_{R_{t,n}}, \quad (3.17)$$

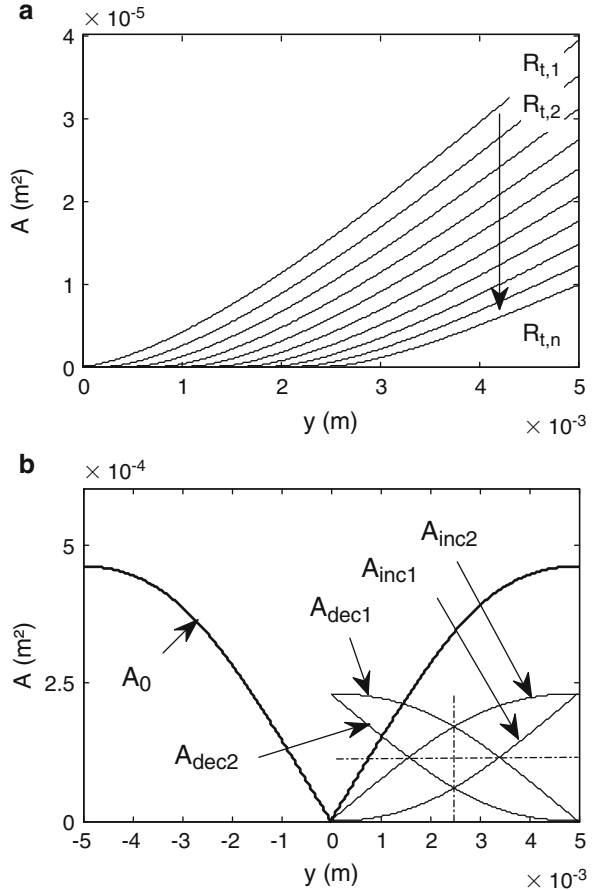
the decreasing area for $\{y \leq 0 < R_o\}$ ($A_{dec,1}$) is given by the reflection of $A_{inc,1}$ over the axis $A = \max(A_{inc,1}) / 2$. In the same way the increasing area function $A_{inc,2}$ and the decreasing area function $A_{dec,2}$ for $\{y \leq R_o < 2R_o\}$ are given by the reflection of $A_{dec,1}$ over the axis $y = R_o / 2$ and by reflection of $A_{dec,2}$ over the axis $A = \max(A_{inc,1}) / 2$, respectively. The resulting overall overlapping area function A_o is a combination of the partial area functions. For $\{y \leq R_o < 2R_o\}$ it is given by:

$$A_o = \max(A_{inc,1}) + A_{inc,2} - A_{dec,2}. \quad (3.18)$$

The result for the example coil is shown Fig. 3.20b. Because a homogeneous field distribution is assumed between the magnets the magnetic flux is directly proportional to the gradient of the overlapping area function. Hence the nonlinear saturation effect for high displacement amplitudes is already visible. The resulting magnetic flux linkage of the example coil (for arbitrary $B_z = \pm 1$ T) is shown in Fig. 3.21a. It is simply given by:

$$\varphi_m = N_{long} A_o B_z. \quad (3.19)$$

Fig. 3.20 (a) Overlapping area functions of an example coil with 10 circular windings on the lateral side. (b) Overall differential area function A_o for the geometrical situation of the “Magnet across coil architectures”. The *dashdotted lines* indicate the reflection axis of the partial area functions



The corresponding flux gradient (which equals the transduction factor) is shown in Fig. 3.21b. Note that the maximum value is therein identical to the transduction factor of the linearized model from the analytical analyses (2.20). In the optimization procedure the transduction factor at the resting position of the magnet is used which corresponds to the maximum value.

3.6.4 Simulation of “Magnet Across Coil” Architecture with Back Iron

The simulation of the “Magnet across coil” architecture with back iron A VIII is essentially the same as for the “Magnet across coil” architecture without back iron. That means that the calculation of the transduction factor is likewise based on

Fig. 3.21 (a) Magnetic flux linkage vs. displacement for the considered example coil. (b) Due to the saturation in the magnetic flux the resulting magnetic flux gradient decreases for large displacement amplitudes. The *dashed curve* indicates the constant transduction factor of the linearized model

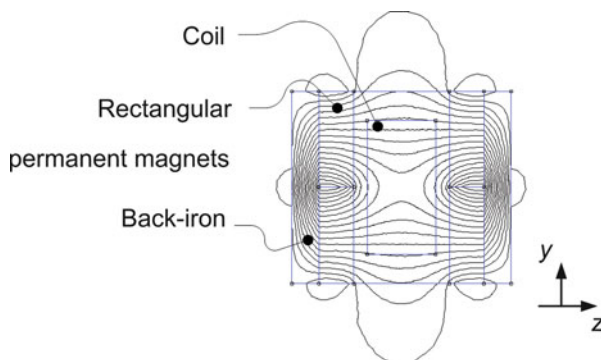
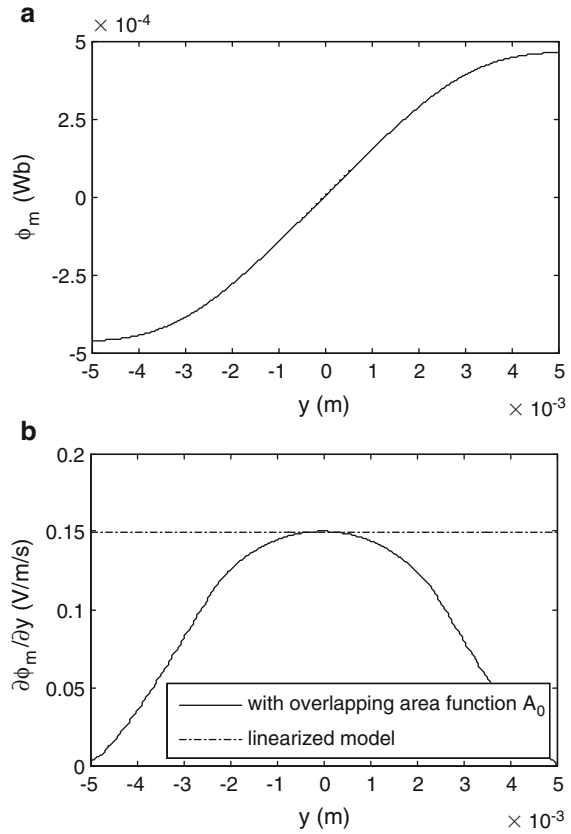
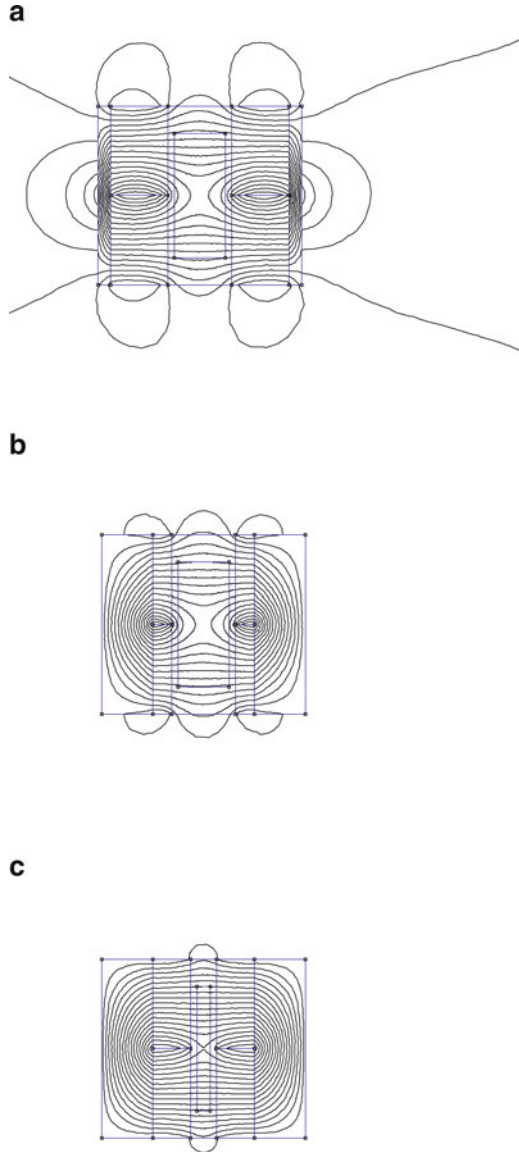


Fig. 3.22 Path of magnetic flux of "Magnet across coil" architecture with back iron A VIII calculated with FEA

Fig. 3.23 Flux-lines for different example calculation results of A VIII. Appreciable flux leakage results for large gap between the magnets and thin back iron sheet (**a**). For thicker back iron sheet the magnetic flux mainly spreads through the gap (**b**). For thin back iron sheet and small gap the magnetic field between the magnets is quite homogeneous and the flux leakage can be reduced to a minimum (**c**)



the overlapping area function together with the assumption of homogeneous field distribution between the magnets. The only difference is that the magnetic field in the coil is not obtained with a semi-analytical calculation but with static magnetic FEA (Fig. 3.22). The mean value of the z -component of the magnetic induction (refer also to Fig. 3.7 for the convention of the coordinates) is simply obtained by the integral of the magnetic induction over the coil volume divided by the coil volume.

This value depends on magnetic flux leakage effects. For a large gap between the magnets and for a thin back iron sheet the magnetic flux density in the coil decreases due to high magnetic flux leakage. Obviously, small gaps between the magnets and a thicker back iron sheet result in higher mean value of the magnetic flux density, more homogeneous field distribution and smaller magnetic flux leakage (Fig. 3.23a–c).

Chapter 4

Optimization Results and Comparison

4.1 Introduction

The previous chapter introduced and classified the considered electromagnetic coupling architectures. Overall boundary conditions for centimeter scale vibration transducers were defined. In order to compare the performance limits of the architectures these boundary conditions are applied to all architectures. Then an optimization approach was formulated to assess the optimal dimensions with respect to the output power and the output voltage. For architectures with a 6–dimensional search space the evolution strategy optimization technique is used. Furthermore the architecture specific calculation of the magnetic flux gradient was discussed. The calculation of architectures without back iron is based on Maxwell’s equations whereas the calculation of architectures with back iron is based on static magnetic 2–dimensional FEA.

Based on these assumptions this chapter discusses the results of the optimization and concludes with a comparison of the architectures’ performance limits. This chapter is divided into four further subsections. In Sect. 4.2 the optimization results for the “Magnet in–line coil” architectures based on a cylindrical construction volume with a radius of 6 mm and a height of 8.90 mm (1 cm^3) are discussed. In the same manner, Sect. 4.3 considers the optimization results for the “Magnet across coil” architectures. For architecture A VI the cubic construction volume is defined as $10 \cdot 10 \cdot 10 \text{ mm}^3$ and for the architectures A VII and A VIII $8.70 \cdot 8.70 \cdot 1.32 \text{ mm}^3$ (in each case 1 cm^3). The reason for the different dimensions of the construction volume will be discussed in the subsections. Section 4.4 covers the comparison of the architectures’ performance limit. Therein the advantages and disadvantages of each architecture are discussed and it is shown which architecture is best suited for maximum output power and maximum output voltage performance.

4.2 “Magnet In-Line Coil” Architectures

4.2.1 Architecture A I

In A I a cylindrical magnet oscillates inside a cylindrical coil. The geometrical parameters are shown in Fig. 4.1. A special characteristic of this architecture is that the optimal resting position of the magnet is not directly apparent. It is plausible that when a magnet moves through the coil, the magnetic flux will increase until a maximum is reached and then decrease again. In between there is a point where the magnetic flux gradient has a maximum (exemplarily shown in Fig. 4.2). Because the magnetic flux gradient is directly proportional to the output voltage, this position defines the optimal resting position for output voltage maximization. However, due to the constrained construction volume condition the situation for maximum output power generation is different. This is because the power is dependent on both the voltage and the resistance of the coil. This results in a trade off and the first task for the optimization of A I is to find the optimal resting positions for both output power and output voltage generation, respectively.

The optimal resting position for arbitrary dimensions of the magnet in a fixed construction volume (defined by R_0 and h) can be obtained by varying the height of the coil and calculating the output power and output voltage (Fig. 4.3a). This was done for different magnet dimensions. The result shows that the optimal resting position is independent of the ratio of magnet and coil radii but depends on the ratio of their heights (Fig. 4.3b). Due to the dependence of the output power on the coil resistance, the optimal resting position for maximum power generation is shifted to lower values compared to the optimal resting position for maximum voltage generation. The least square polynomial curve fits of degree = 4 of the numerically determined optimal resting positions are:

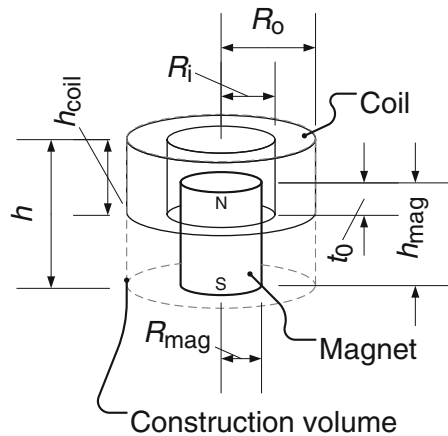


Fig. 4.1 Geometrical parameters of “Magnet in-line coil” architecture without back iron A I

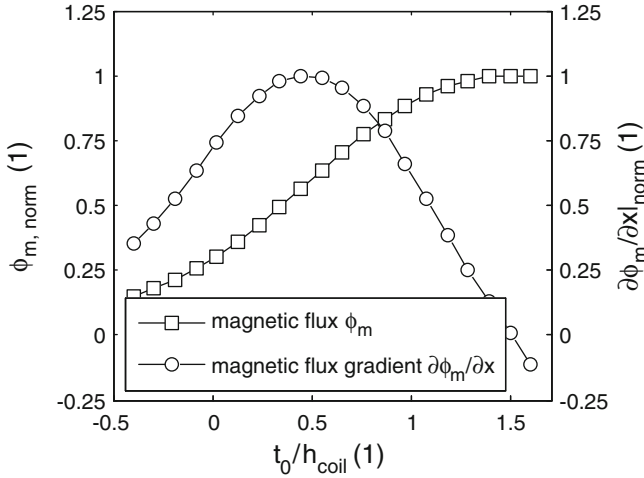


Fig. 4.2 When a magnet moves through a coil there is a point where the magnetic flux gradient is maximal. This point defines the optimal resting position of the magnet for output voltage generation but not for output power generation

Fig. 4.3 (a) To assess the optimal resting position in the fixed construction volume (defined by R_0 and h) the output power and output voltage has been calculated for different magnet dimensions and coil heights. **(b)** Resulting optimal resting positions for power- and voltage generation

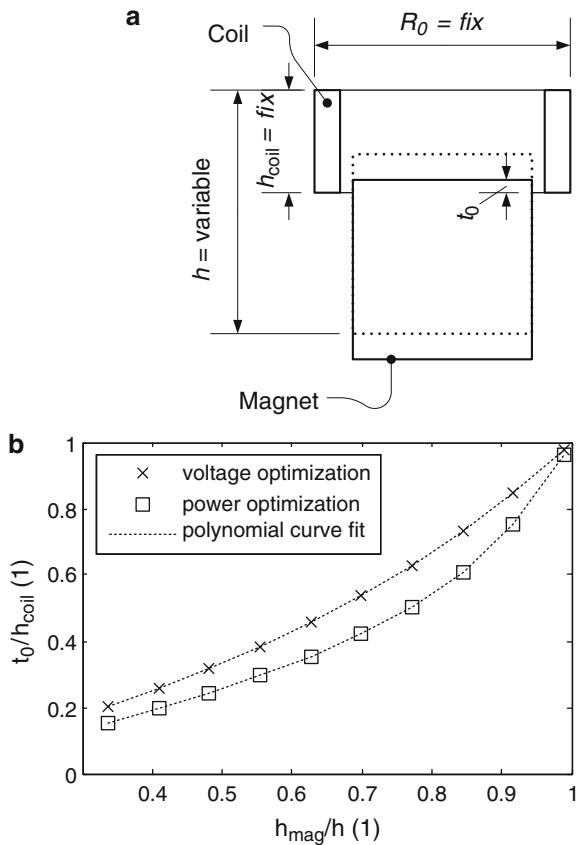
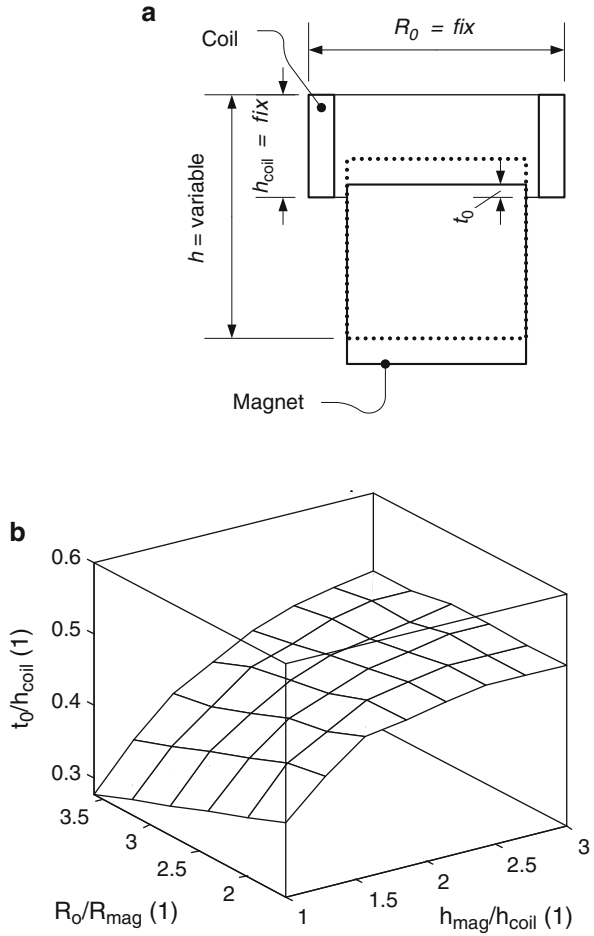


Fig. 4.4 (a) Variable construction volume condition has been applied in a previous publication to assess the optimal resting position [22]. (b) Resulting maximum magnetic flux gradient point for different ratios of coil to magnet height and radii



$$\frac{t_0}{h_{coil}} = 5.403 \left(\frac{h_{mag}}{h} \right)^4 - 11.089 \left(\frac{h_{mag}}{h} \right)^3 + 8.838 \left(\frac{h_{mag}}{h} \right)^2 - 2.502 \frac{h_{mag}}{h} + 0.348, \quad (4.1)$$

for output power generation and:

$$\frac{t_0}{h_{coil}} = 0.643 \left(\frac{h_{mag}}{h} \right)^4 - 1.065 \left(\frac{h_{mag}}{h} \right)^3 + 1.245 \left(\frac{h_{mag}}{h} \right)^2 + 0.124 \frac{h_{mag}}{h} + 0.052, \quad (4.2)$$

for output voltage generation. In a previous publication by the author of this book the optimal resting position has been calculated by varying the height of the construction volume as shown in Fig. 4.4a [22]. In this case the optimal resting

position depends on the radii and the height of magnet and coil (Fig. 4.4b). However this approach is in contrast to the fixed construction volume condition considered in this book. Beyond this the maximum magnetic flux gradient point has been used as the resting position for the output power optimization. Hence the previous presented output power performance can further be increased using the optimal resting positions for output power generation.

Now that the optimal resting position has been defined the question to be answered is which height and inner radius of the coil yields a maximum power and voltage output? Note that due to the condition of fixed construction volume condition the height and radius of the magnet follows from the height and inner radius of the coil by using the optimal resting position and the gap size (defined by the boundary conditions). Hence there are two geometrical parameters to be optimized namely the inner radius and the height of the coil yielding a 2-dimensional search space. Using the optimal resting position for output power generation the optimization results with respect to the given boundary conditions are shown in Fig. 4.5. The resulting output parameters for different values of the coil radius and height are represented as contour plots. Starting with the inner displacement (Fig. 4.5a) it is evident that the higher the oscillating mass and the smaller the electromagnetic damping the higher the inner displacement. Hence, the highest inner displacement amplitude is obtained for the smallest winding area of the coil (h_{coil} small and R_i large). Because the oscillating mass depends on both the inner radius and the coil height, the isolines are somehow diagonal. Consequently, the coil's internal resistance increases with the coil winding area. In contrast to the inner displacement the highest resistances are obtained for large winding areas (h_{coil} large and R_i small) which is also valid for the optimal load resistance. Note that consistent with the EDAM, the values of the optimal load resistance (Fig. 4.5c) are greater than the internal resistance of the coil (Fig. 4.5b). Remember that this is due to the additional term of the parasitic damping electrical analog. Even more exciting is the result for the transduction factor (Fig. 4.5d), the output voltage (Fig. 4.5e) and the output power (Fig. 4.5f), where a maximum is inside the defined design domain (optimum marked with x, o and ▼, respectively). With respect to the transduction factor maximum the maximum for the output voltage is shifted to smaller coil heights and larger radii or in other words to higher oscillating amplitudes! This is plausible because the *emf* depends on both the transduction factor and the oscillating velocity. However, the goal at this point is not the optimization of the transduction factor or the output voltage but the output power. The optimum for the output power (Fig. 4.5f) is further shifted to higher oscillation amplitudes and smaller resistances with respect to the maximum of the output voltage. These results show that there are separate maxima for the transduction factor, the output voltage and the output power. The highest possible output power with respect to the given boundary conditions is 2.94 mW at 1.47 V for a coil with 5.41 mm inner radius and 2.53 mm height (53.5 mm³ coil volume). The corresponding optimal ratio is $h_{\text{mag}}/h = 0.92$ and $t_0/h_{\text{coil}} = 0.75$ (Fig. 4.7a). Beyond these optimal dimensions the output power drops significantly which emphasizes the importance of optimized dimensioning. In general the output power of A I is rather sensitive to the coil inner

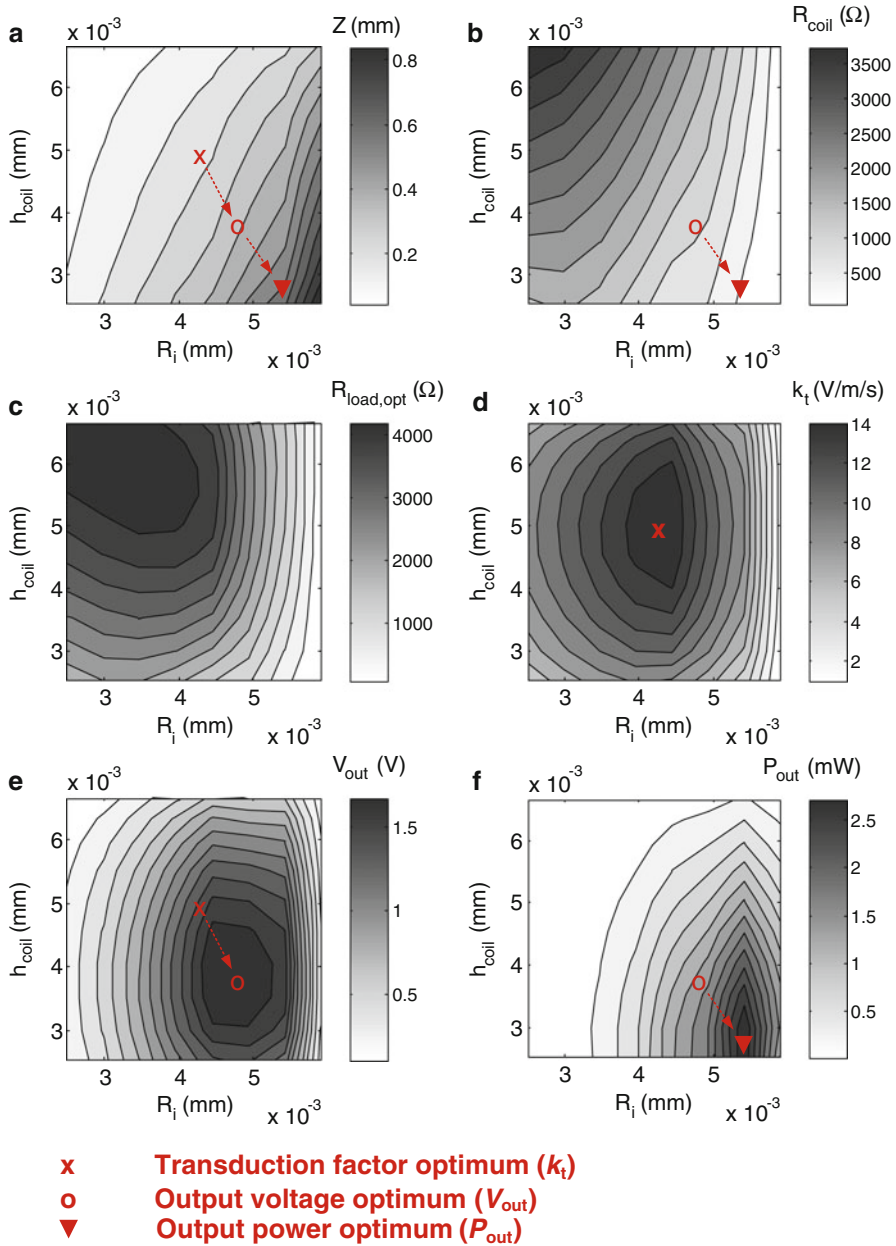


Fig. 4.5 Output power optimization result for A I in a construction volume of 1 cm³. The figures show the resulting (a) inner displacement amplitude, (b) coil resistance, (c) optimal load resistance for different dimensions of the coil. There are definitely different optimal dimensions for maximizing (d) the magnetic flux gradient, (e) the output voltage and (f) the output power

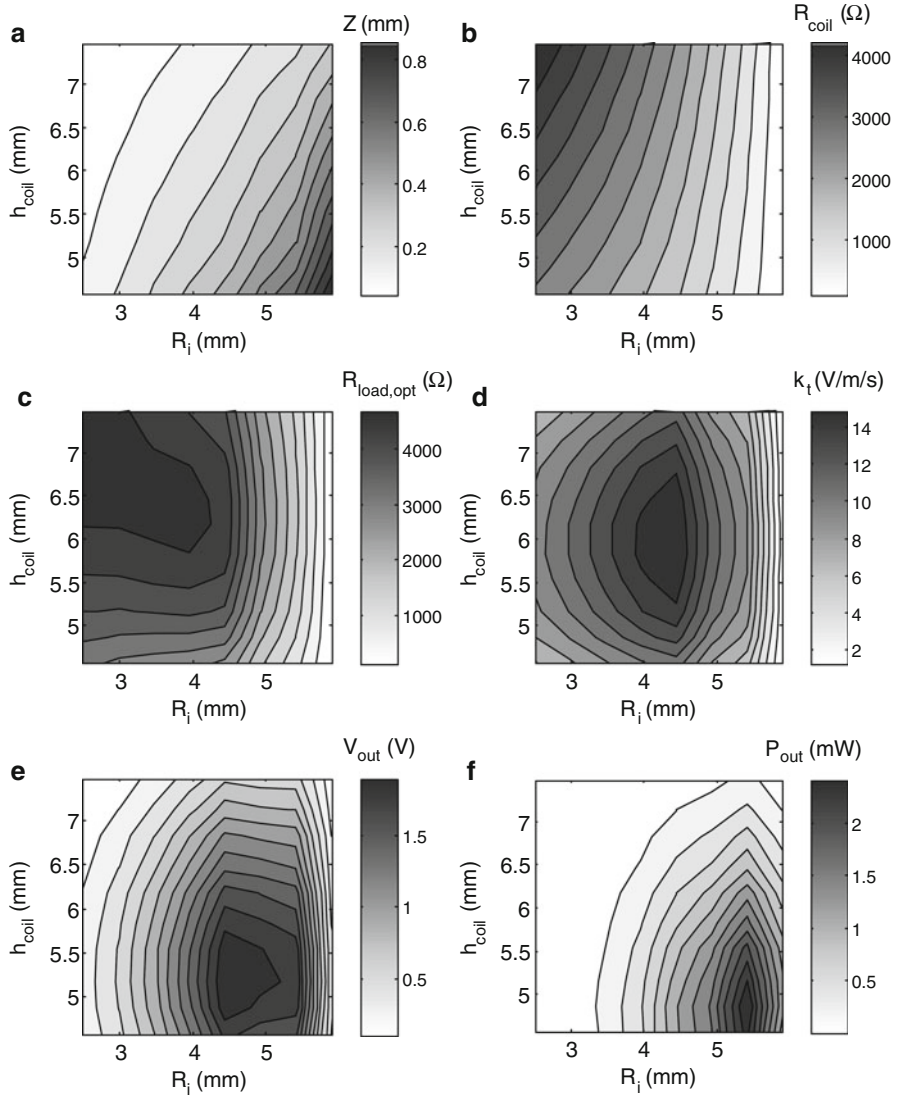
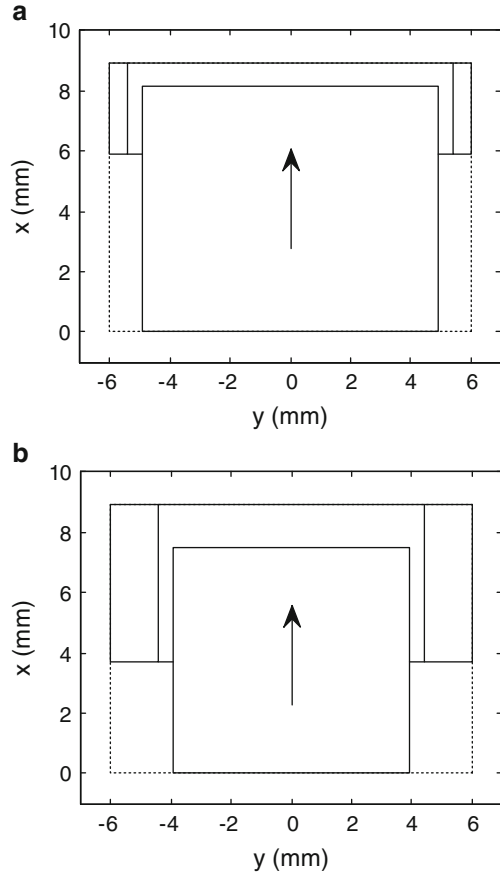


Fig. 4.6 Optimization result for A I in construction volume of 1 cm^3 for operation at maximum magnetic flux gradient resting position (Voltage optimization). The arrangement of the figures is the same as in Fig. 4.5. Due to the different resting positions compared to the power optimization all the values are slightly higher apart from the output power which drops from 2.95 to 2.60 mW

radius as to the coil height. The result of output voltage optimization is shown in Fig. 4.6. In this case the optimal resting position for voltage generation has been applied. As previously explained, this point coincides with the maximum magnetic flux gradient point. Because this resting position comes along with a larger coil

Fig. 4.7 Optimal dimensions for (a) output power and (b) output voltage generation with A I. The *arrows* point from north to south pole

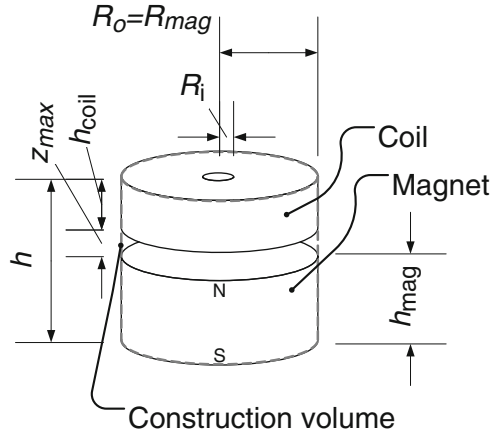


winding area all the output parameters are slightly higher except the output power which drops slightly. The highest possible output voltage is 2.04 V at 1.08 mW for a coil with 4.44 mm inner radius and 5.14 mm height (263 mm^3 coil volume). The corresponding optimal ratio is $h_{\text{mag}}/h = 0.84$ and $t_0/h_{\text{coil}} = 0.73$ (Fig. 4.7b). Thus the coil volume for power optimized dimensions is five times greater than the coil volume for voltage optimized dimensions.

4.2.2 Architecture A II

In A II a cylindrical magnet oscillates towards a cylindrical coil. In contrast to A I the magnet does not immerse into the coil. Hence the oscillation range of the magnet is limited and the resting position of the magnet is defined by the maximum inner displacement specified by the boundary conditions. The geometrical parameters are

Fig. 4.8 Geometrical parameters of “Magnet in-line coil” architecture without back iron A II



shown in Fig. 4.8. The geometrical parameters to be optimized are the inner radius and the height of the coil. The height of the magnet follows from the height of the coil:

$$h_{mag} = h - h_{coil}. \quad (4.3)$$

The results of the optimization in the cylindrical construction volume (again 6 mm radius and 8.9 mm height) are shown in Fig. 4.9. In A II the mass of the magnet depends on the height of the coil but not from the inner radius of the coil. Hence, the relative inner displacement amplitudes are almost horizontal isolines. However, for large inner radii the number of windings and hence also the electromagnetic coupling and the electromagnetic damping decreases. For this reason the inner displacement amplitude slightly increases. The optimum of the transduction factor and consequently also the optimum of the output voltage are limited to the minimum inner radius of the coil (set to $R_{i,min} = 0.5$ mm). Though, the output power is not limited to the inner radius even if the influence is barely observable. This is because the resistance of the inner windings are disproportional to their flux gradient. In the same way as for A I (refer to Fig. 4.5) the optimum of the transduction factor is shifted to higher inner displacement amplitudes with respect to the optimum of the output voltage. The optimum of the output voltage is in turn further shifted to higher oscillation amplitudes and smaller resistances concerning the optimum of the output power. The highest possible output power is 4.38 mW at 2.03 V for a coil with 2.50 mm inner radius and 0.82 mm height (76 mm³ coil volume). The output voltage is maximized for a coil with 0.50 mm inner radius and 2.67 mm height (300 mm³ coil volume). Therewith 3.59 V can be obtained at a power level of 2.87 mW. Note that the coil volume for voltage optimized dimensions is four times greater than the coil volume for power optimized dimensions. The optimal dimensions are shown in Fig. 4.10. In A II both the output power and the output voltage optimized dimensioning is more sensitive to the coil height than to the coil inner radius.

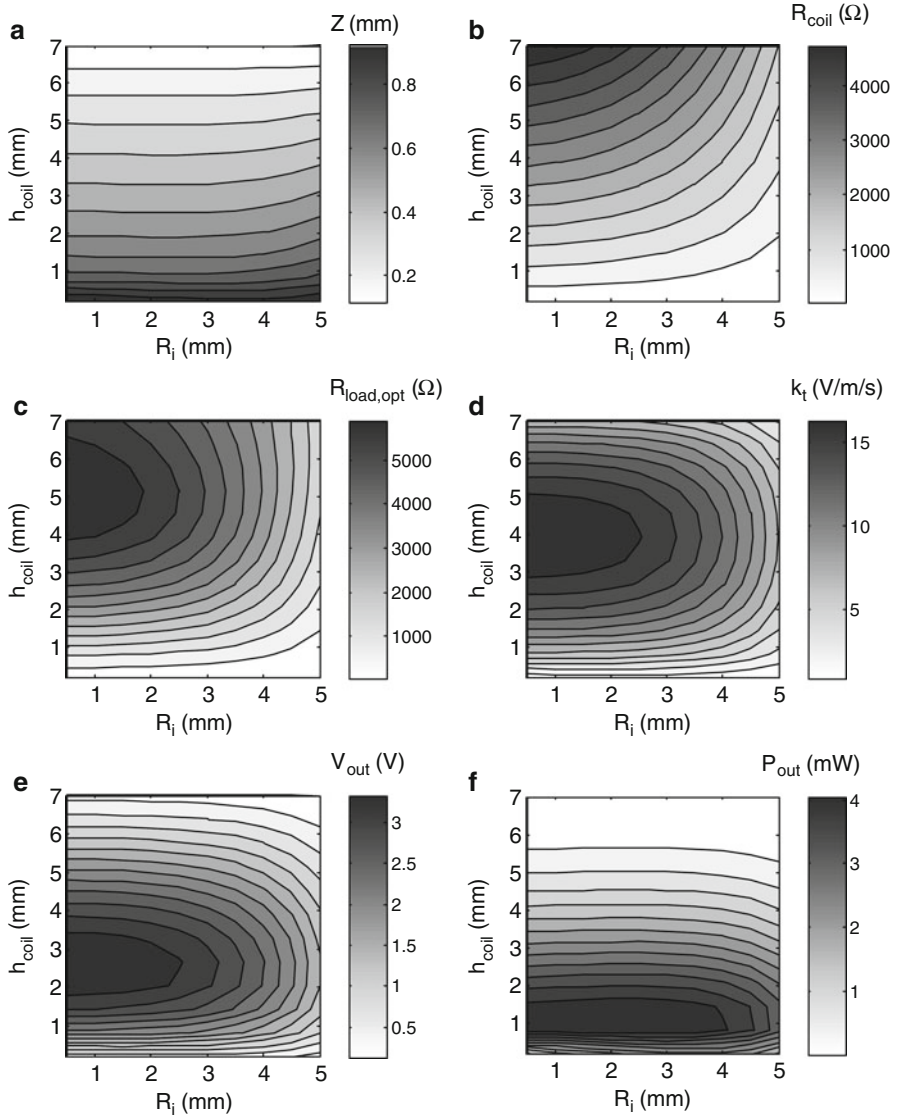
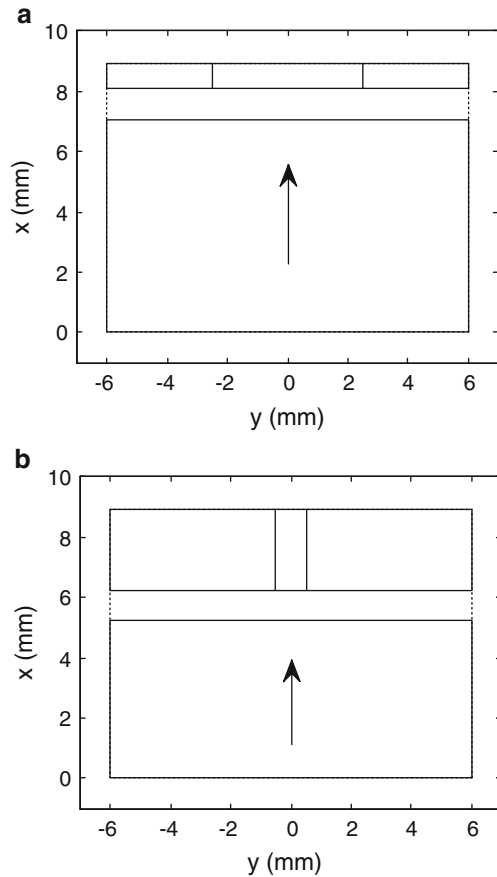


Fig. 4.9 Optimization result for A II in a construction volume of 1 cm^3 . The figures shows the resulting (a) inner displacement amplitude, (b) coil resistance, (c) optimal load resistance for different dimensions of the coil. There are definitely different optimal dimensions for maximizing (d) the magnetic flux gradient, (e) the output voltage and (f) the output power

4.2.3 Architecture A III

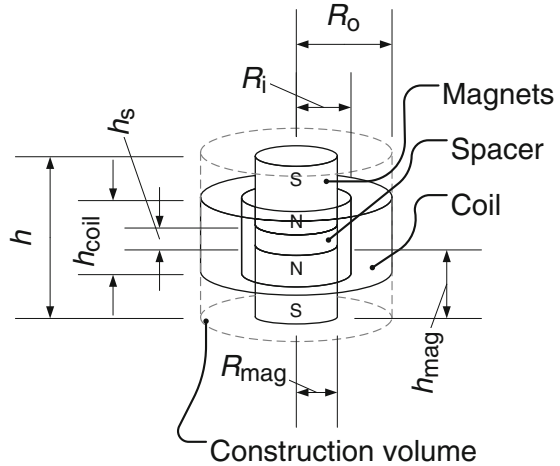
Architecture A III consists of two opposite polarized magnets which oscillate inside a coil. To reduce the repulsive forces between the magnets and to avoid

Fig. 4.10 Optimal dimensions for (a) output power and (b) output voltage generation with A II. The arrows point from north to south pole



demagnetization effects they are separated by a spacer. The geometrical parameters are shown in Fig. 4.11. In application the spacer is made of soft-magnetic material. To be able to compute the magnetic field distribution based on the semi-analytical magnetic field calculation approach the magnetic property of the spacer in the simulation is that of air. Note that this is a simplification because a soft magnetic material with high permeability will act as a flux connector and reduces the magnetic resistance. However as will be shown in (Sect. 5.2.3) the experimental verification of the simulation model shows that a ferromagnetic spacer has only a marginal influence and the results obtained with an “air” spacer are still accurate. The density of the spacer is equal to that of the back iron components defined by the boundary conditions. In the simulation a fixed height of the spacer $h_s = 2$ mm is used (in principle this dimension should be as small as possible but cannot be reduced arbitrary due to the repulsive forces). By doing so the parameters to be optimized are again the inner radius and the height of the coil. Due to the symmetry of the architecture the resting position is in the middle of the coil. Note that in the

Fig. 4.11 Geometrical parameters of “Magnet in-line coil” architecture without back iron A III



simulation the magnetic flux gradient is calculated for only one magnet. Afterwards it is multiplied by two to obtain the overall magnetic flux gradient produced by both magnets.

The optimization results are shown in Fig. 4.12. In A III the mass of the magnet depends on the inner radius of the coil but not on the coil height. The relative inner displacement amplitudes are therefore almost vertical isolines. As for the previous architectures the maximum of the transduction factor is shifted to higher oscillation amplitudes concerning the output voltage and further to higher oscillation amplitudes and smaller internal resistances concerning the output power. The highest possible output power is 1.68 mW at 2.07 V for a coil with 5.34 mm inner radius and 4.93 mm height (37 mm³ coil volume). The output voltage is maximized for a coil with 4.79 mm inner radius and 6.87 mm height (282 mm³ coil volume). Therewith 2.64 V can be obtained at a power level of 1.06 mW. The optimal dimensions are shown in Fig. 4.13. The coil volume for voltage optimized dimensions is 7.6 times greater than the coil volume for power optimized dimensions. Beyond this the output power as well as the output voltage optimized dimensioning of A III is more sensitive to the coil inner radius than to the coil height.

4.2.4 Architecture A IV

A IV is the first architecture with a magnetic circuit based on back iron components. The geometrical parameters are shown in Fig. 4.14. The construction volume is defined by the outer radius R_o and the height h . In accordance to the previous convention all the components have to fit into the construction volume at the resting position of the oscillating mass. From there the coil is flush with the upper pole plate. However in practice the coil is required to protrude beyond the upper pole

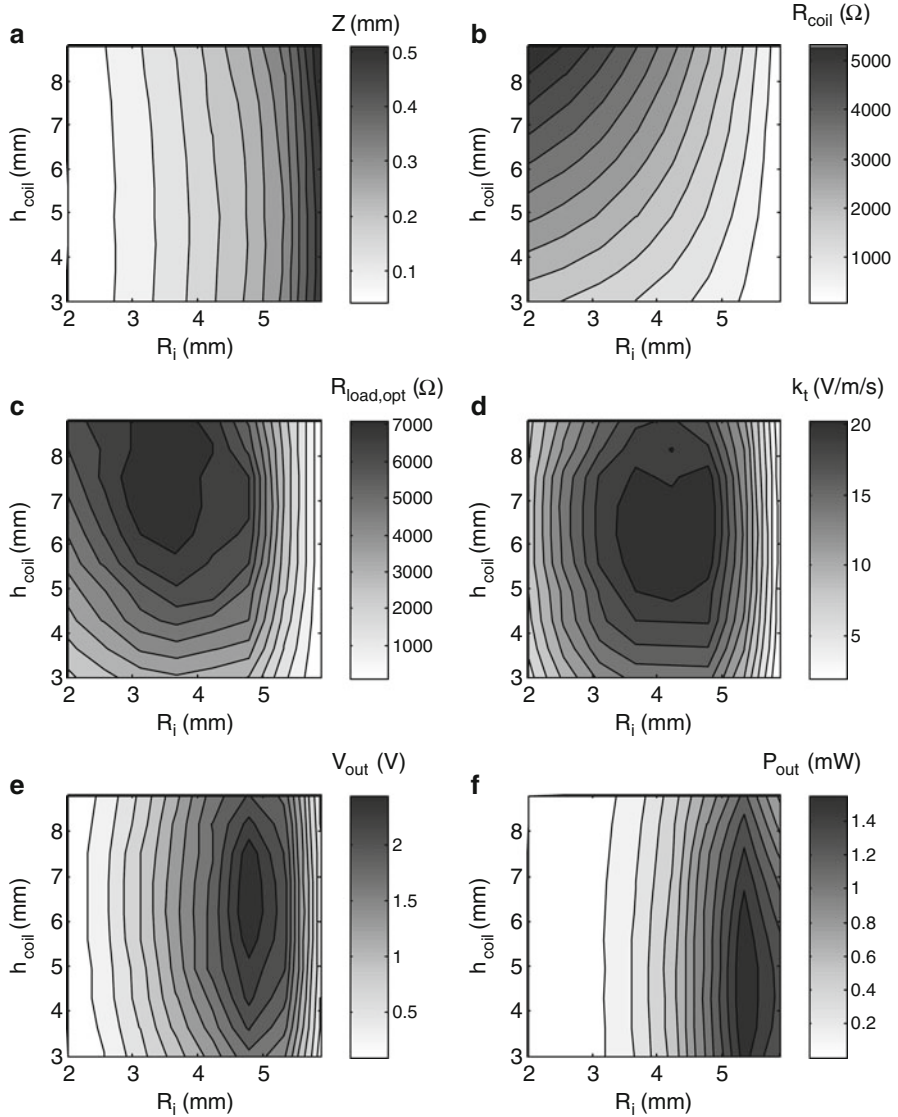
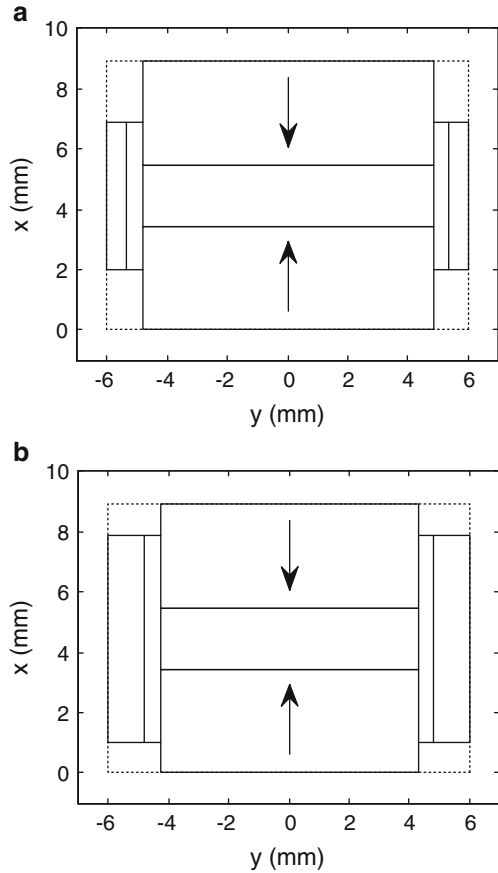


Fig. 4.12 Optimization result of A III in a construction volume of 1 cm³. The figures shows the resulting (a) inner displacement amplitude, (b) coil resistance, (c) optimal load resistance for different dimensions of the coil. There are definitely different optimal dimensions for maximizing (d) the magnetic flux gradient, (e) the output voltage and (f) the output power

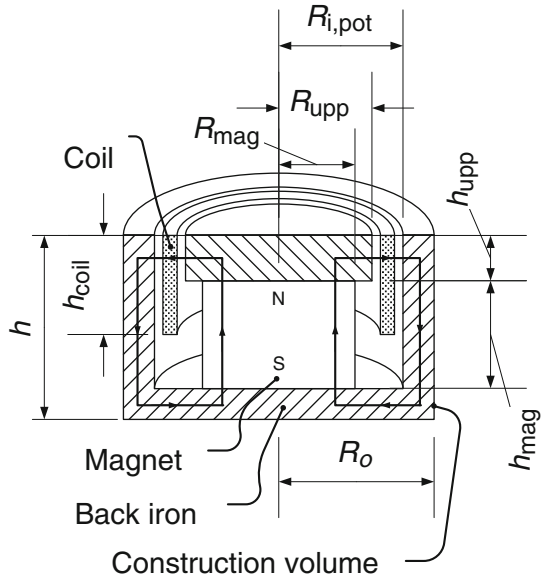
plate, so that it can be fixed at a PCB or the housing. By looking at the geometrical parameters of A IV it is evident that, in contrast to the previous architectures, there are more than two independent geometrical parameters to be optimized.

Fig. 4.13 Optimal dimensions for (a) output power and (b) output voltage generation with A III. The arrows point from north to south pole



These parameters are namely the height of the coil h_{coil} , the radius and height of the magnet R_{mag} and h_{mag} , the radius and the height of the upper pole plate R_{upp} and h_{upp} and the inner radius of the pot $R_{\text{i,pot}}$. These parameters lead to a 6-dimensional search space. In order to find optimal parameter sets for the output power and the output voltage generation the calculation procedure was integrated in an evolution strategy (ES) optimization technique (as discussed in Sect. 3.5.2). Figure 4.15a shows the convergence of an output power ES optimization run where the mean value of the fitness (output power) of the selected individuals is plotted versus the number of generations. After 80 generations the optimization converges and there is no significant increase of the fitness of further generations. At this point the selected individuals are very similar and the best individual of the optimization run (taken from generation 78) can be assumed to be an optimal parameter set. Figure 4.15b is a plot of the corresponding success rate and the standard deviation. Because the success rate after the 3rd generation is already below 1/5 the standard deviation steadily decreases from the maximum of 0.08 to the minimum of 0.005. In the same

Fig. 4.14 Geometrical parameters of “Magnet in-line coil” architecture with back iron A IV. The *closed loop* indicates the direction of magnetic flux



manner Fig. 4.15c, d shows the result for an output voltage ES optimization run. Here the algorithm converges already after 30 generations. The best individual is within generation 23. The magnetic field pattern for output power and output voltage optimized dimensions of A IV is shown in Fig. 4.16a, b. With these optimized dimensions a maximum output power of 5.81 mW can be generated at a voltage level of 1.73 V and a maximum output voltage of 3.14 V at a power level of 3.25 mW. The coil volume of the output power optimized design (37 mm³) is more than five times smaller than the volume of the output voltage optimized design (195 mm³). Note that due to the effect of field homogenisation and concentration it is advantageous in moving coil loudspeakers to make the radius of the magnet smaller than the radius of the upper pole plate ($R_{\text{mag}} < R_{\text{upp}}$) [1]. However in vibration transducers this advantage cannot compensate the disadvantage of the lost mass. That's why the radius of the magnet should always be equal to the radius of the pole plate.

4.2.5 Architecture A V

Architecture A V is similar to A IV. However in A V a ring magnet is used instead of a cylindrical magnet. The geometrical parameters are shown in Fig. 4.17. Again, the number of independent geometrical parameters for the optimization led to a 6-dimensional search space and ES optimization is applied to find optimal parameter sets. The parameters are namely the height of the coil h_{coil} , the inner

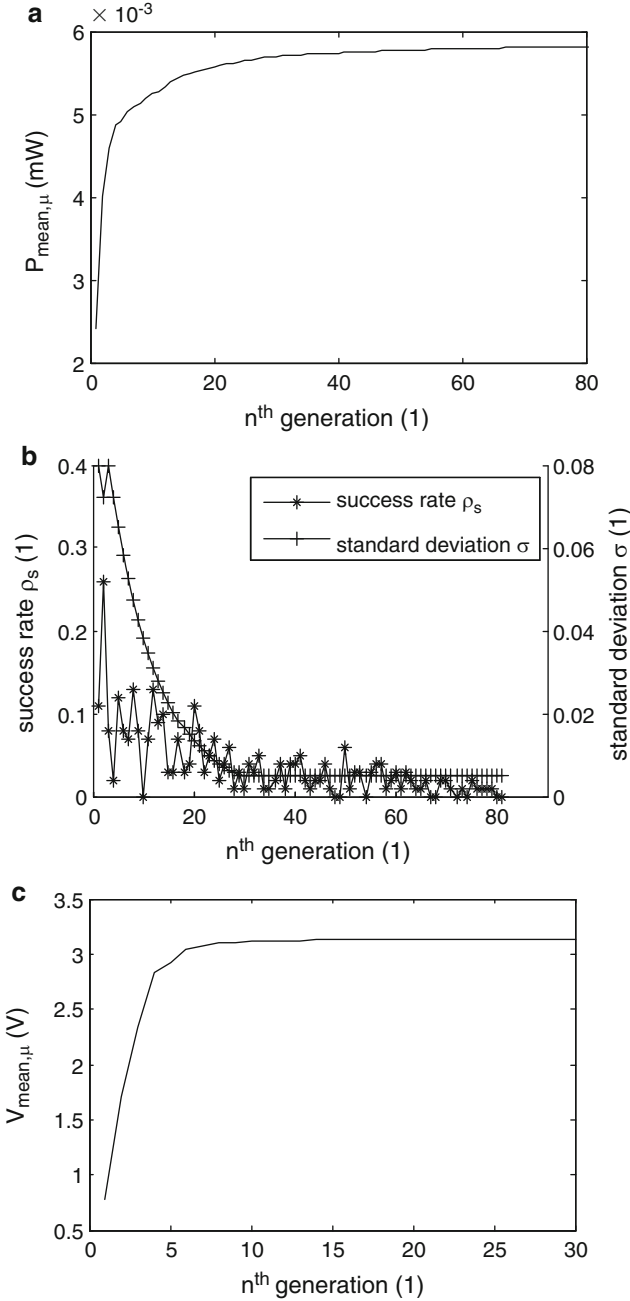


Fig. 4.15 Typical convergence of the optimization of A IV. In (a) the mean value of the output power of the μ selected individuals is plotted versus the number of generation. The corresponding decrease of the variance (as long as the success rate is $<1/5$) is shown in (b). Accordingly the graphs for a voltage optimization run are plotted in (c) and (d)

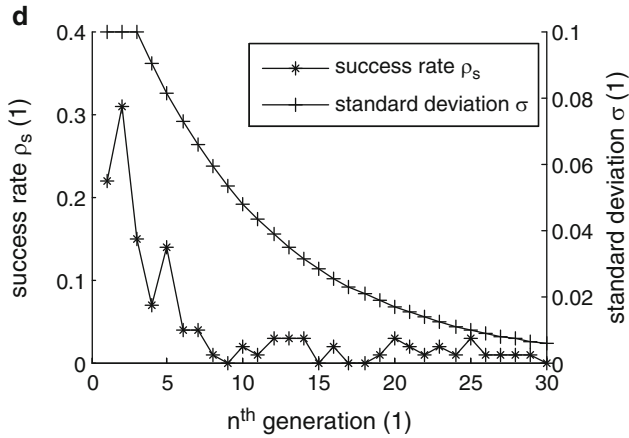


Fig. 4.15 (continued)

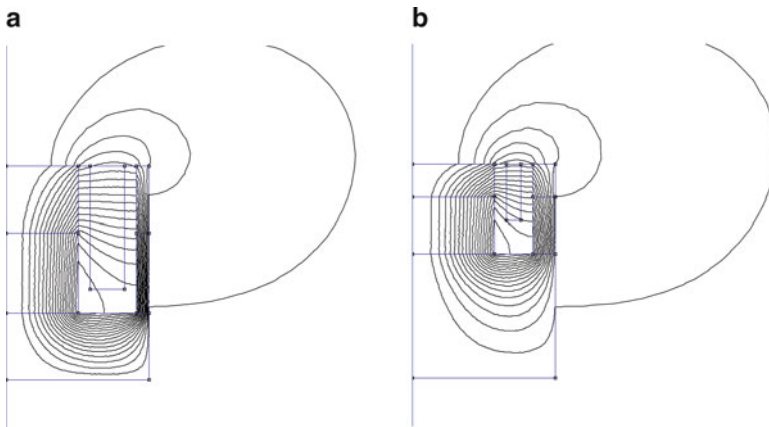
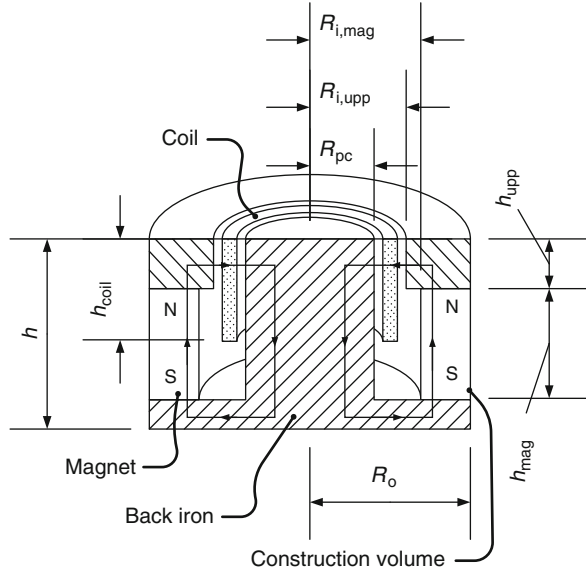


Fig. 4.16 (a) power optimized dimensions and (b) voltage optimized dimensions of A IV

radius $R_{i,mag}$ and the height of the ring magnet h_{mag} , the inner radius $R_{i,upp}$ and the height of the upper pole plate h_{upp} and the radius of the pole core R_{pc} . Figure 4.18a, b show the convergence of an output power ES optimization run. About 30 generations are necessary until the output power shows no significant increase and the stop criterion is fulfilled. The best individual was taken from generation 28. In this optimization run the success rate after the 3rd generation was smaller than 1/5 which causes the standard deviation to decrease continuously from the fourth generation on. The convergence of an output voltage optimization run is shown in Fig. 4.18c, d. The best individual was within the 25th generation. As for A IV the algorithm for output voltage optimization converges faster than for the output power optimization. A possible reason for that is that the voltage optimized coils are

Fig. 4.17 Geometrical parameters of “Magnet in-line coil” architecture with back iron A V. The *closed loop* indicates the direction of magnetic flux



greater than the output power optimized coils which downsize the interval between the parameter bound.

The magnetic field pattern for output power and output voltage optimized dimensions of A V is shown in Fig. 4.19a, b. With these optimized dimensions a maximum output power of 6.72 mW can be generated at a voltage level of 1.99 V and a maximum output voltage of 3.49 V at a power level of 4.00 mW. Just as for A IV the coil volume of the output power optimized design (38 mm³) is almost five times smaller than the volume of the output voltage optimized design (179 mm³). Another characteristic as to that observed in A IV is that it is advantageous to set the inner radius of the upper pole plate equal to the inner radius of the magnet.

4.3 “Magnet Across Coil” Architectures

4.3.1 Architecture A VI

In architecture A VI two opposite polarized magnets move across a cylindrical coil. This is the first architecture with a cubic geometry. The geometrical parameters are shown in Fig. 4.20. As stated in the introduction the 1 cm³ construction volume (defined by the cuboid $a \cdot b \cdot h$) is 10·10·10 mm³. Because the magnetic circuit is not closed the magnetic field drops rapidly after the magnetic pole. Hence an elongated construction volume will be rather disadvantageous. By definition the border of the

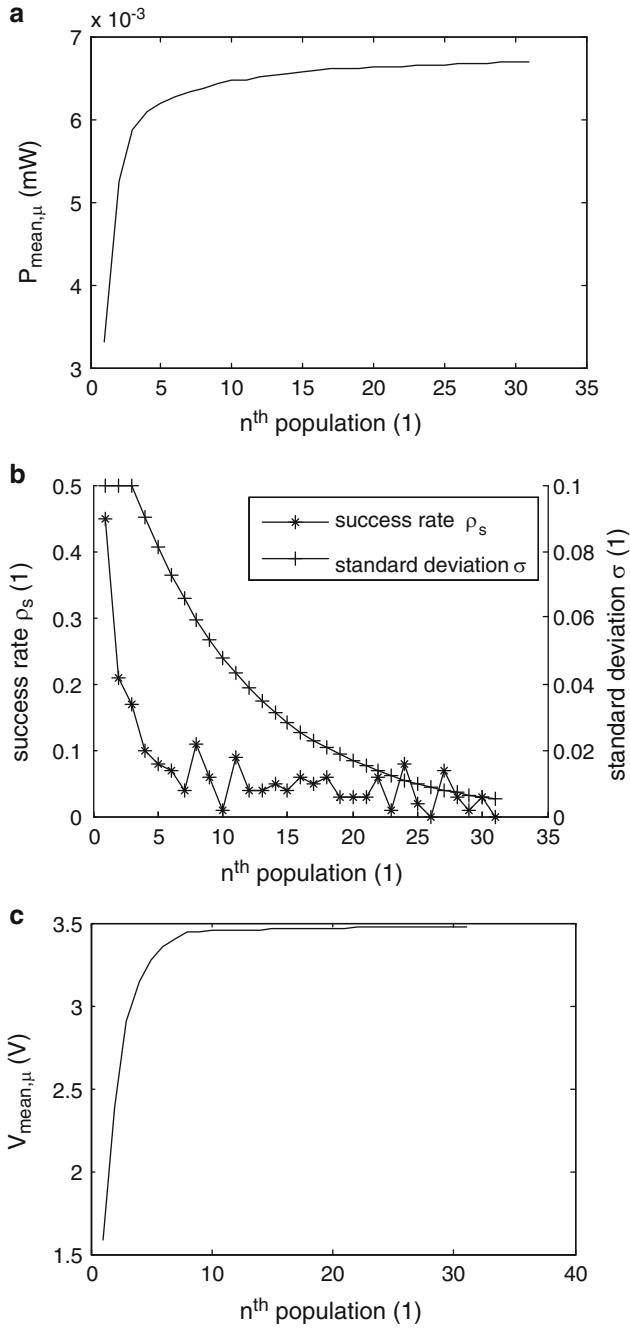


Fig. 4.18 Typical convergence of the optimization of A V. The mean value of the output power of the μ selected individuals is plotted in (a). The corresponding decrease of the variance (as long as the success rate is $<1/5$) is shown in (b). Accordingly the graphs for a voltage optimization run are plotted in (c) and (d)

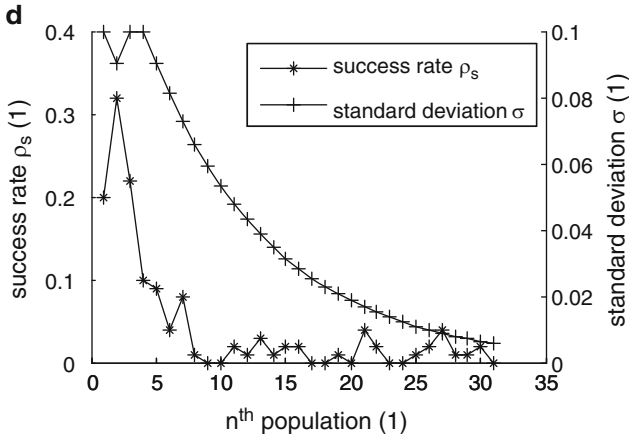


Fig. 4.18 (continued)

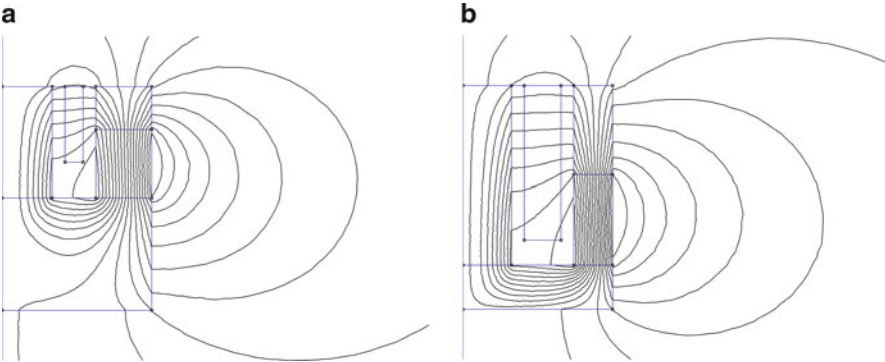


Fig. 4.19 (a) power optimized dimensions and (b) voltage optimized dimensions of A V

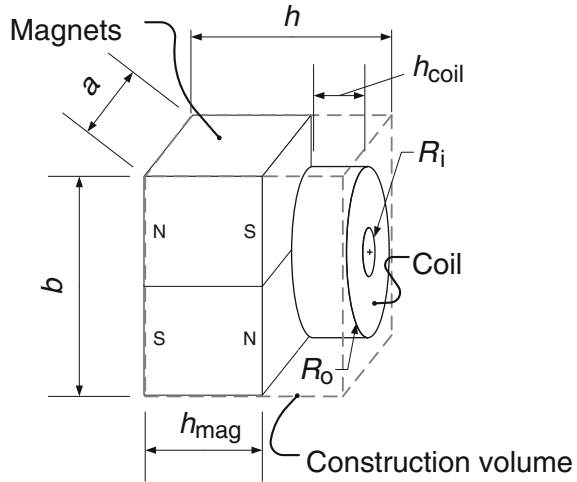
coil must not exceed the construction volume at the maximum inner displacement. On this note the outer radius of the coil R_o is given by:

$$R_o = \frac{b}{2} - z_{\max}. \tag{4.4}$$

(This definition of the outer radius is also valid for the architectures A VII and A VIII). Therewith the outer radius of the coil is fixed and two independent geometrical parameters remain, which need to be optimized. In the same manner as for the “Magnet in-line coil” architectures without back iron these are namely the inner radius and the height of the coil.

The results of the optimization are shown in Fig. 4.21. Because the mass of the magnet depends on the height of the coil but not on the inner radius of the coil the relative inner displacement amplitudes are almost horizontal isolines. However, at large inner radii and small coil heights the electromagnetic damping drops and

Fig. 4.20 Geometrical parameters of “Magnet across coil” architecture without back iron A VI



thus the inner displacement amplitude rises for mentioned reasons (refer to A II in Sect. 4.2.2). Another similarity to A II is that the maximum of the transduction factor and the optimum of the output voltage are located at the minimum inner radius of the coil (as in A II set to $R_{i,\min} = 0.5$ mm). However in A VI this is also the case for the output power. As for the architectures A I–A III the maximum of the transduction factor is shifted to higher inner displacement amplitudes with respect to the optimum of the output voltage and the optimum of the output power is further shifted to higher oscillation amplitudes and smaller resistances with respect to the optimum of the output voltage. The highest possible output power is 3.76 mW at 1.58 V for a coil with 0.5 mm inner radius and 1.3 mm height (55 mm³ coil volume). The optimal output voltage is obtained for a coil with minimal inner radius of 0.5 and 3.2 mm height (100 mm³ coil volume). Therewith 1.96 V can be obtained at a power level of 2.26 mW. The optimal dimensions are shown in Fig. 4.22. The coil volume for voltage optimized dimensions is two times greater than the coil volume for power optimized dimensions. Consequently both the output power and the output voltage optimized dimensioning are more sensitive to the coil height than to the coil inner radius.

4.3.2 Architecture A VII

In contrast to the architecture A VI there are two opposite polarized magnets on both sides of the coil in architecture A VII. The geometrical parameters are shown in Fig. 4.23. Due to the field homogenization between the magnets (refer to Sect. 3.4) the aspect ratio of the 1 cm³ construction volume applied in the optimization is rather elongated ($a = 8.7$ mm, $b = 8.7$ mm and $h = 13.21$ mm). Apart from this difference, the inner radius and the height of the coil are again the geometrical parameters which need to be optimized. The results of the optimization are shown in Fig. 4.24.

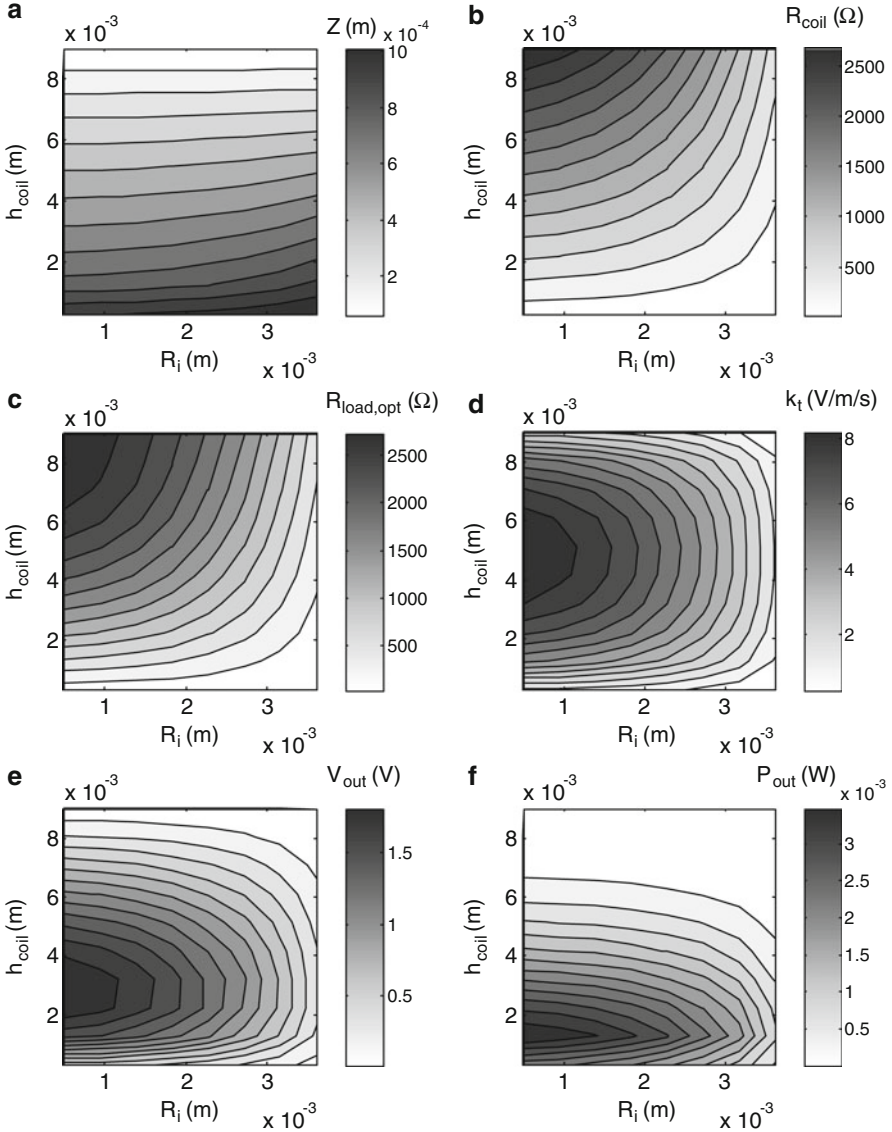


Fig. 4.21 Optimization result for A VI in a construction volume of 1 cm^3 . The figures show the resulting (a) inner displacement amplitude, (b) coil resistance, (c) optimal load resistance for different dimensions of the coil. There are definitely different optimal dimensions for maximizing (d) the magnetic flux gradient, (e) the output voltage and (f) the output power

Due to the similarity to A VI the results are also quite similar from the qualitative point of view. The highest possible output power is 5.56 mW at 2.17 V for a coil with the minimum inner radius of 0.5 and 1.54 mm height (53 mm^3 coil volume).

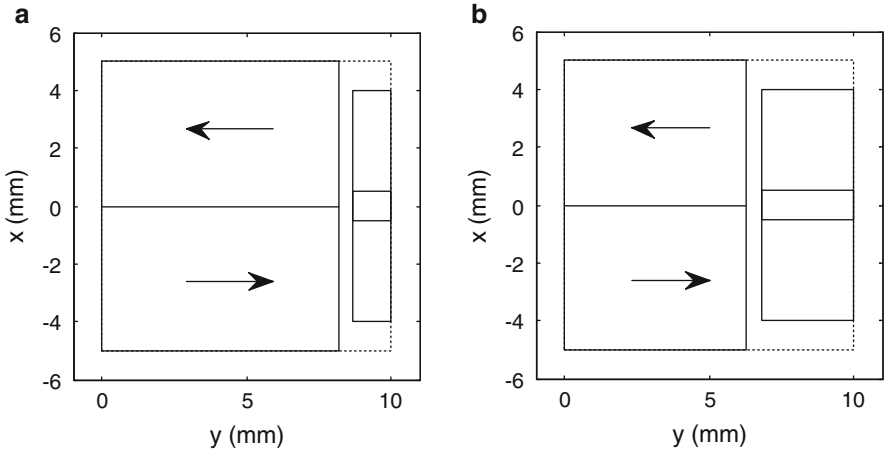
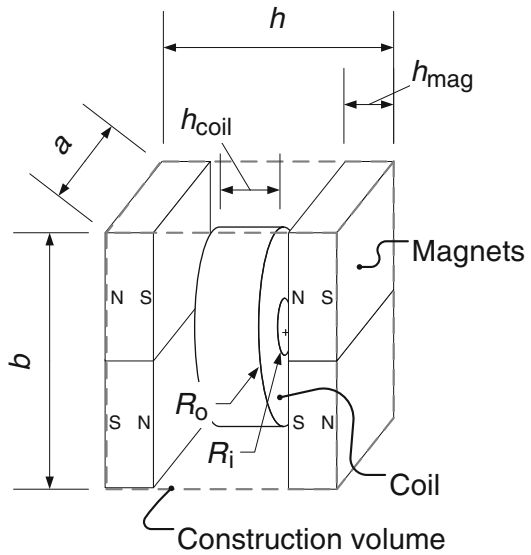


Fig. 4.22 Optimal dimensions for (a) output power and (b) output voltage generation with A VI. The arrows point from north to south pole

Fig. 4.23 Geometrical parameters of “Magnet across coil” architecture without back iron A VII



The optimal output voltage results with a minimal inner radius of 0.5 mm and a coil height of 2.79 mm (96 mm³ coil volume). Therewith 2.51 V can be obtained at a power level of 4.25 mW. The optimal dimensions are shown in Fig. 4.25. The coil volume for voltage optimized dimensions is approximately two times greater than the coil volume for power optimized dimensions. It is apparent that in accordance to A VI both the output power and the output voltage optimized dimensioning are more sensitive to the coil height than to the coil inner radius.

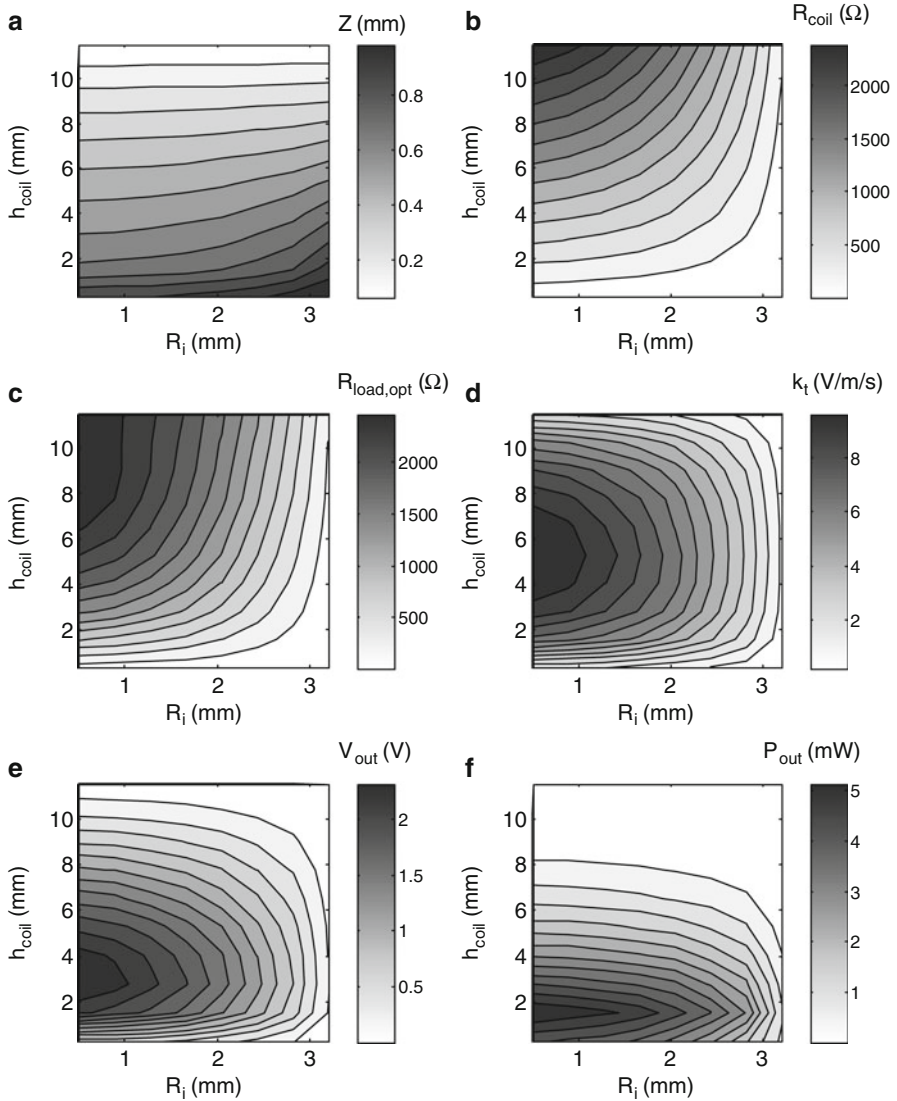


Fig. 4.24 Optimization result for A VII in a construction volume of 1 cm^3 . The figures shows the resulting (a) inner displacement amplitude, (b) coil resistance, (c) optimal load resistance for different dimensions of the coil. There are definitely different optimal dimensions for maximizing (d) the magnetic flux gradient, (e) the output voltage and (f) the output power

4.3.3 Architecture A VIII

In this architecture back iron is used to close the magnetic circuit partly. Apart from that the architecture is identical to A VII. The geometrical parameters are shown

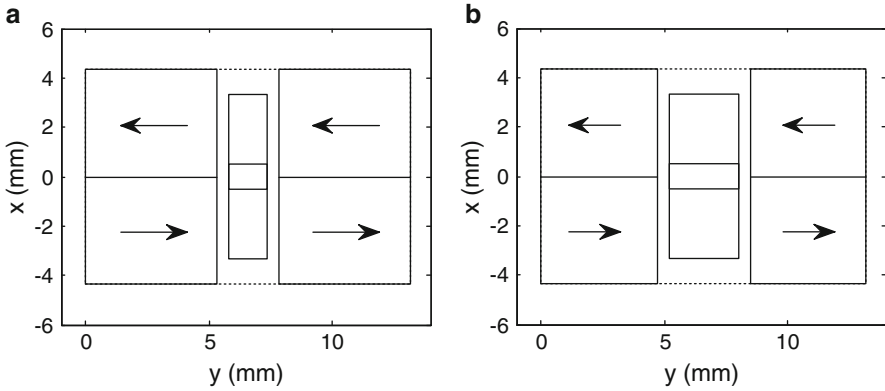
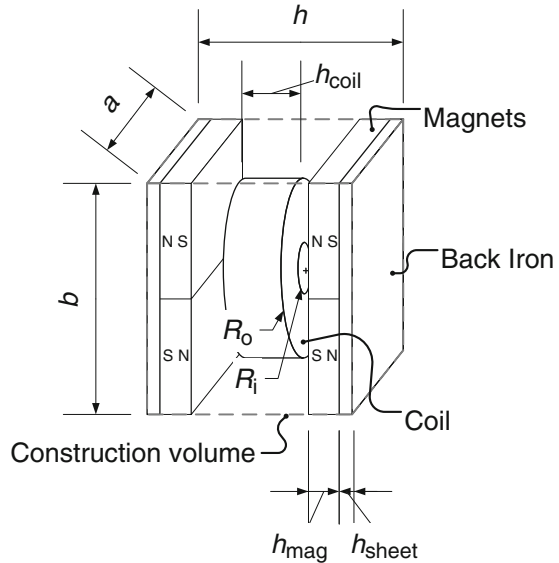


Fig. 4.25 Optimal dimensions for (a) output power and (b) output voltage generation with A VII. The arrows point from north to south pole

Fig. 4.26 Geometrical parameters of “Magnet across coil” architecture with back iron A VIII



in Fig. 4.26. The height of the back iron sheet implicates a further geometrical parameter (h_{sheet}) which needs to be optimized. The results from the last “Magnet across coil” architectures show that the optimum of the output power and the optimum of the output voltage is obtained for a minimal inner radius of the coil. Moreover the output performance is quite insensitive against the inner radius of the coil. Consequently, it is expected that this is also true for A VIII. The inner radius of the coil has therefore been fixed to the minimum value of 0.5 mm. Therewith the remaining geometrical parameters to be optimized are the height of the magnet

h_{mag} and the height of the back iron sheet h_{sheet} . Because the height of the coil is a function of the height of the magnet and the back iron sheet:

$$h_{coil} = h - 2(h_{mag} - h_{sheet} - G), \quad (4.5)$$

it would also be possible to choose the height of the coil as a geometrical parameter. However, some interesting results can be shown when using the height of the magnet and the height of the back iron sheet as the geometrical parameters. The results of the optimization are shown in Fig. 4.27. Due to the different geometrical parameters with respect to the previous “Magnet across coil” architectures the diagrams look different.

The triangle shaped white area in the diagrams indicates the region that is not allowed because the sum of the two gaps, the back iron– magnet– and minimum coil height (set to 0.3 mm) are greater than the predefined construction volume length (13.21 mm). Apart from that the interpretation of the results is quite clear. The inner displacement (Fig. 4.27a) depends on the oscillating mass. Even though the density of the magnet and the back iron material are slightly different it does not matter whether the mass is produced by a thick magnet and a thin back iron sheet or vice versa. Hence the isolines of the inner displacement are just diagonal. Concerning the internal resistance it is clear that the thinner the sum of the magnet and the back iron sheet height the larger the height of the coil and consequently also the internal resistance. The same holds for the optimal load resistance. However for the magnetic flux gradient there is a maximum within the defined design domain. Again the maximum is shifted towards higher oscillation amplitudes concerning the output voltage and further shifted to higher oscillation amplitudes and smaller resistances concerning the output power. An interesting outcome of the optimization is that the dimensioning of A VIII is more sensitive to the sum of the magnet and the back iron sheet height than to the height of each single parameter. That means that it does not matter whether the oscillating mass is provided by a large magnet height and a small back iron sheet height or vice versa. A low–cost implementation of A VIII would therefore use a small magnet and large back iron sheet without having a disadvantage in the output performance. With the optimal magnet height of 3.30 mm and back iron sheet height of 2.29 mm an output power of 5.83 mW can be generated at a voltage level of 1.72 V. The optimal output voltage dimensions are 2.97 mm magnet height and 1.67 mm sheet height. With these dimensions 2.47 V can be generated at a power level of 4.09 mW. The optimal dimensions are shown in Fig. 4.28.

4.4 Conclusion and Comparison of the Coupling Architectures

In the previous subsections the results of the output power and output voltage optimization of eight different electromagnetic coupling architectures have been presented. In order to assess the most efficient coupling architectures this subsection

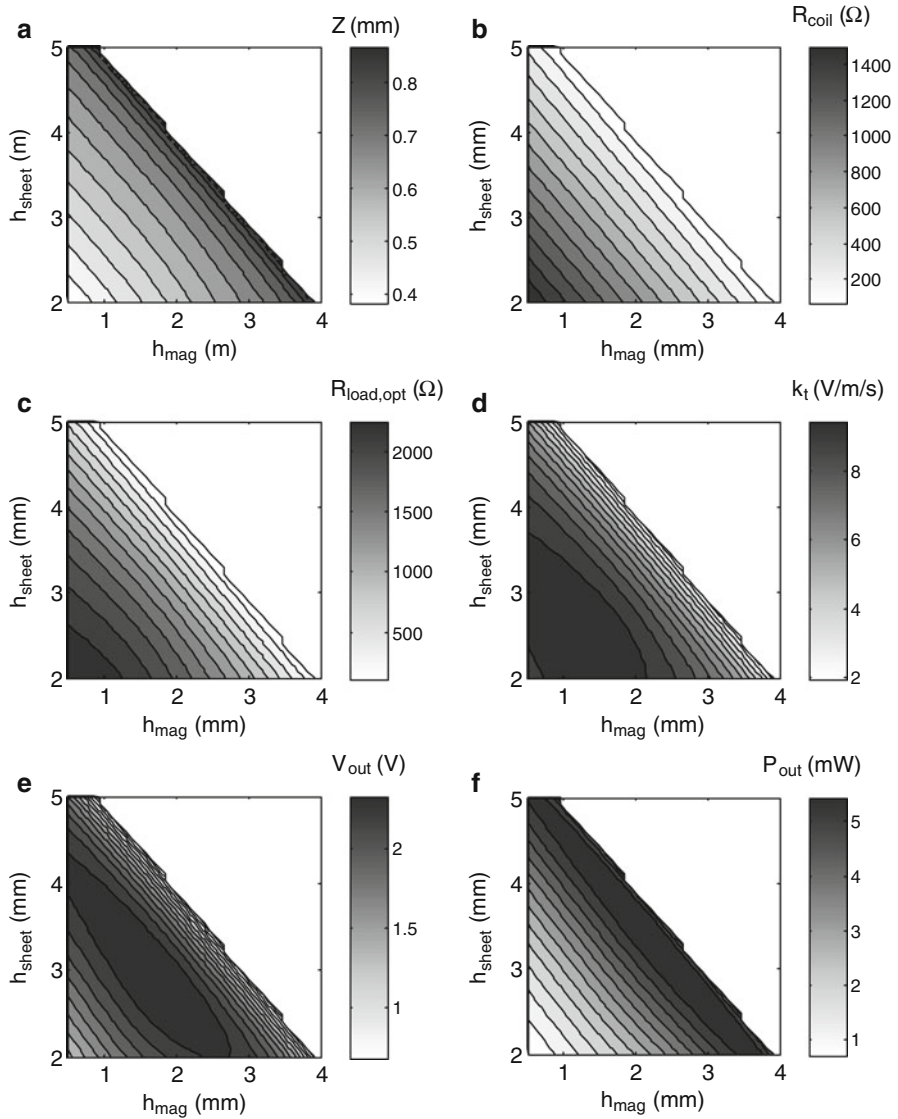


Fig. 4.27 Optimization result for A VII in a construction volume of 1 cm³. The figures shows the resulting (a) inner displacement amplitude, (b) coil resistance, (c) optimal load resistance for different dimensions of the magnet and back iron sheet. There are definitely different optimal dimensions for maximizing (d) the magnetic flux gradient, (e) the output voltage and (f) the output power

is concerned with the comparison of the architectures performance limit. As a basis for this comparison the same boundary conditions (including the parasitic damping) have been applied in the optimization calculations. Nevertheless the

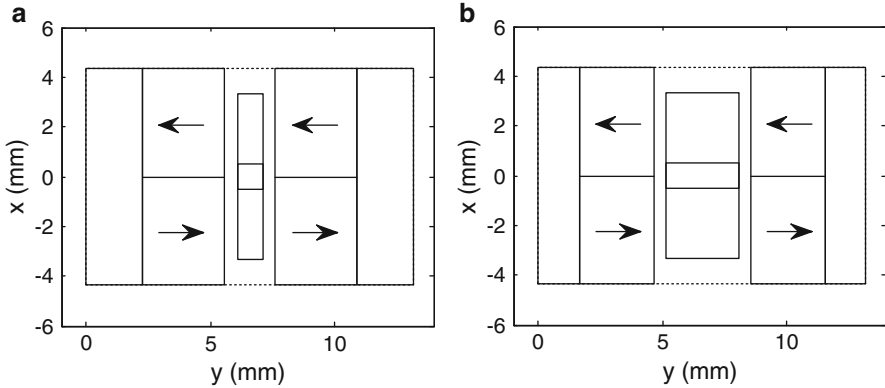


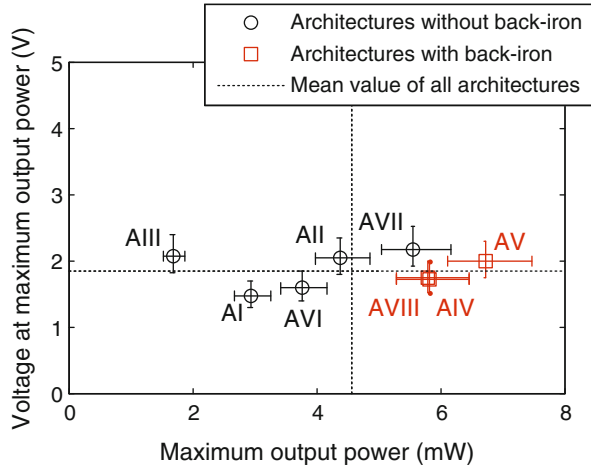
Fig. 4.28 Optimal dimensions for (a) output power and (b) output voltage generation with A VIII. The arrows point from north to south pole

parasitic damping is assumed to be dominated by the aerodynamic resistance which depends on the reference area and the drag coefficient. However these values depend on the design of the architecture. In order to investigate the variation of the performance limits with respect to the parasitic damping the optimization calculations have been repeated with $\pm 10\%$ of the parasitic damping coefficient. In the following comparison graphs these results are included as error bars.

4.4.1 Output Power Generation Capability

So far the dimensions of the architecture specific geometrical parameters (magnet, coil and back iron components) have been optimized. A basic outcome from the optimization procedure is that for each architecture there exists a different set of optimal geometrical parameters for maximum output power and maximum output voltage performance. Any other than these optimal dimensions will decrease the output performance. Fig. 4.29 shows a comparison of the architecture dependent maximum output power and the corresponding output voltage (dashed lines indicate the mean values of all architectures). The result shows that with respect to the overall boundary conditions architecture A V is definitely capable of generating the highest output power in a construction volume of 1 cm^3 . With almost the same output power architecture A VIII and A IV perform second best. Note that these best three architectures are the architectures with back iron. From there it seems that back iron has a general advantage for output power generation even though there is less space for the magnetic material. Although the loudspeaker based architectures A IV and A V are rather similar there is a moderate difference of 15% in the output power performance. The fourth best architecture with respect to the output power is A VII. At the same time this is the best architecture without back iron. The

Fig. 4.29 Comparison of the maximum output power obtained with the optimal output power dimensions together with the corresponding voltage at the optimal output power points. The *dashed curve* indicates the mean value of all architectures. The *errorbars* indicate a variance of $\pm 10\%$ of the parasitic damping

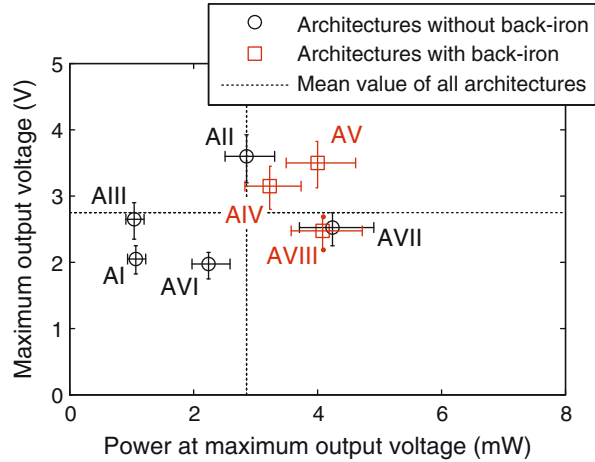


remaining architectures are below the mean value of all architectures. The lowest output power is predicted with architecture A III. Note that there is a factor of 4 between the highest and the lowest output power. This emphasizes the fact, that beyond the optimization of the geometrical parameters it is of great importance to choose the right architecture for the application. The corresponding output voltage level at the maximum output power points can be used for further evaluation (primarily of the best architectures). In detail that means that an architecture with low output power performance does not become really better if the corresponding output voltage level is high but an architecture with high output power performance becomes even better if the output voltage level is also high. A prime example is the comparison of A VII and A VIII. With respect to the output power A VIII is only slightly better (5%). However the output voltage at optimal power point of A VII is 25% higher than in A VIII. In application this may be a reason to prefer A VII. There is no general advantage of the “Magnet in–line coil” or the “Magnet across coil” architecture class. In both classes there are architectures which are within the best.

4.4.2 Output Voltage Generation Capability

In the same way as for the output power Fig. 4.30 shows a comparison of the architectures maximum output voltage. It is architecture A II which is capable of generating the highest output voltage followed from the two loudspeaker based architectures A V and A IV. The “magnet across coil” architectures perform all below the mean value of all architectures. The “Magnet in–line coil” architectures seem to have a general advantage for output voltage generation (except architecture A I). The difference between the lowest and the highest values is not that large as

Fig. 4.30 Comparison of the architectures maximum output voltage obtained with the optimal output voltage dimensions together with the corresponding power at the optimal output voltage points. The *dashed curve* indicates the mean value of all architectures. The *errorbars* indicate a variance of $\pm 10\%$ of the parasitic damping



for the output power optimization but is still a factor of 1.8. Accordingly the power level at the optimal voltage points can be used for further evaluation. Even though A II is capable of generating a slightly higher output voltage than A V the output power level of A V is significantly higher (40%). Hence A V should be preferred whenever possible. Another interesting fact is that A III has indeed a moderate voltage generation capability but the corresponding output power is quite low.

Chapter 5

Experimental Verification of the Simulation Models

5.1 Introduction

In Chap. 4 the results from the parameter optimization for each architecture were discussed in detail. As a basic outcome, the optimum values of certain geometrical parameters were identified which yield either in a maximum output power or in a maximum output voltage. At the end of Chap. 4 the performance limits have been compared and architectures which perform best with respect to the output power and the output voltage became apparent. However, especially for the quantitative comparison of the architectures, it is of great importance to verify the simulation models to ensure that the supposed advantage or disadvantage does not result from inaccuracies in the simulation model. This chapter is concerned with the experimental verification of the simulation models.

The most critical source of error in the simulation is the transduction factor. This is because it is calculated in different ways dependent on the architecture class. In order to investigate the transduction factor experimentally a measurement setup has been developed and built up as illustrated in Fig. 5.1. The measurement setup includes a lab shaker on which the oscillating components of the electromagnetic coupling architectures (magnets and if existent the back iron components) are mounted. The shaker is installed in a fixing stage which also contains a xyz adjustment unit. With this xyz adjustment unit a coil can be positioned relative to the oscillating components. Together with an acceleration sensor, a controller unit and an amplifier the shaker is operated in a closed loop, which allows controlling the vibration amplitude (pure z -direction). In case of a vibration at a given amplitude and frequency the open circuit *emf* amplitude $\hat{\varepsilon}$ is measured at different zero crossing positions of the magnet relative to the coil (illustrated for the example of architecture A VI in Fig. 5.2). Because the peak velocity of the oscillation \hat{Z} (defined by the amplitude and frequency of the vibration) becomes maximal at the zero crossing point the transduction factor is simply given by the quotient of the *emf* amplitude and the peak velocity (2.21). However, the transduction factor will

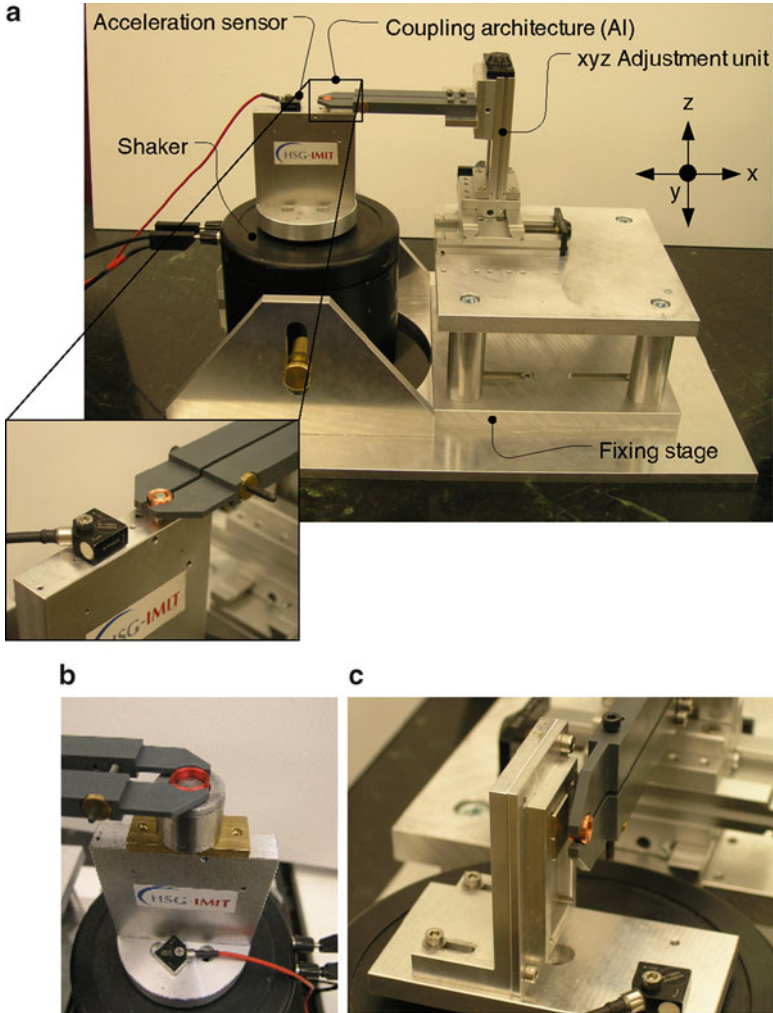


Fig. 5.1 (a) Measurement set up for the experimental verification of the simulation models. Several test devices of the electromagnetic coupling architectures (in the figure A I is pictured) are mounted on a lab shaker. The shaker oscillates with controlled amplitude in z-direction. The induced voltage is measured with an oscilloscope. Therewith the transduction factor can be derived and compared to the simulation results. Exemplarily a test device of A IV is shown in (b) and a test device of A VI in (c)

not be equal over a large displacement range which results in nonlinearity. In this case the quotient of the *emf* amplitude and the peak velocity of the oscillation will not yield the transduction factor at the zero crossing position of the coil.

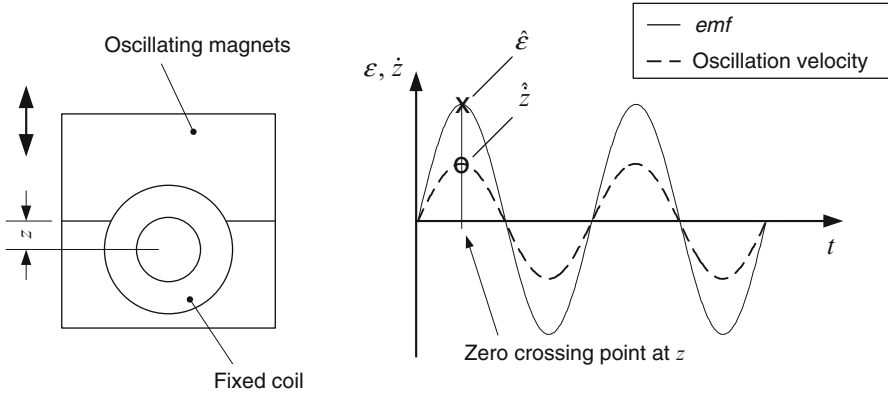


Fig. 5.2 Measurement principle on the example of architecture A VI. With the amplitude of the *emf* (marked with *x*) and the oscillation velocity (marked with *o*) the transduction factor at the zero crossing position at *z* can be determined according to (2.21)

To avoid this effect small vibration amplitudes ($<100 \mu\text{m}$) have been applied in the measurements. Within this small oscillation range the transduction factor can be assumed to be constant. As an indicator for nonlinear behavior the phase shift between the velocity and the *emf* (which must be zero) have been used, too. For each architecture several measurements were performed using different magnet, coil and back iron components. The dimensions and parameters of the used coils and magnets (NdFeB) are listed in Table 5.1. In the following sections the results of the measurements will be introduced and discussed. To verify the simulation models the measurement results are consequently compared with the simulation results. Since the validation of the simulation models is addressed in this chapter, arbitrary test devices were used. Because the dimensions of these test devices are not optimized it is not appropriate to draw general conclusions with respect to the output performance from the measurement results! An important parameter for the computation of the transduction factor is the residual flux density of the magnet. However the absolute value of the discrete magnets used for the measurements is commonly within a certain range (denoted in the manufacturer specification). Note that in reality the residual flux density is sometimes even higher than the maximum value of the specification range. Due to the fact that the exact value is not explicitly known a value within the manufacturer range has been employed in the simulation. The same situation holds for the resistance per meter of the enamelled copper wire. Because all the coils used for the measurements are made of $40 \mu\text{m}$ wire diameter the nominal value based on IEC 60317 ($13.6 \Omega/\text{m}$) has been used in the simulation (maximum value is $14.92 \Omega/\text{m}$ and the minimum value $12.28 \Omega/\text{m}$).

Table 5.1 Discrete magnet- and coil components used for the assembling of the electromagnetic coupling architecture test devices

Coils							
Symbol	Description	Coil 1	Coil 2	Coil 3	Unit		
d_{co}	Wire diameter	40	40	40	μm		
R_o	Outer radius	5.85	7.85	7.15	mm		
R_i	Inner radius	2.6	5.85	5.8	mm		
h_{coil}	Coil height	5	4.5	4.5	mm		
R_{coil}	Resistance	2,893	2,061	1,266	Ω		
L_{coil}	Impedance	307	176	650	mH		
Cylindrical magnets							
Symbol	Description	Magnet C1	Magnet C2	Magnet C3	Magnet C4	Magnet C5	Unit
R_{mag}	Radius	1.5	2	5	5	5	mm
h_{mag}	Height	5	6	3	5	10	mm
B_r	Residual flux density	1.33-1.37	1.30-1.33	1.17-1.25	1.17-1.25	1.17-1.25	T
H_c	Coercivity	>955	>1,512	>860	>860	>860	kA/m
Rectangular magnets							
Symbol	Description	Magnet R1	Magnet R2	Magnet R3	Unit		
a	Length	12	12	12	mm		
b	Width	7	7	7	mm		
h_{mag}	Height	2	2.5	5	mm		
B_r	Residual flux density	1.28-1.35	1.18-1.22	1.18-1.22	T		
H_c	Coercivity	>1,027	795-875	795-875	kA/m		

5.2 “Magnet In-Line Coil” Architecture

With the test devices of the “Magnet in-line coil” architectures mounted on the measurement set-up the transduction factor was measured at different positions of the magnet in z -direction.

5.2.1 Architecture A I

Four different test devices of architecture A I have been assembled. An overview of the used components is given in Table 5.2. The results of the measurement in comparison to the simulation results are shown in Fig. 5.3. Obviously the simulation results are in good agreement with the measurement. As expected (refer to Sect. 4.2.1) there is a maximum of the transduction factor for each of the four test devices apparent. The position of this maximum depends on the magnet and coil length- and radii ratio. Because the measurements correspond to variable construction volume conditions the measured maxima can be directly transferred to Fig. 4.4. Even though the measurement points are in the border area they are very close to the simulated surface which confirms the results obtained with the A I simulation model (Fig. 5.4).

Table 5.2 Used components for the A I test devices

Device	Coil	Magnet
1	1	C1
2	1	C2
3	2	C4
4	2	C5

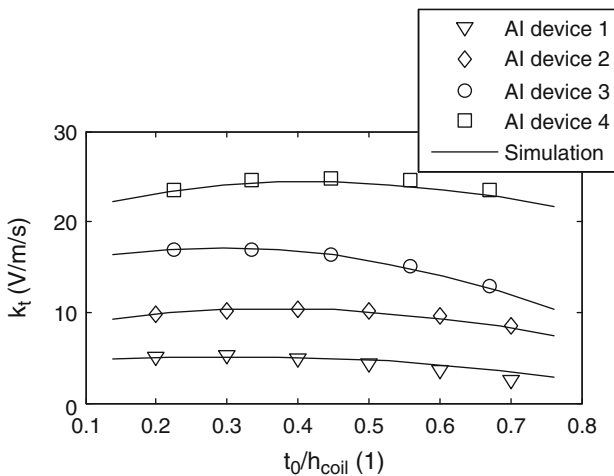


Fig. 5.3 Measurements with four different test devices have been performed to verify the A I simulation model

Fig. 5.4 The measured maximal transduction factor points are in good agreement with the predicted surface

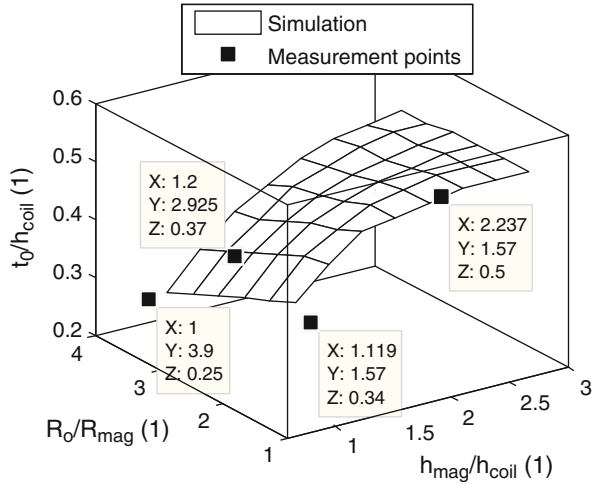


Table 5.3 Used components for the A II test devices

Device	Coil	Magnet
1	1	C3
2	1	C4
3	1	C5

5.2.2 Architecture A II

For the verification of architecture A II three different devices have been built-up from magnet C3, C4 and C5 in each case in combination with coil 1 (Table 5.3). A comparison of the measurement and simulation results is shown in Fig. 5.5. The transduction factor monotonically increases for smaller distances between the magnet and the coil in z -direction. Due to the fact that the A II simulation model is basically the same as the A I simulation model the measured and simulated data are consequently also in good agreement.

5.2.3 Architecture A III

For the verification of the architecture A III simulation model six different devices have been built-up based on magnets C3, C4 and C5 in combination with coil 2 and different spacer heights (Table 5.4). The results of the measurements in comparison to the results obtained from the simulation are shown in Fig. 5.6. For named reasons the magnetic property of the spacer in the simulation is that of air (refer to Sect. 4.2.3). Due to this the maximum transduction factor from the measurement is about 10% higher than in the simulation even though the maximum specified value of the residual flux density of 1.25 T has been applied in the simulation. The accuracy of the simulation increases for increasing distance from the central position in

Fig. 5.5 Measurements with three different test devices have been performed to verify the A II simulation model

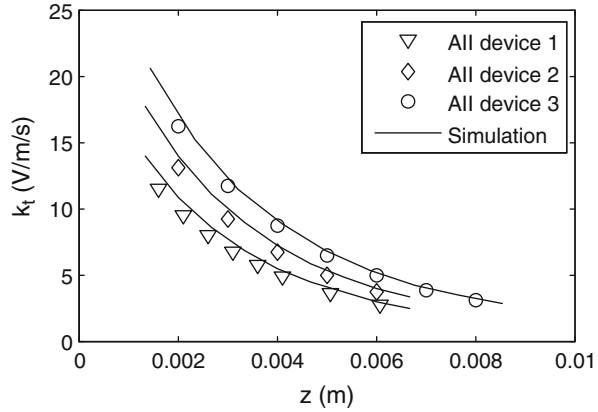


Table 5.4 Used components for the A III test devices

Device	Coil	Magnet	Spacer height (mm)
1	2	C3	3
2	2	C4	3
3	2	C5	3
4	2	C3	4
5	2	C4	4
6	2	C5	4

z-direction. Nevertheless to avoid an unfairness in the comparison introduced in Sect. 4.4 the optimization simulations for A III have been repeated. Therein the simulated transduction factor was by default increased by 10% to compensate the discrepancy between a soft magnetic spacer and an “air” spacer. The results show that although the maximum output power increases from 1.68 to 1.77 mW (increase of 5%) and the maximum output voltage from 2.64 to 2.90 V (increase of 10%) there is no change in the architectures order neither for the output power nor the output voltage!

5.2.4 Architecture A IV

For the verification of the A IV simulation model four different test devices were assembled. The devices are based on two stacked C5 magnets in combination with coil 3. The dimensions of the back iron components are shown in Fig. 5.7a. The remaining parameters namely the height of the upper and lower pole plate are indicated in Table 5.5. The measurement of the transduction factor has been performed at different depths of immersion of the coil in the air gap. The obtained results are shown in Fig. 5.7b. The experimental data corresponds very well with the simulation results. The transduction factor is only slightly dependent on the height of the upper pole plate. However this should not lead to a general conclusion. The reason for this is that the 6 mm upper pole plate height is greater than the coil height and the 3 mm lower pole plate height already yields a quite low flux leakage.

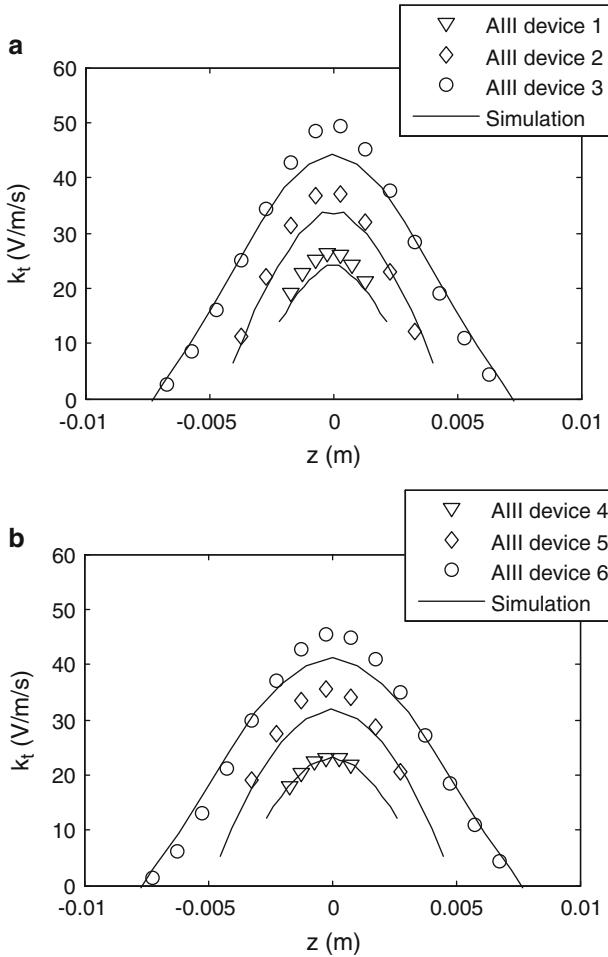


Fig. 5.6 Measurements with six different devices have been performed to verify the simulation model of A III. (a) A 3 mm spacer is used for device 1–3, (b) a 4 mm spacer in device 4–6

5.2.5 Architecture A V

As for architecture A IV four different A V test devices have been assembled based on coil 3. The dimensions of the ring magnet as well as the dimensions of the back iron components are shown in Fig. 5.8a. The four test devices differ again in the height of the upper and the lower pole plate (refer to Table 5.5). The results of the measurement and the simulation are shown in Fig. 5.8b. The comparison of the data yields again a very good agreement. As for A IV the transduction factor is more sensitive to the lower pole plate than to the upper pole plate height.

Fig. 5.7 (a) Dimensions of the back iron components of the A IV test devices. (b) Measured and simulated transduction factor for different depths of immersion of the coil in the air gap

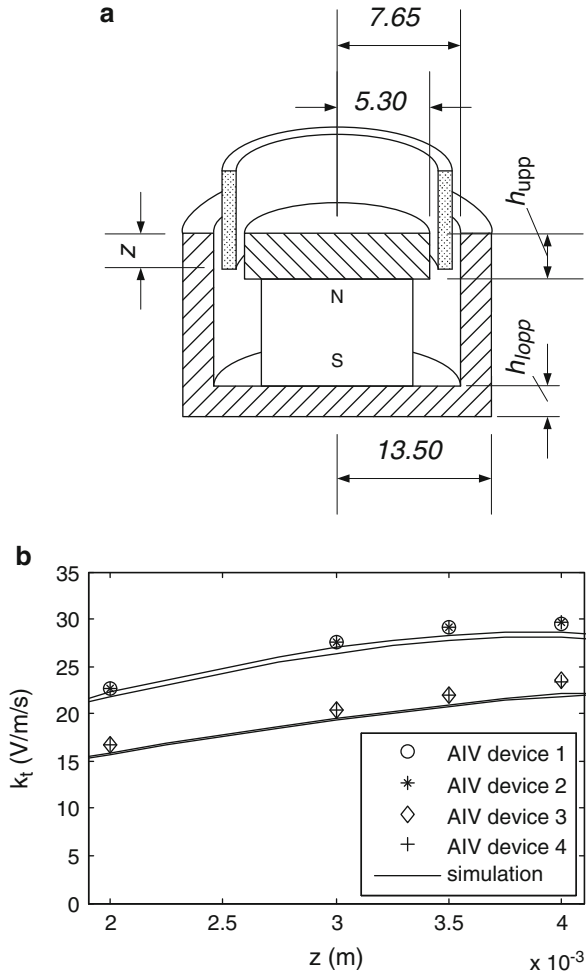


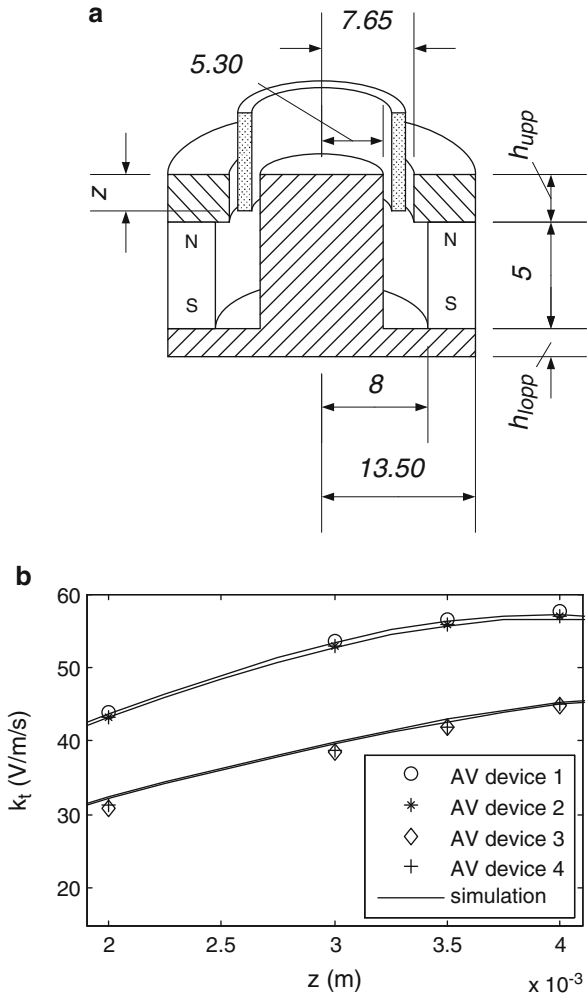
Table 5.5 Dimensions of the AIV and AV test devices

AIV/AV device	h_{lopp} (mm)	h_{upper} (mm)
1	3	3
2	3	6
3	6	3
4	6	6

5.3 “Magnet Across Coil” Architecture

As for the “Magnet in–line coil” architectures the transduction factor of the “Magnet across coil” architectures has also been measured at different positions of the magnet using the measurement set–up. However, in contrast to the “Magnet in–line coil” architectures the gap size between the magnet and the coil can be adjusted with

Fig. 5.8 (a) Dimensions of the ring magnet and the back iron components of the A V test devices. (b) Measured and simulated transduction factor for different depths of immersion of the coil in the air gap



the measurement set-up as well. Hence the gap size is also used as a measurement parameter in addition to the position of the magnet in z -direction (shown in Fig. 5.9 on the example of A VI).

5.3.1 Architecture A VI

For the verification of the architecture A VI simulation model three different devices have been assembled from magnet R1, R2 and R3 in combination with coil 1. The results of the measurements in comparison to the results obtained from the simulations are shown in Fig. 5.10. Both the decrease of the transduction factor

Fig. 5.9 In the “Magnet across coil” architectures the gap between the coil and the magnet has been used as a measurement parameter beyond the position of the magnet in z -direction

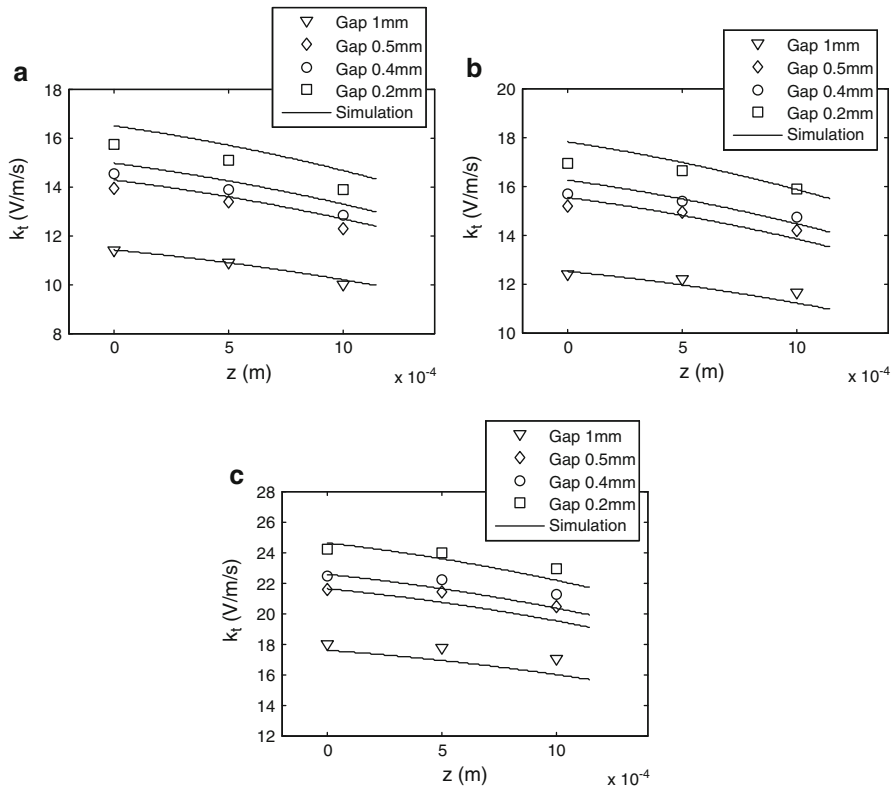
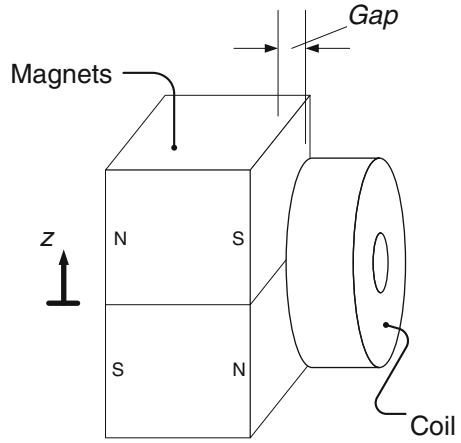


Fig. 5.10 Measured and simulated transduction factor with (a) A VI device 1, (b) A VI device 2 and (c) A VI device 3

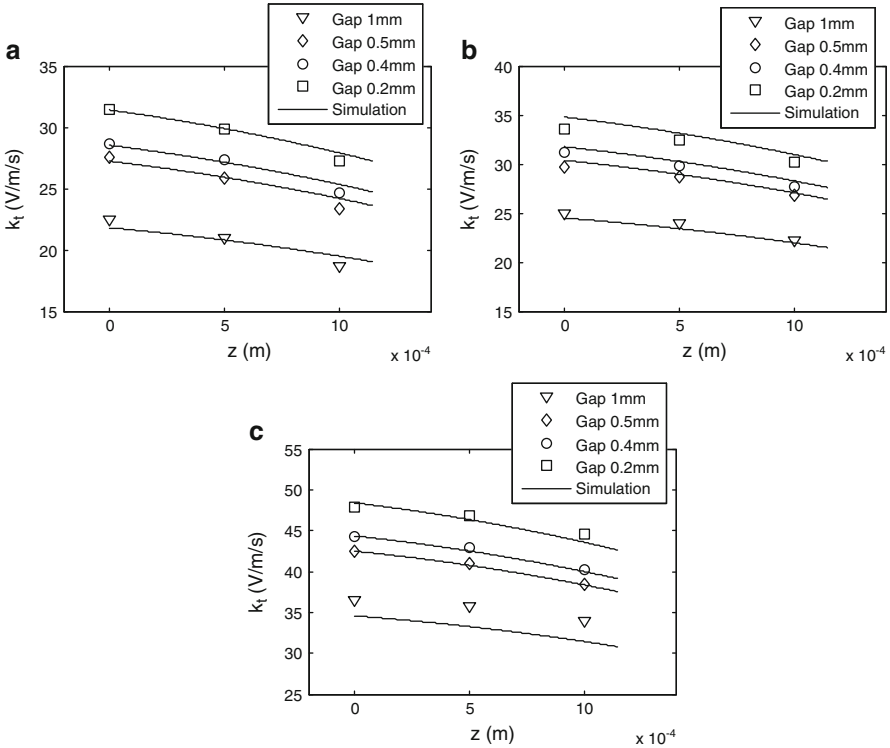


Fig. 5.11 Measured and simulated transduction factor with (a) A VII device 1, (b) A VII device 2 and (c) A VII device 3

for increasing distance from the middle position (at $z=0$) in z -direction and the influence of the gap size between the magnet and coil can be reproduced accurately with the simulation model.

5.3.2 Architecture A VII

For the verification of the architecture A VII simulation model the A VI devices have been used. However the rectangular magnets have been arranged on both sides of the coil. The results of the measurements in comparison to the simulation results are shown in Fig. 5.11. Because the magnetic field between the magnets is more homogeneous in A VII than in A VI the model fits slightly better (remember that homogeneous field distribution is also what is assumed in the simulation model).

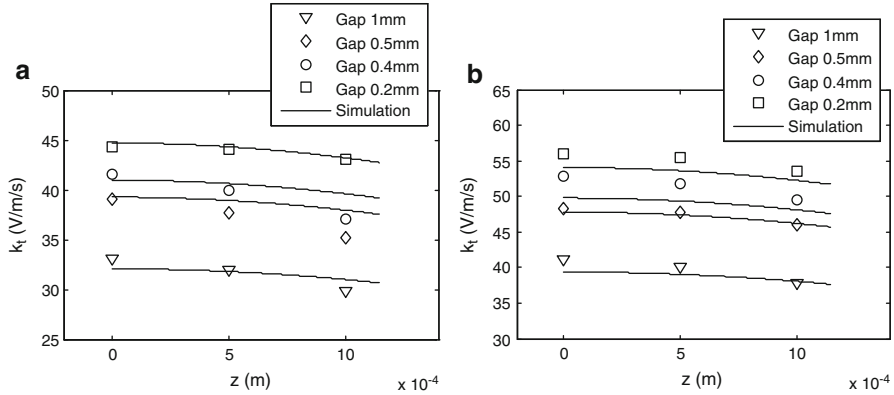


Fig. 5.12 Measured and simulated transduction factor with (a) A VIII device 1 and (b) A VIII device 2

5.3.3 Architecture A VIII

For the verification of the A VIII simulation model two different devices were assembled from magnets R2 and R3 in each case with coil 1. For both devices a 2 mm thick steel sheet is used as the back iron. The results of the measurements in comparison to the results obtained from the simulations are shown in Fig. 5.12. For given reasons (refer to Sect. 3.5.1) a static magnetic finite element analysis is used in the simulation of A VIII. The obtained accuracy is in the same range as for the “Magnet across coil” architectures A VI and A VII where the magnetic field calculation is based on Maxwell’s equation.

5.4 Conclusions

This chapter discussed the experimental verification of the simulation models. The transduction factor has been identified as the most critical parameter in the simulation. For this purpose a measurement setup to measure the transduction factor has been assembled. For each architecture several test devices were built up for the measurements using discrete components of magnets and coils. After the measurements simulations have been performed with the parameters of the test devices. The parameters which are directly available are namely the geometrical dimensions, the coil resistance and the parameters of the excitation. The number of windings has been deduced using the coil resistance and the nominal value of the resistance per meter. Moreover the residual flux density has been taken from the specification of the magnetic material. Finally the experimental and simulation results have been compared in order to verify the simulation models. It was shown that the accuracy of the simulation models guarantees that for all architectures a fair comparison of the maximum output performance was performed in Sect. 4.4.

Chapter 6

Coil Topology Optimization for Transducers Based on Cylindrical Magnets

6.1 Introduction

The previous chapters have been concerned with the optimization and comparison of eight different coupling architectures in electromagnetic vibration transducers. In summary, geometrical dimensions were found which yield to a maximum output power and output voltage, respectively. The comparison of the maximum performance limits yield the most efficient architectures which should consequently be favoured in the application whenever possible. However a basic characteristic of all the architectures (independent of the architecture class) is that the topology of the coil has always been predefined to be cylindrical. Hence the underlying optimization approach is strictly speaking a sizing optimization. Obviously this makes sense because cylindrical coils, especially made of enamelled copper wire, are state of the art and easy to fabricate. Moreover the optimized dimensions (especially for the “Magnet across coil” architecture class) show that the resulting coils are rather thin. Consequently there is not much space left for an optimization of the coil topology. But for all that an interesting question arises from this:

Is there an axially symmetrical coil topology for an arbitrary cylindrical magnet, which results in a higher output power than a cylindrical coil, and how does it look like?

To answer this question a coil topology optimization procedure was developed which is the topic of this chapter. The chapter is divided into four sections. Section 6.2 introduces the basic idea behind the topology optimization formulation strategy. Section 6.3 presents results of the output power topology optimization based on a predefined cylindrical magnet. To evaluate the performance of the topology optimized coil, architecture A II was chosen as benchmark because it performs best within the architectures based on cylindrical magnets without back iron (refer to Sect. 4.4.1). The chapter concludes with a summary and a discussion of the benefit and the applicability of topology optimized coils. Note that in spite of the previously presented sizing optimization, where the output power and the output voltage are considered separately the topology optimization focuses only on

the output power. This is because the limited construction volume condition is no more valid. However, the magnet dimensions must be predefined which results in a variable construction volume. Hence, even coil windings that are very far from a given cylindrical magnet will contribute to the overall output voltage, since the transduction factor is still greater than zero, regardless of the resistance or volume. Consequently a voltage topology optimization would result in huge coils which provide no practical advantage.

6.2 Formulation Strategy

As explained in the introduction, the aim of the topology optimization procedure is to find a coil topology which yields maximum output power based on a given predefined cylindrical magnet. The underlying magnet dimensions used here are adopted from the optimization results of A II ($R_{\text{mag}} = 6$ mm, $h_{\text{mag}} = 7.08$ mm). Moreover, the previous applied boundary conditions (Table 3.2) are still valid. The topology optimization is essentially based on four steps (Table 6.1). First, a global design domain Ω is defined around the magnet such that it is larger than the resulting design. In the calculation example the axis-symmetric design domain range from $x = 0.5$ mm to $x = 12$ mm and from $y = 3.6$ mm to $y = 14$ mm. Note that the distance between the design domain and the magnet is defined by the boundary conditions (gap size of 0.5 mm and maximum inner displacement of 1 mm). Second, the design domain is discretized into n cells. Each cell contains a number of coil windings (dependent on the cell size) which is calculated using (2.25). Third, the cells are evaluated with respect to their output power generation capability and sorted in descending order. The optimized topology is found by starting a virtual winding process which begins at the most efficient cell followed by the second best and so on. After each cell the output power is calculated. As will be shown the output power increases rapidly at the beginning of the virtual winding process. However at a certain point the output power is maximal and decreases with any further cell. At this point the virtual winding process stops and the optimal topology can be interpreted in step 4.

The most complex step in the topology optimization procedure is to evaluate the cells of the global coil design domain. In this regard the most important cell parameters are the transduction factor and the resistance. An ideal cell has a high transduction factor and a small resistance whereas cells with small transduction factors and comparatively high resistances are disadvantageous. The resistance produced by the coil windings in the cells R_{cell} is plotted in Fig. 6.1a. Because the absolute value is dependent on the cell size (discretization refinement) the values are normalized to the maximum cell resistance. The cell resistance is dependent on the total length of wire which is in turn dependent on the x -position of the cell (radius) but not on the y -position. That's why the contour lines are vertical. The generated transduction factor of the cells $k_{t,\text{cell}}$ is plotted in Fig. 6.1b. This plot shows that the windings which are closest to the pole region of the magnet contribute with the highest transduction factors. However, for quantifying the cell evaluation, it

Table 6.1 Illustration of the principal steps applied to find an optimal coil topology

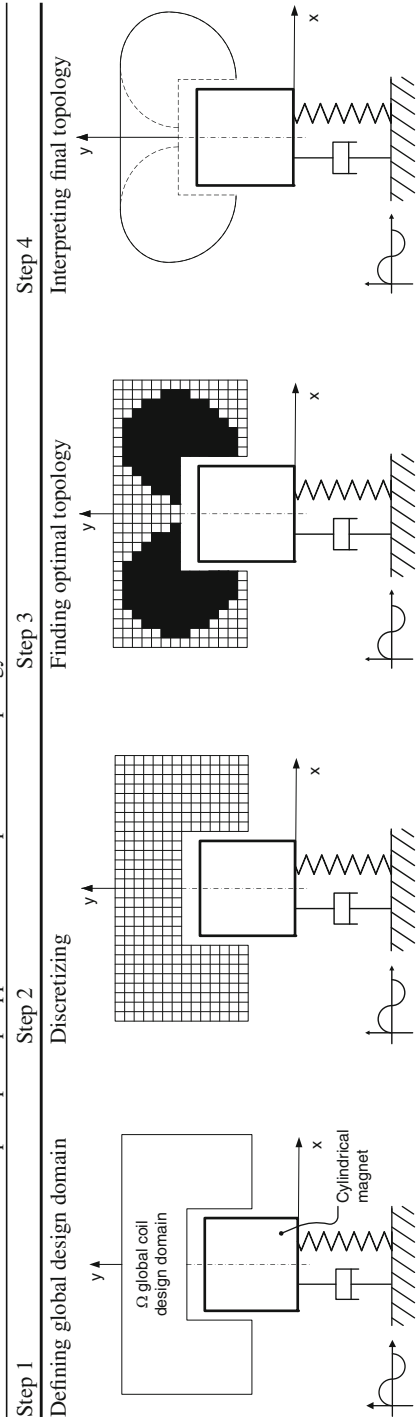
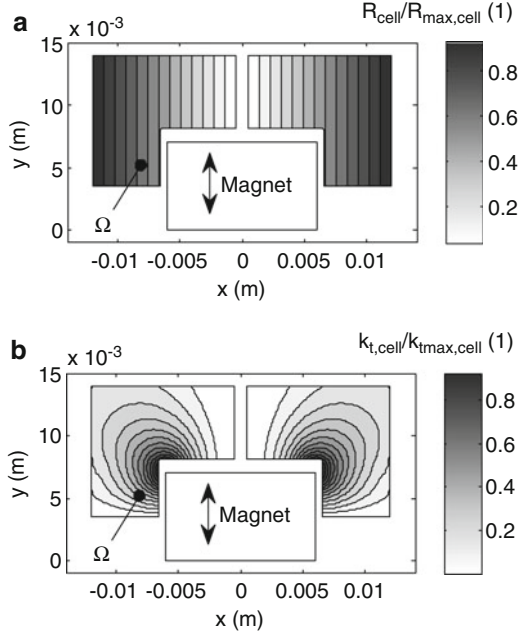


Fig. 6.1 (a) Cell resistance and (b) transduction factor of the cells in the global design domain



is necessary to know how the output power depends from the resistance and the transduction factor. Based on the analytical analyses the proportionalities of the electromagnetic damping, the optimal load resistance and the inner displacement amplitude are given by:

$$\begin{aligned}
 d_{e,cell} &\propto \frac{k_{t,cell}^2}{R_{cell} + R_{cell,opt}}, \\
 R_{cell,opt} &\propto R_{cell} + k_{t,cell}^2, \\
 Z &\propto \frac{1}{\sqrt{1 + \left(\frac{k_{t,cell}^2}{2R_{cell} + k_{t,cell}^2}\right)}}.
 \end{aligned} \tag{6.1}$$

In addition the proportionalities for the cell *emf* and the voltage divider of the cell resistance and the optimal load resistance of the cell are:

$$\begin{aligned}
 emf_{cell} &\propto \frac{k_{t,cell}}{\sqrt{1 + \left(\frac{k_{t,cell}^2}{2R_{cell} + k_{t,cell}^2}\right)}}, \\
 V_{R_{cell,opt}} &\propto k_{t,cell} \cdot \sqrt{\frac{R_{cell} + k_{t,cell}^2}{2 \cdot k_{t,cell}^2 + 4 \cdot R_{cell}}}.
 \end{aligned} \tag{6.2}$$

Fig. 6.2 Output power proportionality factor in the global coil design domain

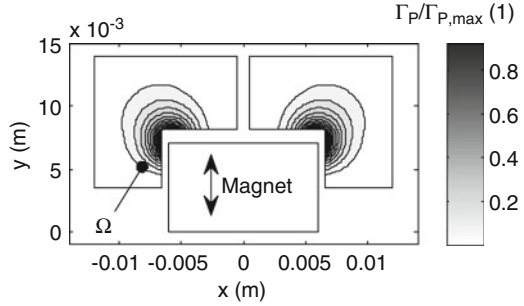
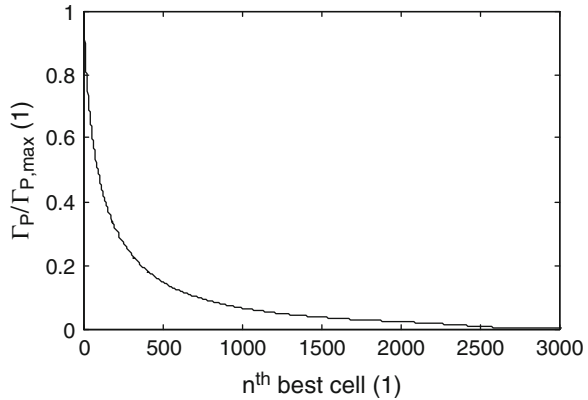


Fig. 6.3 Cells of the global coil design domain sorted in descending order with respect to the output power generation capability



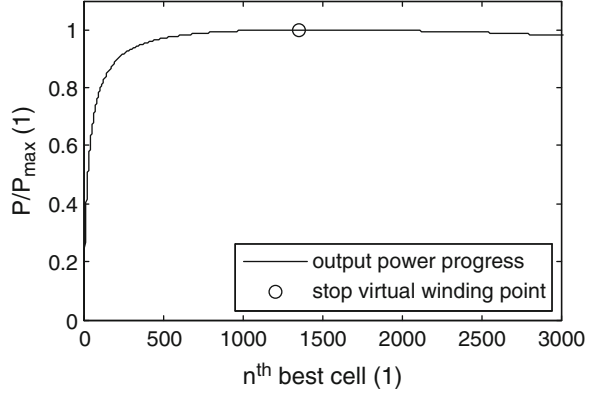
Finally the factor of proportionality for the output power is found to be:

$$P_{cell} \propto \frac{k_{t,cell}^2}{(k_{t,cell}^2 + R_{cell})} = \Gamma_P. \tag{6.3}$$

This proportionality factor is used to evaluate the output power capability of the cells. A plot of the output power proportionality factor in the global coil design domain is shown in Fig. 6.2. Due to the increasing resistance in x -direction the isolines of the output power proportionality are slightly bent to the axis of symmetry with respect to the transduction factor. Moreover the result shows that the output power capability of the cells decreases rapidly. This becomes even more apparent if the cells are sorted in descending order (Fig. 6.3).

Now that the most efficient cells in the global coil design domain have been identified the “virtual winding process” starts consequently at the best cell and goes along the cells in descending order. With the total transduction factor and the total resistance:

Fig. 6.4 Increase of the output power during the virtual winding process. At cell 1,354 the output power is maximal and the virtual winding process stops



$$\begin{aligned}
 k_{t,total} &= \sum_{i=1}^n k_{t,cell}^i \\
 R_{cell,total} &= \sum_{i=1}^n R_{cell}^i,
 \end{aligned} \tag{6.4}$$

the corresponding progress of the total output power, given by:

$$P_{total} = \sum_{i=1}^n P_{cell}^i = \sum_{i=1}^n \frac{U_{cell}^i{}^2}{R_{cell,opt}^i} = \sum_{i=1}^n \frac{(k_{t,cell}^i \dot{Z}_{cell}^i)^2}{R_{cell}^i + \frac{k_{t,cell}^i}{d_m}}, \tag{6.5}$$

is shown in Fig. 6.4. In this equation the amplitude of the oscillation velocity is given by:

$$\dot{Z}_{cell}^i = \frac{m\omega Y_{acc}}{\sqrt{(k - m\omega^2)^2 + \left((d_m + d_{e,cell}^i) \omega \right)^2}} \tag{6.6}$$

At cell 1,354 the output power is maximal. Hence the resistance of any further cell is disproportionate to the cell transduction factor. At this point the “virtual winding process” is stopped and the optimal topology can be interpreted in step 4. This is the basic idea behind the formulation strategy. A detailed discussion of the simulation results and the interpretation in step 4 is part of the following section.

6.3 Results of the Topology Optimization

6.3.1 Progress of Important System Parameters

As a basic result the progress of the output power has been used in the last section to explain the formulation strategy and to underline that there is an optimum in the output power during the “virtual winding process”. However for more detailed understanding it is necessary to know the progress of other parameters like the resistance, the transduction factor, the *emf* and the electromagnetic damping. The cell resistance is shown in Fig. 6.5. Because the “virtual winding process” starts at the pole region in the global coil design domain and goes along the circular isolines of the output power proportionality it is apparent that the cell resistance starts at a medium value and somehow swings up. However at approximately cell 2,300 the border region of the global coil design domain is reached and the cell resistance cannot exceed the limit which corresponds to the outer radius and cannot fall below the limit which corresponds to the minimum inner radius of the global coil design domain. The cumulative resistance as a sum along the cell resistances together with the optimal load resistance is shown in Fig. 6.6. According to the EDAM the optimal load resistance is obviously greater due to the additional term including the mechanical analog. The cell transduction factor is shown in Fig. 6.7. Because the highest output power proportionalities are in the same region of the global coil design domain as the highest transduction factors the transduction factor starts with the highest values and trends to decrease almost exponentially until the border region is reached and the decrease is almost linear. The cumulative transduction factor is shown in Fig. 6.8. It is apparent that this curve would converge to a horizontal asymptote if the global coil design domain would be further increased. The same characteristic holds for the corresponding *emf* and the output voltage which are shown in Fig. 6.9. This result clearly underlines the statement

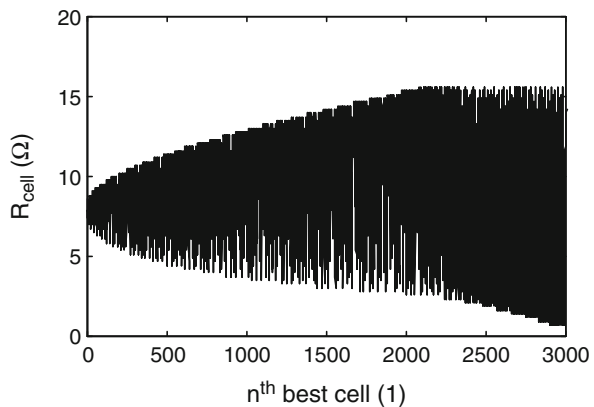


Fig. 6.5 Resistance of the cells

Fig. 6.6 Progress of the cumulative resistance and the optimal load resistance

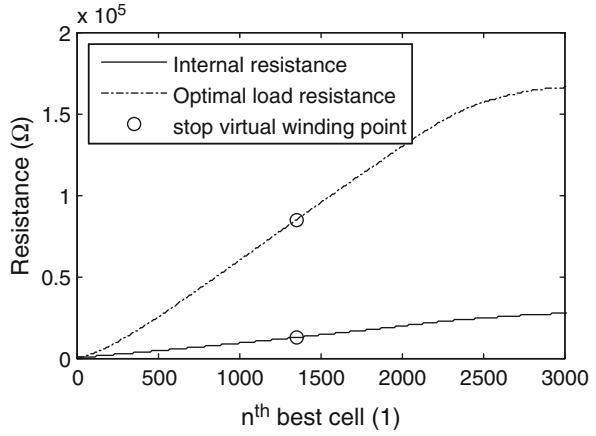


Fig. 6.7 Transduction factor of the cells

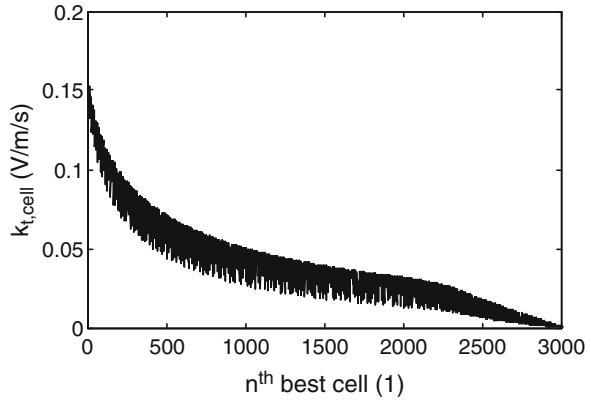


Fig. 6.8 Progress of the cumulative transduction factor during the “virtual winding” process

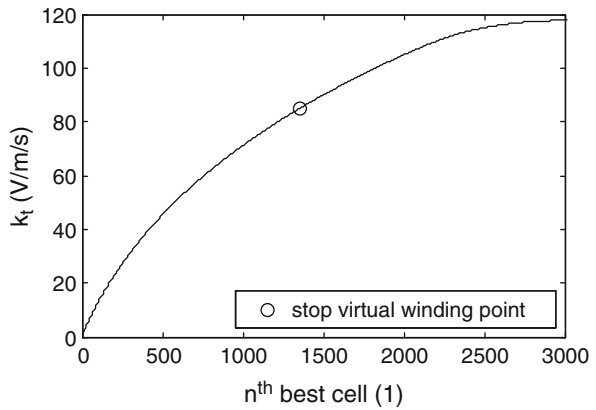


Fig. 6.9 Progress of the cumulative emf and the voltage at the optimal load resistance

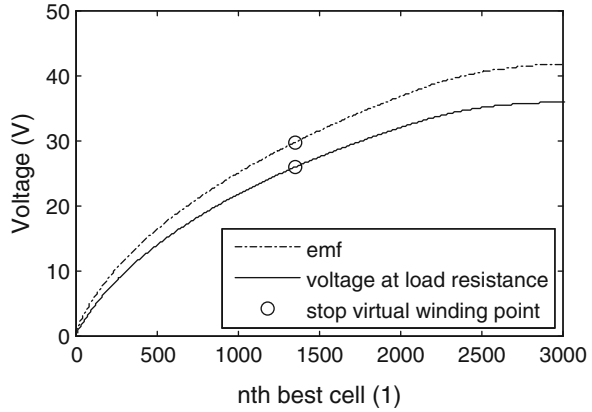
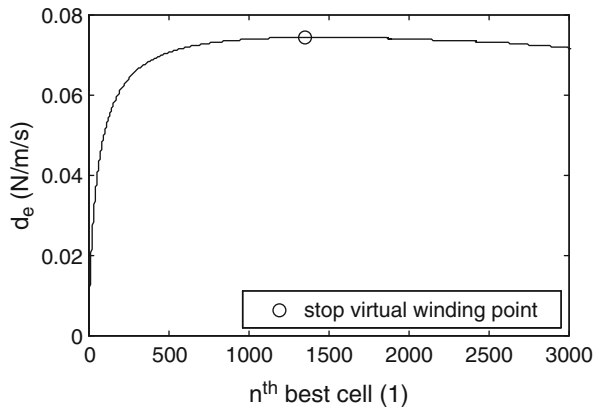


Fig. 6.10 Progress of the electromagnetic damping



mentioned in the introduction that an output voltage optimized topology does not make sense because it would result in huge coils. Another interesting result is the progress of the electromagnetic damping which is shown in Fig. 6.10. Therein the maximum is practically identical with the “stop virtual winding” point and hence also the maximum output power point. Qualitatively this result corresponds to the results from the analytical treatment (Sect. 2.4.2). The reason for this is that the construction volume in the topology optimization is not limited. Hence the seismic mass and the electromagnetic damping are independent in spite of the sizing optimization presented in Chap. 3 where the seismic mass and the electromagnetic damping are not independent (refer also to the calculation example in 2.6 where the maximum electromagnetic damping is identical with the maximum output voltage point). Finally the progress of the inner displacement is shown in Fig. 6.11. Note that the minimum inner displacement amplitude corresponds to the maximum electromagnetic damping and hence also the maximum output power point.

Fig. 6.11 Progress of the inner displacement amplitude

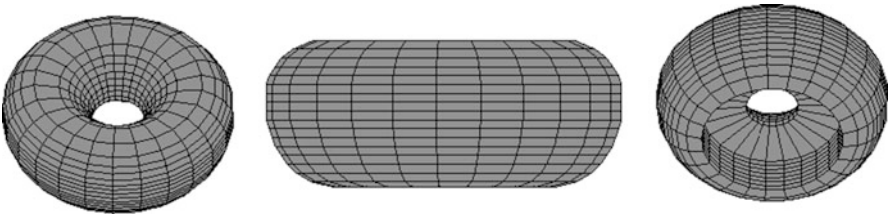
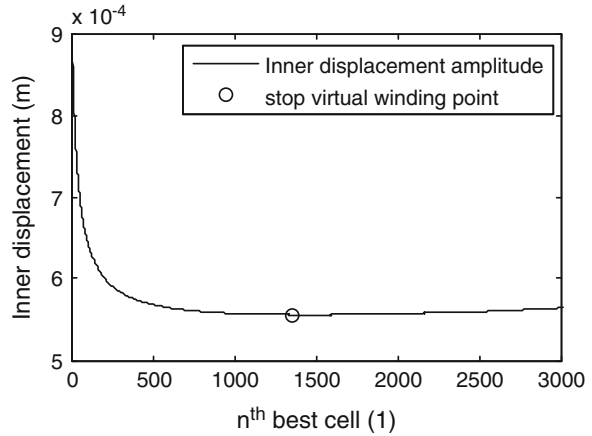


Fig. 6.12 Optimal doughnut-shaped coil topology for a cylindrical magnet. On the *right* picture the recess for the oscillating magnet is visible

6.3.2 Final Interpretation and Performance of the Optimal Topology

In the calculation example the coil topology which yields the maximum possible output power is obtained if the “virtual winding process” goes along the isolines of the output power proportionality factor and stops at the 1,354th best cell. Due to this procedure Fig. 6.2 already denotes the topology of the output power optimized coil. Nevertheless the final interpretation of the topology as a surface of revolution is shown in Fig. 6.12. The topology optimized coil looks somehow like a doughnut-shaped torus with a recess for the magnet. For the given magnet dimensions and boundary conditions this coil yields an output power of 7.89 mW. Note that with respect to the given boundary conditions no other coil is capable of generating a higher output power for the given cylindrical magnet. However the progress of the output power during the virtual winding process shows only a marginal decrease beyond the “stop virtual winding point” (Fig. 6.4). For simplification matters the optimal topology can thus be idealized to a cap like shape without an appreciable loss in the output power (Fig. 6.13). The idealized coil just encompasses the optimal coil. Another advantage of the idealization is that standard fabrication technology for coils made of enamelled copper wires can be used for the manufacturing

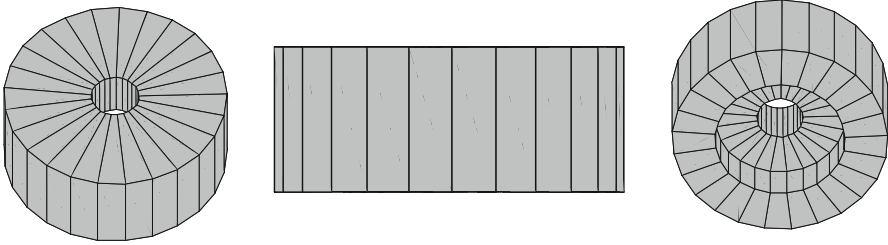


Fig. 6.13 Without an appreciable loss in the output power the optimal coil topology can be idealized to a cap like shape

Fig. 6.14 Topology optimized coils made of enamelled copper wire. The “doughnut” shaped coil (a) cannot be fabricated using batch process. The radii are rather imprecise even for customized coils. The idealized cap like coil (b) can be batch-fabricated with standard tolerances



in contrast to the “doughnut” shaped coil where the outside radii eliminate the possibility for batch process. Figure 6.14 shows a manufactured customized coil where the outside radii are nevertheless rather imprecise. With the idealized coil the output power reduces negligible to 7.85 mW. However for final evaluation of the performance it is necessary to compare the results to the previous optimization results. For mentioned reasons the benchmark for the topology optimized coil is the architecture A II. After the sizing optimization A II was capable of generating an output power of 4.39 mW (refer to Sect. 4.2.2). Hence with the topology optimization the output power can be increased by approximately 80%. In the first glance this is a considerable increase. However one has to keep in mind that A II is optimized for a construction volume of only 1 cm³. In spite of this the cylindrical construction volume which encompasses the idealized coil and the magnet at the resting position is 4.75 cm³ which is obviously higher. For a final evaluation A II has been optimized again in this larger construction volume. The result shows that for a maximum inner displacement of 1 mm the output power is 22.12 mW. Thus architecture A II is capable of generating almost three times more output power than the topology optimized coil. This is due to the fact that in the topology optimization

Fig. 6.15 The idealized optimal coil topology is as a combination of the architectures A I and A II

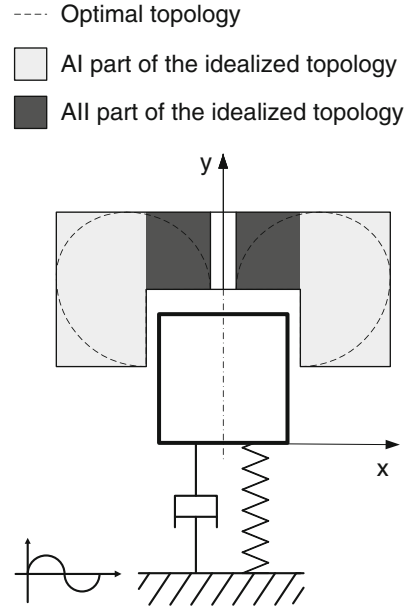
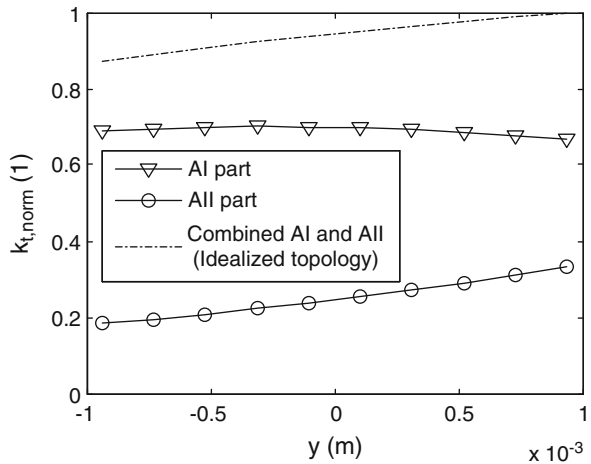


Fig. 6.16 Transduction factor of the idealized coil as a superposition of the A I and the A II part



the magnet dimensions are fixed and the construction volume is variable whereas in the sizing optimization the construction volume is fixed and the dimensions of the magnet are variable which finally results in a better output performance. For a better understanding of this conclusion it is helpful to have a look at the transduction factor. The shape of the idealized optimal coil is in principle a combination of

the architectures A I and A II (Fig. 6.15). Hence the overall transduction factor is a superposition of the separate transduction factors of the A I and the A II part (Fig. 6.16). Even though the A I part contributes with almost 75% of the transduction factor (at the resting position at $y=0$) it can finally not compensate the loss in weight and magnetic flux gradient if the volume occupied by the windings would be magnetic material. This is consistent with the outcome of the sizing optimization where A II has a considerable better output performance than A I which can be attributed to the fact that in the topology optimization the magnet dimensions are fixed and the construction volume is variable whereas in the sizing optimization of A II the construction volume is fixed and the dimensions of the magnet are variable. For construction volume constrained condition architecture A II finally performs better.

Nevertheless if the specifications in application force fixed magnet dimensions or there is unused space left after the housing of the transducer the results of the topology optimization can be used to maximize the harvested output power. However such specifications are rather untypical which limits the applicability of the topology optimization.

Chapter 7

Application Oriented Design of a Prototype Vibration Transducer

7.1 Introduction

Chapter 4 confirmed important results from the optimization approach in Chap. 3: Regardless of the considered coupling architecture there are dimensions for magnet, coil and (if existent) back iron components which result in a maximum output performance. Because there are separate optima for the output power and output voltage every electromagnetic vibration transducer can be designed either as a voltage- or a power source. Moreover there are architectures which inherently have a better output performance. These architectures should be preferred whenever possible. However, because different design constraints will apply even these architectures must be optimized for each application. Therefore, the optimization procedure developed provides a tool for the development of application oriented electromagnetic vibration transducers. To demonstrate the benefit of the optimization approach in the design process this chapter outlines the development of a prototype vibration transducer based on architecture A II. This architecture was chosen because of the simple assembly and the good voltage generation capability. However a basic drawback of this architecture is that the magnetic field is not channeled with back iron part. Hence the oscillator is sensitive against nonlinear forces generated by ferromagnetic components in the environment. Moreover, eddy currents will take place in metal components that are close to the generator reducing its power output.

The chapter is divided into five further sections. Section 7.2 introduces the basis for the development. The intended operation environment of the vibration transducer is the engine compartment of a four cylinder in-line diesel car engine. The definition of the design specifications and the most energetic resonance frequencies of the stochastic vibration source are identified in a first step. This is achieved using vibration data that has been measured in the engine compartment. The following section covers the optimization of the electromagnetic coupling architecture using the optimization approach presented in Chap. 3. The dependency of the output performance on additional parameters like the residual magnetic flux density of

the magnet, the aspect ratio and the total construction volume are investigated. Section 7.4 addresses the design of the mechanical resonator. Transient analyses based on the measured acceleration profiles are used to find the optimal spring characteristic. In this respect nonlinear hardening– and softening springs are considered as well as pure linear springs. Consequently FEA modal and static structural analyses are used for the design of the spring element. Section 7.5 covers the performance of the assembled prototypes. Frequency response measurements have been performed and the prototypes have also been tested for excitation with measured acceleration data using a field data replication function of the lab shaker set–up. Finally, the experimental results are compared to transient analyses obtained with a full system model.

7.2 Basis for the Development

7.2.1 Underlying Vibration Characteristic

The most important condition parameter for any application oriented development of resonant vibration transducers is the available vibration. The operational environment for the development considered here is in the engine compartment of a four cylinder in–line diesel car engine. More precisely the harvester is intended to convert the vibration of fluid pipes that are connected to the engine block. Of course the ideal condition for resonant vibration conversion is a well defined vibration source with constant amplitude and frequency. However the vibration characteristic of car engines depends on the load condition and changes over time. Hence the first step in the development is to find the most energetic vibration frequencies in order to define the resonance frequency of the transducer.

To understand the speed related vibration of the car engine (acceleration) measurements have been performed under various driving conditions (city, country, and highway driving route). For this purpose two different measurement points (as shown in Fig. 7.1) have been investigated using 3–axis accelerometers. A typical result of the vibration measurements during city driving route is shown in Fig. 7.2. In the spectrogram (the magnitude of the short–time Fourier transform of the vibration signal) there are three dominant vibration frequency ranges visible (marked with the dashed lines). These frequencies are correlated to the rpm of the engine. This is due to the crankshaft drive as shown in Fig. 7.3. The rotation of the crankshaft produces oscillating and rotating inertial forces. The oscillating forces can be derived using the acceleration of the piston:

$$\ddot{x} = R \cdot (2\pi N)^2 \cdot (\cos \varphi + \lambda_{cp} \cos 2\varphi), \quad (7.1)$$

where N indicates the number of revolutions per second and λ_{cp} is the ratio of the crank arm length R_{ca} to the piston rod length l_{pr} . The mass that produce oscillating forces m_{osc} is the sum of the piston mass m_p and the mass of the piston rod m_{pr} . Note

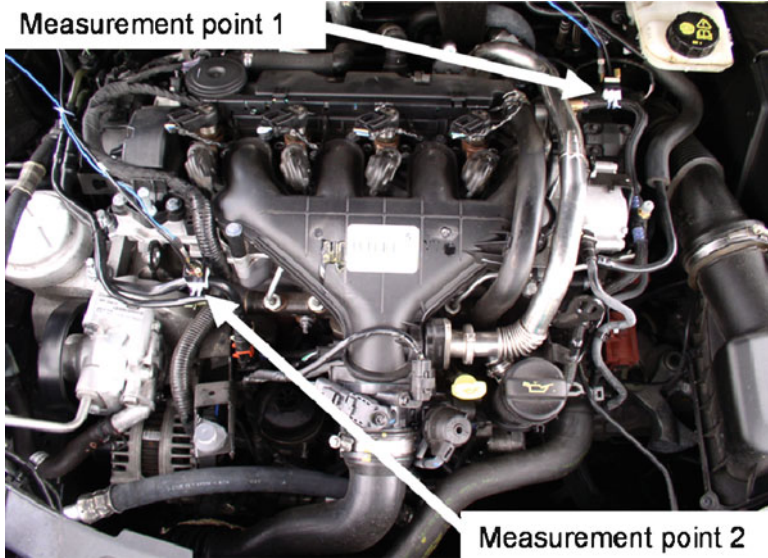


Fig. 7.1 Vibration measurements in the engine compartment of a four-cylinder in-line diesel engine

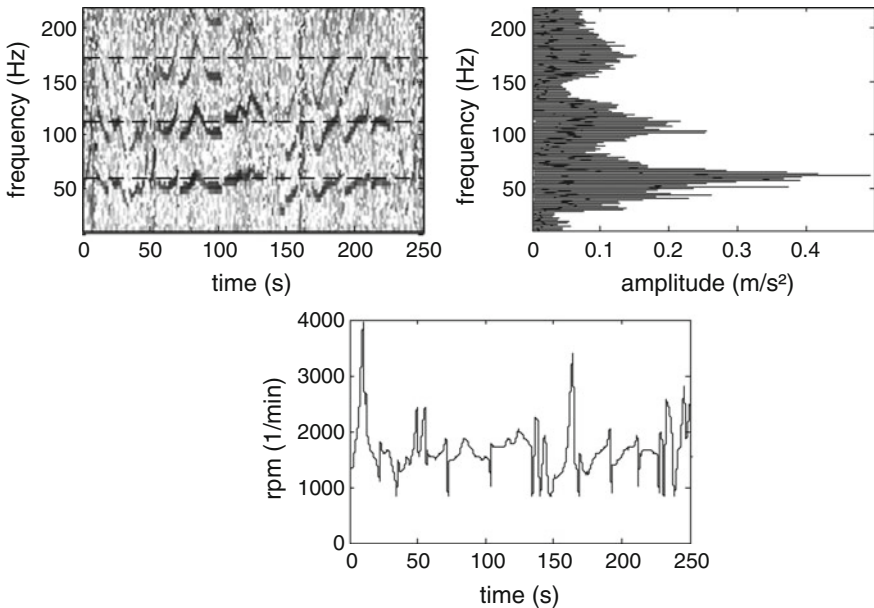
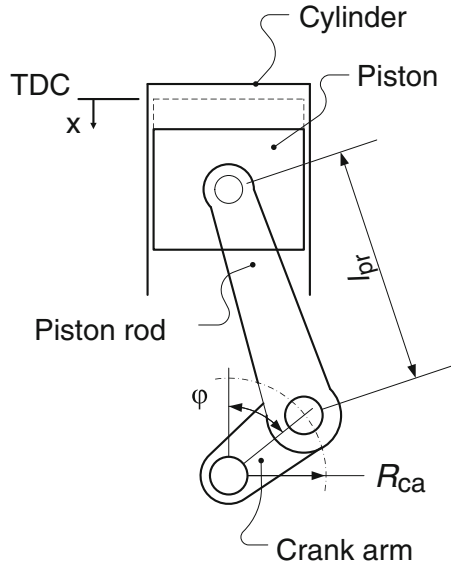


Fig. 7.2 In the spectrogram (*above left*) there are three dominant frequencies visible (*dashed horizontal lines* at about 60, 115 and 180 Hz). Consequently these frequencies are also visible in the amplitude spectrum (*above right*). The magnitude in the spectrogram is correlated to the rpm (*below*)

Fig. 7.3 Car engine crankshaft drive



that the crank arm is assumed to be balanced. Hence it does not produce oscillating forces in the first glance. Now the oscillating forces can be defined as:

$$F = m_{osc} \cdot \ddot{x} = \underbrace{m_{osc} \cdot R\omega^2 \cos \varphi}_{\text{first order}} + \underbrace{m_{osc} R\omega^2 \lambda_{cp} \cos 2\varphi}_{\text{second order}}, \quad (7.2)$$

where $\omega = 2\pi N$ is the angular speed. In this equation the inertia forces of the first and second order are apparent. Because in the considered four-cylinder engine the four pistons have a pairwise 180° phase shift (Cylinder 1 $\rightarrow 0^\circ$, Cylinder 2 $\rightarrow 180^\circ$, Cylinder 3 $\rightarrow 360^\circ$, Cylinder 4 $\rightarrow 540^\circ$) the first order terms will be compensated ($\cos \varphi = 1$, $\cos \varphi = -1$, respectively) in contrast to the second order terms which will be added. In general the lowest measurable engine order is obtained by dividing the number of cylinders by two. The revolution dependent frequency of the n th order can be calculated with:

$$f = \frac{rpm}{60} \cdot n, \quad (7.3)$$

where rpm indicates the revolution per minute. This is a simple but quite important equation because it correlates the predominant vibration frequency with the revolution per minute. The order related vibration frequencies are shown in Fig. 7.4. The frequencies of 2nd, 4th and 6th order at an rpm of about 1,600–1,700 1/min correlate with the dashed curves in the spectrogram. In order to identify the most frequent rpm of the total measured data (215 min of city, 92 min of country, and 16 min of highway driving route) a statistical evaluation has been performed. The result is shown in Fig. 7.5. Due to the traffic signals the idle speed is clearly present in the histogram. Altogether the most frequent rpm is between 1,600 and 1,700 1/min.

Fig. 7.4 The dominant frequencies in the spectrogram (Fig. 7.2) yield an rpm of 1,650 1/min

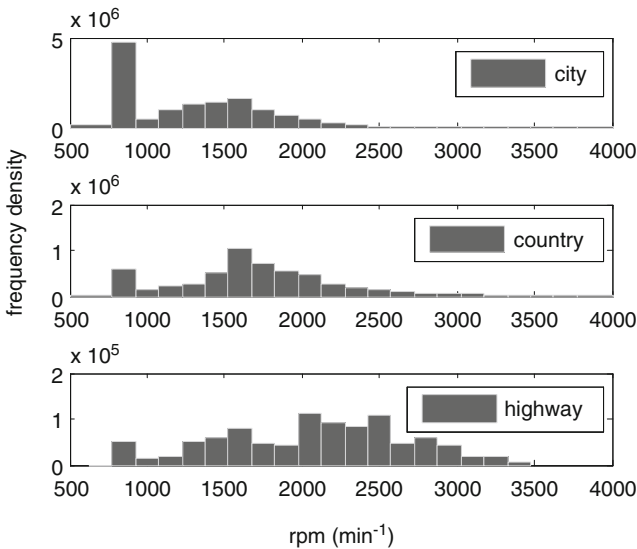
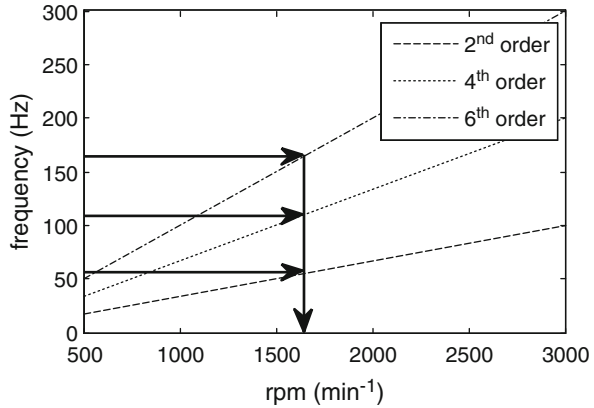


Fig. 7.5 Revolution per minute histogram for city–country–and highway driving route. In the city driving route the idle speed is dominant

According to Eq. 7.3 this corresponds to vibration frequencies of 55, 110 and 165 Hz for the 2nd, 4th and 6th order conversion, respectively. The resonance frequency of the vibration transducer should correspond to these frequencies. Beyond this fact the acceleration level at these frequencies is important to identify the most energetic resonance frequency. As indicated in Fig. 7.2 the highest acceleration level is within the 2nd engine order. The expected vibration as a mean value of the amplitudes that has been determined using discrete Fourier transform (DFT) of the measurement profiles is 2 m/s². However because the absolute value depends on the time interval where the DFT has been calculated the amplitude information is somehow delicate. It can be used as a reference value which can be significantly higher and also smaller than in reality.

Table 7.1 Specified design parameters for the optimization of the prototype electromagnetic coupling architecture

Symbol	Description	Value	Unit
<i>Geometry</i>			
V_{constr}	Construction volume	2.5	cm ³
Z_{max}	Maximum inner displacement	1.5	mm
<i>Magnet</i>			
B_r	Residual flux density	1.1	T
ρ_{mag}	Density of magnet	7.6	g/cm ³
<i>Coil</i>			
k_{co}	Copper fill factor	0.6	1
d_{co}	Wire diameter	40	μm
R'	Resistance per unit length	13.6	Ω/m
<i>Other</i>			
Y_{acc}	Excitation amplitude	2	m/s ²
f	Excitation frequency	60	Hz
d_m	Parasitic damping	0.1	N/m/s

7.2.2 Design Specifications

As already done for the optimization and comparison of the electromagnetic coupling architectures in Sect. 3.3 it is necessary to define design specifications and initial boundary conditions before the development process can be started. In this case the boundary conditions and the specifications are imposed by the application. Table 7.1 gives a summary of the used parameters. Because the previous defined boundary conditions (refer to Table 3.2) are already based on centimeter scale vibration transducers a few parameters (like the density of the magnet, the copper fill factor, the wire diameter, the parasitic damping, . . .) are still valid. However the construction volume ($h_{\text{cyl}} = 14.14 \text{ mm}$, $R_0 = 7.5 \text{ mm}$) has been slightly increased as well as the intended inner displacement limit. Moreover the operational excitation conditions (amplitude and frequency) have been adapted according to the findings of the previous section. In general an output power optimized design is requested. Moreover the focus of the presented prototype development lies on the conversion of the 2nd engine order (60 Hz). However two different spring elements will be designed which enables also the conversion of the 4th engine order (110 Hz) with the same prototype design.

7.3 Optimization of the Prototype Electromagnetic Coupling Architecture

7.3.1 Optimization Based on the Design Specifications

The approach for the optimization of the prototype electromagnetic coupling architecture is exactly the same as in Chap. 3. With respect to the underlying design

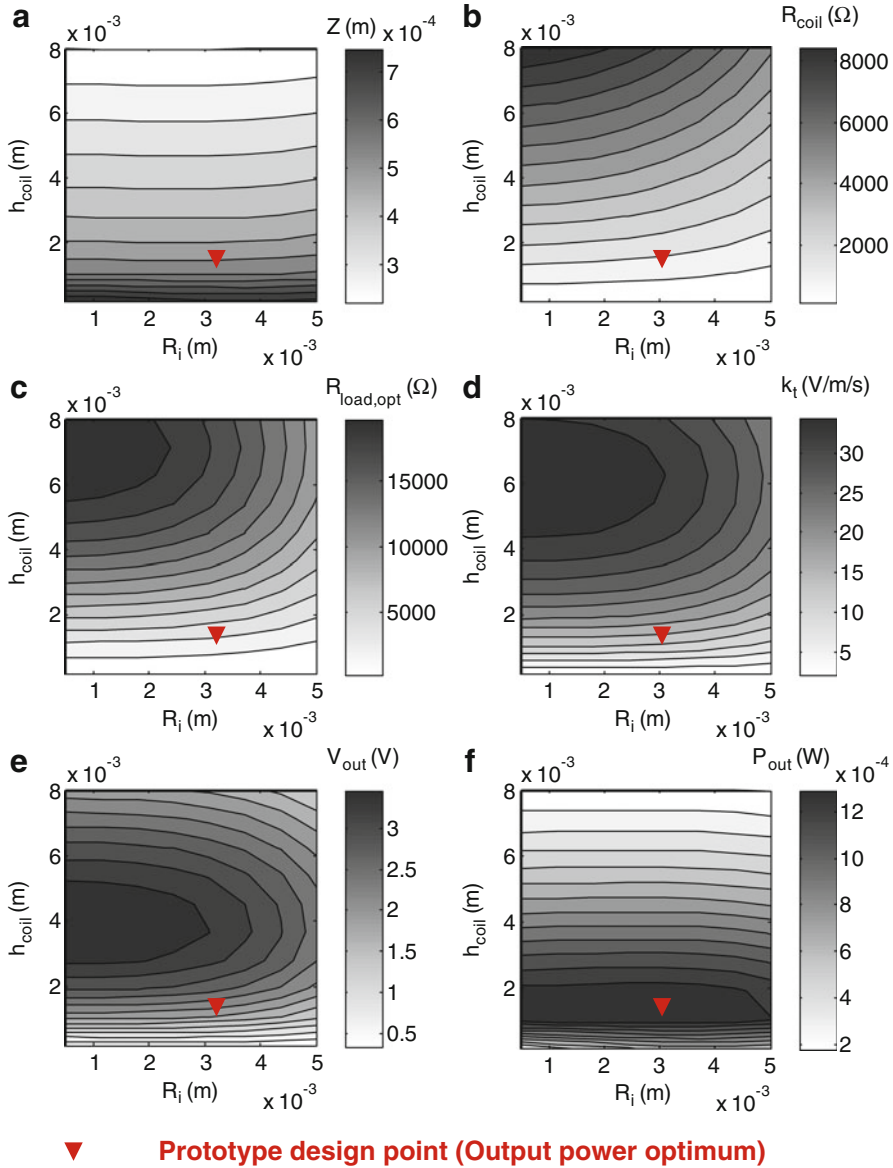


Fig. 7.6 Optimization based on the boundary conditions from application (Table 7.1). The figures shows the resulting (a) inner displacement amplitude, (b) coil resistance, (c) optimal load resistance for different dimensions of the coil. There are definitely different optimal dimensions for maximizing (d) the magnetic flux gradient, (e) the output voltage and (f) the output power

specifications and the dimensioning (as in Fig. 4.8) the results of the optimization are shown in Fig. 7.6. According to this the highest possible output power is 1.38 mW at 1.88 V for a coil with 3.07 mm inner radius and 1.70 mm height

Table 7.2 Comparison of the optimal dimensions and the dimensions that are finally used in the prototype

Symbol	Description	Optimal values (simulation)	Prototype component	Unit
R_{mag}	Outer radius of the magnet	7.50	7.50	mm
h_{mag}	Magnet height	9.57	10.00	mm
R_o	Outer radius of the coil	7.5	8.00	mm
R_i	Inner radius of the coil	3.07	3.00	mm
h_{coil}	Coil height	1.70	2.00	mm

(prototype design point). The output voltage is maximized for a coil with 0.50 mm inner radius and 3.67 mm height. With these dimensions 3.73 V can be obtained at a power level of 0.96 mW. The remaining parameter values that correspond to the optimal output power operation point can be obtained from the contour plots. Note that the resulting inner displacement amplitude for a voltage optimized design (400 μm) is smaller than for the power optimized design (560 μm). This effect is due to the volume constraint and has already been observed for the simplified model in Sect. 2.6 (Fig. 2.21). At the optimal output power point the oscillation range of the proof mass (560 μm) is about one-third of the maximal inner displacement (1.5 mm). The dimensions finally used in the prototype are based on the output power optimization results. Nevertheless they have been slightly modified in order to use standard cylindrical magnet dimensions. A comparison of the optimal values as a result of the optimization calculation and the values applied for the implementation of the prototype are given in Table 7.2.

7.3.2 Influence of Boundary Condition Parameters

In the design specifications boundary conditions have been defined which may be variable for the implementation. This section investigates the influence of these parameters on the maximum of the output power and output voltage. The first one is the aspect ratio of the cylindrical construction volume. The applied dimensions of the radius and the height yield an aspect ratio of 0.53. However, the output performance will depend on this aspect ratio. Therefore the optimization has been repeated with different aspect ratios where the maximum values of the output power and the output voltage have been recorded. The result in Fig. 7.7 shows that there are different optimal aspect ratios for the output power and the output voltage. According to this the aspect ratio used for the prototype development lies in between the optimal aspect ratio for power and voltage optimized design. Figure 7.8a–e show the results of other parameter studies where each point is the result of a separate optimization calculation. In accordance with the analytical theory the output voltage is linearly and the output power quadratically dependent on the

Fig. 7.7 There are different optimal aspect ratios for the construction volume where the output power and output voltage is maximal

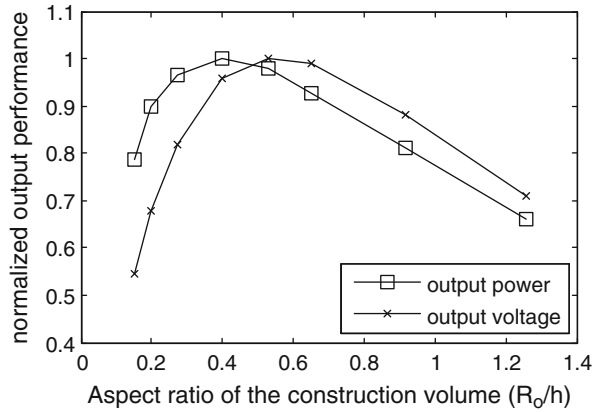


Fig. 7.8 Effect of boundary condition parameter variation on the output performance of the prototype. The diagrams show the influence of (a) the excitation amplitude, (b) the damping coefficient, (c) the wire diameter, (d) the overall construction volume and (e) the residual magnetic flux density

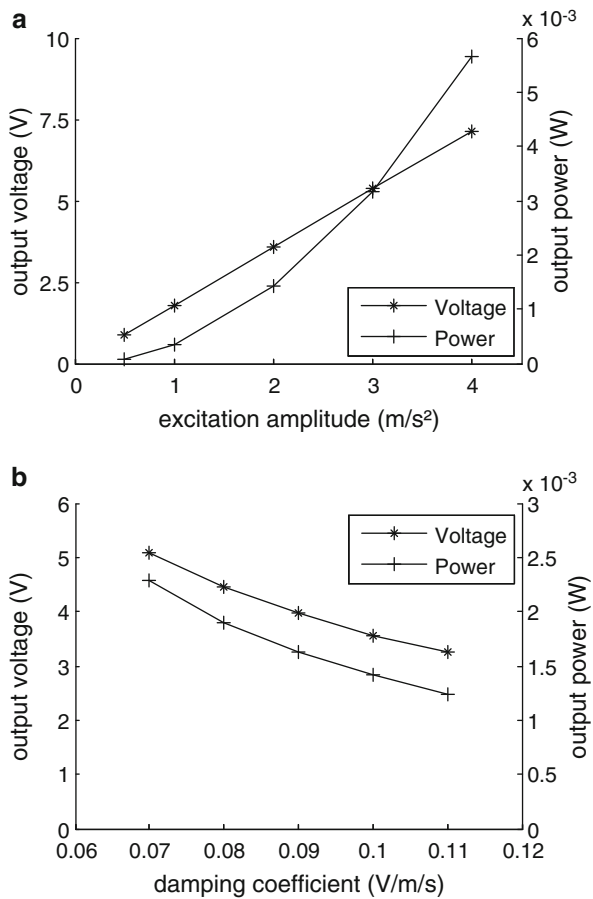


Fig. 7.8 (continued)

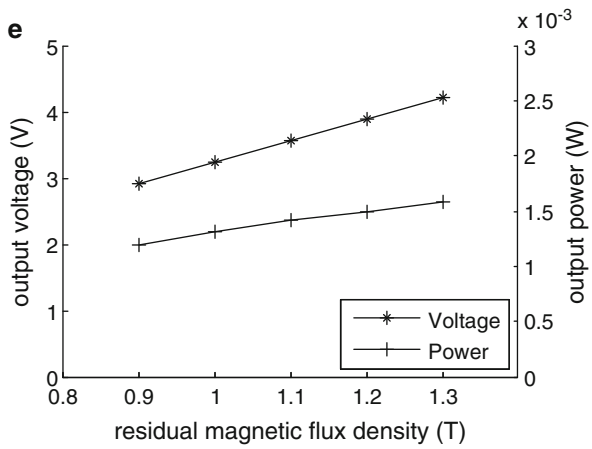
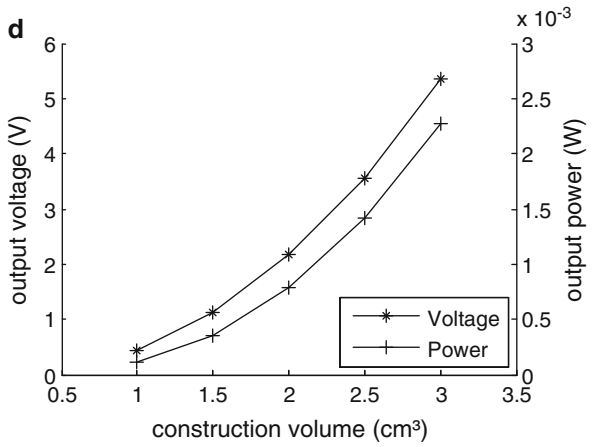
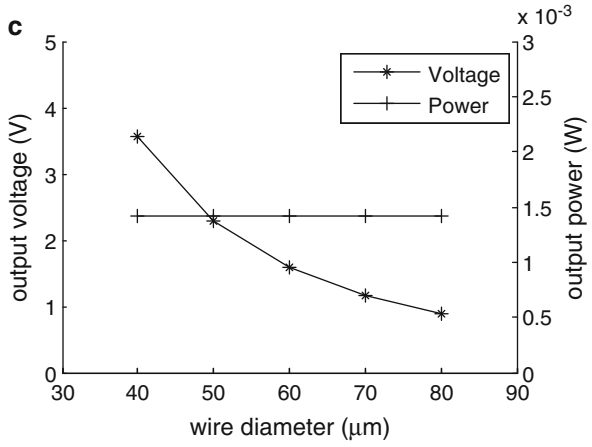
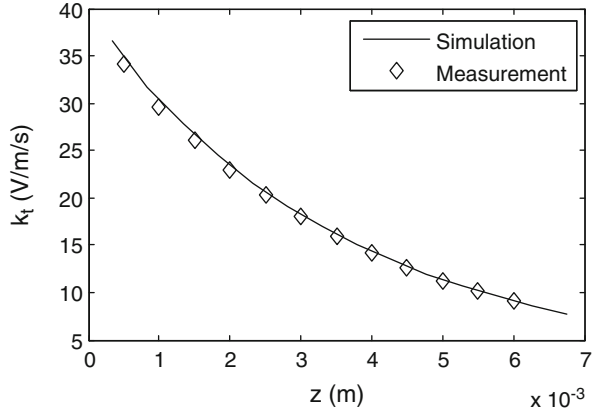


Fig. 7.9 Measured transduction factor in comparison to simulation results based on the components used in the prototype development



acceleration amplitude (a). Both the output voltage and the output power decrease with a one over x function with respect to the parasitic damping (b). Even more interesting is the influence of the wire diameter (c). Assuming a constant copper fill factor the output voltage obviously drops with larger wire diameter because the number of windings decreases. However, because the resistance decreases as well, the output power remains constant. The overall construction volume has a polynomial dependence for both the output voltage and the output power (d). Finally the influence of the residual magnetic flux density has been investigated (e). The result shows that in the typical range of NdFeB magnets the output voltage and the output power is linearly depend from the residual magnetic flux density.

7.3.3 *Experimental Characterization of the Coupling Architecture*

With the measurement setup that has already been used in Chap. 5 for the verification of the simulation models the transduction factor has been measured with the prototype components (magnet and coil). Based on the dimensions and the underlying winding process the coil has a resistance of $1,925 \Omega$ and a reactance of 789 mH . The nickel plated magnet is of grade N48 with a corresponding residual magnetic flux density of 1.38 T . The result of the measurement in comparison to the simulation is shown in Fig. 7.9. The measurement is in good agreement with the simulation results. At the resting position of the magnet ($z = 1.5 \text{ mm}$) the transduction factor is about 25 V/m/s . Later on in Sect. 7.5 this measured transduction factor function is implemented in a transient simulation model to simulate the prototype performance in application.

7.4 Resonator Design

7.4.1 Finding the Optimal Spring Characteristic

In Sect. 7.2.1 the most energetic resonance frequencies have been identified based on the order domain analysis. This information is sufficient to start the design process of the spring element. However, in addition it is interesting to investigate also the effect of a nonlinear spring characteristic on the output power of the resonant vibration transducer. This can be done by means of transient simulations. A schematic diagram of the underlying numerical model used for this purpose is shown in Fig. 7.10. A basic feature of this simulation model is that the dissipated power in the electromagnetic damping element can be calculated during transient simulations with the measured stochastic acceleration data as the excitation. Moreover the nonlinearity of the spring can be predefined and the oscillation range is limited (as it is for any application oriented device). The limitation of the oscillation range has been implemented by applying partially elastic collision at mechanical stoppers [2]. Some basic effects of mechanical stoppers can be explained using Fig. 7.11 where a transient oscillation is depicted for the case of unrestricted motion and several limited oscillation ranges. With respect to the unrestricted motion the limitation of the oscillation range results in a phase shift which increases with decreasing oscillation range. Moreover bouncing effects take place if the oscillation range is much smaller than the amplitude of the unrestricted motion. As steady state condition this must be avoided in application in order to reduce reliability problems.

Based on the order domain analyses results (Sect. 7.2.1) a resonance frequency range between 25 and 120 Hz is investigated using transient simulations with different spring characteristics. With the oscillation mass of the magnet (13.4 g) this corresponds to a spring rate from 315 to 7,600 N/m. Note that for the expected optimal resonance frequency of 60 Hz the spring rate is 1,900 N/m. The range of the nonlinearity is limited as well. The convention applied here is that the maximum

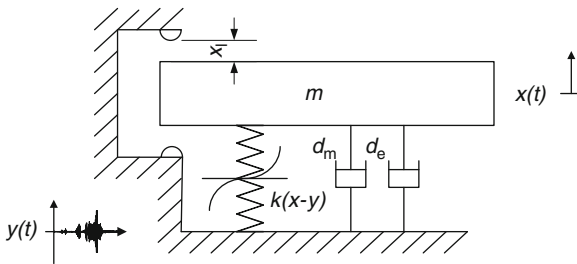


Fig. 7.10 Schematic diagram of the numerical model used for transient simulations (implemented in Matlab/Simulink®). Basic features are that the measured acceleration profile is used as the excitation, the nonlinearity of the spring can be adjusted and the oscillation range is limited by inelastic collision at mechanical stoppers

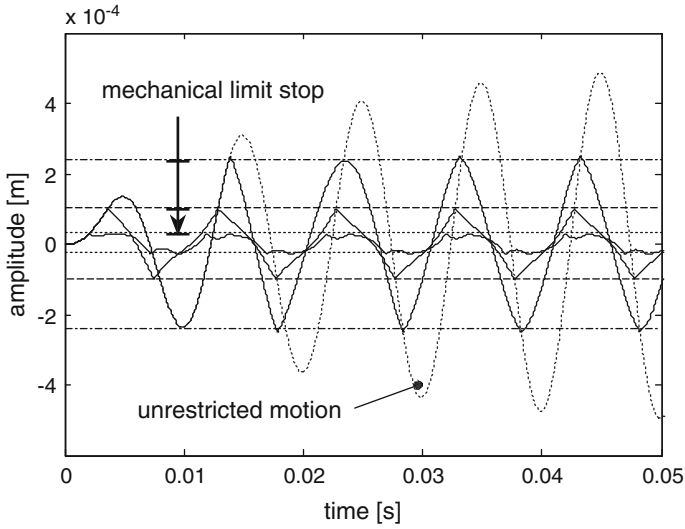


Fig. 7.11 Transient behavior of an unrestricted oscillation compared to limited oscillation ranges

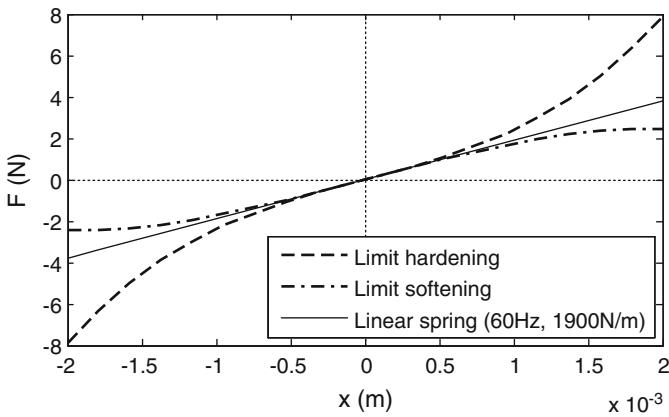


Fig. 7.12 In the simulations the nonlinearity of the spring is limited. By definition the restoring force of the hardening spring at 2 mm inner displacement is twice as much as for the linear spring and the softening spring must be monotonically increasing

restoring force of hardening springs at 2 mm internal displacement is twice the amplitude as for the linear spring and the softening spring must be monotonically increasing. For the 60 Hz respectively 1,900 N/m spring this limitation is shown in Fig. 7.12.

The simulation result for a city driving route and a displacement limit of $x_1 = 1.5$ mm is used to explain some important characteristics (Fig. 7.13). Note that for clearness the linear spring rate k on the x -axis has been converted into the

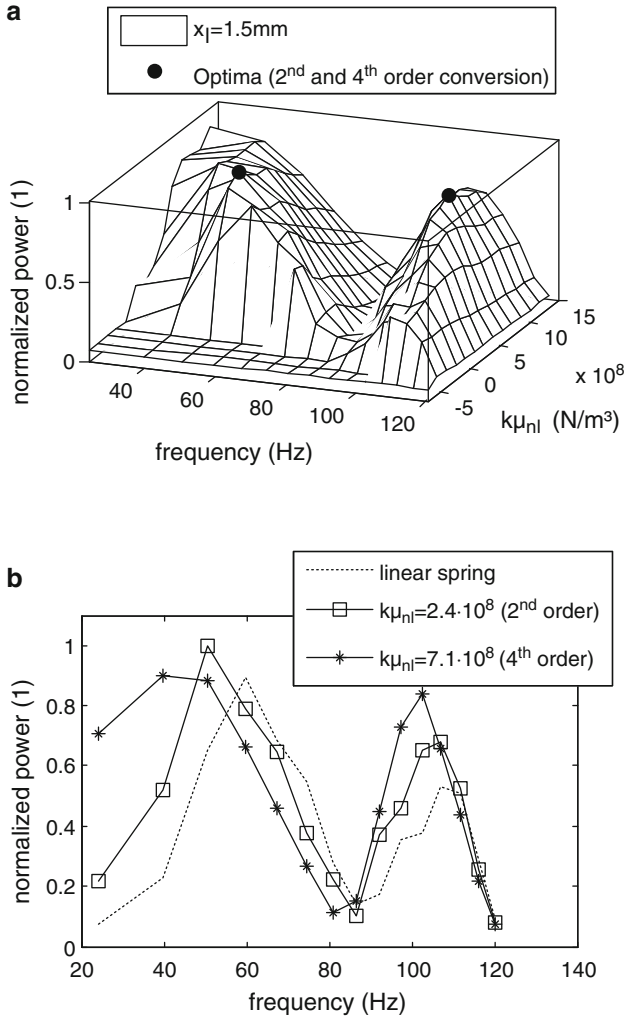
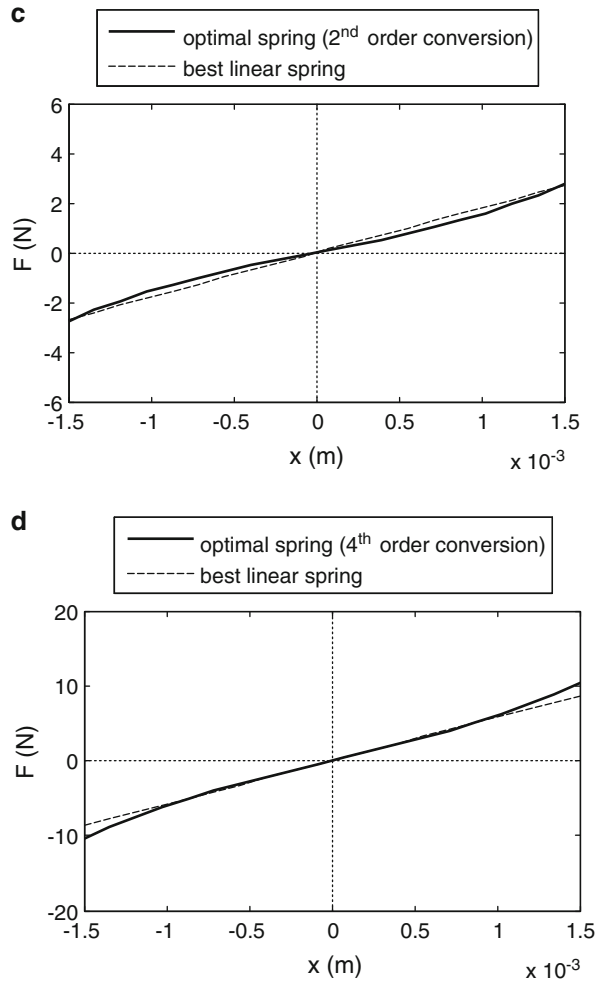


Fig. 7.13 (a) Normalized output power for an example (city driving route) excitation and different spring characteristics. (b) The output power can be increased by 10% for the 2nd and by 25% for the 4th order conversion using nonlinear hardening springs. (c) and (d) Optimal spring characteristic in comparison to the best linear springs

frequency using $f = \sqrt{k/m} / 2\pi$. Moreover the output power that corresponds to spring characteristics beyond the bounds is set to zero. First of all the 2nd and 4th engine order are clearly visible in the output power surface (Fig. 7.13a). For pure linear springs ($k\mu_{nl} = 0$) the highest output power is obtained at a frequency that correspond to the second order conversion. For both frequencies (2nd and 4th order) the output power decreases for softening springs ($k\mu_{nl} < 0$) but increases for hardening springs ($k\mu_{nl} > 0$). With respect to the 2nd order conversion this effect

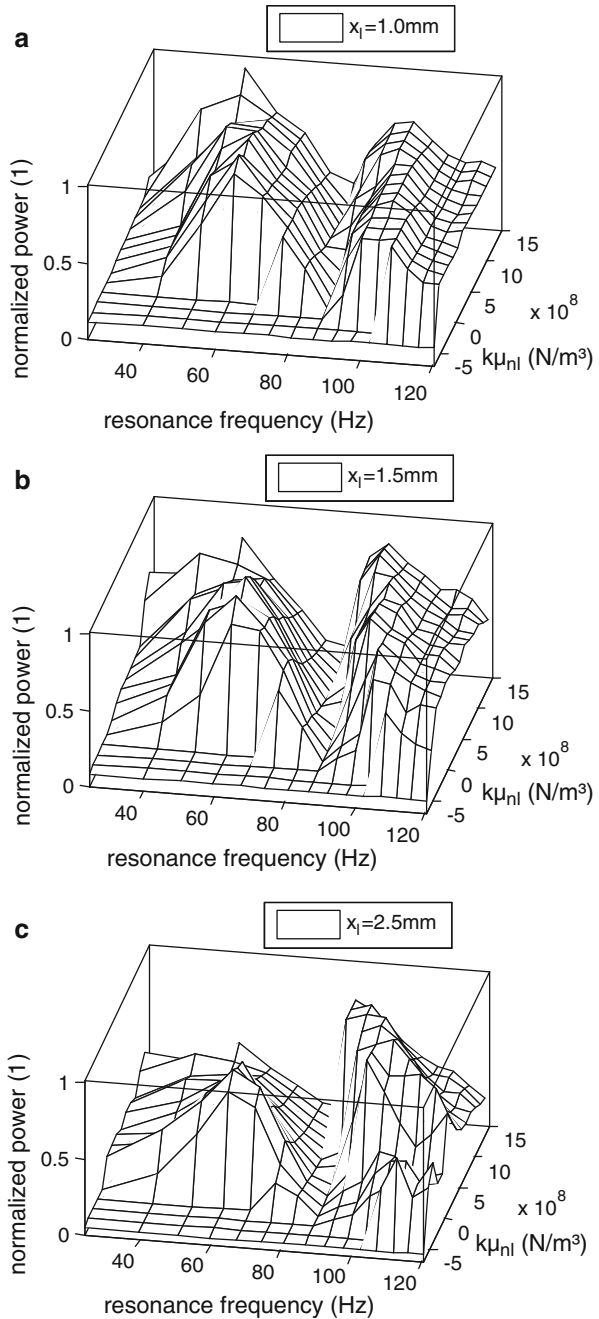
Fig. 7.13 (continued)



is marginal in contrast to the 4th order conversion. In Fig. 7.13b the output power for a linear spring and for the nonlinearity that corresponds to the optima of the 2nd and 4th order is plotted. This result shows that for pure linear springs the output power is 40% higher for the 2nd order conversion with respect to the 4th order conversion. Using nonlinear hardening springs the output power can further be increased by about 10% for the 2nd order conversion and by about 25% for the 4th order conversion. Note that in this example the output power for 4th order conversion with an optimized hardening spring is almost the same as for the 2nd order conversion with a linear spring. The spring characteristic corresponding to the optima in comparison to the best linear springs are given in Fig. 7.13c, d.

So far the inner displacement limit x_1 was used in the simulation. However, the optimal spring characteristic depends on the value of x_1 . To show the influence

Fig. 7.14 Normalized output power for different spring characteristics and inner displacement limits. The 4th order conversion increases with the inner displacement limit. Finally at 2.5 mm inner displacement the 4th order conversion become more efficient than the 2nd order conversion



simulation results of a country driving route at different inner displacement limits are shown in Fig. 7.14. Again the 2nd and 4th order are clearly distinct. The output power of the 2nd order conversion at $x_1 = 1.0$ mm is about 30% higher than for the

4th order conversion. At this point the use of nonlinear springs is not advantageous because the output power can only be increased marginally (about 5% for 2nd order conversion and 2% for 4th order conversion). For $x_1 = 1.5$ mm the efficiency of both orders are somehow equivalent and even though the benefit is still marginal nonlinear hardening springs are capable of maximizing the output power of the 4th order conversion. For further increase of $x_1 = 2.5$ mm the 4th order conversion becomes more effective (about 20%) than the 2nd order conversion. However in the simulation it is easy to apply an arbitrary inner displacement limit. In the application this value is always limited by the fatigue limit of the spring material. Altogether the investigations presented in this section lead to the conclusion that nonlinear hardening springs are capable to maximize the output power especially for the 4th order conversion and $x_1 \geq 1.5$ mm. Nevertheless the benefit is not significant and the realization of predefined nonlinear springs with high oscillation ranges evokes further challenges especially for the stiff system required for the 4th order conversion. For the development of the presented prototype it is still reasonable to focus on the 2nd order conversion with a linear system. Nevertheless Appendix C introduces an approach for the realization of predefined nonlinear hardening springs for vibration transducers based on cantilever beams.

As a final conclusion it must be pointed out that even though nonlinear springs have the potential to increase the converted output power in resonant vibration transducers there is no general advantage. To determine the capability the underlying vibration source, the desired resonance frequency and the inner displacement limit have to be taken into account and numerical transient simulations should be involved into the design process.

7.4.2 FEA Based Design of the Spring Element

In vibration transducers the resonator is primarily defined by the spring element together with the oscillating mass. The resonator assembly used here is shown in Fig. 7.15. The cylindrical magnet is placed in a pot like support (casting component). Both components create the oscillating mass which is connected to a planar spring element using ultrasonic riveting. The most essential requirements for the spring element are to provide the stiffness which yields the desired resonance frequency and to provide a preferably high oscillation amplitude without causing fatigue problems. FEA based modal- and static structural analyses have been used to achieve the correct stiffness and to determine the maximum allowable deflection. The solid model of the planar spring element (Fig. 7.16a) consists essentially of three spiral beams, a central bore hole for the magnet support and outer bore holes to provide the casting of the spring element in the housing. In the defeatured model for FEA calculations (Fig. 7.16b) the parameters height, width, length and the inclination of the beam elements define the stiffness of the CuSn6 spring element. These parameters need to be adjusted in order to achieve the desired resonance frequency. The most important material parameter is the

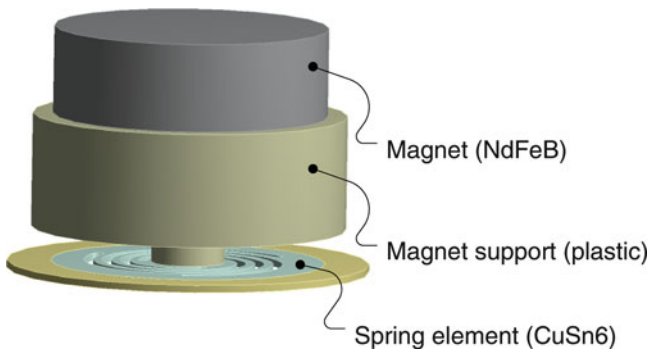


Fig. 7.15 Considered resonator assembly

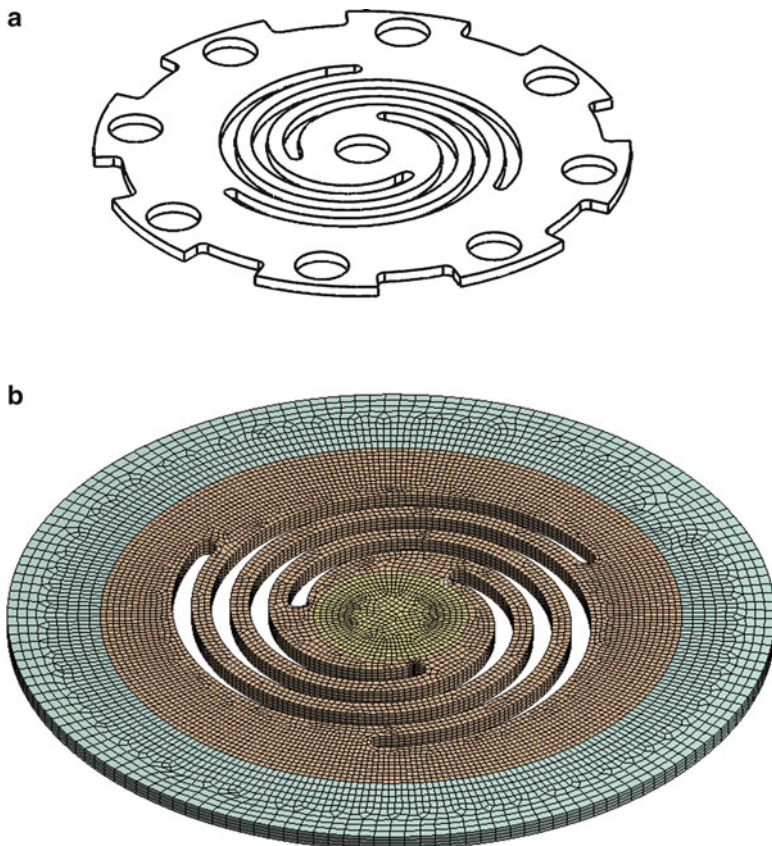


Fig. 7.16 (a) Spring element with central hole for the magnet support and with outer holes to provide the mould process. (b) Defeatured and meshed solid model of the spring element used for FEA simulations

Table 7.3 Most important material parameters of the spring material CuSn6 R550 (UNS C51900)

Symbol	Description	Value	Unit
ρ_{CuSn6}	density	8.82	g/cm ³
E	Young's modulus (at 20°C/annealed)	118	kN/mm ²
S_U	Tensile strength	550–650	N/mm ²
$R_{p0.2}$	Yield strength	≥500	N/mm ²

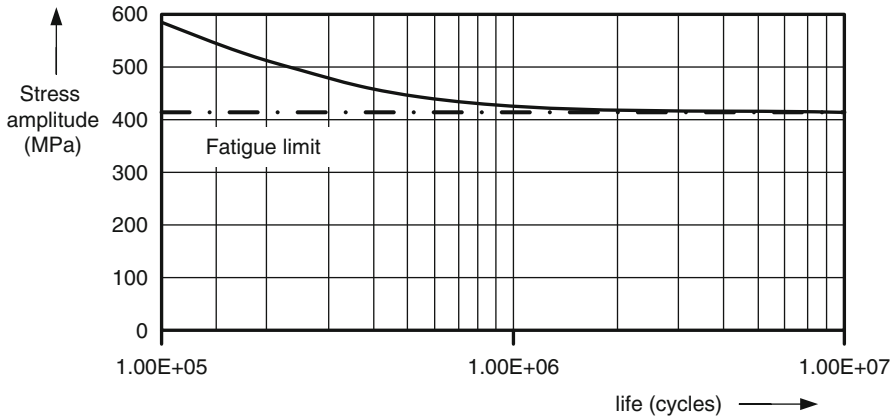


Fig. 7.17 Wöhler curve of CuSn6 R550 (UNS C51900) [10]

Young’s modulus. Further material parameters are summarized in Table 7.3. To operate below the fatigue limit of the material the maximum cyclic stress amplitude (at maximum displacement) has to be well below the Yield strength. The exact material performance is characterized in the Wöhler curve (Fig. 7.17). Based on this curve the maximum stress amplitude has to be smaller than about 410 MPa. Note that the continuous operation at 60 Hz for about half a year already results in about 10^9 cycles. Modal analyses have been performed to find a parameter set of the beam structure that yields the desired resonance frequencies. The first three modes are depicted in Fig. 7.18. Mode one and two are unwanted rotary oscillations whereas mode three is a pure axial movement which is desired for the single degree of freedom energy conversion. In principle these modes are the same for the 2nd and 4th order conversion prototype. The von–Mises stress in the spring element at the 3rd mode is shown in Fig. 7.19. The highest stress amplitudes result where the beam elements merge into the outer ring (detail view). This is the region where fatigue problems will appear first. The results of the simulated resonance frequencies beside the maximum displacement amplitudes for both prototypes are summarized in Table 7.4. At this point it is apparent that especially for the 4th order conversion prototype the system is limited by the fatigue limitation of the spring element even though the output power could further be increased for higher inner displacement limits.

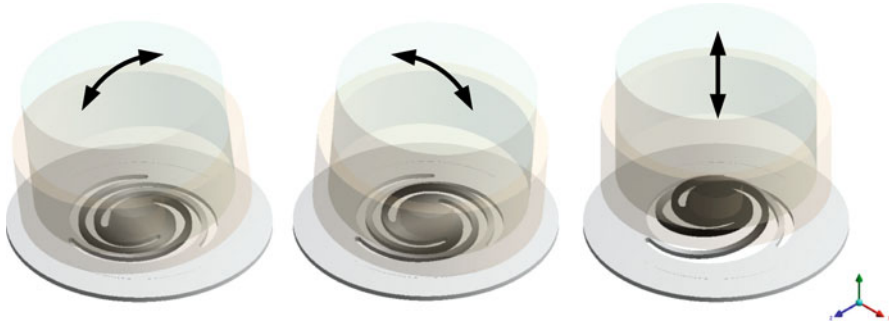


Fig. 7.18 First three modes of the resonator system. The linear oscillation of the 3rd mode is used for energy conversion

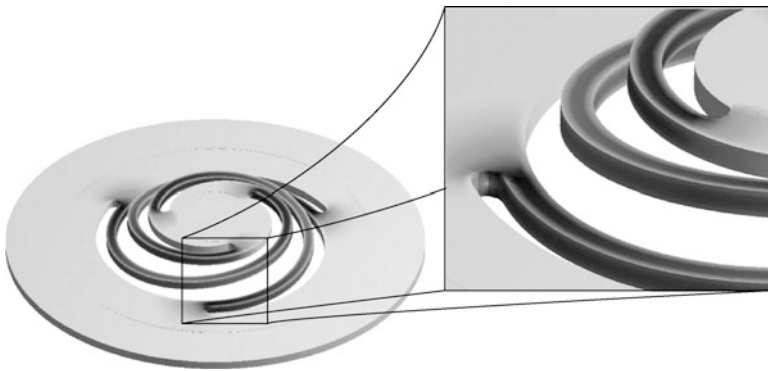


Fig. 7.19 Equivalent (von-Mises) stress in the spring element. The highest stress level results where the beam merges into the outer ring

Table 7.4 Eigenfrequencies and maximum amplitudes for operation below the fatigue limit

Spring element	1st mode (Hz)	2nd mode (Hz)	3rd mode (Hz)	Maximum amplitude (mm)
2nd order conversion	27.63	27.64	59.52	1.0
4th order conversion	43.27	43.95	102.09	0.5

7.4.3 Experimental Characterization of the Spring Element

The spring elements are manufactured using laser precision cutting (Fig. 7.20). A picture of a manufactured spring element before and after the mould process in the casing is shown in Fig. 7.21. In static measurements the force–deflection relation of ten samples of the manufactured spring elements has been measured. The results are shown in Fig. 7.22. The mean value of the spring constant for 2nd order conversion is 1,650 N/m and for the 4th order conversion 5,290 N/m. Both

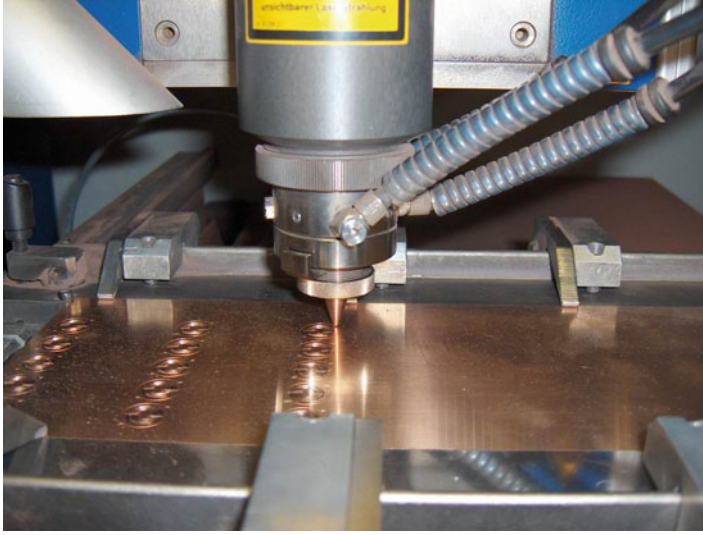


Fig. 7.20 Laser precision cutting of the CuSn6 spring element

spring types have practically a pure linear behavior in the denoted oscillation range. The deviation of the spring constant caused by manufacturing tolerances yields a resonance frequency shift in the range of ± 1 Hz. This is quite reasonable for the considered application. To proof the fatigue limitation the spring has further been overstressed by exceeding the specified oscillation range. As predicted in the FEA results fatigue problems appears at the maximum stress point (Fig. 7.23). In the prototypes this is avoided by adjusting the inner displacement limit according to the FEA results of the last section.

7.5 Prototype Assembling and Performance

The last two sections cover the design and optimization of the most basic components of the resonant vibration transducer prototype. These are namely the magnet, the coil and the spring element. The assembly of the complete prototype is based on a standard injection moulding process with an aluminium prototype casting-mould. The used material is polyamide PA 12. The design is shown in Fig. 7.24. With the spring element moulded in the casing the order of assembly is as follows:

1. First the magnet is glued into the magnet support.
2. These two components are connected to the spring element using ultrasonic riveting.
3. The coil is glued on the assembled PCB.

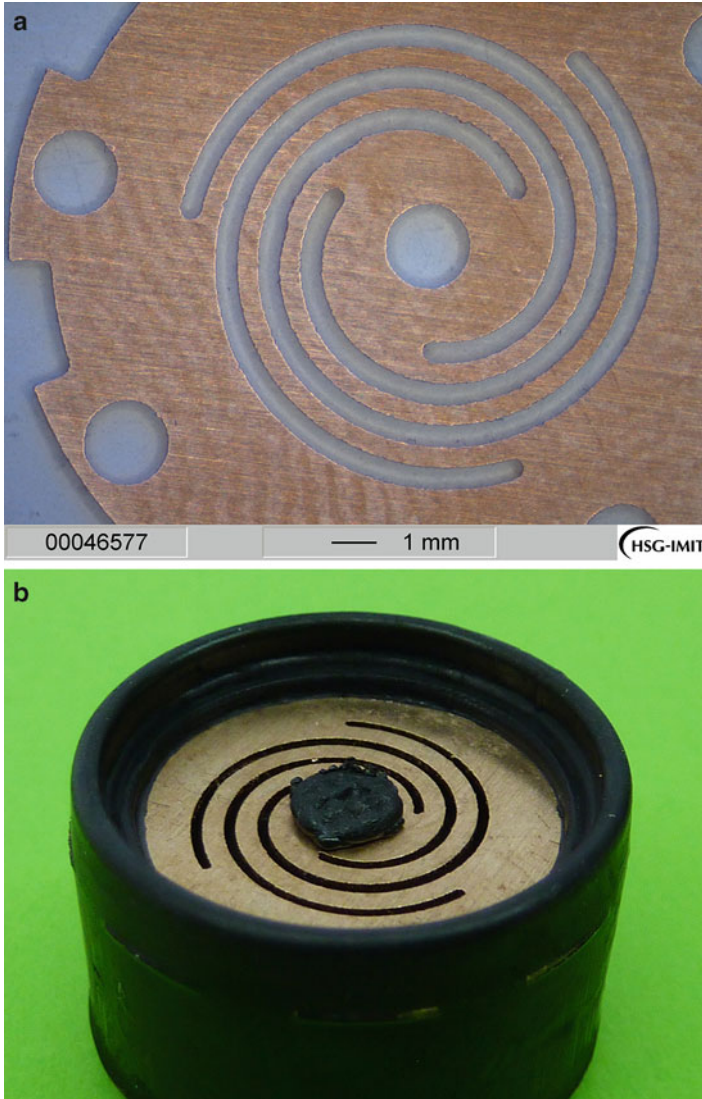


Fig. 7.21 CuSn6 spring element (a) before and (b) after the mould process. In the middle the rivet head of the magnet support is visible. The spring element in (a) is for 2nd order conversion (smaller beam width) and in (b) for 4th order conversion prototype

4. The PCB (together with the coil), the casing (with the cast-in spring and the magnet) and the spacer can afterwards be inserted into the cap.
5. Finally the base with the fixing clip is glued together with the cap. Alternatively ultrasonic welding can be used.

Fig. 7.22 Measured characteristic of the 2nd order and the 4th order conversion spring

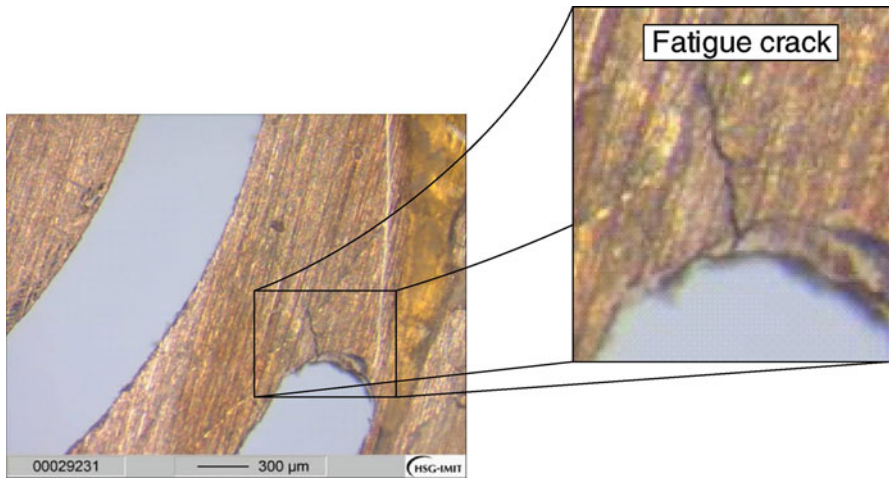
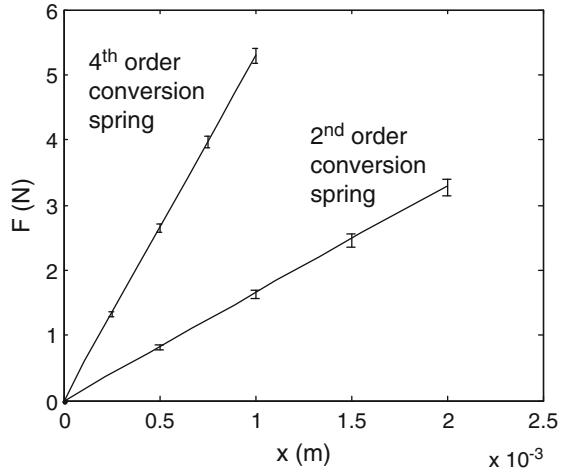


Fig. 7.23 In accordance with the FEA simulation fatigue problems appears first at the maximum stress point

Based on these steps a series of 2nd order and 4th order conversion prototypes (the only difference between the prototypes is the spring element) have been fabricated and tested. The limitation of the oscillation range is defined by the rivet head (lower bound) and the magnet support together with the spacer (upper bound). However the rivet head could not be realized as flat as expected which finally reduces the oscillation range to about 0.4 mm. As a first experimental characterization the frequency response of the prototypes mounted on a shaker setup has been measured. The results at different excitation amplitudes for the 2nd order conversion prototype are shown in Fig. 7.25 and for the 4th order

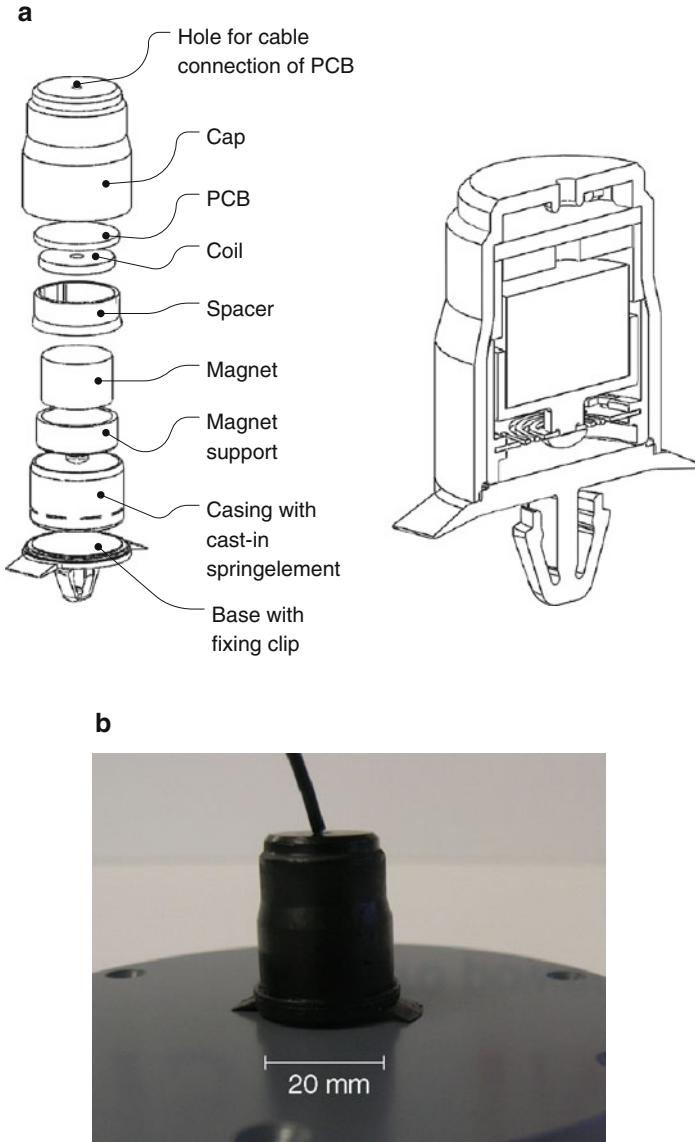
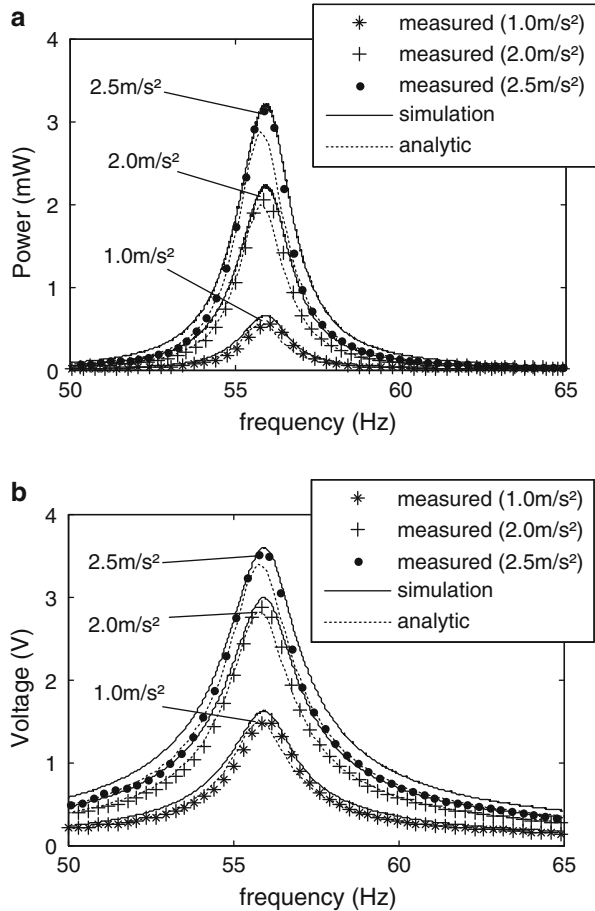


Fig. 7.24 (a) Exploded and sectional view of the prototype. (b) Photograph of an assembled device

conversion prototype in Fig. 7.26. The measured resonance frequencies (55.90 Hz for 2nd- and 107.20 for 4th order conversion prototype) are in good agreement with the prediction from the FEA (6% and 5% deviation). Note that at the specified excitation level (refer to Table 7.1) the voltage level is in the range of 3 V which

Fig. 7.25 Measured output voltage (a) and output power (b) of the 2nd order conversion prototype at different excitation amplitudes and a resistive load of 4 kΩ. The measured values are compared to results obtained from transient simulation and to analytically calculated curves



is comfortable for rectification. The power is greater than 2 mW. The simulated curves have been obtained using transient simulations. For this reason the model already used for the design of the resonator (Fig. 7.10) has been enhanced such that the electrical load circuit (pure resistive load) can be included. To perform the transient simulations the parasitic damping coefficient d_m must be specified in the first step. With the data of the measured (voltage) frequency response the combined electromagnetic and parasitic damping coefficient ($d_e + d_m$) can easily be calculated with (Fig. 7.27):

$$Q = \frac{\omega_0}{\Delta\omega} \longrightarrow d = d_e + d_m = \frac{m\omega_0}{Q} = m\Delta\omega. \tag{7.4}$$

Q is the quality factor, ω_0 the angular resonance frequency and $\Delta\omega$ the angular bandwidth (at -3 db). The pure parasitic damping coefficient can be obtained by

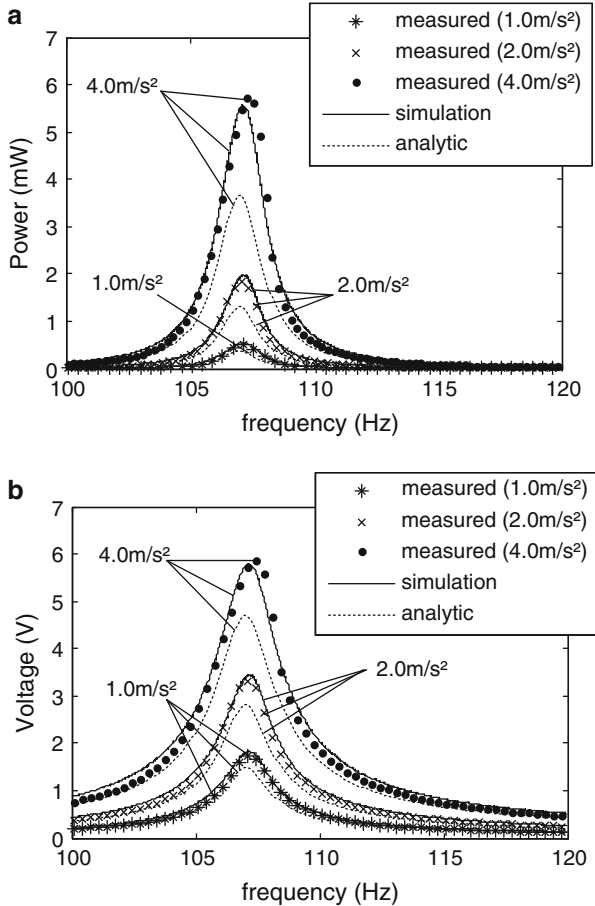
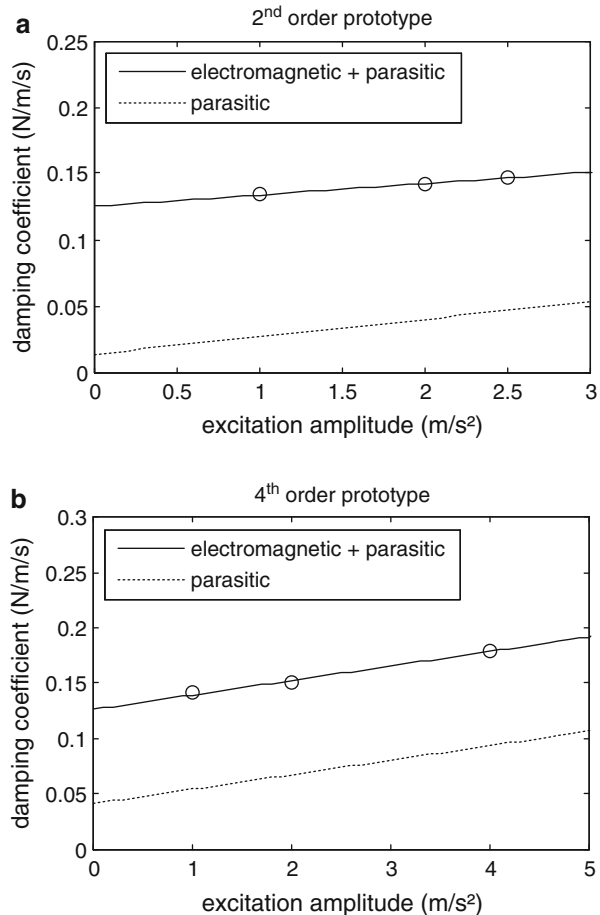


Fig. 7.26 Measured output voltage (a) and output power (b) of the 4th order conversion prototype at different excitation amplitudes and a resistive load of 6 k Ω . The measured values are compared to results obtained from transient simulation and to analytically calculated curves

calculation of d_e using (2.32). Note that due to eddy currents it is not feasible to determine the parasitic damping directly from the open circuit voltage frequency response.

Beside the damping coefficients the measured curve of the transduction factor (Fig. 7.9) has been implemented in the transient simulation model using a lookup table. As in reality this results in a nonlinear electromagnetic damping because the transduction factor depends on the position of the oscillating magnet. With the measured parameters included in the transient simulation model the simulation results are in very good agreement with the measured frequency response data and thus the transient simulation model is verified. In the next step it is adequate to assess the prototype performance for the stochastic excitation in the actual application.

Fig. 7.27 Damping coefficient of (a) prototype for 2nd – and (b) prototype for 4th order conversion. The damping coefficient depends linearly on the excitation amplitude respectively the inner displacement



In the simulation this has been done by replacing the harmonic frequency sweep function with the measured acceleration data. Typical results of the output voltage and output power at a 4 kΩ load resistance for a city driving route is shown in Fig. 7.28 and for a country driving route in Fig. 7.29. The measured values (red transparent) have been obtained with a 2nd order prototype and a field data replication using a shaker setup. Because the control unit needs some time until the shaker acceleration matches the field data acceleration the first 30 s are truncated in the measurement. Again the results of the measurement and simulation are in very good agreement. Qualitatively the high energy sequences (>1 V) in the city driving routes are smaller than in the country driving route and there are periods (up to tens of seconds) where the generated power is not easily applicable (<1 V). The mean value of the output power for all city driving routes is about 82 μW with a standard deviation of 25 μW. By increasing the inner displacement limit to the specified value of $x_1 = 1.5$ mm the mean power increases to 176 μW. For country driving routes the

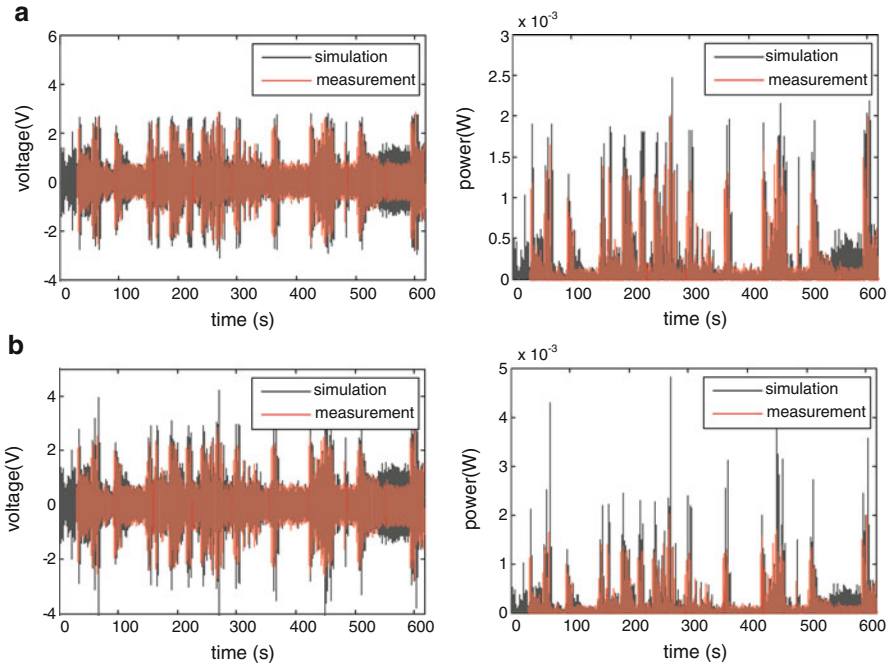


Fig. 7.28 Measured and simulated voltage and power for excitation with a city driving route vibration profile. In (a) the inner displacement limit in the simulation is set to 0.4 mm and in (b) to 1.5 mm

mean value of the output power is $143 \mu\text{W}$ with a standard deviation of $47 \mu\text{W}$. By increasing the inner displacement limit to the specified value the mean power can be increased to $321 \mu\text{W}$. The output power with the 4th order conversion prototype is significantly smaller (about 50%). The measured output power for city driving routes is $45 \pm 25 \mu\text{W}$ and for country driving routes $98 \pm 29 \mu\text{W}$.

7.6 Conclusions

To show how the optimization approach presented in Chap. 3 can be integrated into the design flow of resonant vibration transducers this chapter described an application oriented development of an electromagnetic vibration transducer. As a basis for the design the underlying vibration source (four cylinder in-line diesel engine) was characterised in the first step. Using the order domain analyses together with statistical evaluation of measured *rpm* and DFT calculations the most energetic resonance frequency was identified (60 Hz). In the next step the electromagnetic coupling architecture has been dimensioned based on specified design parameters (Table 7.1). The investigation of design parameter variations on

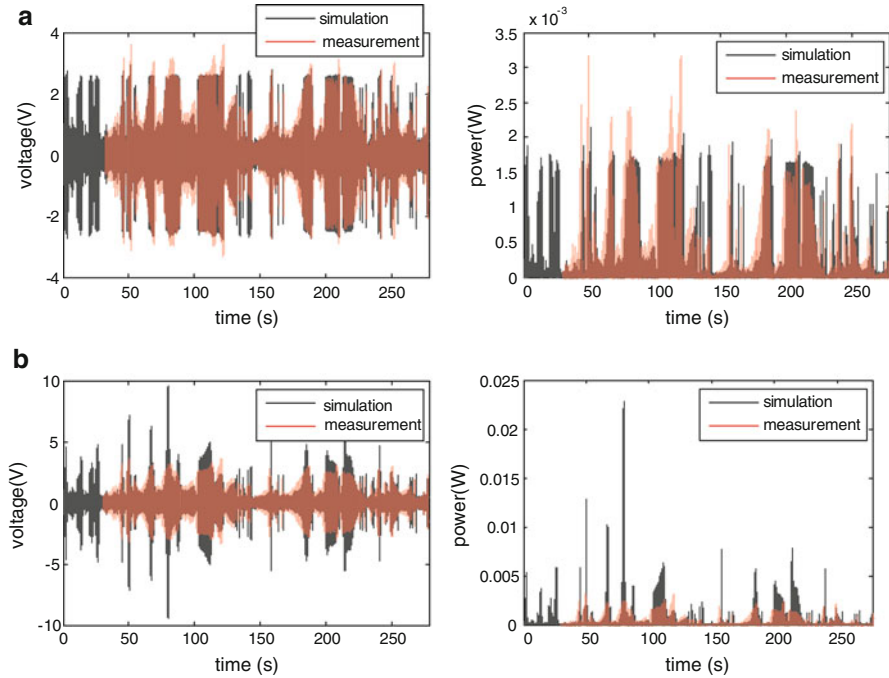


Fig. 7.29 Measured and simulated voltage and power for excitation with a country driving route vibration profile. In (a) the inner displacement limit in the simulation is set to 0.4 mm and in (b) to 1.5 mm

the output performance reveals further important dependencies. One of them is that there exists an optimal aspect ratio of the construction volume. This aspect ratio is different for voltage and power generation.

Afterwards the optimal spring characteristic has been defined using transient simulations with the measured acceleration data as excitation. It could be shown that the 2nd order conversion is more effective than the 4th order conversion. Moreover nonlinear hardening springs have the potential to increase the output power. However, to determine the capability the underlying stochastic vibration source, the desired resonance frequency and the inner displacement limit have to be taken into account. Based on these results static mechanic and modal FEA calculations have been used to design a planar spring element which was manufactured from CuSn6 using laser precision cutting. In order to avoid fatigue problems the inner displacement limit has been reduced such that the maximum stress in the spring is smaller than 410 MPa. This guarantees that the spring survives at least 10^7 cycles. The overloading of a spring element evokes crack initiation. The point where this fatigue problem emerges is in accordance with the FEA calculations.

Consequently prototype vibration transducers for 2nd and 4th order conversion have been assembled based on a standard injection moulding process.

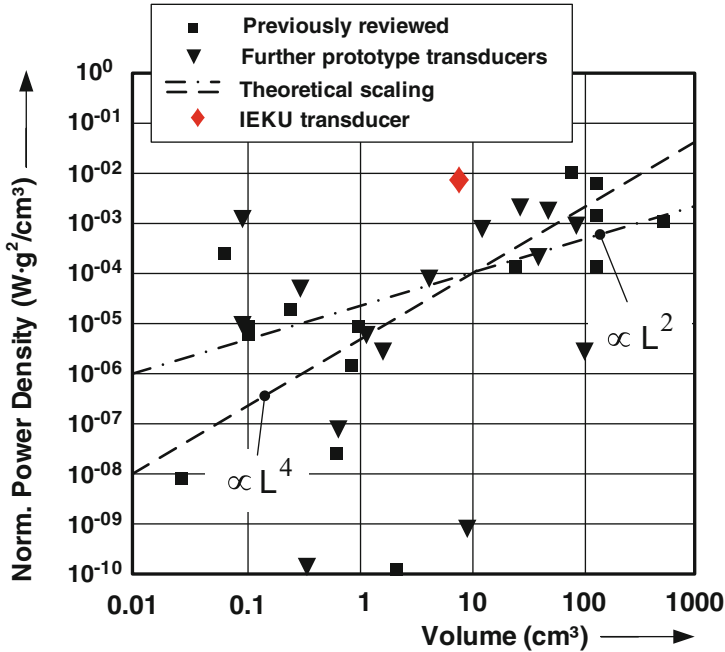


Fig. 7.30 Previously reviewed vibration transducer prototypes in [27] and transducers reviewed in this book. This figure is identical with Fig. 1.6. However the normalized power density of the prototypes developed in this book based on the presented optimization approach has been added

The prototypes have first been qualified on a lab shaker set-up with harmonic frequency sweeps as excitation. The measurement results shows that the power density of the prototype transducers developed in this book based on the presented optimization approach are among the best of the reviewed transducers in [27] and in Sect. 1.2 (Fig. 7.30). With the measured data the parasitic damping factor could be determined. Together with the measured transduction factor function the measured damping factors has been included into an enhanced transient model. Finally the simulated frequency response values are in good agreement with the measured curves. Afterwards the field data replication function of the shaker set-up has been used to assess the output performance of the transducers for the stochastic vibration as in the application. Also in this case the transient simulation model is capable to predict the measured values. In the application this enables the prediction of expected maximum values, mean values or the time periods which need to be overcome. As expected in application the 2nd order prototype definitely performs better than the 4th order prototype in the application.

Chapter 8

Conclusions

This book focused on the design optimization of application oriented electromagnetic vibration transducers. An essential part of the book considered the dimensioning of the magnet, the coil and if existent the back iron components in eight different commonly applied coupling architectures. With the established optimization procedure the optimal dimensions can be determined either for maximum output power or maximum output voltage generation. The results lead to an overall comparison of the coupling architectures. It was shown that the architectures inherently have different output power and output voltage generation capabilities. The best architectures have been identified and should be preferred in application whenever possible. An application oriented prototype development was realized to show how the optimization procedure can be integrated in the design-flow. The research in this book leads to further results which are summarized in the following.

8.1 Overview of Main Findings

In general the following conclusions can be drawn from this book:

- For the design of electromagnetic vibration transducers the task is to find optimal dimensions of the coupling architecture components (magnet, coil and if existent back iron components) rather than optimizing damping factors as stated in the analytical theory. This is due to the volume constraint condition which is the regular case in applications but has not explicitly been considered in the analytical theory so far.
- There are different optimal dimensions for maximum output voltage and maximum output power generation. Power optimization should of course be preferred except perhaps for cases where the output voltage may be too low (e.g. $<1V$ because of small construction volume, small vibration amplitudes, ...) where an output voltage optimized design is recommended.

- Many different coupling architectures have been applied in literature. The comparison of the optimized output performance (for each architecture) allows an overall comparison. There are definitely architectures which should be preferred in application because of the high output performance capability.
- Of the eight architectures investigated the one with the highest output power performance is A V. With optimized dimensions the output power can be increased by a factor of 4 with respect to the architecture with the lowest output power performance (A III).
- The architecture with the highest output voltage performance is A II. With optimized dimensions the output voltage can be increased by a factor of 1.8 with respect to the architecture with the lowest output voltage performance (A VI).
- In comparison to the architectures without back iron the investigated coupling architectures with back iron have a general advantage (especially for output power generation) and should be preferred whenever possible.
- Another advantage of back iron based architectures is that they are insensitive against unwanted nonlinear magnetic forces and eddy current losses in operation environments with ferromagnetic materials and materials with nonzero conductivity.
- Beside the optimal dimensions of the coupling architecture components there are different optimal form-factors for output power and output voltage generation.
- The established coil topology optimization can be used to define a coil which maximizes the output power for fixed cylindrical magnet dimensions. However, for the fixed construction volume condition in most applications the topology optimized coils are not advantageous. Nevertheless, if there is unused space left in the housing of the transducer the topology optimization approach can be used to maximize the output power.
- Nonlinear hardening springs have the potential to maximize the output power (up to 25% compared to optimal linear spring). For the evaluation the vibration characteristic, the desired resonance frequency and the available inner displacement limit need to be taken into account.

8.2 Suggestions for Further Work

The research results from the output power and output voltage optimization calculations as well as the design of the prototype vibration transducer presented in this book lead to several suggestions for further work that may be conducted in future. In summary, they are:

- This book considers the output performance as the optimization goal. However in the application other parameters like the packaging, power management, robustness or costs may be taken into account as well. Whenever it is proven that the output power of the vibration transducer is sufficient this leads to a multi objective optimization.

- Using transient simulations it is shown that nonlinear hardening springs have the potential to increase the output power. Moreover it is shown how nonlinear hardening springs may be realized. However, because in the end a linear spring has been implemented in the prototype development, the verification and further investigation of this result should be performed.
- In this book eight different commonly used coupling architectures have been optimized. But there are even more architectures that could be investigated. However, it is assumed that the possible increase of the output performance of further architectures is not appreciable.
- There is a great demand for the implementation of tunable devices. Based on electromagnetic conversion, these devices contain also a certain coupling architecture that may require optimization as shown in this book.
- In most of all cases it is rather challenging to provide the demanded power and voltage level even with miniaturized fine-mechanical transducers. As long as the output power is the limiting factor the reduction of construction volume is counterproductive for any application oriented development.

Appendices

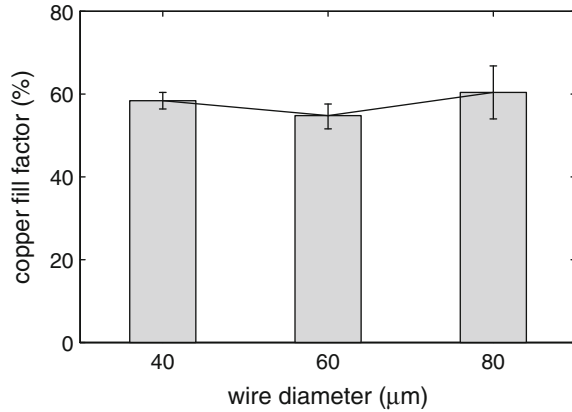
Appendix A

For mentioned reasons the copper fill factor of coils made of wire diameter smaller than 200 μm cannot be calculated theoretically [47]. Instead the value has to be determined experimentally. This has been done for coils made of different wire diameters. The parameters of the reference coils used for the measurements are summarized in Table A.1. The corresponding copper fill factor has been determined using (2.24) together with the rearrangement of (2.26). The results are given in Fig. A.1. The copper fill factor used for the optimization of the coupling architectures in this book (Table 3.2) is based on these experimental results.

Table A.1 Measured parameters of the coils used as reference to determine the copper fill factor

Symbol	Description	Coil 1	Coil 2	Coil 3	Unit
d_{co}	Wire diameter	40	60	80	μm
R_{o}	Outer radius	11.8	11.9	12	mm
R_{i}	Inner radius	5	5	5	mm
h_{coil}	Coil height	4.9	5	5	mm
R_{coil}	Resistance	1,360–1,450	2,900–3,000	530–560	Ω

Fig. A.1 Measured copper fill factor of coils made of enamelled copper wire based on IEC 60317



Appendix B

The calculation of the static magnetic field distribution is an essential part in the calculation procedure of the coupling architectures without back iron. In this book a semianalytical approach based on the vector potential model has been used. In order to verify the results static magnetic FEA calculations have been performed for different cylindrical and rectangular magnet dimensions. The comparison of the axial magnetic flux density based on the formalism presented in Sect. 3.4 and the results obtained with FEA calculations is shown in Fig. B.1 for cylindrical magnets and in Fig. B.2 for rectangular magnets. Especially for the curves beyond the pole regions (x respectively $z \geq h_{\text{mag}}/2$) the results are in very good agreement. However at the point of discontinuity the results obtained with the semianalytical calculations exceed the accuracy of the FEA calculations.

Appendix C

The results presented in Sect. 7.4.1 shows that nonlinear hardening spring have the potential to maximize the generated output power of a vibration transducer. Actually one way to implement nonlinear hardening springs has already been presented in Sect. 1.2 where the repelling force of opposite polarized magnets has been used. Another approach for vibration transducers based on cantilever beams considers the reduction of the effective beam length during the oscillation using a shaped profile Fig. C.1a (also suggested in [66]). With the shape of the profile the specified hardening characteristic can be adjusted. In the presented approximation procedure the profile is a linear interpolation of i suspension points (Fig. C.1b). The distances x_i and y_i need to be determined such that the specified and resulting spring characteristics are in accordance. The underlying model for the calculation of the

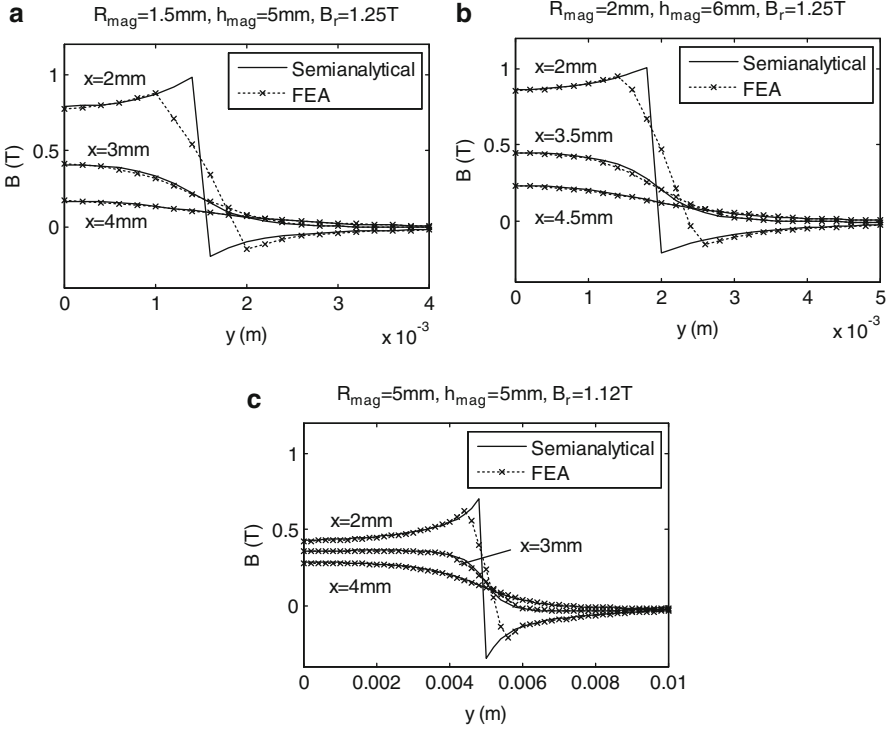


Fig. B.1 Comparison of the axial magnetic flux density (B_x) of different magnet dimensions (a–c) calculated with the semianalytical approach based on the vector potential model and static magnetic FEA

shape is based on a cantilever beam with a fixed end and a single suspension point with an offset in the y -direction (Fig. C.2). Using the direct stiffness method (DSM) the beam deflection curve for $x < x_i$ can be found to be:

$$y_1(x) = -\frac{F(l-x_i)x^2}{4EI} + \frac{1}{4}\frac{F(l-x_i)}{EIx_i}x^3 + \frac{1}{2x_i^3}(3lx^2 - x^3), \quad (\text{C.1})$$

and for $x > x_i$:

$$y_2(x) = y_i + \left(\frac{F(l-x_i)x_i}{4EI} + \frac{3y_i}{2x_i}\right)(x-x_i) + \dots + \frac{F}{6EI}(x-x_i)^2(3l-2x_i-x), \quad (\text{C.2})$$

where F indicates the force at the end of the cantilever, E indicates the Young's modulus of the beam material and I indicate the moment of inertia. The force which causes the deflection y is given by:

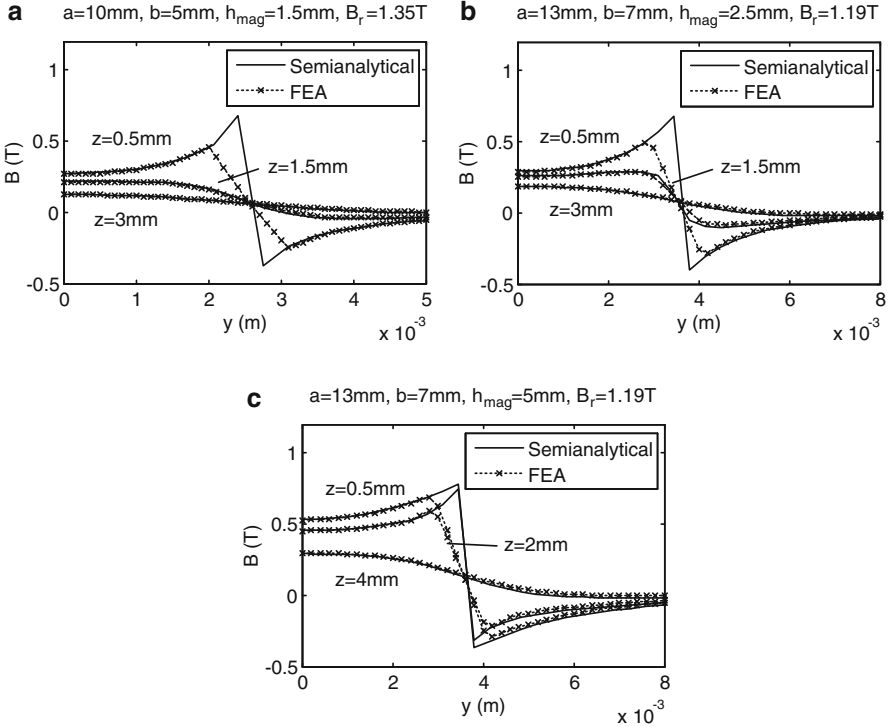


Fig. B.2 Comparison of the axial magnetic flux density (B_z) of different magnet dimensions (a–c) calculated with the semianalytical approach based on the vector potential model and static magnetic FEA

$$F = -6EI \frac{(y_i x_i - 3y_i l + 2yx_i)/x_i}{(x_i - l)/(-5x_i l + x_i^2 + 4l^2)}. \quad (\text{C.3})$$

As a calculation example Fig. C.3a shows a nonlinear hardening characteristic to be realized with the method described in this Appendix. In the first step the spring characteristic in the first quadrant is piecewise linear interpolated with i equidistant points (at equally spaced $\Delta y = 0.2$ mm). This yields a vector containing linear spring constants $K = [k_0, k_1, \dots, k_n]$. The first spring constant k_0 (942 N/m) must be provided by the cantilever beam itself without a suspension point. With the parameters of Table C.1 the beam length becomes:

$$l = \sqrt[3]{\frac{3EI}{k_0}} = 20.37 \text{ mm}. \quad (\text{C.4})$$

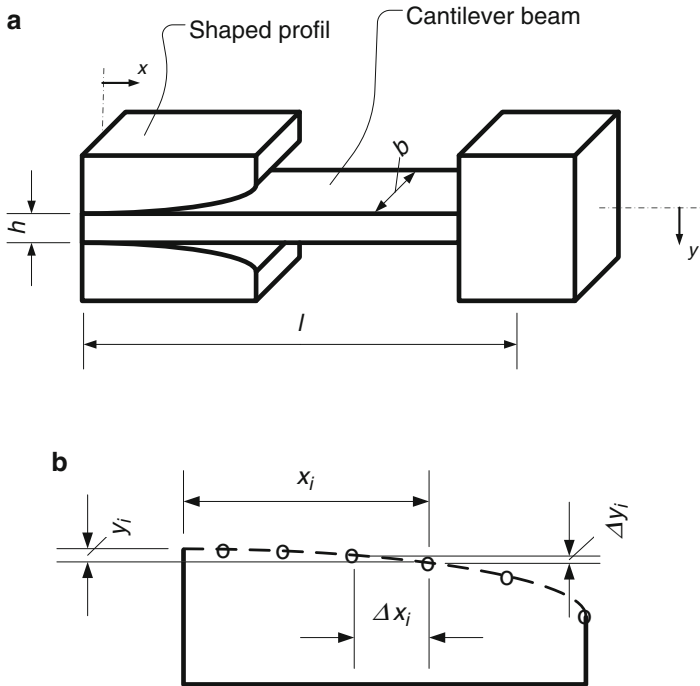
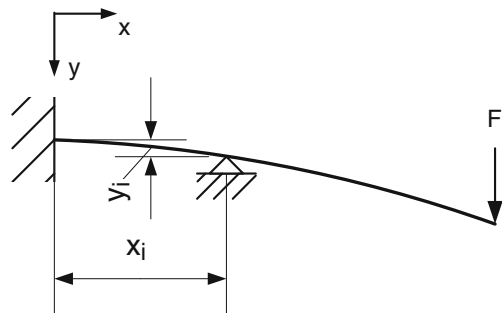


Fig. C.1 (a) Nonlinear hardening spring realized with a cantilever beam clamped between two blocks. With the shape of the block profile the nonlinearity can be defined. (b) The shape of the block is an interpolation of i non equidistant suspension points

Fig. C.2 The underlying model for the calculation approach is based on a cantilever beam with a single suspension point. The suspension point has an offset in the y -direction



In the next step the remaining spring constants (k_1, \dots, k_n) are assigned to particular distances (x_1, \dots, x_n) of a single suspension point using:

$$k_i = \frac{1}{\left(x_i(l - x_i)^2 / 4EI\right) + \left((l - x_i)^3 / 3EI\right)}. \tag{C.5}$$

Fig. C.3 (a) The specified nonlinearity is divided into piecewise linear functions. (b) The spring constant can be assigned to a distance x_i between the fixing point of the cantilever and the suspension point

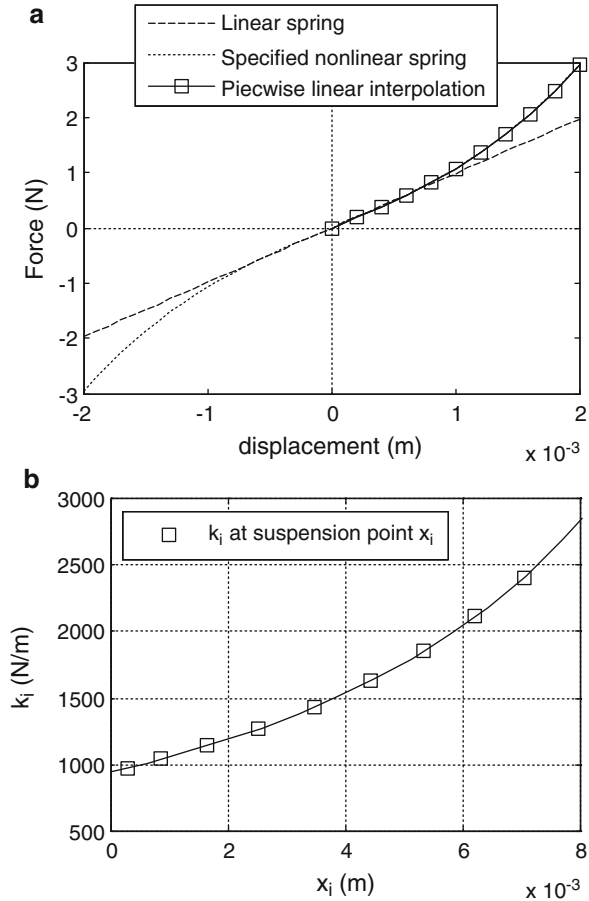


Table C.1 Underlying parameters for the calculation of the shape profile

Symbol	Description	Value	Unit
E	Youngs modulus	118	GPa
h	Cantilever beam height	0.3	mm
b	Cantilever beam width	10	mm
m	Oscillating mass	10	g

In this step y_i is set to zero which results in an appropriate approximation because the deflections are very small. The result of this step is shown in Fig. C.3b. The shape of the profile is found by following the flow chart in Fig. C.4. This has been done with and without the influence of gravity. The resulting block shapes are shown in Fig. C.5. Note that the axes of the diagram have a different scaling. For the predefined characteristic the shape is rather flat. The last point of the shape has the coordinates $P_9 = (7.049, 0.151 \text{ mm})$. In general the higher the nonlinearity

Fig. C.4 Flow chart of the block shape calculation

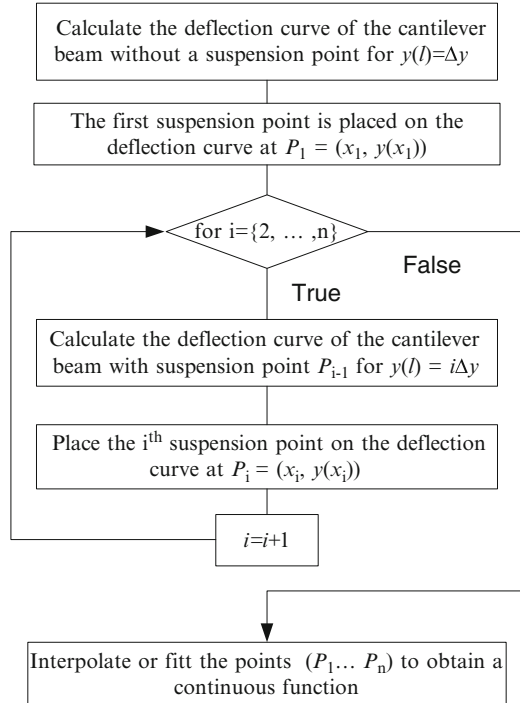
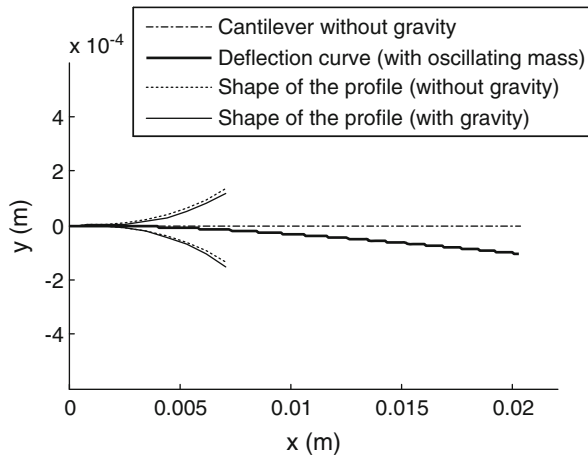
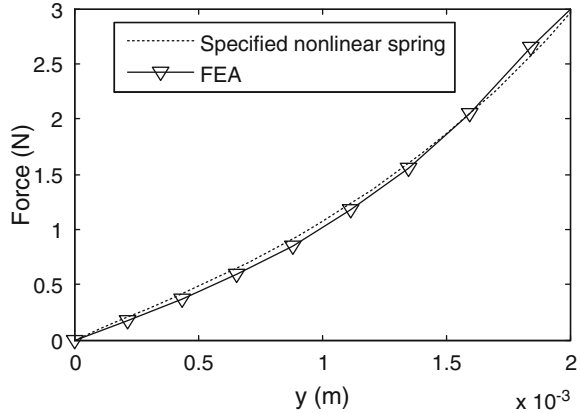


Fig. C.5 Shape of the block for the specified nonlinear spring characteristic



the flatter the block shapes. To verify the approach 2–dimensional static mechanic FEA calculations have been performed where the spring characteristic have been calculated based on the calculated block shape. The results are in good agreement (Fig. C.6).

Fig. C.6 Specified nonlinearity in comparison to FEA simulation of the spring characteristic based on the calculated block shape



Appendix D

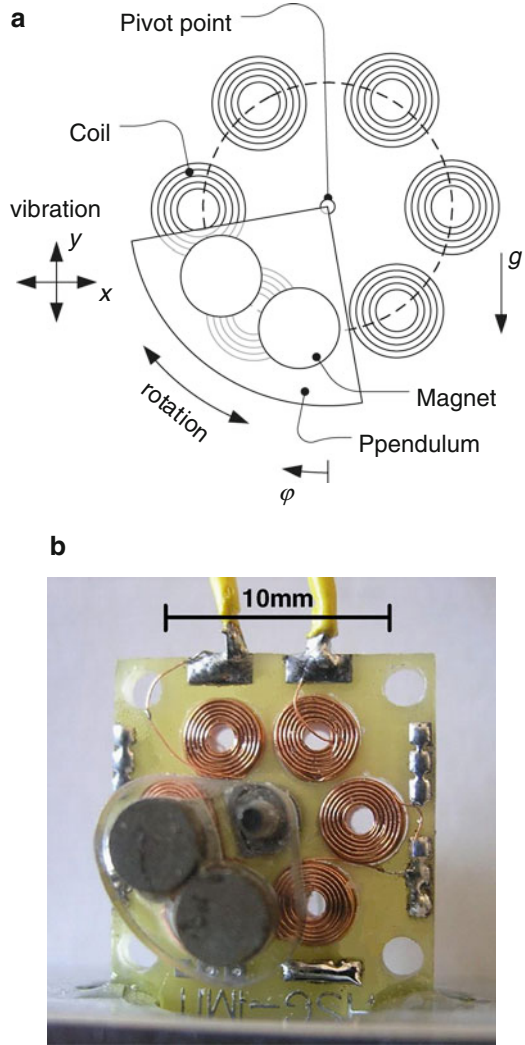
Preliminary Investigations

In the concept phase of this PhD book two different mechanisms for vibration energy harvesters have been developed. Both of them target one of the main challenges of vibration conversion identified in the literature review. This is namely the restriction to narrow band operation. Both developments (a non-resonant and a tunable transducer) have not been considered further since the general applicability could not be confirmed. Nevertheless the mechanisms are quite interesting from the scientific point of view. For this reason and for the sake of completeness this introduction section gives a brief overview of the two transduction mechanisms and the reasons why they have not been pursued in this PhD book.

Non-resonant Vibration Transducer

In order to obtain an efficient energy conversion over a wide frequency range, the aim of the first transducer was to create a transduction mechanism apart from the commonly used resonance phenomenon. This is possible with a springless system. The idea arising from this was to convert the linear vibration into a rotary motion. This can be realized using a pendulum system as shown in Fig. D.1a [24]. The pivot point of the pendulum is subjected to a vibration in the xy -plane. This oscillating linear movement is (under certain conditions) capable of enforcing a rotation of the pendulum. Once in rotation, the rotation frequency follows the change of the excitation frequency. Thus, a non-resonant conversion can be realized. The electromagnetic coupling is originated by the two opposite polarized magnets on the pendulum which cause a change of magnetic flux in the static coils. An experimental prototype is shown in Fig. D.1b.

Fig. D.1 (a) Schematic diagram of the non-resonant transducer design. (b) Experimental prototype used to confirm the expected behavior



The non-resonant transducer mechanism can be investigated using the equation of motion of a pendulum driven by an arbitrary motion of its pivot [32]:

$$\frac{d^2\varphi}{dt^2} + d\frac{d\varphi}{dt} + \omega_n^2 \sin \varphi = -\frac{d^2(x_0(t)/l_{red})}{dt^2} \cos \varphi + \frac{d^2(y_0(t)/l_{red})}{dt^2} \sin \varphi, \quad (D.1)$$

where l_{red} is the reduced length of the physical pendulum, d is the damping coefficient (as a combination of parasitic losses and electromagnetic damping), $x_0(t)$ and $y_0(t)$ are the coordinates of the pivot point, $\omega_n = \sqrt{g/l_{red}}$ the eigenfrequency

of the undamped motion and g is the acceleration of gravity. For pure vertical oscillation of the pivot point with the (displacement) amplitude Y and frequency f Eq. D.1 may be rewritten as:

$$\frac{d^2\varphi}{dt^2} + d\frac{d\varphi}{dt} + \omega_n^2 \sin \varphi = - \left((2\pi f)^2 Y / l_{red} \right) \cos(2\pi f t) \sin \varphi. \quad (D.2)$$

Even though this nonlinear problem exhibits chaotic behavior there are basically two cases which are interesting for vibration conversion purposes.

The first case considers a vibration transducer in the cubic centimeter range where the pendulum length is assumed to be at least one order of magnitude greater than the underlying vibration amplitude. In this case the vibration is not capable to start the rotation without an initial angular rate. Consequently the pendulum remains in the equilibrium position imposed by the acceleration of gravity. For vibration transducers this situation is not relevant. However, if an initial angular rate (which must be close to the vibration frequency) is applied to the system the vibration amplitude is capable of keeping the rotation alive. Example calculation results for a pendulum with $l_{red} = 5$ mm and a vibration amplitude of $Y = 100$ μm at different excitation frequencies are shown in Fig. D.2a. Because the direction of rotation does not change the angle simply increases steadily.

The second case considers a micro-scale vibration transducer where the pendulum length is assumed to be in the same order of magnitude as the vibration amplitude. In this case the vibration can start the rotation without an initial angular rate. However the system exhibits chaotic behavior and the direction of rotation changes in an unforeseeable manner. Typical calculation results for a pendulum with $l_{red} = 500$ μm and a vibration amplitude of $Y = 400$ μm at different vibration frequencies are shown in Fig. D.2b. The results show that a micro-scale device starts the rotation without an initial condition. Beyond this the considered mechanism offers the possibility for low frequency operation with a micro-scale system.

To verify the possibility of the non-resonant vibration conversion mechanism measurements with an experimental prototype on a lab-shaker have been performed. The results are shown in Fig. D.3. The applied vibration sweeps from 30 to 80 Hz with a linear decreasing vibration amplitude of 100 μm at 30 Hz and 75 μm at 80 Hz. The initial angular rate has been applied manually. Once in rotation the rotational frequency follows the excitation frequency. With a total volume of 1.5 cm^3 an output power between 415 μW and 2.95 mW can be generated in a load resistance of 20 Ω for the denoted frequency range. The measurement results clearly confirm the characteristic of non-resonant energy conversion.

In summary the major benefits of the established non-resonant vibration conversion mechanism are:

- The vibration can be converted over a wide frequency range
- The conversion mechanism is 2-dimensional in the xy -plane
- Low frequency vibration can be converted with a micro-scale device
- In case of chaotic behavior fundamental and harmonic modes in the vibration can be converted simultaneously

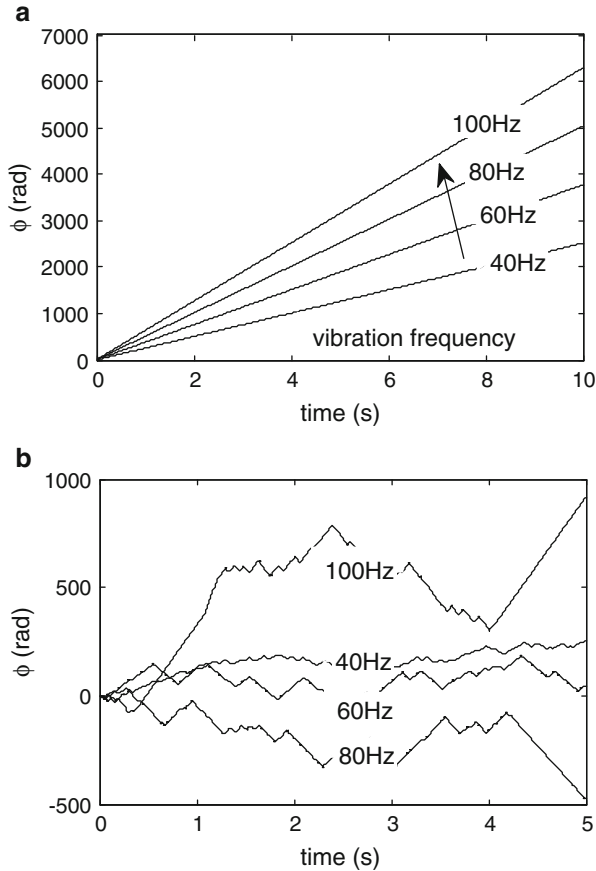
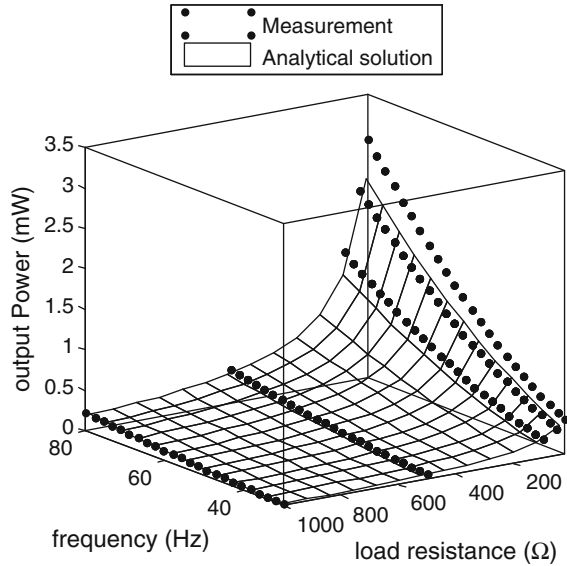


Fig. D.2 (a) With initial angular rate the (linear) vibration can drive the rotational movement of a (cubic centimeter range) transducer pendulum. (b) If the vibration amplitude is in the same magnitude of order as the pendulum length the system exhibits chaotic behavior. The rotation starts without an initial angular rate (expected for micro-scale device)

In spite of these advantages the transducer has not been studied further because of the following reasons.

For cubic centimeter range devices there are a couple of serious challenges which reduce the applicability. Actually the most important one is the necessity to apply an initial angular rate. This start-up condition can only be realized with an initial energy source. However if the initial energy source is empty the system can not return into an active mode by itself. In the application this is an important criterion for exclusion! Moreover a suitable sensor system is necessary to detect the vibration and to measure the vibration frequency in order to apply the correct initial angular rate. This sensor system needs energy as well. Beyond this the transducer must also be able to act as a motor in the first step. Both attributes increase the

Fig. D.3 Measured and predicted output power at different load resistances and vibration frequencies



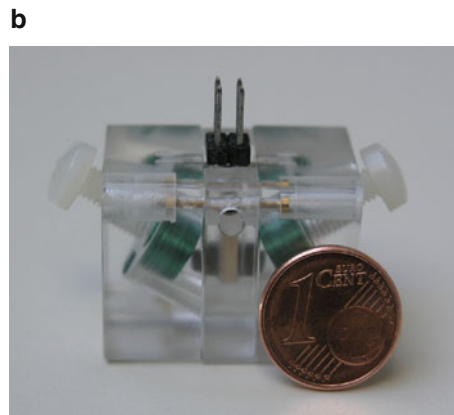
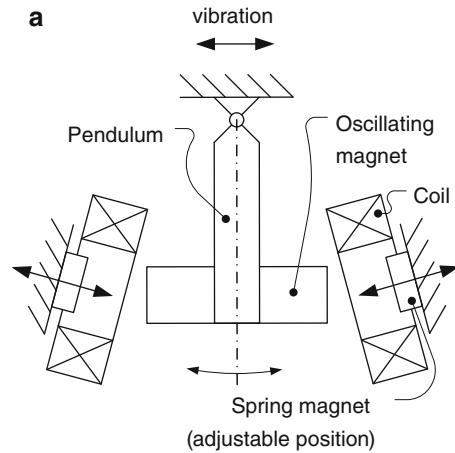
system complexity and costs and reduce the robustness. Another characteristic for cubic centimeter range devices is that harmonics in the vibration and high dynamic changes of the vibration frequency (i.e. gearshift in automobile) may disturb the continuous rotation. However in “the real world” the vibration often contains appreciable noise and harmonic components. Last but not least the rotating unbalance is an improper load condition for the bearing which challenges also the long term stability.

For micro-scale devices chaotic behavior is predicted which avoids the need for an initial condition. This significantly eases the requirements. As a rule of thumb the system turns into chaotic behavior not before the vibration amplitude is in the same magnitude of order as the pendulum length. However typical vibration amplitudes are tens of μm which is still quite small even for rotors in MEMS technology [71]. Moreover the fabrication of rotary bearings is rather delicate and not state of the art in MEMS fabrication. Even if the fabrication was feasible the expected output power scales with the fifth power of the linear dimension and at the end the performance will not be sufficient for an application.

Low Frequency Tunable Transducer

The intention of the second preliminary development was to design a vibration transducer with a self powered automatic frequency tuning mechanism. In this manner the narrow band operation should be expanded. The idea is based on existing resonators in which a linear suspended magnet oscillates (in a cylinder) between

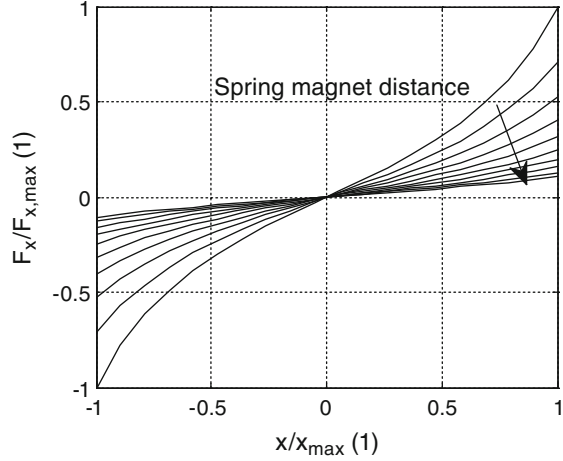
Fig. D.4 (a) Schematic diagram of tunable transducer design. (b) Experimental prototype used to confirm the expected behavior



two opposite polarized magnets. The repelling magnetic forces result in a nonlinear spring characteristic [17, 19, 26, 34]. However, in these devices an additional torque (also generated by the magnetic forces due to imperfection in symmetry) tries to rotate the oscillating magnet which causes a considerable friction loss at the cylinder wall.

The first enhancement of the presented approach is to implement a rotary suspension of the oscillating magnet as shown in Fig. D.4a. Therewith the unwanted friction can be decreased significantly. The second enhancement considers the nonlinear magnetic spring force. A general benefit of a nonlinear magnetic spring is that low resonance frequencies can be achieved within a small generator volume because the magnet requires only a small volume and the restoring forces decrease rapidly with increasing distance of the magnets. The idea of the presented development is to use the nonlinearity to adjust the resonance frequency. To understand this approach, magnetic force calculations have been performed using the vector potential model.

Fig. D.5 The stiffness of the system (and also the resonance frequency) depends on the spring–magnet distance



In this model the magnets are equivalent to thin coaxial coils in air. A comfortable equation for numerical calculation is presented in [72] where the force between two coaxial coils becomes:

$$F_x = \frac{N_1 N_2}{(2K + 1)(2m + 1)} \sum_{g=-K}^{g=K} \sum_{l=-m}^{l=m} F(g, l), \quad (\text{D.3})$$

with:

$$F(g, l) = \frac{\mu_0 z(g, l) I_1 I_2 k}{4\sqrt{R_1 R_2}} \left[\frac{2 - k^2}{1 - k^2} E(k) - 2K(k) \right]$$

$$z(g, l) = x - \frac{a}{2K + 1} g + \frac{b}{2m + 1} l$$

$$g = -K, \dots, 0, \dots, K; l = -m, \dots, 0, \dots, m$$

$$k^2(g, l) = \frac{4R_1 R_2}{(R_1 + R_2)^2 + z^2(g, l)} \quad (\text{D.4})$$

In this equation N_1 and N_2 are the total number of coil turns, I_1 and I_2 are the current in the coils, μ_0 indicates the relative permeability and K and m are control variables. The radius of the coils are denoted with R_1 and R_2 and the length with a and b respectively. The distance between the centre of the coils is x . The symbols $E(k)$ and $K(k)$ indicate elliptic integrals of the first and second kind which are typical in magnetic field calculations and appear also Sect. 3.4. The forces exerted on an oscillating magnet by two spring magnets in a coaxial arrangement are shown in Fig. D.5. The stiffness (and hence also the resonance frequency) obviously depends

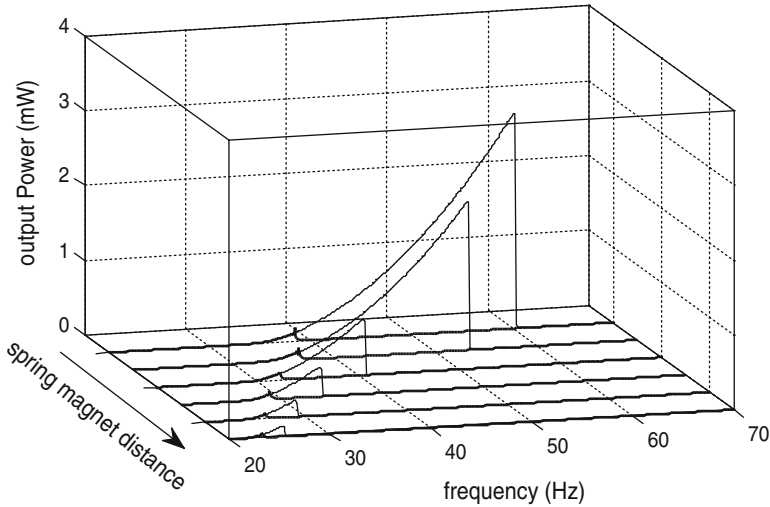


Fig. D.6 Measured output power for increasing (*light lines*) and decreasing (*bold lines*) frequency sweeps for different positions of the spring magnets. By manually adjusting the spring magnet position (in the mm-range) the resonance frequency of the experimental prototype can be shifted by 35 Hz

on the distance between the two spring magnets. Note that for the simulation in the time-domain Eq. D.1 can also be used here. However a term of the nonlinear angle dependent spring force $F(\varphi)$ must be added.

An experimental prototype used to confirm the intended behavior is shown in Fig. D.4b. To verify the possibility of the tunable low frequency vibration conversion mechanism, measurements with this prototype have been performed on a lab-shaker. Frequency response curves of the output power for different spring magnet positions and a vibration amplitude of $80 \mu\text{m}$ are shown in Fig. D.6. In this measurement the spring magnet position has been varied by 2.5 mm which results in a frequency shift of about 35 Hz (from 25 to 60 Hz). The corresponding output power varies from $130 \mu\text{W}$ to about 3.18 mW. Further increase of the resonance frequency can be obtained by reducing the spring magnet distance or by increasing the spring magnet dimension or magnetization and vice versa.

The major benefits of the established tunable vibration transducer mechanism are:

- Low parasitic damping due to ball-bearing
- Possibility of resonance frequency tuning by adjusting the spring magnet position
- Low resonance frequencies within small generator volume by using nonlinear magnetic spring forces
- Progressive spring force reduces the need for mechanical stoppers which increase the long term stability of the system

In spite of these advantages the transducer has not been studied further because of the following reasons.

Actually the reasons for this are not as clearly as for the previous non-resonant mechanism. The objective of this development was a low frequency actively tunable device. The manual tunability could already be demonstrated. However there are definitely a couple of challenges on the way to self tuning. The first one is due to the fact that the spring magnets have no electrical tuning capability (like i.e. piezoelectric material). This requires the integration of actuators which need energy and are difficult to realize within the available volume and the necessary adjusting range of the spring magnets (the sensitivity is about 15 Hz/mm). Moreover an important part of any active tunable device is a sensor system which provides the control variable and a control circuit itself. Both of them require energy and space. Altogether the system complexity increases dramatically and the device robustness decreases which lead to the conclusion that the established transducer mechanism is improper for implementing an active tunable device. However due to the hysteresis of the nonlinear system the mechanism is also improper for passively tunable devices. This is due to the fact that for a manually adjusted resonance frequency the state of the oscillation depends on the history of the system. Hence the requested state of the inner oscillation amplitude at resonance can usually not be guaranteed in the application. Nevertheless in the meanwhile the idea has been adopted and enhanced by several research groups. A very similar device with separated spring- and electromagnetic induction magnets has been presented in [83]. Also a piezoelectric transducer which uses nonlinear magnetic spring forces for tunability has been presented in [79].

About the Authors

Dirk Spreemann received the Dipl.-Ing. (FH) degree in Physical engineering from the University of Applied Sciences Ravensburg-Weingarten, in 2005. His diploma thesis focused on miniaturized electromagnetic vibration transducers. Beside the resonant vibration conversion he established one of the first nonresonant conversion mechanisms. While studying Microsystems engineering at the University of Freiburg he worked as a research engineer in the “Energy autonomous systems” group at the Institute of Micromachining and Information Technology HSG-IMIT in Villingen-Schwenningen. In this position he gained considerable experience in developing customized vibration transducers for industrial applications. His research interests lie in the area of micro power generation with a special focus on electromagnetic vibration conversion. In 2011 he received the Dr.-Ing. degree from the University of Freiburg. Currently he is with SICK AG where he works in the development of photoelectric sensors.

Yiannos Manoli holds the Fritz Huettinger Chair of Microelectronics at the Department of Microsystems Engineering (IMTEK), University of Freiburg, Germany. Since 2005 he additionally serves as director of the applied research “Institute of Micromachining and Information Technology” of the “Hahn- Schickard Gesellschaft” (HSG-IMIT).

His research interests are the design of low-voltage and low-power mixedsignal systems with over 300 papers published in these areas. The emphasis lies in Analog-to-Digital converters as well as in energy harvesting and sensor readout CMOS circuits. Additional research activities concentrate on motion and vibration energy transducers and on inertial sensors. Prof. Manoli received Best Paper Awards from ESSCIRC 2010 and 1988, MWSCAS 2007, MSE 2007, and PowerMEMS 2006. For his creative and effective contributions to the teaching of microelectronics and the design of a web-based animation and visualization of analog circuits (Spicy VOLTsim, www.imtek.de/svs) he received various awards including the Excellence in Teaching Award of the University of Freiburg and the Teaching Award of the State of Baden-Württemberg, both in 2010.

Professor Manoli is a Distinguished Lecturer of the IEEE. He is on the Senior Editorial Board of the IEEE “Journal on Emerging and Selected Topics in Circuits and Systems” and on the Editorial Board of the “Journal of Low Power Electronics”. He served as guest editor of the “Transactions on VLSI” in 2002 and the “Journal of Solid-State Circuits” in 2011. Professor Manoli has served on the committees of a number of conferences such as ISSCC, ESSCIRC, IEDM and ICCD, and was Program Chair (2001) and General Chair (2002) of the IEEE International Conference on Computer Design (ICCD).

He holds a B.A. degree (summa cum laude) in Physics and Mathematics, a M.S. degree in Electrical Engineering and Computer Science from the University of California, Berkeley and the Dr.-Ing. Degree in Electrical Engineering from the Gerhard Mercator University in Duisburg, Germany.

References

1. A. Timotin, M. Marinescu, Die optimale projektierung eines magnetischen kreises mit dauermagnet für lautsprecher. *Archiv für Elektrotechnik* **54**, 229–239 (1971)
2. Available in the internet: www.bahorb.de/~ga/PDF.Files/SimuMechAnsch.pdf, state April 2010
3. Available in the internet: <http://http://www.ibsmagnet.de/>, state April 2010
4. Available in the internet: <http://www.batteryuniversity.com/>, state April 2010
5. Available in the internet: <http://www.ferrosi.com/>, state April 2010
6. Available in the internet: <http://www.kcftech.com/>, state April 2010
7. Available in the internet: <http://www.lumedynetechnologies.com/>, state April 2010
8. Available in the internet: <http://www.perpetuum.com/>, state April 2010
9. Available in the internet: <http://www.vacuumschmelze.de/>, state April 2010
10. Available in the internet: <http://www.wieland.de/>, state April 2010
11. B. Yang et al., Electromagnetic energy harvesting from vibrations of multiple frequencies. *J. Micromech. Microeng.* **19**(3), 035001 (2009)
12. C. Peters, D. Maurath, W. Schock, F. Mezger, Y. Manoli, A closed-loop wide-range tunable mechanical resonator for energy harvesting systems. *J. Micromech. Microeng.* **19**(9), 094004 (2009)
13. C. Peters, D. Spreemann, M. Ortmanns, Y. Manoli, A CMOS integrated voltage and power efficient AC/DC converter for energy harvesting applications. *J. Micromech. Microeng.* **18**(10), 104005 (2008)
14. C. Serre, A. Perez-Rodriguez, N. Fondevilla, E. Martincic, S. Martinez et al., Design and implementation of mechanical resonators for optimized inertial electromagnetic microgenerators. *Microsyst. Technol.* **14**(4–5), 653–658 (2008)
15. C.B. Williams, R.B. Yates, Analysis of a micro-electric generator for microsystems, in *Proceedings of Transducers'95: Eurosensors IX. The 8th International Conference on Solid-State Sensors and Actuators, and Eurosensors IX*, Stockholm, June 1995, pp. 369–372
16. C.R. Mc Innes, D.G. Gorman, M.P. Cartmell, Enhanced vibrational energy harvesting using non-linear stochastic resonance. *J. Sound Vib.* **318**(4–5), 655–662 (2008)
17. C.R. Saha, T. O'Donnel, N. Wang, P. Mc Closkey, Electromagnetic generator for harvesting energy from human motion. *Sens. Actuators A* **147**, 248–253 (2008)
18. D. Hoffmann, C. Kallenbach, M. Dobmaier, B. Folkmer, Y. Manoli, Flexible polyimide film technology for vibration energy harvesting, in *Proceedings of PowerMEMS 2009*, Washington, DC, USA, December 2009, pp. 455–458
19. D. Spreemann et al., Tunable Transducer for low frequency vibrational energy scavenging, in *Proceedings of 20th Eurosensors Conference*, Göteborg, 2006

20. D. Spreemann, A. Willmann, B. Folkmer, Y. Manoli, Characterization and in situ test of vibration transducers for energy-harvesting in automobile applications, in *Proceeding of PowerMEMS 2008*, Sendai, Japan, November 2008, pp. 261–264
21. D. Spreemann, B. Folkmer, Y. Manoli, Optimization and comparison of back iron based coupling architectures for electromagnetic vibration transducers using evolution strategy, in *Proceedings of PowerMEMS 2009*, Washington, DC, USA, December 2009, pp. 372–375
22. D. Spreemann, D. Hoffmann, B. Folkmer, Y. Manoli, Numerical optimization approach for resonant electromagnetic vibration transducer designed for random vibration. *J. Micromech. Microeng.* **10**, 104001 (2008)
23. D. Spreemann, D. Hoffmann, E. Hymon, B. Folkmer, Y. Manoli, Über die Verwendung nicht-linearer Federn für miniaturisierte Vibrationswandler, in *Proceedings of Mikrosystemtechnik Kongress*, Dresden, 15–17 Oct 2007 (in German)
24. D. Spreemann, Y. Manoli, B. Folkmer, D. Mintenbeck, Non-resonant vibration conversion. *J. Micromech. Microeng.* **16**, 169–173 (2006). doi:10.1088
25. D. Zhu, S. Roberts, J. Tudor, S. Beeby, Design and experimental characterization of a tunable vibration-based electromagnetic micro-generator. *Sens. Actuators A* **158**(2), 284–293 (2010)
26. D.J. Domme, Experimental and analytical characterization of a transducer for energy harvesting through electromagnetic induction, Master book, Virginia State University, Petersburg, 2008
27. D.P. Arnold, Review of microscale magnetic power generation. *Trans. Magn.* **43**(11), 3940–3951 (2007)
28. D.J. Inman, *Engineering Vibration*, 2nd edn. (Prentice Hall, Upper Saddle River, 2000). ISBN ISBN 0–13–726142–X
29. E. Bouendeu, A. Greiner, P.J. Smith, J.G. Korvink, An efficient low cost electromagnetic vibration harvester, in *Proceedings of PowerMEMS 2009*, Washington, DC, USA, December 2009, pp. 320–323
30. E.I. Rivin, *Passive Vibration Isolation* (ASME Press, New York, 2003). ISBN 0-79-180187-X
31. E. Koukharenko et al., Microelectromechanical systems vibration powered electromagnetic generator for wireless sensor applications. *Microsyst. Technol.* **12**, 1071–1077 (2006)
32. F.J. Elmer (1998), <http://www.elmer.unibas.ch/pendulum/index.html>, state March 2010
33. G. Hatipoglu, H. Ürey, FR4-based electromagnetic energy harvester for wireless sensor node. *Smart Mater. Struct.* **19**(1), 015022 (2010)
34. G. Naumann, Energiewandlersystem für den Betrieb von autarken Sensoren in Fahrzeugen, PhD book, Technische Universität Dresden, Dresden, 2003 (in German)
35. G. Genta, *Vibration of Structures and Machines: Practical Aspects*, 3rd edn. (Springer, New York/Berlin/Heidelberg, 1998). ISBN 978–0–387–98506–0
36. H. Toepfer et al., Electromechanical design and performance of a power supply for energy-autonomous electronic control units, in *Proceedings of 51st IWK – Internationales Wissenschaftliches Kolloquium*, Technische Universität Ilmenau, Ilmenau, September 2006
37. H.A. Sodano, D.J. Inman, Comparison of piezoelectric energy harvesting devices for recharging batteries. *J. Intell. Mater. Syst. Struct.* **16**(10), 799–807 (2005)
38. H.A. Wheeler, Simple inductance formulas for radio coils. *Proc. IRE* **16**(10), 1398–1400 (1928)
39. I. Karaman et al., Energy harvesting using martensite variant reorientation mechanism in a NiMnGa magnetic shape memory alloy. *Appl. Phys. Lett.* **90**(17), 172505 (2007)
40. I. Rechenberg, *Evolutionsstrategie: Optimierung technischer Systeme nach Prinzipien der biologischen Evolution* (Frommann Holzboog, Stuttgart, 1973), 176 pp
41. I. Sari, T. Balkan, H. Kulah, A micro power generator with planar coils on parylene cantilevers, *IEEE Ph.D. Research in Microelectronics and Electronics (PRIME) Conference*, Istanbul, June 2008
42. J.K. Ward, S. Behrens, Adaptive learning algorithms for vibration energy harvesting. *Smart Mater. Struct.* **17**(3), 035025 (2008). 9 pp
43. J.O. Mur Miranda, Electrostatic vibration to electric energy conversion, PhD book, Massachusetts Institute of Technology MIT, Cambridge, 2004

44. J.T. Tanabe, *Iron Dominated Electromagnets: Design, Fabrication, Assembly and Measurement* (World Scientific, Singapore, 2005). ISBN 981-256327-X
45. K. Foelsch, Magnetfeld und Induktivität einer zylindrischen Spule, *Electr. Eng.* (Archiv für Elektrotechnik). **30**(3), 18 (1936)
46. K. Takahara, S. Ohsaki, H. Kawaguchi, Y. Itoh, Development of linear power generator: conversion of vibration energy of a vehicle to electric power. *J. Asian Electr. Veh.* **2**(2), 639–643 (2004)
47. E. Kallenbach, R. Eick, P. Quendt, T. Ströhla, K. Feindt, M. Kallenbach, *Elektromagnete Grundlagen, Berechnung, Entwurf und Anwendung* (Teubner, Stuttgart, 2003). ISBN ISBN 3-519-16163-X
48. L. Meirovitch, *Elements of Vibration Analysis* (Tata McGraw-Hill, New York, 1986). ISBN ISBN-10: 9780070413429
49. L. Wang, F.G. Yuan, Vibration energy harvesting by magnetostrictive material. *Smart Mater. Struct.* **17**(4), 045009 (2008)
50. L. Zuo, B. Scully, J. Shestani, Y. Zhou, Design and characterization of an electromagnetic energy harvester for vehicle suspensions. *Smart Mater. Struct.* **19**(4), 045003 (2010)
51. M. Bousonville, Optimierung von Lautsprecher Magnetsystemen mit dem Finite-Elemente-Verfahren, Diploma book, department Engineering sciences, Fachbereich Informationstechnologie und Elektrotechnik, Wiesbaden
52. M. Mizuno, D.G. Chetwynd, Investigation of a resonance microgenerator. *J. Micromech. Microeng.* **13**, 209–216 (2003)
53. M. Pereyma, Overview of the modern state of the vibration energy harvesting devices, in *Proceedings of MEMSTECH 2007*, Lviv-Polyana, (2007), pp. 107–112. ISBN: 978-966-553-614-7
54. M. Rossi, *Acoustics and Electroacoustics* (Artech House, Norwood, 1988). ISBN ISBN-10 0890062552
55. M. Ruellan, S. Turri, H.B. Ahmed, B. Multon, Electromagnetic resonant generator, in *Proceedings of 40th Industry Applications Conference Annual Meeting*, Hong Kong, October 2005, pp. 1540–1547
56. M.S.M. Soliman, E.M. Abdel-Rahman, E.F. El-Saadany, R.R. Mansour, A wideband vibration-based energy harvester. *J. Micromech. Microeng.* **18**(11), 115021 (2008). 11 pp
57. N. Wang, D.P. Arnold, Fully batch-fabricated MEMS magnetic vibrational energy harvesters, in *Proceedings of PowerMEMS 2009*, Washington, DC, December 2009, pp. 348–351
58. N.G. Stephen, On energy harvesting from ambient vibration. *J. Sound Vib.* **293**, 409–425 (2005)
59. N.N.H. Ching, H.Y. Wong, W.J. Li, P.H.W. Leong, Z. Wen, A laser-micromachined multi-modal resonating power transducer for wireless sensing system. *Sens. Actuators A* **97–98**, 685–690 (2002)
60. P. Niu, P. Chapman, L. DiBerardino, E. Hsiao-Weckslar, Design and optimization of a biomechanical energy harvesting device, in [PowerElectronicsSpecialistsConferencePESC, Rhodes, June 2008, pp.40624069](#)
61. P. Wang, X. Dai, X. Zhao, G. Ding, A micro electromagnetic low level vibration energy harvester based on MEMS technology. *Microsyst. Technol.* **15**(6), 941–951 (2009)
62. P. Wang, X. Dai, X. Zhao, G. Ding, A micro electromagnetic vibration energy harvester with sandwiched structure and air channel for high energy conversion efficiency, in *Proceedings of PowerMEMS 2009*, Washington, DC, 2009, pp. 296–299
63. P.D. Mitcheson, Analysis and optimisation of energy-harvesting micro-generator systems, PhD book, University of London, London, 2005
64. P.D. Mitcheson, T.C. Green, E.M. Yeatman, A.S. Holmes, Architectures for vibration-driven micropower generators. *IEEE/ASME J. Microelectromech. Syst.* **13**(3), 429–440 (2004)
65. R. Amirtharajah, Design of low power VLSI systems powered by ambient mechanical vibration, PhD book, Massachusetts Institute of Technology, Cambridge, 1999
66. R. Ramlan, Effects of non-linear stiffness on performance of an energy harvesting device, PhD book, University of Southampton, Southampton, 2009

67. S. Cheng, D.P. Arnold, A study of a multi-pole magnetic generator for low-frequency vibrational energy harvesting. *J. Micromech. Microeng.* **20**(2), 25015–25024 (2010). 10 pp
68. S. Cheng, N. Wang, D.P. Arnold, Modeling of magnetic vibrational energy harvesters using equivalent circuit representations. *J. Micromech. Microeng.* **17**, 2328–2335 (2007)
69. S. Park, K.C. Lee, Design and analysis of a microelectromagnetic vibration transducer used as an implantable middle ear hearing aid. *J. Micromech. Microeng.* **12**(5), 505–511 (2002). 7 pp
70. S. Roundy, On the effectiveness of vibration-based energy harvesting. *J. Intell. Mater. Syst. Struct.* **16**(10), 809–823 (2005)
71. S. Sundararajan, B. Bhushan, Static friction and surface roughness studies of surface micromachined electrostatic micromotors using an atomic force/friction force microscope. *J. Vac. Sci. Technol. A* **19**(4), 1777–1785 (2001)
72. S.I. Babic, C. Akyel, Magnetic force calculation between thin coaxial circular coils in air. *IEEE Trans. Magn.* **44**(4), 445–452 (2008)
73. S.J. Roundy, Energy scavenging for wireless sensor nodes with a focus on vibration to electricity conversion, PhD book, University of California, Berkeley, 2003
74. S.P. Beeby et al., A micro electromagnetic generator for vibration energy harvesting. *J. Micromech. Microeng.* **17**(7), 1257–1265 (2007)
75. T. Bäck, *Evolutionary Algorithms in Theory and Practice* (Oxford University Press, New York, 1996). ISBN 0-19-509971-0
76. T. Lai, C. Huang, C. Tsou, Design and fabrication of acoustic wave actuated microgenerator for portable electronic devices, in *Symposium on Design, Test, Integration and Packaging of MEMS/MOEMS*, Nice, April 2008, pp. 28–33
77. T. Link, Strukturdynamische Fehlermodellierung mikromechanischer Drehratensensoren für den Einsatz in der inertialen Navigation, PhD book, University of Freiburg, Freiburg, 2007 (in German)
78. T. von Büren, G. Tröster, Design and optimization of a linear vibration-driven electromagnetic micro-power generator. *Sens. Actuators A* **135**, 765–775 (2007)
79. V.R. Challa, M.G. Prasad, Y. Shi, F.T. Fisher, A vibration energy harvesting device with bidirectional resonance frequency tenability. *Smart Mater. Struct.* **17**(1), 15–35 (2008). 10 pp
80. W.T. Thomson, *Theory of Vibrations with Applications* (Prentice Hall, Upper Saddle River, 1998). ISBN 0-13-651068-X
81. X. Cao, W.J. Chiang, Y.C. King, Y.K. Lee, Electromagnetic energy harvesting circuit with feedforward and feedback DC-DC PWM boost converter for vibration power generator system. *Trans. Power Electron.* **22**(2), 679–685 (2007)
82. X. Gou, Y. Yang, X. Zheng, Analytic expression of magnetic field distribution of rectangular permanent magnets. *Appl. Math. Mech.* **25**(3), 297–306 (2004)
83. Z. Hadas, C. Ondrusek, V. Singule, Power sensitivity of vibration energy harvester. *Microsyst. Technol.* **16**(5), 691–702 (2010)

List of Figures

Fig. 1.1 Commonly applied coupling architecture where a magnet oscillates inside a coil. (a) Microfabricated implementation [14], (b) AA size transducer with multi modal resonating structure [59] and (c) with opposite polarized magnets used in a rucksack [17] 4

Fig. 1.2 Often favoured coupling architecture in microfabricated transducers where a magnet oscillates towards a coil without immersion. (a) Harvester with electroplated copper planar spring and discrete NdFeB magnet [61], (b) multi-frequency energy harvester based on acrylic beam [11] and (c) transducer based on micro-machined flexible polyimide films and planar coils [18] 5

Fig. 1.3 Coupling architecture based on opposite polarized magnets [78] 6

Fig. 1.4 (a) Silicon micromachined moving coil version of a magnet across coil arrangement [31]. (b) Moving magnet version based on discrete components [74] and (c) complete fine-mechanical implementation used to convert human motions [60]..... 7

Fig. 1.5 Electromagnetic coupling architecture typically used in moving coil loudspeakers has been considered for vibration transducers in [42] 9

Fig. 1.6 Normalized Power density of previous reviewed vibration transducer prototypes [27] supplemented by transducers reviewed in this book. The *dashed curves* indicate the theoretical scaling 9

Fig. 1.7 As a vital key role in the design of vibration transducers this book focuses the optimization of the output performance 12

Fig. 2.1	(a) Linear single degree-of-freedom (<i>SDOF</i>) spring-mass-damper model of a resonant vibration transducer with harmonic base excitation. (b) Dynamic free body diagram of the oscillating mass with the forces associate with the spring F_s and the damping element F_d	14
Fig. 2.2	(a) and (b) shows plot of Eq. 2.9, (c) and (d) shows plot of Eq. 2.10. Note that in contrast to the relative motion (a) the natural frequency for absolute motion decreases with increasing damping (c).....	17
Fig. 2.3	Nondimensional plot of the nonlinear restoring force. Softening behavior results for $\mu x_m^2 < 0$ and hardening behavior for $\mu x_m^2 > 0$. A pure linear spring is obtained for $\mu x_m^2 = 0$	17
Fig. 2.4	Frequency response for nonlinear hardening system. The <i>dash dotted curve</i> indicates the response of a linear system	18
Fig. 2.5	Frequency response of nonlinear system at different damping factors. The <i>dotted line</i> is the so called backbone or skeleton curve.....	19
Fig. 2.6	Popular models for linearized electromagnetic transducer analysis. Induction coil arranged in constant magnetic field with (a) rectangular cross section and concentrated windings and (b) circular cross section with spacious windings. Beyond the magnet boundary the magnetic field is assumed to be zero.....	20
Fig. 2.7	Circuit diagram representation of the electromagnetic subsystem for analytical analyses	21
Fig. 2.8	(a) Frequency- and (b) Phase response of the electrical network	22
Fig. 2.9	(a) Example of cylindrical air cored coil with inner radius of 1 mm (b) Ratio of resistance R_{coil} to reactance X_{coil} in per cent for different winding areas A_w of the example coil at 100 Hz. For typical winding areas the resistance dominates the impedance	23
Fig. 2.10	(a) Magnitude and (b) phase response for the subsystems and the overall transducer system. The <i>dashed curves</i> indicate the influence of the inductance	26
Fig. 2.11	Block diagram of the overall transducer model for simulation in Matlab/Simulink®	26
Fig. 2.12	Output power as a function of the electromechanical and parasitic damping	28
Fig. 2.13	Acceleration (<i>left</i>) and frequency content (<i>right</i>) of different example vibration sources. (a) air-filter housing of a car engine during country driving route, (b) tunnel boring machine close to the chisel and (c) mould for fabrication of concrete products.....	30

Fig. 2.14 First order power estimation for unconstrained condition for the vibration of the air-filter housing **(a)** and the vibration of the tunnel borer machine **(b)** 31

Fig. 2.15 Due to the high acceleration amplitude of the mould vibration it is appropriate to apply constrained condition for the first order power estimation 31

Fig. 2.16 Model of resonant electromagnetic vibration transducer used to investigate volume dependent effects 32

Fig. 2.17 Magnetic flux gradient at different ratios of h_{mag} and h_{coil} 33

Fig. 2.18 The optimal load resistance is dependent on the parasitic damping factor 34

Fig. 2.19 There are optimal ratio of h_{mag} and h_{coil} where the output voltage gets maximal 35

Fig. 2.20 The optimal ratio of h_{mag} and h_{coil} for output power generation are different as for output voltage generation 35

Fig. 2.21 The optimum output voltage is generated at the maximum possible damping factor ratio. In spite to this the damping ratio for optimum output power is less than the maximum value 36

Fig. 3.1 Development potential of $(BH)_{max}$ for permanent magnets [9] 42

Fig. 3.2 Maximal operating temperature for Neodymium magnets dependent on the material grade 42

Fig. 3.3 Initial BH-curve of steel 1010 which is used as material for the back iron components 43

Fig. 3.4 For FEA the $\mu(B)$ function needs to be monotonically decreasing. The *dashed curve* indicates the real characteristic 43

Fig. 3.5 In the applied vector potential model the magnet is equivalent to a current sheet 44

Fig. 3.6 **(a)** Half-section of a cylindrical permanent magnet (respectively thin layered coil) with four solution domains depending on whether the point of interest is in region 1, 2, 3 or 4. **(b)** Isolines of the magnetic flux density B_x in the centre plane of a cylindrical permanent magnet calculated with the semi-analytical approach 44

Fig. 3.7 **(a)** Geometrical parameters and coordinate system for rectangular permanent magnets. **(b)** Isolines of the magnetic flux density B_z in the xz - centre plane of a rectangular permanent magnet. The *arrow* points from north- to south-pole 47

Fig. 3.8 Isolines of the axially symmetric magnetic flux density component in x -direction on the centre plane of two opposite polarized cylindrical magnets (as in A III). The *arrows* point from north- to south-pole 48

Fig. 3.9	(a) Isolines of the magnetic flux density B_z in the yz -plane of symmetry of two rectangular permanent magnets (as in A VI). The <i>dashed curves</i> indicate the position of the magnets as in A VII. The magnetic flux density of this architecture is plotted in (b). The <i>arrows</i> point from north- to south-pole	48
Fig. 3.10	Flow chart of the calculation procedure used in the optimization approach. For each set of geometry parameters (n -dimensional vector dependent on architecture) the output power and output voltage is calculated	50
Fig. 3.11	Flowchart of evolution strategy (<i>ES</i>)	51
Fig. 3.12	Probability density function of a normal distribution used for the mutation of the genes	52
Fig. 3.13	Architecture specific calculation of the transduction factor as a part of the general calculation procedure	54
Fig. 3.14	(a) Coil turns between the magnet poles have regions with positive and negative magnetic flux. The discontinuity occurs at $\rho = R_{mag}$. (b) In coil turns above the magnet pole the magnetic flux is positive over the whole coil turn area	55
Fig. 3.15	To reduce the computation time the winding area of the “Magnet in–line coil” architectures without back iron is divided into cells and the number of windings in a cell are assumed to be concentrated in the centre	55
Fig. 3.16	Path of magnetic flux lines for “Magnet in–line coil” architectures with back iron. (a) Architecture A V is build–on a ring magnet whereas architecture A VI is based on a cylindrical permanent magnet (b)	57
Fig. 3.17	Flux–lines for different example calculation results of A V. The magnetic field spreads mainly on the circumference	58
Fig. 3.18	Flux–lines for different example calculation results of A VI. The magnetic field spreads mainly on the upper side	58
Fig. 3.19	(a) Geometrical situation for a single circular coil turn which moves towards a magnet. This basic geometry is used to obtain the overlapping area function for the situation in the “Magnet across coil” architectures (b)	59
Fig. 3.20	(a) Overlapping area functions of an example coil with 10 circular windings on the lateral side. (b) Overall differential area function A_o for the geometrical situation of the “Magnet across coil architectures”. The <i>dashdotted lines</i> indicate the reflection axis of the partial area functions	60

Fig. 3.21 (a) Magnetic flux linkage vs. displacement for the considered example coil. (b) Due to the saturation in the magnetic flux the resulting magnetic flux gradient decreases for large displacement amplitudes. The *dashed curve* indicates the constant transduction factor of the linearized model 61

Fig. 3.22 Path of magnetic flux of “Magnet across coil” architecture with back iron A VIII calculated with FEA 61

Fig. 3.23 Flux–lines for different example calculation results of A VIII. Appreciable flux leakage results for large gap between the magnets and thin back iron sheet (a). For thicker back iron sheet the magnetic flux mainly spreads through the gap (b). For thin back iron sheet and small gap the magnetic field between the magnets is quite homogeneous and the flux leakage can be reduced to a minimum (c) 62

Fig. 4.1 Geometrical parameters of “Magnet in–line coil” architecture without back iron A I 66

Fig. 4.2 When a magnet moves through a coil there is a point where the magnetic flux gradient is maximal. This point defines the optimal resting position of the magnet for output voltage generation but not for output power generation..... 67

Fig. 4.3 (a) To assess the optimal resting position in the fixed construction volume (defined by R_0 and h) the output power and output voltage has been calculated for different magnet dimensions and coil heights. (b) Resulting optimal resting positions for power– and voltage generation 67

Fig. 4.4 (a) Variable construction volume condition has been applied in a previous publication to assess the optimal resting position [22]. (b) Resulting maximum magnetic flux gradient point for different ratios of coil to magnet height and radii 68

Fig. 4.5 Output power optimization result for A I in a construction volume of 1 cm³. The figures show the resulting (a) inner displacement amplitude, (b) coil resistance, (c) optimal load resistance for different dimensions of the coil. There are definitely different optimal dimensions for maximizing (d) the magnetic flux gradient, (e) the output voltage and (f) the output power 70

Fig. 4.6	Optimization result for A I in construction volume of 1 cm ³ for operation at maximum magnetic flux gradient resting position (Voltage optimization). The arrangement of the figures is the same as in Fig. 4.5. Due to the different resting positions compared to the power optimization all the values are slightly higher apart from the output power which drops from 2.95 to 2.60 mW	71
Fig. 4.7	Optimal dimensions for (a) output power and (b) output voltage generation with A I. The <i>arrows</i> point from north to south pole	72
Fig. 4.8	Geometrical parameters of “Magnet in-line coil” architecture without back iron A II	73
Fig. 4.9	Optimization result for A II in a construction volume of 1 cm ³ . The figures shows the resulting (a) inner displacement amplitude, (b) coil resistance, (c) optimal load resistance for different dimensions of the coil. There are definitely different optimal dimensions for maximizing (d) the magnetic flux gradient, (e) the output voltage and (f) the output power	74
Fig. 4.10	Optimal dimensions for (a) output power and (b) output voltage generation with A II. The <i>arrows</i> point from north to south pole	75
Fig. 4.11	Geometrical parameters of “Magnet in-line coil” architecture without back iron A III	76
Fig. 4.12	Optimization result of A III in a construction volume of 1 cm ³ . The figures shows the resulting (a) inner displacement amplitude, (b) coil resistance, (c) optimal load resistance for different dimensions of the coil. There are definitely different optimal dimensions for maximizing (d) the magnetic flux gradient, (e) the output voltage and (f) the output power	77
Fig. 4.13	Optimal dimensions for (a) output power and (b) output voltage generation with A III. The <i>arrows</i> point from north to south pole	78
Fig. 4.14	Geometrical parameters of “Magnet in-line coil” architecture with back iron A IV. The <i>closed loop</i> indicates the direction of magnetic flux	79
Fig. 4.15	Typical convergence of the optimization of A IV. In (a) the mean value of the output power of the μ selected individuals is plotted versus the number of generation. The corresponding decrease of the variance (as long as the success rate is <1/5) is shown in (b). Accordingly the graphs for a voltage optimization run are plotted in (c) and (d)	80

Fig. 4.16 (a) power optimized dimensions and (b) voltage optimized dimensions of A IV 81

Fig. 4.17 Geometrical parameters of “Magnet in–line coil” architecture with back iron A V. The *closed loop* indicates the direction of magnetic flux 82

Fig. 4.18 Typical convergence of the optimization of A V. The mean value of the output power of the μ selected individuals is plotted in (a). The corresponding decrease of the variance (as long as the success rate is $<1/5$) is shown in (b). Accordingly the graphs for a voltage optimization run are plotted in (c) and (d) 83

Fig. 4.19 (a) power optimized dimensions and (b) voltage optimized dimensions of A V 84

Fig. 4.20 Geometrical parameters of “Magnet across coil” architecture without back iron A VI 85

Fig. 4.21 Optimization result for A VI in a construction volume of 1 cm³. The figures show the resulting (a) inner displacement amplitude, (b) coil resistance, (c) optimal load resistance for different dimensions of the coil. There are definitely different optimal dimensions for maximizing (d) the magnetic flux gradient, (e) the output voltage and (f) the output power 86

Fig. 4.22 Optimal dimensions for (a) output power and (b) output voltage generation with A VI. The *arrows* point from north to south pole 87

Fig. 4.23 Geometrical parameters of “Magnet across coil” architecture without back iron A VII 87

Fig. 4.24 Optimization result for A VII in a construction volume of 1 cm³. The figures shows the resulting (a) inner displacement amplitude, (b) coil resistance, (c) optimal load resistance for different dimensions of the coil. There are definitely different optimal dimensions for maximizing (d) the magnetic flux gradient, (e) the output voltage and (f) the output power 88

Fig. 4.25 Optimal dimensions for (a) output power and (b) output voltage generation with A VII. The *arrows* point from north to south pole 89

Fig. 4.26 Geometrical parameters of “Magnet across coil” architecture with back iron A VIII 89

Fig. 4.27	Optimization result for A VII in a construction volume of 1 cm ³ . The figures shows the resulting (a) inner displacement amplitude, (b) coil resistance, (c) optimal load resistance for different dimensions of the magnet and back iron sheet. There are definitely different optimal dimensions for maximizing (d) the magnetic flux gradient, (e) the output voltage and (f) the output power	91
Fig. 4.28	Optimal dimensions for (a) output power and (b) output voltage generation with A VIII. The <i>arrows</i> point from north to south pole	92
Fig. 4.29	Comparison of the maximum output power obtained with the optimal output power dimensions together with the corresponding voltage at the optimal output power points. The <i>dashed curve</i> indicates the mean value of all architectures. The <i>errorbars</i> indicate a variance of $\pm 10\%$ of the parasitic damping	93
Fig. 4.30	Comparison of the architectures maximum output voltage obtained with the optimal output voltage dimensions together with the corresponding power at the optimal output voltage points. The <i>dashed curve</i> indicates the mean value of all architectures. The <i>errorbars</i> indicate a variance of $\pm 10\%$ of the parasitic damping	94
Fig. 5.1	(a) Measurement set up for the experimental verification of the simulation models. Several test devices of the electromagnetic coupling architectures (in the figure A I is pictured) are mounted on a lab shaker. The shaker oscillates with controlled amplitude in z-direction. The induced voltage is measured with an oscilloscope. Therewith the transduction factor can be derived and compared to the simulation results. Exemplarily a test device of A IV is shown in (b) and a test device of A VI in (c)	96
Fig. 5.2	Measurement principle on the example of architecture A VI. With the amplitude of the <i>emf</i> (marked with <i>x</i>) and the oscillation velocity (marked with <i>o</i>) the transduction factor at the zero crossing position at <i>z</i> can be determined according to (2.21)	97
Fig. 5.3	Measurements with four different test devices have been performed to verify the A I simulation model	99
Fig. 5.4	The measured maximal transduction factor points are in good agreement with the predicted surface	100
Fig. 5.5	Measurements with three different test devices have been performed to verify the A II simulation model	101

Fig. 5.6 Measurements with six different devices have been performed to verify the simulation model of A III. **(a)** A 3 mm spacer is used for device 1–3, **(b)** a 4 mm spacer in device 4–6 102

Fig. 5.7 **(a)** Dimensions of the back iron components of the A IV test devices. **(b)** Measured and simulated transduction factor for different depths of immersion of the coil in the air gap 103

Fig. 5.8 **(a)** Dimensions of the ring magnet and the back iron components of the A V test devices. **(b)** Measured and simulated transduction factor for different depths of immersion of the coil in the air gap 104

Fig. 5.9 In the “Magnet across coil” architectures the gap between the coil and the magnet has been used as a measurement parameter beyond the position of the magnet in z -direction 105

Fig. 5.10 Measured and simulated transduction factor with **(a)** A VI device 1, **(b)** A VI device 2 and **(c)** A VI device 3 105

Fig. 5.11 Measured and simulated transduction factor with **(a)** A VII device 1, **(b)** A VII device 2 and **(c)** A VII device 3 106

Fig. 5.12 Measured and simulated transduction factor with **(a)** A VIII device 1 and **(b)** A VIII device 2 107

Fig. 6.1 **(a)** Cell resistance and **(b)** transduction factor of the cells in the global design domain 112

Fig. 6.2 Output power proportionality factor in the global coil design domain 113

Fig. 6.3 Cells of the global coil design domain sorted in descending order with respect to the output power generation capability 113

Fig. 6.4 Increase of the output power during the virtual winding process. At cell 1,354 the output power is maximal and the virtual winding process stops 114

Fig. 6.5 Resistance of the cells 115

Fig. 6.6 Progress of the cumulative resistance and the optimal load resistance 116

Fig. 6.7 Transduction factor of the cells 116

Fig. 6.8 Progress of the cumulative transduction factor during the “virtual winding” process 116

Fig. 6.9 Progress of the cumulative *emf* and the voltage at the optimal load resistance 117

Fig. 6.10 Progress of the electromagnetic damping 117

Fig. 6.11 Progress of the inner displacement amplitude 118

Fig. 6.12	Optimal doughnut-shaped coil topology for a cylindrical magnet. On the <i>right</i> picture the recess for the oscillating magnet is visible	118
Fig. 6.13	Without an appreciable loss in the output power the optimal coil topology can be idealized to a cap like shape	119
Fig. 6.14	Topology optimized coils made of enamelled copper wire. The “doughnut” shaped coil (a) cannot be fabricated using batch process. The radii are rather imprecise even for customized coils. The idealized cap like coil (b) can be batch-fabricated with standard tolerances	119
Fig. 6.15	The idealized optimal coil topology is as a combination of the architectures A I and A II	120
Fig. 6.16	Transduction factor of the idealized coil as a superposition of the A I and the A II part.....	120
Fig. 7.1	Vibration measurements in the engine compartment of a four-cylinder in-line diesel engine	125
Fig. 7.2	In the spectrogram (<i>above left</i>) there are three dominant frequencies visible (<i>dashed horizontal lines</i> at about 60, 115 and 180 Hz). Consequently these frequencies are also visible in the amplitude spectrum (<i>above right</i>). The magnitude in the spectrogram is correlated to the rpm (<i>below</i>)	125
Fig. 7.3	Car engine crankshaft drive	126
Fig. 7.4	The dominant frequencies in the spectrogram (Fig. 7.2) yield an rpm of 1,650 1/min	127
Fig. 7.5	Revolution per minute histogram for city-country-and highway driving route. In the city driving route the idle speed is dominant	127
Fig. 7.6	Optimization based on the boundary conditions from application (Table 7.1). The figures shows the resulting (a) inner displacement amplitude, (b) coil resistance, (c) optimal load resistance for different dimensions of the coil. There are definitely different optimal dimensions for maximizing (d) the magnetic flux gradient, (e) the output voltage and (f) the output power	129
Fig. 7.7	There are different optimal aspect ratios for the construction volume where the output power and output voltage is maximal	131

Fig. 7.8 Effect of boundary condition parameter variation on the output performance of the prototype. The diagrams show the influence of **(a)** the excitation amplitude, **(b)** the damping coefficient, **(c)** the wire diameter, **(d)** the overall construction volume and **(e)** the residual magnetic flux density 131

Fig. 7.9 Measured transduction factor in comparison to simulation results based on the components used in the prototype development 133

Fig. 7.10 Schematic diagram of the numerical model used for transient simulations (implemented in Matlab/Simulink®). Basic features are that the measured acceleration profile is used as the excitation, the nonlinearity of the spring can be adjusted and the oscillation range is limited by inelastic collision at mechanical stoppers 134

Fig. 7.11 Transient behavior of an unrestricted oscillation compared to limited oscillation ranges 135

Fig. 7.12 In the simulations the nonlinearity of the spring is limited. By definition the restoring force of the hardening spring at 2 mm inner displacement is twice as much as for the linear spring and the softening spring must be monotonically increasing 135

Fig. 7.13 **(a)** Normalized output power for an example (city driving route) excitation and different spring characteristics. **(b)** The output power can be increased by 10% for the 2nd and by 25% for the 4th order conversion using nonlinear hardening springs. **(c)** and **(d)** Optimal spring characteristic in comparison to the best linear springs 136

Fig. 7.14 Normalized output power for different spring characteristics and inner displacement limits. The 4th order conversion increases with the inner displacement limit. Finally at 2.5 mm inner displacement the 4th order conversion become more efficient than the 2nd order conversion 138

Fig. 7.15 Considered resonator assembly 140

Fig. 7.16 **(a)** Spring element with central hole for the magnet support and with outer holes to provide the mould process. **(b)** Defeatured and meshed solid model of the spring element used for FEA simulations 140

Fig. 7.17 Wöhler curve of CuSn6 R550 (UNS C51900) [10] 141

Fig. 7.18 First three modes of the resonator system. The linear oscillation of the 3rd mode is used for energy conversion 142

Fig. 7.19	Equivalent (von–Mises) stress in the spring element. The highest stress level results where the beam merges into the outer ring	142
Fig. 7.20	Laser precision cutting of the CuSn6 spring element	143
Fig. 7.21	CuSn6 spring element (a) before and (b) after the mould process. In the middle the rivet head of the magnet support is visible. The spring element in (a) is for 2nd order conversion (smaller beam width) and in (b) for 4th order conversion prototype	144
Fig. 7.22	Measured characteristic of the 2nd order and the 4th order conversion spring	145
Fig. 7.23	In accordance with the FEA simulation fatigue problems appears first at the maximum stress point	145
Fig. 7.24	(a) Exploded and sectional view of the prototype. (b) Photograph of an assembled device	146
Fig. 7.25	Measured output voltage (a) and output power (b) of the 2nd order conversion prototype at different excitation amplitudes and a resistive load of 4 k Ω . The measured values are compared to results obtained from transient simulation and to analytically calculated curves	147
Fig. 7.26	Measured output voltage (a) and output power (b) of the 4th order conversion prototype at different excitation amplitudes and a resistive load of 6 k Ω . The measured values are compared to results obtained from transient simulation and to analytically calculated curves	148
Fig. 7.27	Damping coefficient of (a) prototype for 2nd – and (b) prototype for 4th order conversion. The damping coefficient depends linearly on the excitation amplitude respectively the inner displacement	149
Fig. 7.28	Measured and simulated voltage and power for excitation with a city driving route vibration profile. In (a) the inner displacement limit in the simulation is set to 0.4 mm and in (b) to 1.5 mm	150
Fig. 7.29	Measured and simulated voltage and power for excitation with a country driving route vibration profile. In (a) the inner displacement limit in the simulation is set to 0.4 mm and in (b) to 1.5 mm	151
Fig. 7.30	Previously reviewed vibration transducer prototypes in [27] and transducers reviewed in this book. This figure is identical with Fig. 1.6. However the normalized power density of the prototypes developed in this book based on the presented optimization approach has been added.....	152
Fig. A.1	Measured copper fill factor of coils made of enamelled copper wire based on IEC 60317	158

Fig. B.1 Comparison of the axial magnetic flux density (B_x) of different magnet dimensions (a–c) calculated with the semianalytical approach based on the vector potential model and static magnetic FEA 159

Fig. B.2 Comparison of the axial magnetic flux density (B_z) of different magnet dimensions (a–c) calculated with the semianalytical approach based on the vector potential model and static magnetic FEA 160

Fig. C.1 (a) Nonlinear hardening spring realized with a cantilever beam clamped between two blocks. With the shape of the block profile the nonlinearity can be defined. (b) The shape of the block is an interpolation of i non equidistant suspension points 161

Fig. C.2 The underlying model for the calculation approach is based on a cantilever beam with a single suspension point. The suspension point has an offset in the y -direction 161

Fig. C.3 (a) The specified nonlinearity is divided into piecewise linear functions. (b) The spring constant can be assigned to a distance x_i between the fixing point of the cantilever and the suspension point..... 162

Fig. C.4 Flow chart of the block shape calculation 163

Fig. C.5 Shape of the block for the specified nonlinear spring characteristic 163

Fig. C.6 Specified nonlinearity in comparison to FEA simulation of the spring characteristic based on the calculated block shape 164

Fig. D.1 (a) Schematic diagram of the non-resonant transducer design. (b) Experimental prototype used to confirm the expected behavior..... 165

Fig. D.2 (a) With initial angular rate the (linear) vibration can drive the rotational movement of a (cubic centimeter range) transducer pendulum. (b) If the vibration amplitude is in the same magnitude of order as the pendulum length the system exhibits chaotic behavior. The rotation starts without an initial angular rate (expected for micro-scale device) 167

Fig. D.3 Measured and predicted output power at different load resistances and vibration frequencies 168

Fig. D.4 (a) Schematic diagram of tunable transducer design. (b) Experimental prototype used to confirm the expected behavior 169

Fig. D.5 The stiffness of the system (and also the resonance frequency) depends on the spring-magnet distance 170

- Fig. D.6 Measured output power for increasing (*light lines*) and decreasing (*bold lines*) frequency sweeps for different positions of the spring magnets. By manually adjusting the spring magnet position (in the mm-range) the resonance frequency of the experimental prototype can be shifted by 35 Hz 171

List of Tables

Table 1.1 Comparison of vibration transducer prototypes from the literature review 10

Table 2.1 Parameters used in the construction volume constraint calculation example 34

Table 3.1 Considered electromagnetic coupling architectures 39

Table 3.2 Fixed parameters of the overall boundary conditions used for the optimization 41

Table 3.3 Applied parameters of the evolution strategy for the optimization of “Magnet in–line coil” architectures with back iron in 6–dimensional search room 53

Table 5.1 Discrete magnet– and coil components used for the assembling of the electromagnetic coupling architecture test devices 98

Table 5.2 Used components for the A I test devices 99

Table 5.3 Used components for the A II test devices 100

Table 5.4 Used components for the A III test devices 101

Table 5.5 Dimensions of the AIV and AV test devices 103

Table 6.1 Illustration of the principal steps applied to find an optimal coil topology 111

Table 7.1 Specified design parameters for the optimization of the prototype electromagnetic coupling architecture 128

Table 7.2 Comparison of the optimal dimensions and the dimensions that are finally used in the prototype 130

Table 7.3 Most important material parameters of the spring material CuSn6 R550 (UNS C51900) 141

Table 7.4 Eigenfrequencies and maximum amplitudes for operation below the fatigue limit..... 142

Table A.1 Measured parameters of the coils used as reference to determine the copper fill factor..... 157

Table C.1 Underlying parameters for the calculation of the shape profile..... 162

Index

B

- Back iron, 11, 12, 38, 90, 92
- Battery, 1, 3
- Boundary condition, 12, 38, 41, 43, 49, 110, 128

C

- Coil, 21, 22, 49, 56
- Comparison, 8, 38, 41, 65, 101
- Construction volume, 32, 36, 38, 41, 65, 82, 85, 110
- Copper fill factor, 22, 43
- Coupling architecture, 3, 4, 10–12, 32, 35, 37, 128
- Customized development, 3

D

- Damping, 10, 14, 24, 25, 27, 31, 32, 34, 49, 92, 117, 133, 149
- Dimensioning, 6, 10, 12

E

- Electromagnetic damping element, 31
- Electromagnetic transduction mechanism, 2
- Electromagnetic vibration transducer, 9, 19, 36
- Electromotive force, 20
- Elliptic integral, 45, 54
- Energy harvesting, 1, 13
- Evolution strategy (ES), 51, 78

H

- Hardening, 17, 18

K

- Kinetic energy, 2

L

- Laplace transformation, 15
- Load resistance, 24, 33, 49, 115
- Loudspeaker, 8

M

- Magnet, 38, 41, 57
- Magnetic field, 11, 13, 19, 36, 43, 46, 49, 56, 62
- Magnetic field calculation, 38
- Magnetic flux, 20, 54, 56
- Magnetic forces, 3
- Mechanical stoppers, 134
- Modal analyses, 141

N

- Nonlinear spring system, 3, 13, 16

O

- Optimization, 6, 12, 35, 37, 38, 53, 109
- Output performance, 3, 10–12, 92, 97
- Output power, 2, 13, 27, 29, 31, 32, 34, 36, 49, 69, 92, 109, 128, 137
- Output voltage, 11, 34, 49, 93

P

- Prototype, 10, 12

R

Residual flux density, 33, 97, 100,
107
Resonance frequency, 11, 29
Resonant, 2, 10, 12
Resting position, 40, 49, 66,
133

S

Search space, 49, 69, 78, 79
Softening, 17, 18
Spacer, 75
Spring rate, 14
Stochastic vibrations, 3
Subsystem, 13, 14, 24, 32, 36
Success rate, 53, 78

T

Topology, 109
Transduction factor, 21, 24, 33, 34, 38, 40, 49,
57, 60, 95, 110, 115, 149

V

Verification, 95
Vibration transducer, 2, 10, 14, 29, 41, 79
Virtual winding process, 110, 113, 115

W

Wireless sensor networks (WSN), 1

Y

Young's modulus, 141